



Aalborg Universitet

AALBORG UNIVERSITY
DENMARK

Hybrid Interval-Stochastic Optimal Operation Framework of a Multi-carrier Microgrid in the Presence of Hybrid Electric and Hydrogen-Based Vehicles Intelligent Parking Lot

Agabalaye-Rahvar, Masoud ; Mirzapour-Kamanaj, Amir ; Zare, Kazem; Anvari-Moghaddam, Amjad

Published in:
Energy Systems Transition

DOI (link to publication from Publisher):
[10.1007/978-3-031-22186-6_8](https://doi.org/10.1007/978-3-031-22186-6_8)

Publication date:
2023

[Link to publication from Aalborg University](#)

Citation for published version (APA):

Agabalaye-Rahvar, M., Mirzapour-Kamanaj, A., Zare, K., & Anvari-Moghaddam, A. (2023). Hybrid Interval-Stochastic Optimal Operation Framework of a Multi-carrier Microgrid in the Presence of Hybrid Electric and Hydrogen-Based Vehicles Intelligent Parking Lot. In *Energy Systems Transition: Digitalization, Decarbonization, Decentralization and Democratization* (pp. 209-236). Springer. https://doi.org/10.1007/978-3-031-22186-6_8

General rights

Copyright and moral rights for the publications made accessible in the public portal are retained by the authors and/or other copyright owners and it is a condition of accessing publications that users recognise and abide by the legal requirements associated with these rights.

- Users may download and print one copy of any publication from the public portal for the purpose of private study or research.
- You may not further distribute the material or use it for any profit-making activity or commercial gain
- You may freely distribute the URL identifying the publication in the public portal -

Take down policy

If you believe that this document breaches copyright please contact us at vbn@aub.aau.dk providing details, and we will remove access to the work immediately and investigate your claim.

Power Systems

Vahid Vahidinasab
Behnam Mohammadi-Iva

Energy System Transition

Digitalization, Decarbonization,
Decentralization and Democratization

 Springer

Power Systems

Electrical power has been the technological foundation of industrial societies for many years. Although the systems designed to provide and apply electrical energy have reached a high degree of maturity, unforeseen problems are constantly encountered, necessitating the design of more efficient and reliable systems based on novel technologies. The book series Power Systems is aimed at providing detailed, accurate and sound technical information about these new developments in electrical power engineering. It includes topics on power generation, storage and transmission as well as electrical machines. The monographs and advanced textbooks in this series address researchers, lecturers, industrial engineers and senior students in electrical engineering.


****Power Systems is indexed in Scopus****


Vahid Vahidinasab •
Behnam Mohammadi-Ivatloo

Energy Systems Transition

Digitalization, Decarbonization,
Decentralization and Democratization

 Springer

Vahid Vahidinasab 
Department of Engineering
School of Science and Technology
Nottingham Trent University
Nottingham, UK

Behnam Mohammadi-Ivatloo 
School of Energy Systems
LUT University
Lappeenranta, South Karelia, Finland

ISSN 1612-1287

ISSN 1860-4676 (electronic)

Power Systems

ISBN 978-3-031-22185-9

ISBN 978-3-031-22186-6 (eBook)

<https://doi.org/10.1007/978-3-031-22186-6>

© The Editor(s) (if applicable) and The Author(s), under exclusive license to Springer Nature Switzerland AG 2023

This work is subject to copyright. All rights are solely and exclusively licensed by the Publisher, whether the whole or part of the material is concerned, specifically the rights of translation, reprinting, reuse of illustrations, recitation, broadcasting, reproduction on microfilms or in any other physical way, and transmission or information storage and retrieval, electronic adaptation, computer software, or by similar or dissimilar methodology now known or hereafter developed.

The use of general descriptive names, registered names, trademarks, service marks, etc. in this publication does not imply, even in the absence of a specific statement, that such names are exempt from the relevant protective laws and regulations and therefore free for general use.

The publisher, the authors, and the editors are safe to assume that the advice and information in this book are believed to be true and accurate at the date of publication. Neither the publisher nor the authors or the editors give a warranty, expressed or implied, with respect to the material contained herein or for any errors or omissions that may have been made. The publisher remains neutral with regard to jurisdictional claims in published maps and institutional affiliations.

This Springer imprint is published by the registered company Springer Nature Switzerland AG
The registered company address is: Gewerbestrasse 11, 6330 Cham, Switzerland

Preface

Energy systems are in a global evolution phase to face the conflicting challenges of energy trilemma including the security of supply, affordability, and sustainability which is now a public demand. Solving the energy trilemma called for a holistic approach to energy that addresses the interactions and inter-dependencies within the energy landscape and its connections with other sectors and systems and integrating social, economic, technical, and environmental issues. All the stakeholders and active players of this area emphasize not seeing the energy sectors in isolation and they all believe that the interaction of the energy sectors with each other, including the electricity, renewables, heat and cool, gas, hydrogen, and transport, is of great importance to successfully meet the trilemma with the least costs to the customers and environment.

There are four challenges in the way toward the future whole energy systems which are indeed driving pillars of this field. They are called “4D Energy Transition” and refers to Decarbonization, Decentralization, Digitalization, and Democratization. The 4D energy challenges call for a modern approach to energy systems operation.

This book is an attempt to bring together the experts from the different disciplines related to the energy systems as we strongly believe that there is a wealth of knowledge available in each discipline that is not widely known in the other disciplines and could be usefully employed to face with the challenges we are facing at this time and provide a comprehensive and in-depth reference for the researchers.

Chapter 1, entitled “*Energy Systems Decarbonization: Design Optimization of a Commercial Building MG System Considering High Penetration of Renewable Energies*,” studies the optimum design and energy management of an MG system considering reliability indices. The authors have used Particle Swarm Optimization (PSO) to solve the problem with different goals, including maximizing RESs’ penetration, minimizing CO₂ emissions, and total cost of the system. The penetration impacts of renewable energy resources and the yearly load growth are considered.

Chapter 2, entitled “*Data Analytics Applications in Digital Energy System Operation*,” presents algorithms and tools in the area of data analysis as well as the application of these tools to solve problems and challenges in modern electric power systems. This chapter provides basic concepts in data analysis methods, technical approaches and research opportunities for analyzing energy data, and its application in digital electric energy systems operation. Data security challenges, data management, and visualization are among the other topics covered in this chapter.

Chapter 3, entitled “*A New Stable Solar System for Electricity, Cooling, Heating, and Potable Water Production in Sunny Coastal Areas*,” aims to investigate the possibility of supplying cooling, power, heating, and freshwater in hot weather areas using solar systems. The optimal system design is provided in this chapter. The proposed system is composed of several subsystems to generate each product with high efficiency and reliability. To have continuity in energy supply (during nights), molten salt energy storage is used to establish the steady operation of the system. Then, the system is evaluated from thermodynamic and exergoeconomic viewpoints, and a parametric study is accomplished to study the effect on the system performance of key variables. In the end, the system is optimized to determine its best operating condition for different cases.

Chapter 4, entitled “*Investigation of a New Methanol, Hydrogen, and Electricity Production System Based on Carbon Capture and Utilization*,” introduces a new trigeneration system to decrease atmospheric carbon dioxide emission and produce methanol, hydrogen, and power. A flue gas stream with a defined composition, solar energy, and the atmospheric air are the system’s inlets. The organic Rankine cycle (ORC) is used to convert the flue gas to electric power. The proton exchange membrane electrolyzer using solar energy is used to generate hydrogen from water. Then, mass, energy, and exergy balance equations are applied for each subsystem to investigate the system’s thermodynamic performance. Also, the effect of changing operating parameters on the performance of each subsystem is studied.

Chapter 5, entitled “*Protection and Monitoring of Digital Energy Systems Operation*,” provides an insight into the protection and monitoring needs of advanced power grids. The key features of the protection systems and definitions of different protection functions are provided and bottlenecks of microgrids protection are presented. Fault responses of Inverter-Based Resources (IBRs) are studied in detail. The challenges of the conventional protection systems in IBR-dominated grids are studied and different solutions are proposed for such grids.

Chapter 6, entitled “*Optimizing Wind Power Participation in Day-Ahead Electricity Market Using Meta-Heuristic Optimization Algorithms*,” discusses the decision-making process of wind power plants in the electricity markets. The uncertainty of wind power is considered and a new procedure is presented to quantify probability density function (PDF) of each uncertainty interval based on wind power plant’s information. A probabilistic approach is presented for participation of wind power producers in day-ahead electricity markets.

Chapter 7, entitled “*Robust Energy Management of Virtual Energy Hub Considering Intelligent Parking Lots for the Plug-In Hybrid Electric Vehicles*,” investigates the modeling and optimal operation of electrical vehicles in the multi-energy virtual energy hubs. The electrical and thermal energy markets are considered and the virtual energy hub participates in both markets simultaneously. Different uncertainties such as PHEVs behavior, the output power of renewable energy resources, energy price, and energy demand are modeled using robust optimization approach.

Chapter 8, entitled “*Hybrid Interval-Stochastic Optimal Operation Framework of a Multi-carrier Microgrid in the Presence of Hybrid Electric and Hydrogen-Based Vehicles Intelligent Parking Lot*,” proposes a decision-making framework for multi-carrier microgrids under uncertainty. Multi-energy demands such as electrical, thermal, and cooling are supplied via various technologies besides exchanging power and natural gas from the respective upstream grids. The uncertain behavior of hybrid electric and hydrogen-based vehicles and uncertainty of generation of renewable energy sources (RESs), and different consumptions are considered and modeled using a hybrid interval/stochastic optimization.

To conclude, we would like to sincerely thank all of the authors who contributed to this book and also all the reviewers for their insightful observations and helpful comments.

Also, the editors would like to extend their deep gratitude to the following reviewers (sorted alphabetically) for their thoughtful comments on all the submitted book chapters including those that were accepted and published in this book:

Masoud Agabalaye-Rahvar
Ali Ahmadian
Farkhondeh Jabari
Arash Moradzadeh
Sajad Najafi-Ravadanegh
Younes Noorollahi
Ramin Nourollahi
Arman Oshnoei
Omid Sadeghian
Abbas Rabiee

The editors, authors, and reviewers of this book have dedicated their time and enthusiasm to creating it in the hope that it will be useful to researchers, graduate students, and practitioners interested in this field.

Nottingham, UK
Lappeenranta, Finland

Vahid Vahidinasab
Behnam Mohammadi-Ivatloo

Contents

1	Energy Systems Decarbonization: Design Optimization of a Commercial Building MG System Considering High Penetration of Renewable Energies	1
	Hamid HassanzadehFard, Vahid Dargahi, and Fatemeh Tooryan	
2	Data Analytics Applications in Digital Energy System Operation . . .	25
	Ali Paeizi, Mohammad Taghi Ameli, and Sasan Azad	
3	A New Stable Solar System for Electricity, Cooling, Heating, and Potable Water Production in Sunny Coastal Areas	53
	Leyla Khani and Mousa Mohammadpourfard	
4	Investigation of a New Methanol, Hydrogen, and Electricity Production System Based on Carbon Capture and Utilization	87
	Leyla Khani and Mousa Mohammadpourfard	
5	Protection and Monitoring of Digital Energy Systems Operation . . .	131
	Reza Jalilzadeh Hamidi and Ananta Bijoy Bhadra	
6	Optimizing Wind Power Participation in Day-Ahead Electricity Market Using Meta-heuristic Optimization Algorithms	163
	Hamed Dehghani and Behrooz Vahidi	
7	Robust Energy Management of Virtual Energy Hub Considering Intelligent Parking Lots for the Plug-In Hybrid Electric Vehicles . . .	183
	Mohammad Seyfi, Mehdi Mehdinejad, and Heidarali Shayanfar	

8 Hybrid Interval-Stochastic Optimal Operation Framework of a Multi-carrier Microgrid in the Presence of Hybrid Electric and Hydrogen-Based Vehicles Intelligent Parking Lot 209
Masoud Agabalaye-Rahvar, Amir Mirzapour-Kamanaj, Kazem Zare,
and Amjad Anvari-Moghaddam

Index 237

Chapter 1

Energy Systems Decarbonization: Design Optimization of a Commercial Building MG System Considering High Penetration of Renewable Energies



Hamid HassanzadehFard, Vahid Dargahi , and Fatemeh Tooryan

Abstract Due to growing electricity requirements, increasing energy cost, environmental emissions, and lack of access to electricity in many places, commercial building microgrid (MG) system based on renewable energy sources (RESs) offers an opportunity to overcome environmental problems and conserve fossil fuels. The penetration of renewable energy—distributed generations (DGs), especially photovoltaic (PV) and wind turbine (WT)—in the hybrid system has been increased. Energy storage systems (ESSs) are utilized to overcome the intermittent nature of RESs and reduce dispatchability of generations from fossil fuels. The main purpose is to determine the optimum design and energy management of an MG system considering reliability indices. A particle swarm optimization (PSO) is implemented to solve the problem with different goals, including maximizing RES's penetration, minimizing CO₂ emissions, and total cost of the system. The penetration impacts and the yearly load growth are considered. It is observed that high penetration of RESs reduces CO₂ emissions.

Keywords Energy systems decarbonization · Energy optimization · Renewable energy resources · Loss of power supply probability · Microgrid systems

H. HassanzadehFard

Department of Electrical Engineering, Miyaneh Branch, Islamic Azad University, Miyaneh, Iran

e-mail: hamid.hassanzadehfard@m-iau.ac.ir

V. Dargahi

School of Engineering & Technology, University of Washington, Tacoma, WA, USA

e-mail: vdargahi@uw.edu

F. Tooryan (✉)

Strategic System Planning, Puget Sound Energy, Bellevue, WA, USA

e-mail: fatemeh.tooryan@pse.com

1.1 Introduction

Nowadays, growing population, modernization across the world, the rising requirements for electrical energy, and limited availability of fossil fuel have led to more attention toward renewable energy-based distributed generation (DG) units, photovoltaics (PVs), and wind turbines (WTs) [1, 2]. Therefore, in the last decade, these types of DGs have been commonly applied to generate power among all energy resources. However, because of the intermittent behavior of renewable energy sources (RESs), flexibility is the main challenge for power system operators to guarantee the demand and supply balance in power systems. To achieve that balance, fossil fuels are still utilizing in a system as an important source to compensate the intermittency of RESs. Energy storage systems (ESSs) have been recognized as important technologies to overcome the deep decarbonization challenges with RESs when the employment of fossil fuels is reduced [3]. In addition, utilization of the ESSs is one of the prominent solutions to increase the RES penetration in isolated systems while reducing the environmental emissions within the system [4].

Numerous studies previously evaluated the microgrid (MG) system design and optimization considering different types of DGs. A multi-objective dynamic optimization methodology is proposed in [5] to reduce the operation cost of hybrid RES, implementation of nonrenewable DG, and environmental emissions. A new methodology is presented in [6] for optimum design of a solar cooling system. Ref. [7] applies a 24-hour-based economic/environmental scheduling of DGs with RESs in a grid connected MG. Particle swarm optimization (PSO) methodology is implemented for optimum scheduling of the MG to reduce the cost of generating units and environmental emissions. A novel energy optimization approach is proposed in [8] for optimization of the smart MG's performance by minimizing the operation cost and environmental emissions. Ref. [9] proposes a hybrid MG which includes PVs, WTs, ESSs, and diesel generators for supplying the electrical demands in a remote area located in Egypt. The primary aims of the proposed objective function are optimizing the cost of electricity, loss of power supply probability (LPSP), and renewable factor (RF). An integer-programming optimization methodology is implemented in [10] to determine different DGs' optimal sizes in a hybrid system, while the operational and initial costs of the system are minimized. A new methodology for optimum design of a hybrid RES is proposed in [11] for the residential buildings in rural areas, while the cost of energy is minimized, and the reliability of the system and an RF is maximized. Hybrid gravitational search and pattern search algorithm is proposed in [12] for optimum energy management and operation strategy of MG including RESs and electric vehicles. A novel optimization approach is presented in [13] to optimize the combination of RESs in existing buildings, while the building upgrade costs are minimized. Ref. [14] implements a game theory-based modeling technique to identify the optimum design and operation strategy of the multi-energy system with RESs. Ref. [15] presents an effective day-ahead resource scheduling framework for an MG, including different types of DGs, ESSs, and plug-in hybrid electric vehicles (PHEVs) for minimizing the total

operation cost during a 24-hour horizon. In [16], a multi-objective optimization methodology is utilized for RES optimal planning for minimizing the electricity cost and to maximize the electrical generation of RESs. An adaptive sparrow search optimization methodology is implemented in [17] to determine different DGs' optimum sizes in the hybrid system, while the investment cost is minimized. A modified seagull optimization approach is presented in [18] to obtain the optimum size of each DG in a hybrid system for minimizing the power generation cost. A novel bi-level optimization methodology is proposed in [19] to find the optimum carbon tax and renewable subsidy for multi-based energy systems.

In addition, the utilization of ESSs in hybrid systems with RESs can significantly improve the system's performance. [20] evaluates the various combinations of RESs and different types of ESSs for an isolated hybrid system. PSO algorithm is employed for optimal design of the proposed hybrid system. A novel optimization methodology is presented in [4] for optimization of an islanded MG including RESs and ESSs. Different meta-heuristic algorithms are implemented in [21] for optimum design of the hybrid system including RESs and different types of battery technologies for a village located in India. The proposed system is evaluated at a different maximum allowable value of LPSP. An economic approach is proposed in [22] to investigate the cost of investment and operation of a hybrid system with RESs and hybrid battery/hydrogen storage. A non-dominated sorting genetic algorithm is implemented in [23] for optimum design of the hybrid system which consists of RESs and various ESSs including pumped-storage hydropower (PSH) and BESSs to minimize the investment cost and CO₂ emissions. A new efficient method is presented in [24] to find the optimum size of a hybrid system with RESs and different types of ESSs including hydrogen and battery storages. Minimizing the life cycle cost of the system is the primary objective of the mentioned work. In [25], the optimum design and energy management of an MG are accomplished, considering RESs and various types of ESSs including electrical/thermal energy storages. PSO technique is applied to minimize the MG total cost, while all electrical/heating/cooling demands are satisfied. In [26], a novel approach is developed to obtain the optimum size of DGs in an MG including PVs, WTs, electrolyzer, hydrogen storage, and fuel cells (FCs). The main aims of this work are to minimize environmental emissions and fuel consumption with minimum total system cost.

[27] reviews the energy-saving options and their environmental effect on buildings and public lighting systems. Besides the direct energy-saving options such as utilization of RESs, available indirect options such as applying ESSs and demand response programs are reviewed. [28] investigates a clustering-based methodology to simultaneously optimum allocation of shunt capacitor and wind farm in distribution networks. In [29], the economic effect of utilization of ESSs on the variable RESs is evaluated. Table 1.1 shows the comparison of the proposed system and methodology with some related literatures.

In the existing literature, various methodologies have been proposed for optimal design of the hybrid systems including different types of demands. Considering the abovementioned works, in the present chapter, the existing gap in knowledge, namely, an optimum energy management and planning of the hybrid commercial

Table 1.1 Comparison of the proposed system and methodology with some related literatures

References	Energy storage	PV	WT	Fixed DG unit	Environmental issues	Reliability indexes	Load growth
[2]	*	*	*	—	—	—	—
[7]	*	*	*	*	*	—	—
[8]	*	*	*	*	*	—	—
[10]	*	*	*	*	—	—	—
[12]	*	*	*	*	—	—	—
[14]	*	*	*	*	*	—	—
[16]	—	*	*	*	—	—	—
[18]	*	*	*	*	—	*	—
[20]	*	*	*	—	—	*	—
[22]	*	*	*	*	—	—	—
[24]	*	*	*	*	—	—	—
[30]	—	*	—	*	—	*	—
Proposed methodology	*	*	*	*	*	*	*

building MG system based on RESs considering reliability indexes, is addressed. In this chapter, the PSO algorithm is employed to determine the optimum size of DGs. The primary objectives can be described as follows: (i) the fuel consumption reduction in the proposed system, (ii) the total minimum costs of the applied DGs, (iii) the environmental emissions reduction, and (v) the system reliability improvement. Therefore, the contribution of the chapter can be summarized as follows:

- Developing a new reliability-based methodology for optimal design of a commercial building MG system including RESs and ESSs
- Decarbonizing MG system by optimal implementing the ESSs and increasing the penetration of RESs
- Considering the commercial MG system load growth

This chapter is organized as follows. Section 1.2 contains the detailed description of different types of applied DGs in the commercial MG system, while the problem formulation is then discussed in Sect. 1.3. The numerical results are discussed in Sect. 1.4. Finally, the conclusions are presented in Sect. 1.5.

1.2 Description of the Proposed Commercial MG System

The proposed commercial MG system consists of PVs, WTs, FCs, and ESSs, which are defined firstly to describe the optimization problem.

1.2.1 PV

Recently, the utilization of PVs has been considered due to their environmental and economic benefits. These types of RES are one of the main DGs applied in most hybrid systems [30]. Various models are presented in the literature for evaluation of the power generated by PVs. The present chapter applies a simplified model to obtain the PV output electricity as follows [31]:

$$P_{PV}^t = \eta_{PV} \times N_{PV} \times P_{mpv} \times \left[\frac{G^t}{1000} \right] \quad (1.1)$$

in which P_{PV}^t is the power produced by PVs at each hour; P_{mpv} is the rated power of each unit under the condition $G_t = 1000$; N_{PV} is the optimum size of PVs; G^t is the solar radiation at time period t ; and η_{PV} is the relative efficiency of the PVs.

1.2.2 Wind Turbine

WTs are implemented to generate electrical power from the kinetic energy of the air. In general, the amount of power generation by the WTs directly depends on the wind velocity [32]. The generated electricity by WTs can be obtained from Eq. (1.2) [33]:

$$P_{WT}^t = N_{WT} \times \begin{cases} 0 & V^t < V_{\text{cut-in}}, V^t > V_{\text{cut-off}} \\ P_{WT}^{\text{rated}} \times \left[\frac{V^t - V_{\text{cut-in}}}{V_{\text{rated}} - V_{\text{cut-in}}} \right]^3 & V_{\text{cut-in}} \leq V^t < V_{\text{rated}} \\ P_{WT}^{\text{rated}} & V_{\text{rated}} \leq V^t \leq V_{\text{cut-off}} \end{cases} \quad (1.2)$$

in which P_{WT}^{rated} is the maximum power of WT; N_{WT} is the optimum size of WT; V^t is the wind velocity; V_{rated} is the nominal wind velocity; $V_{\text{cut-off}}$ is the cutout wind velocity; and $V_{\text{cut-in}}$ is the cut-in wind velocity.

In the proposed commercial MG system, the PVs and WTs are employed as RESs to satisfy the required demand in the system. It should be mentioned that these types of RESs' produce power highly depend on weather conditions. Consequently, having a backup source ensures the reliability of electric power supply.

1.2.3 Fuel Cell

In the proposed system, the FC is considered as a backup DG to have a reliable system. In this chapter, the required hydrogen for FCs is generated from natural gas using high-temperature steam, which is called steam methane reforming (SMR). SMR is currently one of the most commonly used processes for H_2 production [26]. The fuel consumption of the FCs at each hour can be obtained using Eq. (1.3) [34]:

$$\text{Fuel}_{\text{FC}}^t = P_{\text{FC}}^t \times \psi^{\text{Fuel}} \quad (1.3)$$

in which $\text{Fuel}_{\text{FC}}^t$ is the fuel consumption at each hour; P_{FC}^t is the power generated by FCs at each hour; and ψ^{Fuel} is the amount of required fuel to produce 1 kWh energy by FCs.

1.2.4 Electrical Energy Storage

Nowadays, the penetration of RESs such as PVs and WTs has been increased in the power systems because these clean energies have low operational costs; hence, environmental emissions are closed to zero by utilizing these technologies [35]. Furthermore, the produced power of the RESs is not controllable and highly depends on the weather conditions [22]. ESSs have been known as a key technology to overcome deep decarbonization challenges with high penetration of RESs while reducing the utilization of fossil fuels [3]. The surplus produced power of RESs is utilized to store in battery energy storage system (BESS) in the proposed energy management strategy for future uses [36]. The BESSs' stored energy at time period $t + 1$ can be expressed as (Eq. 1.4):

$$E_{\text{BESS}}^{t+1} = \begin{cases} E_{\text{BESS}}^t + \left\{ P_{\text{PV}}^t + P_{\text{WT}}^t - \frac{P_{\text{load}}^t}{\eta_{\text{DC/AC}}} \right\} \times \eta_{\text{BESS}}^{\text{ch}} & \text{charging state} \\ E_{\text{BESS}}^t - \left\{ \frac{P_{\text{load}}^t}{\eta_{\text{DC/AC}}} - (P_{\text{PV}}^t + P_{\text{WT}}^t) \right\} \frac{1}{\eta_{\text{BESS}}^{\text{disch}}} & \text{discharging state} \end{cases} \quad (1.4)$$

Equation (1.5) guarantees that the BESS charging/discharging states do not coincide.

$$S_{\text{BESS,ch}}^t + S_{\text{BESS,disch}}^t = 1 \quad \forall t \quad S_{\text{BESS,ch}}^t, S_{\text{BESS,disch}}^t \in \{0, 1\} \quad (1.5)$$

1.2.5 Loads

The proposed MG system consists of commercial demands. Therefore, the total power generated in the MG system is applied to supply these types of demands. In addition, when the commercial buildings are constructed, the growth in commercial demands is considered as an important factor in planning. Consequently, it is

essential to consider the load growth factor at the beginning of the project [37]. Accordingly, new DGs should be considered to provide the growth of commercial demands. The load curve for different years can be obtained by multiplying the initial load curve and the load growth factor for commercial demands in the mentioned year as follows.

$$P_{\text{Load}}^i = P_{\text{Load}}^{\text{Base}} \times \chi \quad (1.6)$$

where χ is the load growth factor, P_{Load}^i is the load curve at i th year, and $P_{\text{Load}}^{\text{Base}}$ is the commercial load curve at the first year.

1.3 Problem Formulation

The total commercial MG system demand is ensured to be fulfilled by the optimal planning of the system, while the proposed objective function is minimized, and the applied constraints are satisfied. A PSO algorithm is utilized on the proposed optimization problem with different goals and various constraints. The developed objective function and the considered constraints are introduced as follows.

1.3.1 Objective Function

The primary aim of this chapter is to determine the optimum energy management and planning of hybrid commercial MG system based on RESs considering LPSP index. The maximization of the penetration of RESs and the minimization of CO₂ emissions, fuel consumption, and total cost of the system are considered as the objectives of the present chapter. However, the net present cost (NPC) methodology [38–40] is implemented to obtain the total cost of MG system in the project lifetime. The proposed objective function is as follows:

$$\begin{aligned} \text{OF} = \min_{i \in \{\text{DGs, BESS}\}} & \left\{ \sum_i [N_i \times C_i^C] + \sum_i [N_i \times C_i^R \times \Phi^i] + \right. \\ & \frac{1}{\text{CRF}_{\text{ir}}^R} \times \sum_i [N_i \times C_i^{O\&M}] + \frac{\lambda_{\text{Fuel}}}{\text{CRF}_{\text{ir}}^R} \times \left[\sum_{t=1}^{T^{\max}} \text{Fuel}_{FC}^t \right] + \\ & \left. \frac{\lambda_E}{\text{CRF}_{\text{ir}}^R} \times \left[\sum_{t=1}^{T^{\max}} \text{Emission}^t \right] + \frac{\lambda_{\text{ENS}}}{\text{CRF}_{\text{ir}}^R} \times \left[\sum_{t=1}^{T^{\max}} P_{\text{Interrupted}}^t \right] \right\} \quad (1.7) \end{aligned}$$

where

$$\text{CRF}_{\text{ir}}^R = \frac{\text{ir} \times (1 + \text{ir})^R}{(1 + \text{ir})^R - 1} \quad (1.8)$$

$$\Phi_i = \sum_{n=1}^{Y_i} \frac{1}{(1 + \text{ir})^{L_i * n}} \quad (1.9)$$

$$Y_i = \begin{cases} \left\lfloor \frac{R}{L_i} \right\rfloor - 1 & \text{if } R \text{ is dividable to } L_i \\ \left\lfloor \frac{R}{L_i} \right\rfloor & \text{if } R \text{ is not dividable to } L_i \end{cases} \quad (1.10)$$

in which C_i^C , C_i^R , and $C_i^{O\&M}$ are the capital, replacement, and operation and maintenance costs of each applied DG, respectively. λ_{Fuel} , λ_E , and λ_{ENS} are the fuel cost ($\frac{\$}{\text{m}^3}$), penalty for environmental emissions ($\frac{\$}{\text{kg}}$), and the penalty for interrupted loads ($\frac{\$}{\text{kWh}}$), respectively. L_i and N_i represent the lifetime and optimum number of each DG. ir is the interest rate, and R is the project lifetime. $\text{Fuel}_{\text{FC}}^t$ is the fuel consumed by FCs at each hour. $P_{\text{Interrupted}}^t$ is the interrupted loads at each hour, and Emission^t is the amount of CO_2 emissions at each hour.

However, each term of the objective function can be provided as follows:

1.3.1.1 The NPC of Each Applied DG

The NPC of each applied DG consists of capital cost, replacement cost, and operation and maintenance cost and can be determined as follows:

$$\text{NPC}_{\text{DG}} = \sum_i [N_i \times C_i^C] + \sum_i [N_i \times C_i^R \times \Phi^i] + \frac{1}{\text{CRF}_{\text{ir}}^R} \times \sum_i [N_i \times C_i^{O\&M}] \quad (1.11)$$

1.3.1.2 Fuel Cost

The NPC of fuel consumed in the proposed MG can be obtained using Eq. (1.12):

$$\text{NPC}_{\text{Fuel}} = \frac{\lambda_{\text{Fuel}}}{\text{CRF}_{\text{ir}}^R} \times \left[\sum_{t=1}^{T^{\max}} \text{Fuel}_{\text{FC}}^t \right] \quad (1.12)$$

1.3.1.3 Penalty for CO₂ Emission

The NPC of CO₂ emission can be calculated as follows:

$$\text{NPC}_{\text{CO}_2} = \frac{\lambda_E}{\text{CRF}_{\text{ir}}^R} \times \left[\sum_{t=1}^{T^{\max}} \text{Emission}^t \right] \quad (1.13)$$

1.3.1.4 Penalty for Interrupted Loads

If the total power produced by DGs cannot provide the required demand, the remaining loads are interrupted. The NPC of the interrupted loads can be obtained by (1.14):

$$\text{NPC}_{\text{Interrupted}} = \frac{\lambda_{\text{ENS}}}{\text{CRF}_{\text{ir}}^R} \times \left[\sum_{t=1}^{T^{\max}} P_{\text{Interrupted}}^t \right] \quad (1.14)$$

1.3.2 Constraints

The multi-objective function is subjected to the following constraints.

1.3.2.1 Electrical Power Balance

The total power produced by DGs in the MG system should satisfy total commercial demand:

$$P_{\text{PV}}^t + P_{\text{WT}}^t + P_{\text{FC}}^t \pm E_{\text{BESS}}^t = P_{\text{Load}}^t - P_{\text{Interrupted}}^t \quad (1.15)$$

$$E_{\text{BESS}}^t \quad \begin{array}{l} + : \text{Discharging mode} \\ - : \text{Charging mode} \end{array}$$

where P_{PV}^t and P_{WT}^t are the power produced by PVs and WTs; P_{FC}^t is the generated electricity by FCs; E_{BESS}^t is the energy stored in BESSs; P_{Load}^t is the commercial demands of the MG system at time period t ; and $P_{\text{Interrupted}}^t$ is the interrupted loads at time period t .

1.3.2.2 Operational of Each Type of DG

The power produced by each type of DG should not exceed its rated power as follows:

$$0 \leq P_{FC}^t \leq P_{FC}^{\max} \quad (1.16)$$

$$0 \leq P_{PV}^t \leq P_{PV}^{\max} \quad (1.17)$$

$$0 \leq P_{WT}^t \leq P_{WT}^{\max} \quad (1.18)$$

where P_{FC}^{\max} , P_{PV}^{\max} , and P_{WT}^{\max} are the maximum power generated by FCs, PVs, and WTs, respectively.

1.3.2.3 Energy Storage Constraint

The stored energy in BESS should remain between its acceptable limits as follows:

$$E_{BESS}^{\min} \leq E_{BESS}^t \leq E_{BESS}^{\max} \quad (1.19)$$

where E_{BESS}^{\max} and E_{BESS}^{\min} are the maximum and minimum capacity of BESS.

1.3.2.4 Energy System Decarbonization

As mentioned, decarbonization is achieved by increasing the penetration of RESs such as PVs and WTs and a corresponding reduction in the consumption of fossil fuels in the proposed MG system. Clearly, the higher penetration level of RESs led to higher generation by these resources, higher amount of fuel savings, and, thereby, higher reduction of environmental emissions. The renewable energy portion (REP) (μ_{re}) is defined as follows:

$$\mu_{re} = \frac{\sum_{t=1}^{T^{\max}} (P_{PV}^t + P_{WT}^t)}{\sum_{t=1}^{T^{\max}} P_{Total}^t} \quad (1.20)$$

where P_{Total}^t is the total power produced in the proposed MG system. The value of REP should be more than a desired value as follows:

$$\mu_{re} \geq \mu_{desired} \quad (1.21)$$

where $\mu_{desired}$ denotes the desired REP.

1.3.2.5 Reliability Constraint

The reliability of the proposed commercial MG system is evaluated in terms of LPSP, which is introduced as the long-term average loss of electrical demand [41, 42]. At LPSP = 0, the load is fully supplied, whereas at LPSP = 1, no amount of the load is supplied. The LPSP can be calculated as follows:

$$\text{LPSP} = \frac{\sum_{t=1}^{T^{\max}} \text{LPS}^t}{\sum_{t=1}^{T^{\max}} P_{\text{Demand}}^t} \quad (1.22)$$

where the loss of power supply is LPS^t at each hour. The reliability constraint is considered as follows:

$$\text{LPSP} \leq \text{LPSP}^{\max} \quad (1.23)$$

where LPSP^{\max} is a predefined desired LPSP value.

1.4 MG Strategy to Supply Electrical Demands

In the understudy MG system, the applied DGs are responsible for satisfying the electrical demands. The PSO is implemented to find the optimum planning and operation strategy of the proposed system. The proposed strategy to fulfill the required demands in the commercial MG system is based on the optimum planning and operation of the system.

The PSO starts by generating random particles, and it searches for optimum parameters by updating generations. The sizes obtained by this algorithm must be checked to provide the required demands in the commercial MG system. However, if the given sizes and the total power produced by applied DGs cannot provide the load, with respect to the reliability indexes, the given sizes are rejected, and the PSO proposes other sizes. It should be mentioned that the proposed objective function is calculated whenever the total power produced by MG is sufficient to serve the required demand. The optimum size of each DG is obtained after reaching the maximum iteration. The obtained optimum sizes realize the economic operation of the MG under the condition of providing the total demands of the system with respect to the reliability indexes. In the studied commercial building MG system, the electricity produced by PVs, WTs, and FCs and energy stored in BESSs are implemented for satisfying the MG demands, based on the following steps.

First, the electrical power generated by PVs and WTs is employed to fulfill the required system demand. If the total energy generated by these RESs is more than the demands, the excess energy is utilized to store in the BESSs. After reaching the

maximum capacity of the BESSs, the remaining surplus energy is considered to be dumped. When the MG demand is more than the total generated electricity by the PVs and WTs, the available energy in BESSs is employed at first, and then the FCs start to produce power to supply the remaining demands. Finally, if the total MG generated power cannot satisfy the required demands, the remaining loads are interrupted with respect to the LPSP index.

1.5 Simulation Results and Discussion

In this chapter, the proposed optimization approach for optimum planning and operation strategy of the commercial building MG system including different types of DGs is numerically studied. The schematic of the commercial MG system under study is presented in Fig. 1.1.

To solve the suggested optimization problem, the PSO technique is implemented in MATLAB software. Interest rate is considered to be 8%, and the lifetime of the project is chosen 20 years [25, 26]. In the present chapter, economic data, hourly wind speed, solar irradiation, and commercial demands during a year are considered as input data in the simulation process [26, 37, 43–45]. The hourly commercial demands (p.u.) for 1 day is depicted in Fig. 1.2.

For more visualization, peak demand in different months during a year is illustrated in Table 1.2.

It should be mentioned that peak of commercial demand in the MG is considered 1000 kW. The yearly wind velocity and solar radiation are also considered in the optimization procedure as depicted for 1 day in Figs. 1.3 and 1.4.

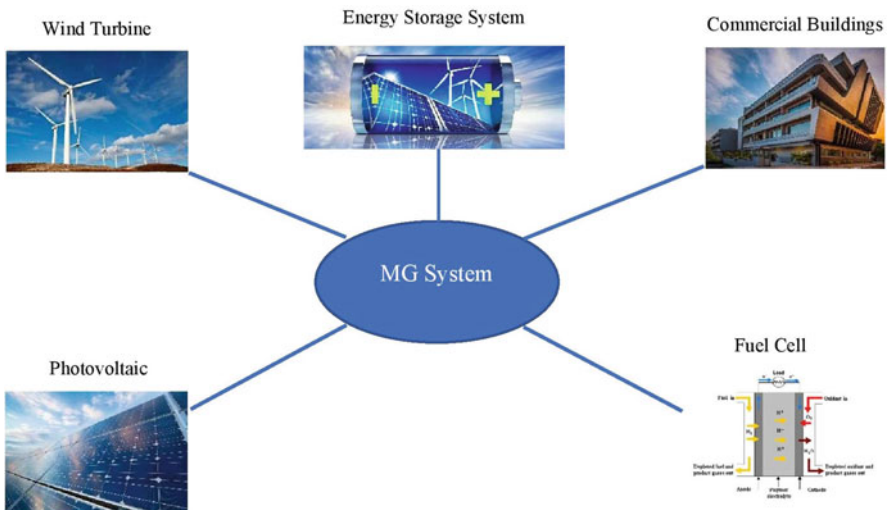


Fig. 1.1 Schematic of the proposed commercial MG system

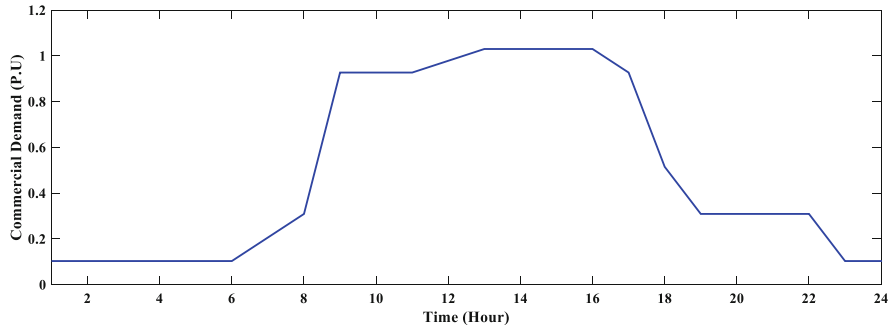


Fig. 1.2 Daily commercial demand

Table 1.2 Peak of commercial demands in different months

No.	Month	Peak of demand (p.u)	No.	Month	Peak of demand (p.u)
1	January	0.9091	7	July	1.0000
2	February	0.9182	8	August	1.0000
3	March	0.9273	9	September	0.9364
4	April	0.9364	10	October	0.9364
5	May	1.0000	11	November	0.9273
6	June	1.0000	12	December	0.9182

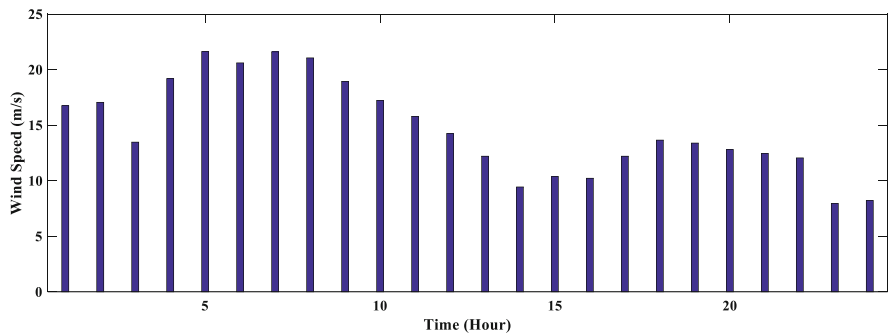


Fig. 1.3 Wind speed variations during a day

To show more details about these data, the wind speed (m/s) and solar radiation (W/m^2) average amount of different seasons are depicted in Table 1.3.

1.5.1 Optimization of the Commercial MG

In the studied MG system, FC is used as a backup DG, to satisfy the required demand when the electricity produced by RESs cannot meet the total demand. In addition,

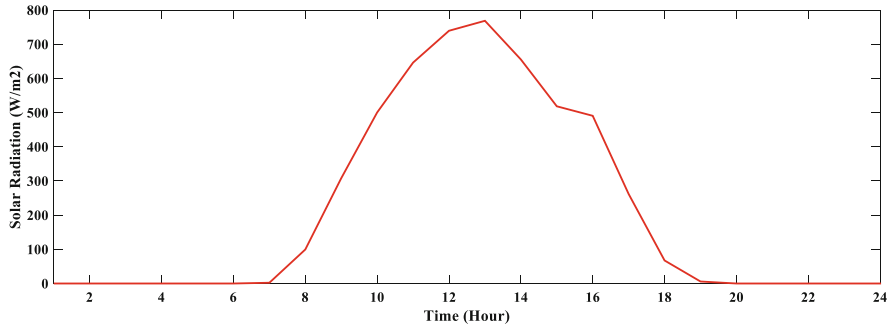


Fig. 1.4 Solar radiation during a day

Table 1.3 The wind speed and solar radiation average amount of different seasons

Season	Wind speed (m/s)		Solar radiations (W/m ²)	
	Average	Maximum	Average	Maximum
Spring	5.73	12.41	482	1005
Summer	6.31	26.2	604	1015
Fall	8.41	25.95	314	883
Winter	5.33	19.73	290	872

Table 1.4 The optimum sizes of each applied DG

PVs (kW)	WTs (kW)	BESSs (kWh)	FCs (kW)
524	487	1380	775

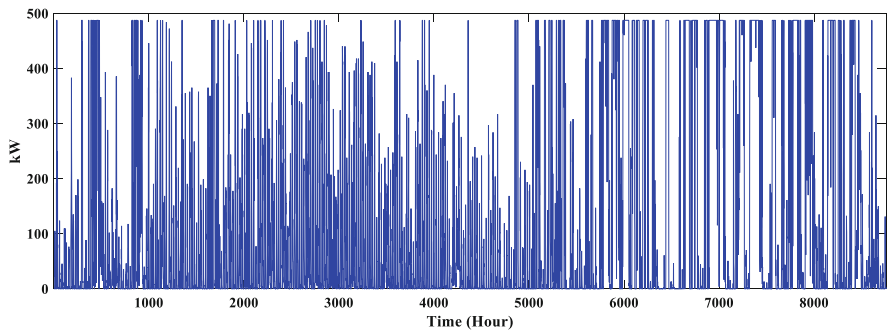


Fig. 1.5 The power produced by WT during a year

BESSs are employed to store the excess power produced by RESs. Utilization of the BESSs increase the RES penetration in the studied commercial MG system and reduce the system environmental emissions. Considering the optimization goals described in the chapter, the optimum sizes of each applied DG are depicted in Table 1.4. The total power generated by RESs is applied to fulfill the total commercial demand. The annual output power of the WTs and PVs is depicted in Figs. 1.5 and 1.6.

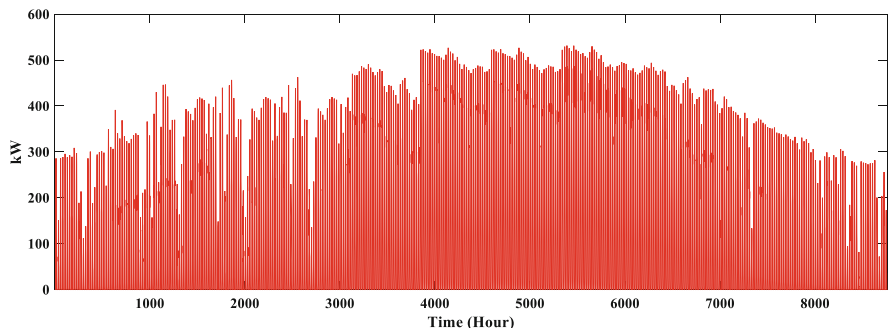


Fig. 1.6 The power produced by PVs during a year

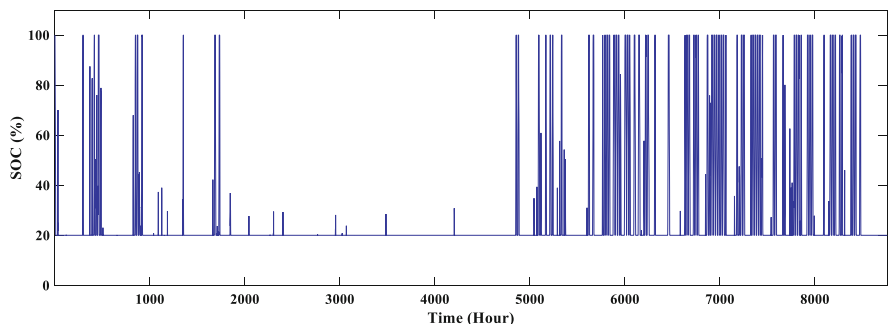


Fig. 1.7 The SOC level of BESSs during a year

If the total power produced by RESs is more than the MG demand, the surplus energy is utilized to store in BESSs. In addition, if the total demand is more than the total power generated by RESs, the remaining demands are satisfied by BESSs. However, the State of Charge (SOC) of the BESSs during a year is shown in Fig. 1.7.

Figure 1.7 demonstrates that the value of SOC varies between 20% and 100%, which represent the minimum level and a fully charged state, respectively. If the total power produced by RESs with available energy in BESSs cannot fulfill the demands, the produced power of FCs is applied to fulfill the required demand. Consequently, the produced electricity of FCs highly depends on the total power generated by RESs. Therefore, the produced power of FCs affected by the seasons according to Fig. 1.8.

From Fig. 1.8, it can be concluded that the percentage amount of FCs produced energy in summer and fall is lower than other seasons (23.25% and 21.47%, respectively). The reason is that the produced energy by RESs is higher in the mentioned seasons (PVs in summer and WTs in fall). In addition, the amount of CO₂ emissions, fuel consumption, interrupted demands, and LPSP is shown in Table 1.5.

It should be noted that if the total power generated by RESs, FCs, with stored energy in BESSs cannot meet the required demand, the remaining demand is

Fig. 1.8 The FCs produced energy in different seasons

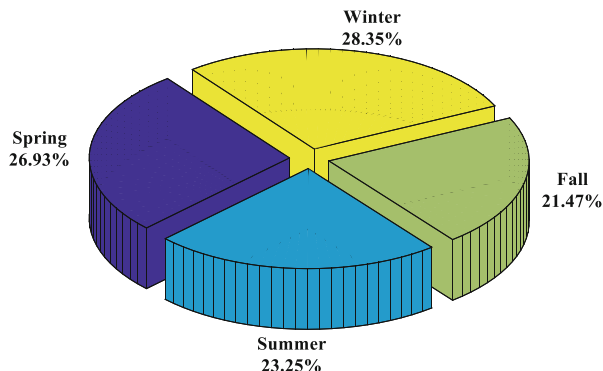


Table 1.5 The amount of CO₂ emissions, fuel consumption, interrupted demands, and LPSP

Fuel (10 ⁶ -m ³)	CO ₂ emissions (1000-tons)	Interrupted demands (MWh)	LPSP (%)
1.2364	0.9025	29.08	0.732

interrupted with respect to the reliability indexes ($LPSP \leq 2\%$). It can be concluded from Table 1.5 that the amount of interrupted demands is equal to 29.08 MWh, while the LPSP is equal to 0.732%.

To evaluate the impact of the RES penetration on the system decarbonization level, the CO₂ emission amount in different seasons is illustrated in Fig. 1.9.

As it shown in Fig. 1.9, the CO₂ emission amount in the summer and fall is lower than other seasons, which are equal to 0.209 (1000 tons) and 0.193 (1000 tons), respectively. The reason is that the highest RESs power generation occurs in the mentioned seasons.

It should be emphasized that the achieved results applying PSO satisfy the commercial demand for all hours during a given period. For more visualization, the RES- and FC-produced power and available energy in BESSs over a 24-hour day-ahead horizon are shown in Fig. 1.10.

According to Fig. 1.10, the PVs generate electricity from 8:00 to 18:00. It is obvious from this figure that the WTs can generate electricity all hours during this day. One can see that the total output power of WTs and PVs with the available energy in the BESSs cannot satisfy the required demand in the MG at the time period between 13:00 and 18:00. Accordingly, the remaining demand is fulfilled by FCs at the mentioned time period. For better explanation, the SOC level of the BESS during a day operation is illustrated in Fig. 1.11.

It can be seen that at the times between 20:00 and 24:00, the total power produced by RESs is more than the total system demand. So the excess power is stored in BESSs. In addition, the SOC of the BESSs is at its maximum level between 1:00 and 09:00.

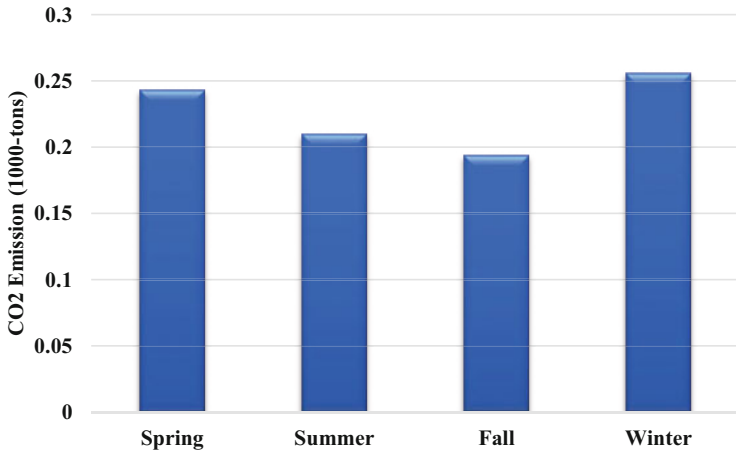


Fig. 1.9 CO₂ emission in different seasons

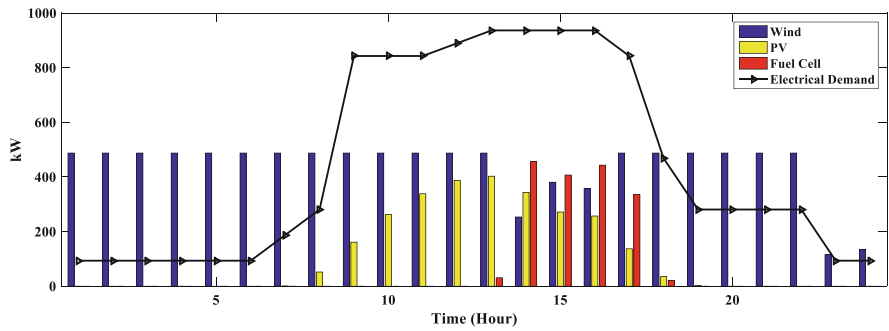


Fig. 1.10 The electricity generation mix over a 24-hour day-ahead horizon

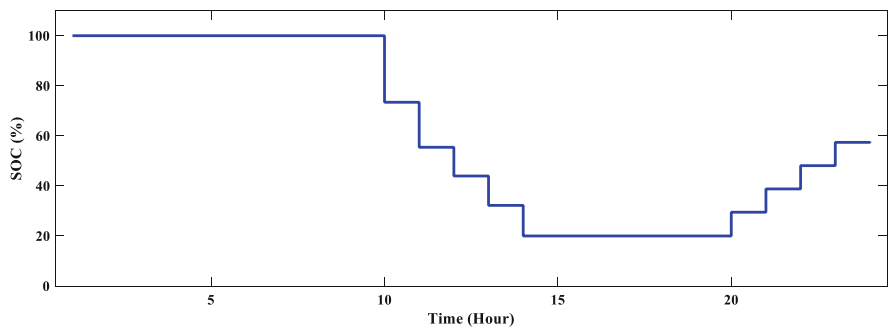


Fig. 1.11 The SOC level of the BESS during a day

1.5.2 Impact of RES and BESS Utilization on System Decarbonization

In this section, different scenarios are considered to evaluate the impact of the utilization of RESs and BESSs on system decarbonization:

1. FC solely: As the first scenario, only the produced power of FCs is applied to satisfy the demand.
2. RESs, FCs: In this scenario, the RES- and FC-generated power are employed to fulfill the required demands in the MG.
3. RESs, BESSs, FCs: As the final scenario, the power produced by RESs, FCs, and available energy in BESSs are applied to satisfy the required commercial demands in the MG.

To depict the efficiency of the developed methodology, a comparison based upon fuel consumption and renewable penetration level between different possible solutions is depicted in Table 1.6.

According to Table 1.6, the amount of fuel consumption at the first scenario is the highest, as it is equal to $2.1177 (10^6\text{-m}^3)$. As a result, employing RESs in the proposed MG system leads to a significant fuel consumption saving. In the second scenario, there is about $0.783 (10^6\text{-m}^3)$ reduction in the amount of fuel consumption when the RESs were applied in the MG. From this table, it can be concluded that there is a significant reduction ($0.88 10^6\text{-m}^3$) in the amount of fuel consumption when RESs and BESSs are employed in the MG system in comparison with the first scenario. It should be emphasized that BESSs would play an important role in increasing the RESs penetration. Table 1.6 indicates that there is a 5% increase in the RESs penetration by utilizing BESS in the MG in comparison to the second scenario.

In this section, the effect of utilization of RESs and BESSs on the system decarbonization is evaluated. The amount CO_2 emission for different scenarios is shown in Fig. 1.12.

In Fig. 1.12, it is seen that utilizing the RESs in the MG reduces the amount of CO_2 emission from 1.546 (1000-tons) to 0.974 (1000-tons). It can be seen from this figure that, after utilizing the BESSs, the amount of CO_2 emission has fallen 643.5 tons during a year in comparison to the first scenario. Consequently, it can be observed that by applying RESs and BESSs in the MG and reducing in the fuel consumption in the MG, the CO_2 emissions would be remarkably reduced.

Table 1.6 Impact of RES and BESS on the performance of MG system

No	Scenario	Renewable penetration	Fuel (10^6-m^3)
1	FC	0%	2.1177
2	FC + RES	37%	1.3353
3	FC + RES + BESS	42%	1.2364

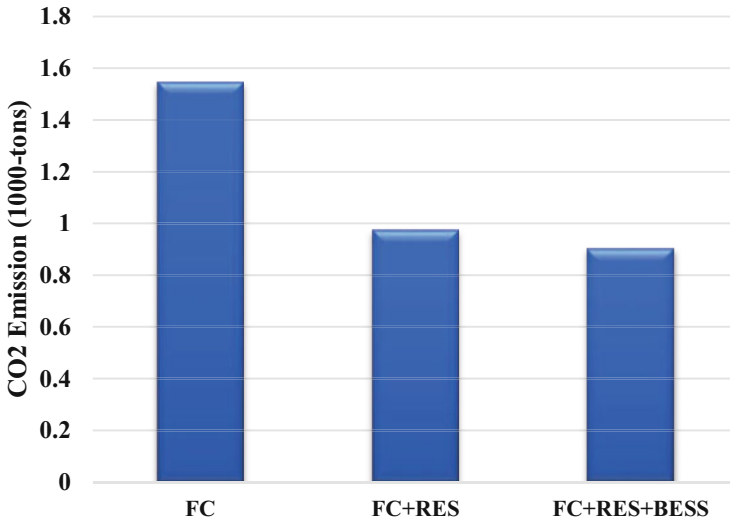


Fig. 1.12 Effect of RESs and BESSs on system decarbonization

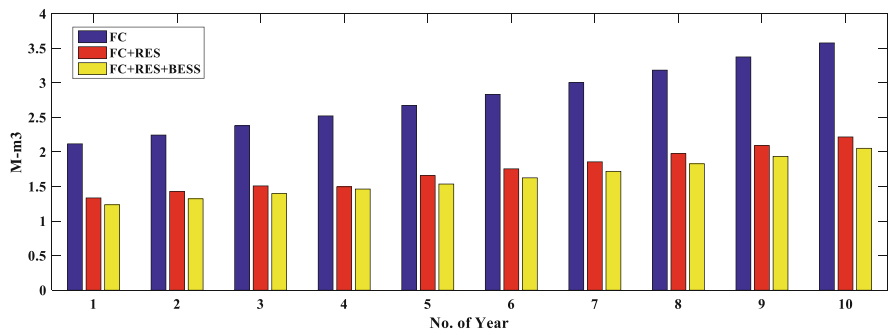


Fig. 1.13 The fuel consumption amount for each year in different scenarios

1.5.3 Considering Load Growth in the MG

In this chapter, the load growth coefficient is considered in order to evaluate the effect of the utilization of RESs and BESSs on system decarbonization during different years. For this purpose, it is assumed that the total commercial demand in the MG increased from 1000 kW in the first year to 1700 kW in 10th year, an average growth rate of 6% [46] per year. In addition, the load growth will be saturated after 10 years. As mentioned before, new DGs should be added in the MG to supply the growth of commercial demands, while the reliability of the system is satisfied. For evaluation of the applying RESs and BESSs in the MG system for different years, the fuel consumption amount for different scenarios is illustrated in Fig. 1.13.

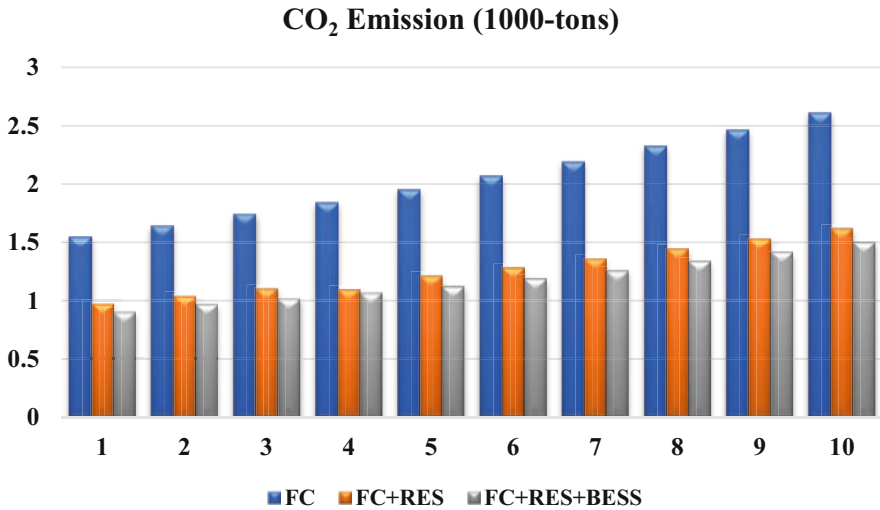


Fig. 1.14 The amount of CO₂ emission at each year for different scenarios

It can be concluded that utilizing the optimum size for RESs and BESSs at each year reduces the fuel consumption during the years. In addition, the amount of CO₂ emission for different scenarios is depicted in Fig. 1.14.

It is clear that utilizing the optimal capacity of RESs and BESSs at each year reduces the CO₂ emission during the years. The results depict that installing the optimal configuration during different years reduces the total amount of CO₂ emission from 46.5 to 26.75 (1000-tons). As a result, applying RESs and BESSs in the MG system implies a significant reduction of about 19.75 (1000-tons) of CO₂ emission (for 20 years), when comparing to the first scenario. It is also worth mentioning that the optimum utilization of RESs and BESSs in different years plays a vital role in system decarbonization.

1.6 Conclusion

In this chapter, a novel methodology is proposed for optimum design and energy management of an islanded hybrid system including PVs, WTs, FCs, and BESSs, considering reliability index. The system is implemented for supplying electricity to commercial building MG. The suggested model was solved applying the PSO methodology and tested on a commercial building MG system to minimize the CO₂ emission, fuel consumption, and total cost of the MG. Due to high volatility of power produced by RESs, which highly depends on the weather conditions, BESSs are used in the proposed commercial MG. In this chapter, different scenarios are considered in order to evaluate the efficiency of the proposed approach. The results, achieved from simulation of the problem, have shown that utilizing the RESs

and BESSs has a positive effect on the system decarbonization. The results depict that by utilizing RESs, there is about 37%, and by utilizing BESSs, there is about 42% reduction in the amount of CO₂ emission. It can be concluded that applying the RESs and BESSs in the MG reduces the amount of CO₂ emission from 1.546 (1000-tons) to 0.9025 (1000-tons). It means that the amount of CO₂ emission has fallen 643.5 tons during a year in comparison to the first scenario. In addition, the load growth coefficient is also considered in the simulation process. It is observed from the results that optimum utilization of the RESSs and BESSs during different years reduces the total amount of CO₂ emission from 46.5 to 26.75 (1000-tons). For future works, the proposed approach can be developed to evaluate the effect of demand response programs on the system performance. In addition, the stochastic behavior of RESs can be considered in the optimization process.

References

1. Khan FA, Pal N, Saeed SH (2021) Optimization and sizing of SPV/wind hybrid renewable energy system: a techno-economic and social perspective. *Energy* 233:121114
2. Aliabadi MJ, Radmehr M (2021) Optimization of hybrid renewable energy system in radial distribution networks considering uncertainty using meta-heuristic crow search algorithm. *Appl Soft Comput* 107:107384
3. He W, Dooner M, King M, Li D, Guo S, Wang J (2021) Techno-economic analysis of bulk-scale compressed air energy storage in power system decarbonization. *Appl Energy* 282:116097
4. Gomes JG, Xu HJ, Yang Q, Zhao CY (2021) An optimization study on a typical renewable microgrid energy system with energy storage. *Energy* 234:121210
5. Sharma R, Kodamana H, Ramteke M (2022) Multi-objective dynamic optimization of hybrid renewable energy systems. *Chem Eng Proc Proc Intens* 170:108663
6. Ferrara M, Santa FD, Bilardo M, Gregorio AD, Mastropietro A, Fugacci U, Vaccarino F, Fabrizio E (2021) Design optimization of renewable energy systems for NZEBs based on deep residual learning. *Renew Energy* 176:590–605
7. Das G, De M, Mandalm KK (2021) Multi-objective optimization of hybrid renewable energy system by using novel autonomic soft computing techniques. *Comput Electr Eng* 94:107350
8. Ullah K, Hafeez G, Khan I, Jan S, Javaid N (2021) A multi-objective energy optimization in smart grid with high penetration of renewable energy sources. *Appl Energy* 299:117104
9. Hemeida AM, Omer AS, Bahaa Eldin AM, Alkhalaf S, Ahmed M, Senjyu T, El-Saady G (2021) Multi-objective multi-verse optimization of renewable energy sources-based micro-grid system: real case. *Ain Shams Eng J* 13(1):101543. Available online 2021
10. Ogunmodede O, Anderson K, Cutler D, Newman A (2021) Optimizing design and dispatch of a renewable energy system. *Appl Energy* 287:116527
11. Mokhtara C, Negrou B, Settou N, Settou B, Samy MM (2021) Design optimization of off-grid hybrid renewable energy systems considering the effects of building energy performance and climate change: case study of Algeria. *Energy* 219:119605
12. Li N, Su Z, Jerbi H, Abbassi R, Latifi M, Furukawa N (2021) Energy management and optimized operation of renewable sources and electric vehicles based on microgrid using hybrid gravitational search and pattern search algorithm. *Sustain Cities Soc* 75:103279
13. Hassan AA, El-Rayes K (2021) Optimizing the integration of renewable energy in existing buildings. *Energy Buildings* 238:110851
14. Liu Z, Wang S, Lim MQ, Kraft M, Wang X (2021) Game theory-based renewable multi-energy system design and subsidy strategy optimization. *Adv Appl Energy* 2:100024

15. Tao H, Ahmed FW, Ahmed HAK, Latifi M, Nakamura H, Li Y (2021) Hybrid whale optimization and pattern search algorithm for day-ahead operation of a microgrid in the presence of electric vehicles and renewable energies. *J Clean Prod* 308:127215
16. Deveci K, Güler Ö (2020) A CMOPSO based multi-objective optimization of renewable energy planning: case of Turkey. *Renew Energy* 155:578–590
17. Liu B, Rodriguez D (2021) Renewable energy systems optimization by a new multi-objective optimization technique: a residential building. *J Build Eng* 35:102094
18. Lei G, Song H, Rodriguez D (2020) Power generation cost minimization of the grid-connected hybrid renewable energy system through optimal sizing using the modified seagull optimization technique. *Energy Rep* 6:3365–3376
19. Martelli E, Freschini M, Zatti M (2020) Optimization of renewable energy subsidy and carbon tax for multi energy systems using bilevel programming. *Appl Energy* 267:115089
20. Javed MS, Ma T, Jurasz J, Canales FA, Lin S, Ahmed S, Zhang Y (2021) Economic analysis and optimization of a renewable energy based power supply system with different energy storages for a remote island. *Renew Energy* 164:1376–1394
21. Kumar PP, Saini RP (2020) Optimization of an off-grid integrated hybrid renewable energy system with different battery technologies for rural electrification in India. *J Energy Storage* 32:101912
22. Zhang Y, Hua QS, Sun L, Liu Q (2020) Life cycle optimization of renewable energy systems configuration with hybrid battery/hydrogen storage: a comparative study. *J Energy Storage* 30:101470
23. Abdelshafy AM, Jurasz J, Hassan H, Mohamed AM (2020) Optimized energy management strategy for grid connected double storage (pumped storage-battery) system powered by renewable energy resources. *Energy* 192:116615
24. Zhang W, Maleki A, Rosen MA, Liu J (2018) Optimization with a simulated annealing algorithm of a hybrid system for renewable energy including battery and hydrogen storage. *Energy* 163(15):191–207
25. Tooryan F, HassanzadehFard H, Collins ER, Jin S, Ramezani B (2020a) Smart integration of renewable energy resources, electrical, and thermal energy storage in microgrid applications. *Energy* 212:118716
26. HassanzadehFard H, Tooryan F, Collins ER, Jin S, Ramezani B (2020) Design and optimum energy management of a hybrid renewable energy system based on efficient various hydrogen production. *Int J Hydrog Energy* 45(55):30113–30128
27. Sadeghian O, Moradzadeh A, Mohammadi-Ivatloo B, Abapour M, Anvari-Moghaddam A, Lim JS, Marquez FPG (2021a) A comprehensive review on energy saving options and saving potential in low voltage electricity distribution networks: building and public lighting. *Sustain Cities Soc* 72:103064
28. Sadeghian O, Oshnoei A, Tarafdar-Hagh M, Khezri R (2021b) A clustering-based technoeconomic analysis for wind farm and shunt capacitor allocation in radial distribution systems. *Int Trans Electr Energy Syst* 31(1):12708
29. Zerrahn A, Schill WP, Kemfert C (2018) On the economics of electrical storage for variable renewable energy sources. *Eur Econ Rev* 108:259–279
30. Gharibi M, Askarzadeh A (2019) Size optimization of an off-grid hybrid system composed of photovoltaic and diesel generator subject to load variation factor. *J Energy Storage* 25:100814
31. Tooryan F, HassanzadehFard H, Collins ER, Jin S, Ramezani B (2020b) Optimization and energy management of distributed energy resources for a hybrid residential microgrid. *J Energy Storage* 30:101556
32. Daneshvar M, Mohammadi-Ivatloo B, Zare K, Asadi S (2020) Two-stage stochastic programming model for optimal scheduling of the wind-thermal-hydropower-pumped storage system considering the flexibility assessment. *Energy* 193(15):116657
33. Tooryan F, Moghaddas Tafreshi SM, Bathaee SM, Hamidhassanzadeh-Fard H (2013) Distributed energy resources optimal sizing and placement in a microgrid. *Int Electr Eng J* 4(2):1059–1070

34. HassanzadehFard H, Tooryan F, Dargahi V, Jin S (2021) A cost-efficient sizing of grid-tied hybrid renewable energy system with different types of demands. *Sustain Cities Soc* 73:103080
35. Bozorgavari SA, Aghaei J, Pirouzi S, Vahidinasab V, Farahmand H, Korpås M (2019) Two-stage hybrid stochastic/robust optimal coordination of distributed battery storage planning and flexible energy management in smart distribution network. *J Energy Storage* 26:100970
36. HassanzadehFard H, Moghaddas-Tafreshi SM, Hakimi SM (2011) Effect of energy storage systems on optimal sizing of islanded micro-grid considering interruptible loads. *Proceedings of the 2011 3rd International Youth Conference on Energetics (IYCE)*
37. HassanzadehFard H, Jalilian A (2018) Optimal sizing and location of renewable energy based DG units in distribution systems considering load growth. *Int J Electr Power Energy Syst* 101: 356–370
38. Berk SD, DeMarzo JP (2014) *Corporate finance*, 3rd edn. Pearson, Canada
39. Grier NSVCIL (2000) *CIM justification and optimization*. Taylor & Francis
40. HassanzadehFard H, Jalilian A (2021) Optimization of DG units in distribution systems for voltage sag minimization considering various load types. *Iranian J Sci Technol Trans Electr Eng* 45(2):685–699
41. Lorestani A, Gharehpetian GB, Nazari MH (2019) Optimal sizing and techno-economic analysis of energy- and costefficient standalone multi-carrier microgrid. *Energy* 178:751–764
42. Hasanzadeh Fard H, Bahreyni SA, Dashti R, Shayanfar HA (2015) Evaluation of reliability parameters in micro-grid. *Iranian J Electr Electron Eng* 11(2):127–136
43. Mohammadi M, Ghasempour R, Astaraei FR, Ahmadi E, Aligholian A, Toopshekan A (2018) Optimal planning of renewable energy resource for a residential house considering economic and reliability criteria. *Int J Electr Power Energy Syst* 96:261–273
44. Ramli MA, Boucekara H, Alghamdi AS (2018) Optimal sizing of pv/wind/diesel hybrid microgrid system using multi-objective self-adaptive differential evolution algorithm. *Renew Energy* 121:400–411
45. Singh S, Chauhan P, Singh N (2020) Capacity optimization of grid connected solar/fuel cell energy system using hybrid abc-pso algorithm. *Int J Hydrog Energy* 45(16):10070–10088
46. McNeil MA, Karali N, Letschert V (2019) Forecasting Indonesia's electricity load through 2030 and peak demand reductions from appliance and lighting efficiency. *Energy Sustain Dev* 49: 65–77

Chapter 2

Data Analytics Applications in Digital Energy System Operation



Ali Paeizi, Mohammad Taghi Ameli, and Sasan Azad

Abstract In today's energy industry, the use of data analytics in modern digital energy system operation is an important research and innovation area. Data analysis has a key role in any modern industries and is a significant part of the optimal modern operation and planning in different industries, especially in smart power systems. This is a motivation for efficient data monitoring and processing methods to operate the digital energy system. This chapter aims to present algorithms and tools in the area of data analysis as well as the application of these tools to solve problems and challenges in modern electric power systems. In addition, basic concepts in data analysis methods, technical approaches, and research opportunities for analyzing energy data and its application in digital electric energy systems operation are discussed. Moreover, data security challenges, data management, and visualization with analysis of system input data are introduced.

Keywords Data analytics · Data analytics application in power systems · Data mining · Machine learning · Digital energy system operation

2.1 Introduction

Nowadays, there is a significant increase in data generation in various power system resources and applications such as power market analysis, state estimation, stability, and security assessment. Accurate energy production, load forecasts, and market prices are essential inputs for a generating or operating company to make better decisions. Data analysis can make many opportunities to improve the power system. Extracting effective features from input data is essential to increase efficiency and optimize power system operation.

Current grid control and monitoring systems are based on Supervisory Control and Data Acquisition (SCADA) and Automatic Meter Reading (AMR). However,

A. Paeizi · M. T. Ameli (✉) · S. Azad
Department of Electrical Engineering, Shahid Beheshti University, Tehran, Iran
e-mail: a.paeizi@mail.sbu.ac.ir; m_ameli@sbu.ac.ir; sa_azad@sbu.ac.ir

advanced measuring systems should be implemented to provide two-way real-time communication, robustness, reliability, and security for future needs [1]. Phasor measurement units (PMUs) estimate the phasor and magnitude of current and voltage at selected locations in the power transmission system. High-precision synchronization of time via Global Positioning System (GPS) allows to compare measured values from different substations and shows a higher resolution of data compared to SCADA. This method helps to immediately identify the state of the network and dynamic events such as power fluctuations and transient phenomena. PMU-measured values (voltage, current, frequency, and rate of change of frequency) with time labels are transmitted for further analysis using the IEEE c37.118 standard [2].

Advanced metering infrastructure (AMI) will play a key role in the future of smart grids. AMIs integrate smart meters and data management to communicate between customers and utilities. Existing large number of smart meters and using a massive amount of data with different sampling rates is one of the main concerns. Analyzing the huge data helps increase reliability, demand-side management and demand response, real-time network awareness, outage management, and electricity theft detection [3]. Advanced data analysis is performed using mathematical techniques, data mining, artificial intelligence, and fuzzy theory [4].

The future of power systems should be integrated with AMI to support intelligent applications. AMI system can collect data every 1–15 minutes, and this wide intelligent distribution network generates large data volumes [5]. AMIs and PMUs will work together to ensure reliability and maintain network robustness in intelligent distribution networks. Therefore, measuring and analyzing massive data generated by the intelligent system is crucial to understand grid features better. Intelligent electronic devices (IEDs) are microprocessor-based controllers that can receive data from power devices in the grid and send control commands based on the data received. IEDs' common applications are in protection, control, monitoring, and measurement. Different types of them include circuit breaker controllers, capacitor bank switches, recloser controllers, and voltage regulators. The IEDs also can provide current, voltage, frequency, active and reactive power, and harmonics measurements [6].

Big data provides a vast amount of monitoring data with RTU, PMU, AMI, and IED that have been potentially collected over days. RTUs transmit telemetry data and collect system operation status data. Data processing with appropriate accuracy and speed for power system operation and planning has become a critical need. Grid operation using big data aims to improve customer service while increasing reliability, stability, resilience, and productivity [7].

Data security and privacy are other challenges in protecting the vital infrastructure of the industry among the growing digital assets and consumers in power systems. Data security techniques maintain reliability even under attack circumstances so that the system's proper functions can be maintained at a certain acceptable level. Cyberattacks can cause outages in parts of even the most advanced power systems for several days [8].

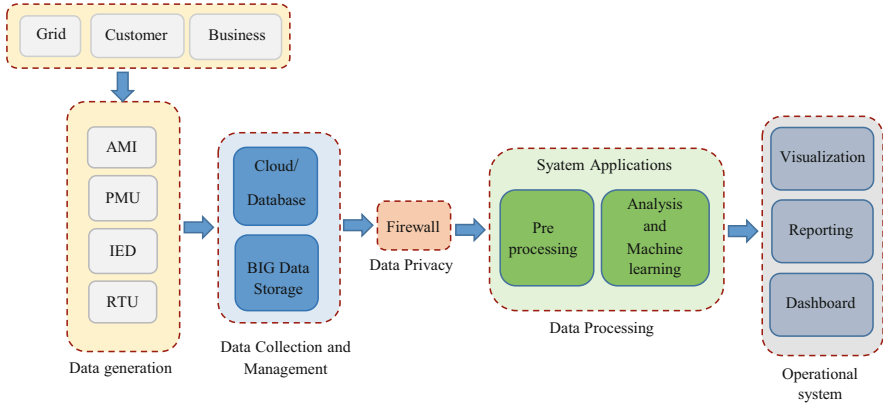


Fig. 2.1 General data analytic process in this chapter

Creating new models and methods for data mining in future will include demand response analysis for customers, big data processing from network sensors and devices, large-scale power market simulation, and predictive maintenance of electrical equipment. Smart grids enable grid controller equipment to reactively reduce loads during tension, maintain network stability to manage complex distributed energy resources, and respond to unpredictable challenges to stability [9].

Recently, significant advancements have been made in energy supply and privacy. These new achievements cover big data mining cryptosystems and data privacy, maintaining intelligent financial applications and data-driven anomaly detection [10]. Figure 2.1 shows the general data analytic process in this chapter at a glance.

The need for efficient, secure, dependable, and sustainable power energy is increasing at an exponential rate, so it is needed to have more efficient data monitoring and processing methods to operate the digital energy system to overcome challenges in data analysis, processing, storage, and security.

In this chapter, an overview of the prospects, principles, and challenges of data analytics in smart grids is presented. In order to have effective data management, the motivation of big data technologies and techniques in the energy system is introduced as a solution for smart grid needs such as massive streaming data processing, storage, and visualization. Data security in smart grids is demonstrated in terms of privacy, integrity, authentication, and cyber threats as one of the key features of energy big data. Moreover, future concerns, discussions, and obstacles associated with big data in future power systems with a comparison of several existing surveys are highlighted.

This chapter provides the following contributions:

1. A comprehensive overview of the big data characteristics, tools, technical features, and architecture from the viewpoints of data generation, acquisition, storage, and processing

Table 2.1 Summary of smart grid data and knowledge

Data	Knowledge
Power generation process	Generator parameters (operating voltage, output power) Connectivity(connected bus numbers) Operational data Status data
Distribution process	Line data (connectivity, resistance, reactance, conductance, power) Transformer data (connectivity, conditions of transformer voltage regulation, transformer base MVA, resistance, and reactance)
Consumer process	Load data (load type, voltage, active and reactive power)
Intelligence process	System monitoring data (event notification, state estimation) Device control (switch control signal, control signal of smart meter and control signal of AMI) Intelligence application (weather and geographical data, planning, pricing, and market data, electricity consumption, data of users)
Manufacturing companies	Operating data and data of power equipment
Energy suppliers	Real-time power demand and power consumption characteristics
Grid operators	Dynamics analysis of power grids at different time scales and equipment parameters

2. A concentration on the applications of data analysis in the digital operation
3. A review of the future issues and challenges of big data, state-of-the-art data technologies in IOT, and blockchain
4. An overview of existing challenges, research directions, and literature review
5. A summarization of the cyber-physical models, attack category identification with a mathematical model, and data security in smart grids from the perspectives of mechanism.
6. A brief overview of machine learning concepts, techniques, and different algorithms

Table 2.1 shows the summary of smart grid data and knowledge.

2.2 Existing Challenges and Literature Review

Data analytics applications in digital electric energy system operation include state estimation, line parameters calculation, identification and location of faults, stability analysis, model validation, frequency stability monitoring, etc. In [11], some concepts and approaches were reviewed to address general present and future power system issues and challenges. A generic methodology for developing mathematical and communication models of smart grid architecture components is described in [12]. Ref. [13] aims to comprehensively study machine learning techniques and their applications in IoT-integrated power systems. In [14], big data analytics applications and their implementation issues with various data science trends are described. In

[15], smart meter data utilization potentials from a user-centric perspective are reviewed. Ref. [16] presents a review of machine learning techniques in the context of power systems and focuses on load forecasting, power flows, power quality, and photovoltaic systems analysis. A novel deep-learning technique incorporating data augmentation for power systems, short-term voltage stability assessment (STVSA), is proposed in [17]. Ref. [18] reviews smart meter data analysis and introduces key applications such as load analysis, forecasting, and management. Research trends are also discussed in [18], such as big data analysis issues, new machine learning algorithms, and data privacy and security. In [19], machine learning algorithms are used for energy prediction in a hybrid energy system with wind, gasoline, and diesel generators. A predictive approach for identifying vulnerable generating units for transient stability using a machine learning algorithm is developed in [20]. Ref. [21] provides a comprehensive literature review for smart grids' secure data analysis (SDA). The nature of SDA and its complexity on smart grids is proposed in [21], and various research challenges such as secure data processing, secure data storage and collection, load management, and data communications are also discussed.

In [22], the interactive features of cyber-physics in power systems are discussed, and different mechanisms of modelling are examined from the perspective of graphs, probability, and simulation. Major issues related to architectures, key technologies, and standardization of big data analysis in intelligent power systems are analyzed in [10]. Ref. [23] comprehensively reviews big data issues in intelligent power systems. In [24], big data and micro grid challenges are presented. Big data opportunities in micro grids, such as stability improvement and renewable energy forecasting, are also presented. In [25], with the aim of scalability and robustness, a distributed data analysis platform for processing high volume data is proposed. Concerns about the privacy and security of smart meters are one of the main obstacles for using them. In [26], cyber-physical power systems in different attack scenarios are studied. In the following, the main challenges and issues are presented:

- *Real-time processing*: Huge amount of data with variety is a challenge in data processing; therefore, an intelligent and real-time operation is required. Designing appropriate architecture and algorithms for analyzing real-time energy demand as a big data problem is difficult [27]. A real-time monitoring framework for anomaly detection from smart data in an intelligent power system has been developed in [28]. Many applications in automation and operation require real-time data collection, control, and monitoring. For some applications, such as transient oscillation identification, time scale is in milliseconds. Although the cloud system is able to provide fast computing services, large data volumes with complex algorithms and network congestion can lead to delays.
- *Reduce redundancy in the database*: Data set contains many redundancies that increase the overhead of the whole system. Data compression reduces the system's total cost [29]. An electricity price forecasting framework, including feature processing and classification, has been proposed in [30] to reduce the feature redundancy and data dimension.
- *Data security and privacy*: There are many online devices and traditional tools for analyzing big data under security threats. A safety mechanism has been proposed

in [31], using big data analysis and integrating fuzzy cluster analysis based on game theory and machine learning. Data encryption and anomaly detection are possible solutions for data security challenge.

- *Data analysis and complex event processing*: Big data system architecture can be presented as a value chain consisting of data generation, acquisition, storage, and processing. An overview of big data analysis issues for large heterogeneous data structures in smart grids is presented in [32]. One of the notable future research issues is integrating big data analysis in the Internet of things (IOT) using blockchain technology [33]. In [34, 35], general concepts of big data, such as data production and storage, are described, and in [34], data management and collection concepts are discussed. In addition, in [36], machine learning tools have been used for data security. A holistic method for evaluating smart grid (SG) prediction models is introduced based on big data analysis for energy consumption in [37]. In [38], data security in big data is examined. An overview of the latest big data technology in smart grids with challenges and opportunities is mentioned in [39]. After presenting the telecommunication concepts in SGs, a comprehensive review of the main architecture issues, key technologies, and smart grid communication infrastructure requirements are analyzed in [40]. The role of cloud computing and IOT in smart grids has also been discussed in [40, 41].
- *Parallelization and scalability*: Data dimension challenge affects many traditional analytical methods. Therefore, these methods require revision and improvement in algorithms that process large dimensions. These methods should be able to process increasing data dimensions without changing the system architecture or adding any equipment. Big data analysis includes extracting new amounts of data that were traditionally discarded as unused data. Dimensional reduction, parallel computing, and cloud computing are possible solutions for the data volume challenge [42].
- *Integration of Operation and Planning*: This ability refers to a program to meet the future conditions of power systems with high probability and accuracy. In operational planning, preparation for weather, load, and production conditions may change in the next minutes, hours, and days [42].
- *Data compression*: Data compression techniques are essential in a wide-area monitoring system. Dealing with large data volumes is a challenge that needs to be addressed [23].
- *Data collection and storage of secure data*: Collected data may be inaccurate, incomplete, and unreliable in some cases. Therefore, it should be estimated securely and accurately. A cyberattack is considered one of the biggest threats in a smart grid design with respect to network connections. Although many security solutions are provided for smart grids, most of them are not based on large data volumes [24].
- *Historical data processing*: Historical data should be integrated with data collected for operation purposes. Effective processing algorithms and reliable databases are needed for power data collected from various sources in the big data processing challenge [24].



Fig. 2.2 Data analytics research challenges in electric energy operation

Figure 2.2 summarizes data analytics research challenges in electric energy operation, and Table 2.2 shows the general reference background and features in this chapter.

2.3 Data Processing Tools and Techniques

In the modern world of information technology and smart devices, large data volumes are generated daily. Our ability to generate data in this century is enormous because large amounts of data are collected for different purposes, such as better monitoring and control in different energy fields, including power systems. In order to take advantage of the data available, we need to develop techniques and tools that can be used to extract effective features, patterns, or knowledge from massive streaming data. Significant patterns and features extracted from a large amount of input data are used for prediction and decision-making, which is the core of data analysis. Big data analysis aims to develop new algorithms and models to address specific big data issues.

2.3.1 Preprocessing and Data Quality

Identifying the most important patterns and extracting features of measured data are important parts of any data analysis method. With recent advances in measuring technologies, power system operators and researchers now have access to real-time systems, loads, and user data. Raw data sets usually require preprocessing to extract

Table 2.2 General reference background and features in this chapter

References	Background	Features and method	Advantages and results	year
[35]	Big data storage	A big data architecture energy scheduling optimization	Consumers cost reduction	2017
[26]	Data analysis and security	Cluster to survive in cascading failure	Studying the robustness of the system with scenarios	2020
[38]	Renewable energies	Holistic article about IOT	Big data security solutions	2017
[22]	Data security	Cyber-physical power system solutions	The strategy of solving problems	
[41]	Energy management	Energy-saving methods in networks	Energy reduction solutions (max flow forecast)	2018
[24]	Big data management	Challenges in big data and micro grids	Opportunities and open challenges	2019
[23]	Data quality and security	Big data technology in smart grid issues	Application, techniques, and opportunities	2017
[21]	Big data analysis	A comprehensive review of secure data analysis	A case study Research challenges	2020
[33]	Blockchain	Blockchain in IOT secure environment	Principles, characteristics, and challenges	2018
[36]	Machine learning	Deep learning method in FDI attack	Using optimization model	2017
[40]	Big data communication	Architecture and technologies	Potentials and research issues	2019
[42]	Big data storage	Energy big data analytics	Potentials and problems in energy data analytics	2018
[16]	Machine learning	Comprehensive review on machine learning	Techniques and application in power systems	2021
[14]	Big data analysis	Big data frameworks in power systems	Challenges and strategies	2020
[27]	Big data analysis	Big data applications in smart grids	Potentials and techniques	2019
[18]	Data security and analysis	Smart meter data analytics	Methodologies and data privacy review	2018
[63]	Data security	BRNN-LSTM	Forecasting cyberattack rates	2019
[62]	Cybersecurity	Discrete and continuous ML models	Literature review on attack prediction methods	2018
[64]	Cybersecurity	Hidden Markov model	Studying systems under network attacks	2020
[67]	Cybersecurity	Attacker behavior forecasting with HMM and fuzzy inference	Techniques for forecasting behavior of attacks	2020

experimental patterns and features for prediction applications. Combining unrelated or additional features as input for machine learning methods is not helpful and may decrease model performance. Thus, feature selection aims to identify the most useful features of measured data. The general process of data analysis for machine learning (ML) input is feature engineering in data mining. Feature engineering consists of feature extraction and feature selection. Probabilistic analysis and data cleaning are possible solutions for data quality challenge.

Analysis of PMU data is related to low-rank matrix analysis, and the problem of recovering lost PMU data is formulated as a special case of the general low-rank matrix problem, which aims to recover a low-rank matrix from partial observations. Then, completion methods can be used to recover lost data. Bad data may result from device malfunctions, communication errors, and cyberattacks. Bad data detection methods require system topology and impedance. However, without any system topology information, bad data can now be located and corrected using measurements and the low-rank feature [43]. Principal component analysis (PCA) is useful for reducing the dimensionality of large datasets by mapping data from the original space to a lower-dimensional subspace. Thus, the size of the data is to be reduced [44].

2.3.2 Machine Learning Techniques

Machine learning (ML) aims to study methods to extract knowledge from data. Using this perspective, traditional signal processing and statistical methods can be considered a subset of this technology field. Artificial neural networks (ANNs) are one of the algorithms in the field of machine learning. ANNs can be considered as parallel signal processors which include neurons, which are a simple processing unit. These units obtain information of a specific issue through integration with a learning algorithm. This knowledge is stored in synaptic weights that connect different neurons. Artificial intelligence (AI) includes the theory, methodology, and techniques used to simulate and expand human intelligence. The extreme objective of AI is to empower computers to think and act like humans and increase human intelligence. AI is particularly great at predicting, sorting data, and finding patterns. ML is a system that focuses on finding data patterns and using them for prediction. By using ML to analyze data and computer predictions, operators can make better decisions. Thus, the nature of ML is to find an objective function f that maps an input variable X and an output variable Y , i.e., $Y = f(X)$. ML's goal is to find the best map for more accurate predictions and outputs. ML can be classified into three categories based on the differences between the input samples. In supervised learning, sample (i) with an input label (x_i) and a corresponding output label (y_i) can be described. In unsupervised learning, there is no output label, and sample i only has input label x_i . The learner's objective is to classify all the samples in the sample space using clustering methods. Semi-supervised learning has partial features and labels. Unlabeled data are used along with labeled data that includes classification, regression, and clustering methods [45].

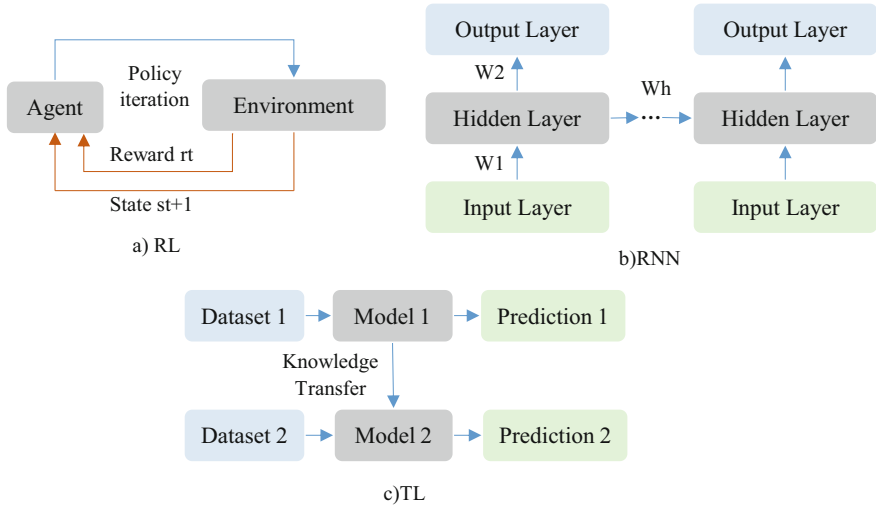


Fig. 2.3 Different machine learning concepts: (a) RL, (b) RNN, and (c) TL

In reinforcement learning (RL), the learner performs a particular action in an environment that aims to maximize the cumulative reward via a trial-and-error mechanism. RL emphasizes actions based on the expected maximum reward mode, as shown in Fig. 2.3a. RL consists of four main elements: decision process (Markov decision process), a value function, value iteration, and policy interaction. Figure 2.3a shows the RL process that an agent factor chooses an action based on the policy in state (st). The environment recognizes the action and changes to the following state ($st + 1$), and then the agent receives reward rt from the environment and selects the next action.

Despite traditional ML, transfer learning (TL) aims to reuse historical topics to extract high-quality samples for guiding training data optimization tasks. TL, therefore, includes knowledge transfer between different domains, tasks, and distributions. TL can present fast solutions for optimization problems in a large-scale power system [45].

Deep learning (DL) has many capabilities and advantages in extracting features. Therefore, it is appropriate to use DL for problems with large data volumes and is widely used in various research fields. DL is a neural network with multi-hidden layers that can be considered a particular sort of ML. Deep learning algorithms are represented by sequential layer structures. The purpose of the architecture is to learn the complex knowledge of data by hierarchically passing through numerous layers. Each layer uses a nonlinear transform to its input and selects features automatically on its output. Input data are received in the first layer, and the output of each layer is sequentially delivered as input to the following layer in this architecture. This helps extract various features from raw input data. The main advantage is extracting features automatically from complex and massive data. Figure 2.3 shows RL and RNN and TL concepts, respectively [45].

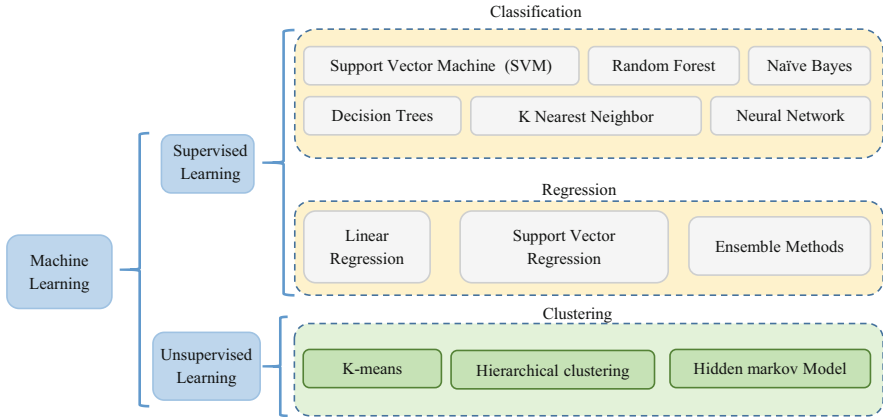


Fig. 2.4 Classification of ML algorithms

Key applications of machine learning methods in power systems are described as follows:

- *Analysis*: The ability to analyze and process the collected data is the main function of a power grid operation. Different data analysis methods and machine learning are used to process data [46].
- *Prediction*: With more uncertainty of possible outcomes, we should understand what could happen in the future. Prediction ability strongly depends on the development of data analysis and machine learning techniques and our understanding of the physical models and underlying mechanisms of power systems [46].
- *Control*: Compared to the control requirements in a traditional power grid, control in a modern power system should be based on a combination of monitoring, analysis, and prediction capabilities so that the short-term and long-term consequences of control decisions can be fully considered [46]. Figure 2.4 shows a classification of ML algorithms.

2.4 Big Data Analysis and Security

Big data has emerged as a novel technology hub in industry and engineering fields. Big data analysis is a collection of methods and technologies for obtaining, storing, and processing heterogeneous data while processing in parallel. However, designing and developing a large data framework ecosystem for a particular application is a challenging task. Many industries are considering smart grid solutions as long-term planning to improve power supply reliability and grid stability, combining distributed generation resources, developing storage solutions, and enabling customers to share control energy consumption. To do this, smart meter systems can be used in the

first stage, leading to the inclusion of other challenges. Smart meters can lead to millions of readings per minute, making a huge amount of data annually. They can be analyzed and exchanged between customers and utilities to provide real-time control and reaction through dynamic demand response (DDR). As a result, customers generate less power in addition to economic benefits. This big data problem requires modern IT technology and Internet infrastructure techniques to deal with and analyze these massive amounts of data.

2.4.1 *Big Data Characteristics*

There have been debates about the meaning of big data; however, the most frequent term is “Vs,” which includes several big data properties beginning with the letter “V.” In this chapter, the definition of “4Vs” (volume, variety, velocity, and veracity) is considered, which are discussed next [42]:

- *Volume*: The term “big data” refers to a large amount of data created by devices and sensors. Therefore, the amount of data that needs to be analyzed is very large.
- *Variety*: A term that refers to different data sources and formats (structured, semi-structured, and unstructured). Data can be presented in the form of images, videos, diagrams, sensor measurements, etc. The storage, extraction, and analysis of data in different formats can be challenging.
- *Velocity*: The rate at which data arrives is known as data velocity. It also includes the time it takes to analyze and comprehend the data collected in order to make decisions.
- *Veracity*: It indicates the correctness or quality of data. Tools that enhance the veracity of big data eliminate noise and anomalies in the data and transform it into reliable data.

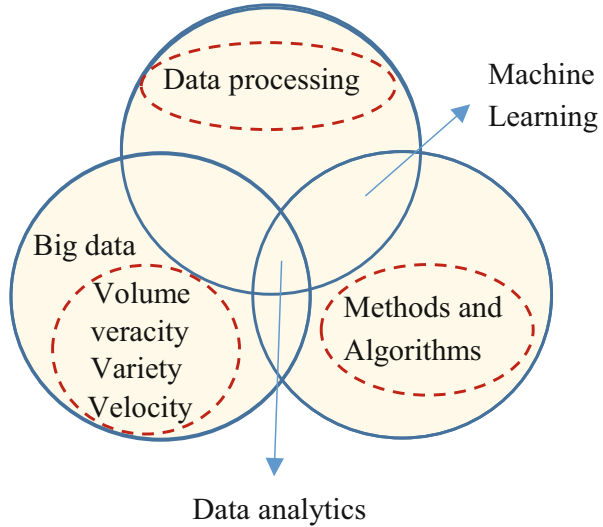
Figure 2.5 shows the concepts of big data, machine learning, data analysis, mathematical algorithms, and software tools and compares the concepts of volume, variety, velocity, and veracity.

Figure 2.7 shows the hierarchical structure of the main components of the smart grid big data frameworks. This framework includes software tools that can be used to implement the big data platform, from data generation to data analytics. In this section, concepts, software tools, and architectural components are introduced.

2.4.2 *Data Generation and Acquisition*

Smart meters generate streaming data that may belong to power plants and wind farms, as well as residential buildings and factories. Furthermore, environmental events such as weather conditions at stations can be beneficial for predicting power generated by a specific wind farm. Considering information from various sources,

Fig. 2.5 Big data, machine learning, and data analysis comparison



including electric vehicles (EVs), residential homes, industrial plants, and various power plants, increases power system reliability. To address specific requirements such as cost-effectiveness and improved accessibility and scalability, cloud computing can be employed as an infrastructure layer for big data systems [42].

Data collection, transmission, and preprocessing are the three sub-tasks of data acquisition for a smart grid system. Collected data is transferred to the main node in the cluster, and depending on the variety of data sources, the collected data may take many formats. In the data preprocessing stage, incomplete and incorrect data is corrected or deleted to improve data quality. There are numerous data analysis tools available, including Tableau that is used for big data visualization and Mahout and Samoa for massive data mining. Flume is an Apache distributed system software tool that effectively collects, integrates, and transfers massive volumes of data from various resources to a centralized store. It can be utilized in Hadoop Distributed File System (HDFS) to capture enormous amounts of sensor data as streaming data in HDFS [47].

2.4.3 Data Storage

Hadoop is a software platform that allows massive amounts of data to be stored and processed. Distributed processing, rather than relying on dedicated and expensive hardware to store and analyze data, allows vast amounts of data to be processed on server clusters (nodes). The Hadoop kernel is divided into two parts: a storage component known as HDFS and a processing component known as map-reduce. Hadoop is an important part of any big data architecture. In the HDFS ecosystem, master nodes retrieve data from slave nodes when requested. The master node is

responsible for locating the data. A master (Job Tracker) and a slave (Task Tracker) per cluster node create the map-reduce processing component. The master node is in charge of scheduling slave tasks, controlling them, and re-executing failed ones. Apache yarn is a Hadoop resource manager that enables other processing frameworks' applications to run on a distributed Hadoop cluster. Yarn's main idea is to split up Job Tracker/Task Trackers tasks into separate entities. The yarn consists of a global resource manager and slave node manager to manage distributed applications. Big data architectures have relied on Hadoop for a long time. Hadoop's following features make it ideal for managing and analyzing smart grid data [47]:

- *Scalability*: Hadoop makes it possible to scale the hardware infrastructure without changing data formats. Storage systems and additional nodes can be added to an existing cluster without compromising the existing node's functionality when new neighborhoods are added to the grid.
- *Efficient computing*: Parallel computing with growing data volume makes smart grids cost-effective. This allows utilities and customers to share data, allowing DDRs to monitor and make decisions in real time. On smart grid stream data, it also provides a low-latency prediction.
- *Flexibility*: Hadoop is designed without any schema and is capable of capturing different types of data from multiple sources. Hence, many challenges of data in smart grids may be handled.
- *Fault tolerance*: To address missing data and computational failures, which occur frequently in smart grids, Hadoop has the capacity to restore data failures or network congestion by distributing computational work and storing information in many nodes.

It is important to have a scalable data storage system, such as Distributed File System (DFS), which enables clients to share and store files. It also allows clients to have a replica of the big data that has been stored. One of these frameworks is HDFS. A second option for a data storage solution is a NoSQL database with column-oriented solutions (HBase and Cassandra), key-value solutions (Voldemort and Dynamo), and document databases solutions (CouchDB and MongoDB). They can all be used for NoSQL databases to overcome the constraints of typical databases. The authentication process confirms the user's identity and ensures that the user has legal access to the data server, which is a fundamental requirement to assure the reliability of data sources. For a traditional database with static data storage, users send queries, and the system returns the results after searching the database. For real-time processing of large amounts of data, the traditional approach cannot meet the need for a massive amount of streaming data. Visualization of Geographic Information System (GIS) is widely used in electrical power systems, which plays a vital role in improving the performance of the power grids [50].

Hive and Impala are high-level software tools for reading and writing data in distributed storage, as well as query massive data management. Hive uses a SQL-like interface to express massive data analytic tasks in Map-Reduce operations. Impala, on the other hand, is a dynamic SQL search tool that runs in real time. Impala does not have to convert a SQL query into a different processing framework, such as

Hive's Map-Reduce operation. An SQL query is executed in the memory of every node in the cluster, providing real-time results [47].

Apache Zeppelin is an interactive data visualization and analysis web interface. HBase and Hadoop clusters can be managed with a distributed configuration service named Apache Zookeeper. Apache Sqoop (SQL to Hadoop) is a software tool for transferring structured data to Hadoop. Smart meter data can be integrated with big data processing using Apache Sqoop. In [49], a system model with features is presented using open-source frameworks and tools such as Apache Hadoop and a distributed database HBase. The aim is to develop an active event detection model using the statistical analysis method in stored data sets. In addition, an efficient event detection algorithm using map-reduce and Hadoop frameworks with PMU data is also proposed.

2.4.4 Data Processing

Map-reduce is a distributed programming approach that allows a cluster to process massive volumes of data in parallel. It has turned into an important software technology in supporting data-intensive applications due to its remarkable features, such as fault tolerance and scalability. Map-reduce is a highly scalable model that can be used to run parallel and distributed computing on thousands of computers. As depicted in Fig. 2.6, computational tasks are divided into map and reduce steps in the map-reduce model. Computations are separated into multiple tasks throughout the mapping process. To run on cluster nodes or virtual machines concurrently, every map task processes an input data block and transforms it into an intermediate result in the form of a key/value pair, which is then saved in local storage. Each reduced task collects the intermediate result and combines the values corresponding to a separate key to generate the result in the reduction step. Job Tracker is a service that runs on the Name Node that divides user jobs into numerous tasks. Task Tracker runs on Data Nodes, receives maps, decreases tasks from Job Trackers, and communicates with Job Tracker on a frequent basis to report progress and complete new tasks [51]. Figure 2.6 shows the map-reduce model architecture.

Mahout is a data-mining software that provides batch machine learning processing and can be used in machine learning applications that are extensible and highly functional. Samoa is a distributed streaming machine learning framework that is used for common data mining and machine learning tasks. Tableau is a data visualization tool with dashboards used for analysis and visualization. Another open-source software tool for processing is Spark, which has the same processing benefits as before. In addition, it can store intermediate results instead of writing in HDFS. Therefore, Spark can be more suitable for data mining and machine learning applications, and Spark is often used as a complement to Hadoop [47].

Apache Spark includes a Spark streaming module for managing data in memory, which speeds up data processing significantly compared to Hadoop, which relies on drives. MLlib is a library that contains machine learning algorithms such as

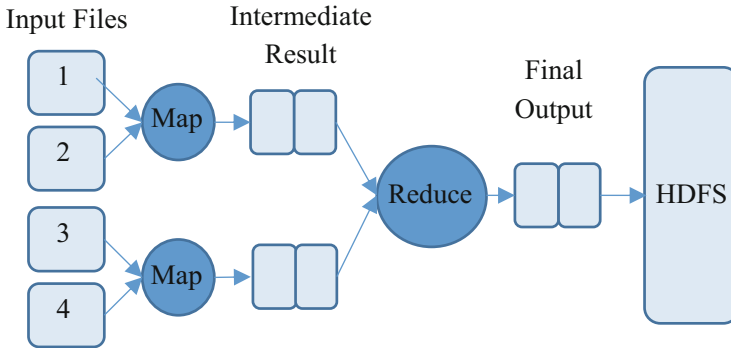


Fig. 2.6 Map-reduce model architecture

regression and clustering, while GraphX is a visualization software tool. In order to deal with big data statistical and post-event analysis, Apache Spark is used. Spark is built to run 100 times faster because of its capabilities for in-memory processing. SQL queries, streaming data, and advanced analyses such as graph algorithms and machine learning are also supported [25].

Apache Flink can be used for both real-time and batch data processing. Flink is a scalable, fault-tolerant, and rapid messaging system. Because of its FlinkML machine learning library, Flink is utilized for machine learning applications. Apache Storm is a software tool that allows analyzing enormous volumes of data in real time. Apache Storm is a fault-tolerant, parallel processing system that is open source and simple to implement. Apache Kafka is a fault-tolerant software tool that can keep data even if it encounters an error. For data integration, Kafka and Storm can be simply combined [24]. Figure 2.7 shows a big data framework's main components.

A blockchain technology is a chain of interconnected blocks that contains data. The key aspect of blockchain technology is that it keeps track of all changes in each new block, making all blocks immutable. This makes it a secure method for transactions like money transfers and property contracts. A Genesis Block is the first block in every blockchain, and it acts as a header for connecting additional blocks appropriately. A hash is used to uniquely identify each block and its contents. In the event of a malicious attack, modifying block information will also change its hash, while the next adjacent block's hash will remain unchanged. This makes all subsequent blocks in the chain invalidated [48]. Game theory is a mathematical tool that can analyze user behavior in various fields. It is suitable to be widely used in the analysis of big data. Game theory can be used in optimization problems and security awareness data analysis [23].

Unusual data patterns or missing data values generated by event failures during data collection, data entry, or communication are considered as anomalies examples. To diagnose an anomaly, time-series-based, time-window-based, and low-rank matrix approaches are used [21]. The transient behavior of a large power system can be represented by equations as follows [52]:

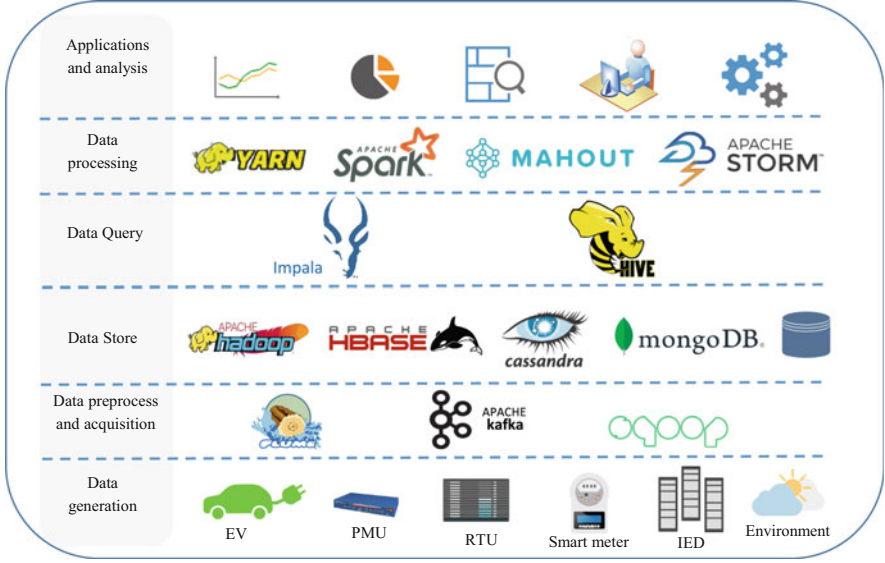


Fig. 2.7 Hierarchical architecture of the main components of a big data framework

$$\dot{x}^{(t)} = f(x^{(t)}, u^{(t)}, h^{(t)}, \omega) \tag{2.1}$$

$$0 = g(x^{(t)}, u^{(t)}, h^{(t)}, \omega) \tag{2.2}$$

where $x^{(t)}$ denotes power state variables, $u^{(t)}$ represents system input parameters, $h^{(t)}$ denotes algebraic variables such as the magnitude of the bus voltage, and w indicates the parameters of the system with constant time. The sample time is t , the number of system variables is m , and bus numbers are represented by p . The linearization of nonlinear equations is the focus of model-based state indicators in (2.1) and (2.2), which indicates (2.3).

$$\begin{bmatrix} \underline{\Delta x} \\ \underline{\Delta u} \end{bmatrix} = \begin{bmatrix} A & -f_u g_u^{-1} g_h \\ 0 & -E \end{bmatrix} \begin{bmatrix} \underline{\Delta x} \\ \underline{\Delta u} \end{bmatrix} + \begin{bmatrix} 0 \\ C \end{bmatrix} \xi \tag{2.3}$$

where f_x and f_u are the Jacobian matrices of f with respect to x and u and $=f_x - f_u g_u^{-1} g_h$. In (2.3), E represents a diagonal matrix with diagonal entries equal to t_{cor}^{-1} , and t_{cor} denotes the load fluctuation correction time. The diagonal entries of a diagonal matrix C are of the respective active (P) or reactive (Q) nominal load values, and ξ is considered to be a vector of independent Gaussian random variables. Estimating the state of the system by solving Eq. (2.3) becomes increasingly challenging, and the assumption that ξ follows a Gaussian distribution would limit the practical application. For practical usage, it is necessary to convert large high-dimensional PMU data streams into tiny PMU data segments. To represent the acquired voltage magnitude

data, a sequence of random matrices (2.4) is generated based on individual window truncated PMU data analysis without knowledge of the power network parameters or topology [52].

$$\{Z_{11}, Z_{12}, \dots, Z_{1q}, \dots, Z_{n1}, Z_{n2}, \dots, Z_{nq}\} \quad (2.4)$$

2.5 Data Security in Smart Grids

By utilizing large-scale sensor metering systems and more sophisticated information communication networks, power grids can improve their operations on a constant basis to maintain a safe, stable, and reliable power supply. Modern power grids are not the same as energy infrastructure networks in the traditional sense, thanks to the continual growth of power systems. Instead, they have evolved into complex and heterogeneous multidimensional physical power systems (CPPS) and interactions with cyber networks. Physical cyber interactions can lead to unpredictable inter-system failures. Therefore, cyber system failure can spread to physical systems and inversely, resulting in cascade failures. Determining the dynamic behavior of CPPS in a systematic and accurate manner is essential to increase the overall system's controllability and stability. The most likely consequences of cyberattacks on smart grids could be operational failures, synchronization failures, power outages, financial losses, data theft, and complete blackouts [22]. The SSH protocol version 2 has been presented in order to construct a smart grid architecture in a safe cluster. This encryption network option enables network systems to communicate securely over an insecure network. In the server-user method, SSH ensures a safe encrypted connection that connects a client to a server. For secure network connections, SSH also enables authentication, encryption, and data integration. It provides a robust connection and explains how one node can be safely connected to another node in a distributed cluster [22].

A common strong public key authentication mechanism is used to authenticate cluster nodes in SSH; therefore, a public key and a private key are created to accomplish this. A public key is distributed to all cluster nodes that need authentication. The private key is used to decrypt all data encrypted with the public key. As a result, each cluster node has a file containing a full list of the other node's keys. Since authentication is dependent on a private key, the key is not sent over the network throughout the authentication process. Cyberattack threats are described in the following.

Under a customer profiling attack, smart meter data provides personal information of users that can be utilized to detect whether or not a customer is at home. It would be harmful if thieves utilize such information. IP spoofing is an attack that can be used to redirect information from a smart network to an enemy computer for more assessment. It also can make the communication nodes of the smart grid appear unreliable and nonresponsive, which reduces its associated trust value.

Man-in-the-middle attack can monitor or change data between two smart grid connection nodes covertly, and denial-of-service attacks can prevent providing smart grid services. A system hijacking attack can get an unauthorized remote connection to a smart grid node. In a data-driven system such as the smart grid, injecting incorrect data can have devastating effects, which is the motivation behind the false data injection attack (FDIA). The purpose of such attacks is to change the original data. Time synchronization attack (TSA) contains the delay of time synchronization pulses being sent from one node to another in a network [10].

When it comes to information transfer, there are three types of CPPS structures: component layer, communication layer, and function layer. As indicated in Fig. 2.8, the above levels are abstracted into layer1, layer 2, and layer 3. Primary equipment includes a generator, transformer, transmission line, and circuit breaker, while secondary equipment includes protection relay, sensor, actuator, etc. Electric devices that all are integrated in a specified architecture make up layer 1. The information gathered in layer 1 would be sent to the control center in layer 2 via the communication network. In CPPSs, communication design has generally played a critical role in ensuring coordination of power grid elements. In the end, the control center in layer 3 would store and process all operational data. Layer 3 is capable of performing a variety of advanced functions as well as operational decision-making. The organization of cyber-physical power systems is shown in Fig. 2.8 [22].

To study the grid behavior under attacks, common attack models in power systems can be described in [22]. When a time synchronization attack (TSA) occurs, transmission line fault location can be described in (2.5).

$$\Delta D = \left(\frac{1}{2\gamma L} \right) \ln \left(\frac{(A + B)(C + De^{j\Delta\theta})}{(C + D)(A + Be^{j\Delta\theta})} \right) \tag{2.5}$$

where $A, B, C,$ and D are formulas formed by voltage and current at the receiving and transmitting ends and ΔD is line fault location error related to TSA. $\Delta\theta$ denotes the phase angle difference between the transmitting and receiving ends, L is the power

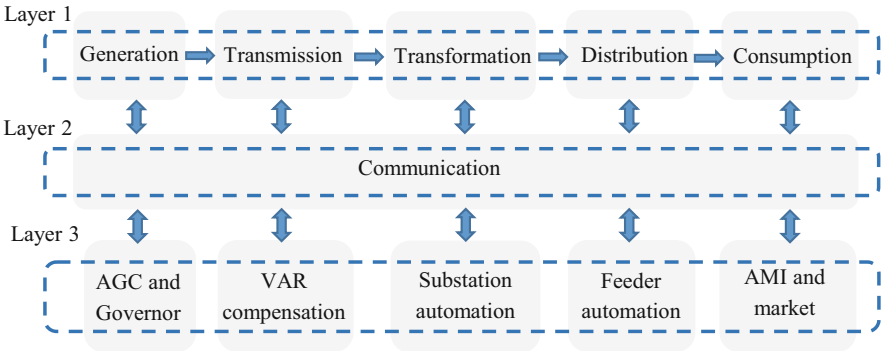


Fig. 2.8 Structure of cyber-physical power systems

transmission length, and γ is the attenuation constant [22]. Voltage stability monitoring under TSA can be represented in (2.6) and (2.7).

$$I_Z = 100 \left(1 - \frac{Z_{th}}{Z_L} \right) \quad (2.6)$$

$$I_P = R \left(Z_{th} \left| \frac{E_{th}}{2Z_{th}} \right|^2 \right) - R \left(Z_L \left| \frac{E_{th}}{Z_{th} + Z_L} \right|^2 \right) \quad (2.7)$$

When it comes to load impedance and the active power delivered to the load, I_Z and I_P are voltage stability margins. TSA may impact on Z_{th} , Z_L , and E_{th} , which are complex impedances and voltages of the T-equivalent of the transmission line. Event location under TSA can be represented in (2.8).

$$(x_i - x_e)^2 + (y_i - y_e)^2 - V_e^2(t_i - t_e)^2 = 0 \quad (2.8)$$

The coordinates of the i -th PMU and the disturbance event are (x_i, y_i) and (x_e, y_e) , respectively, and V_e is event propagation speed; t_i is the disturbance arrival time of the i -th PMU, and t_e is initial transmission time of the signal [22]. AMI under FDI attack can be described in (2.9).

$$VSI = V_S^4 - 4(P_r X - Q_r R)^2 - 4(P_r R - Q_r X)V_S^2 \quad (2.9)$$

where V_S is voltage magnitude at the transmitting end and P_r and Q_r are total injection real and reactive powers at node r , respectively. R and X represent resistance and reactance, respectively, and VSI stands for voltage stability index [22]. AGC under FDI attack can be represented in (2.10).

$$ACE = (P_{tie} - P_{sch}) + \beta(f - 60) \quad (2.10)$$

where ACE is area control error; f is system frequency; P_{tie} is tie-line power flow that may be generated by the attack; P_{sch} is scheduled tie-line power exchange; and β is frequency bias [22]. Real-time pricing under FDI attack can be described in (2.11, 2.12, and 2.13).

$$\lambda_1 = \frac{\sum_{j \in M} \frac{b_j}{2a_j} + \sqrt{K}}{\sum_{j \in M} \frac{1}{a_j}} \quad (2.11)$$

$$K = \sum_{j \in M} \left(\frac{b_j}{2a_j} \right)^2 + 4 \sum_{j \in M} \frac{1}{2a_j} \cdot \sum_{j \in N} w_{i1} \quad (2.12)$$

$$\lambda_2 = \frac{n}{2} + m \sqrt{\left(\frac{n}{2m}\right)^2 + \frac{2}{m} \sum_{j \in N} w_{i2}} \quad (2.13)$$

where λ_1 and λ_2 represent renewable energy prices and traditional power sources, respectively. For demand-user i , w_{i1} and w_{i2} are corresponding preference factors that may be compromised; M and N are number of supply-users and demand-users. m , n , a_j , and b_j are coefficients of cost function [22]. AC state estimation under FDI attack can be represented in (2.14).

$$\|r\| = \left\| \begin{pmatrix} z_1 \\ z_2 \end{pmatrix} - \begin{pmatrix} h_1(x_1) \\ h_2(x_2) \end{pmatrix} \right\| \quad (2.14)$$

where $\|r\|$ denotes AC state estimates residuals; z_2 is measurement, and $h_2(x_2)$ is a state variable that is maliciously changed, while z_1 and $h_1(x_1)$ keep intact [22]. Topology attack in the smart grid can be described in (2.15).

$$\bar{s} = s + b \quad (2.15)$$

In (2.15), $s \in \{0, 1\}$ is correlated with system topology, $b \in \{0, 1\}$ represents the modifications, and \bar{s} is modified network data.

2.5.1 Forecasting Techniques in Data Security

Discrete approaches such as graphs, Markov models, game theory, and Bayesian networks are introduced to address forecasting techniques in cybersecurity. Continuous models, such as gray models and time series, are also studied. Other techniques for cybersecurity prediction, which have recently gained interest, are machine learning and data mining. Many new data mining and machine learning-based approaches have evolved, drastically changing the status of cybersecurity prediction studies. Despite the different solutions that have been provided, there seems to be no clear approach for predicting cyberattacks efficiently and accurately [62].

For predicting cyberattack rates, bidirectional recurrent neural networks with long short-term memory (BRNN-LSTM) are suggested in [63]. Long-range dependence and high nonlinearity are good instances of complex data set issues that the framework could be able to handle.

Hidden Markov mechanisms have been frequently used in the context of a multilevel network attack, but determining the appropriate parameters for training remains a challenge. Algorithms such as expectation-maximization, spectral, and K-means are investigated in [64].

The impact of a type of false data injection attack on wind power forecasting is investigated in [65]. It seems to be possible that malicious data might be inserted into historical data before being detected. In [66], prediction errors of different load

forecasting models such as support vector regression (SVR), multiple linear regression, artificial neural networks (ANN), and fuzzy interaction regression are compared. The goal of [67] is to evaluate existing methods for forecasting attacker behavior and attacker profile needs. It focuses on issues including attacker profile and attribution, as well as how their prediction attack affects. In [67], attack graph-based methods, Hidden Markov (HMM), fuzzy inference, and advanced processing methodologies are all examined as strategies for forecasting attacker behavior. The method includes the following steps:

- Creating primary data sources
- Extracting attributes from the events database
- Categorizing metrics for a profile of attackers
- Evaluating links between data sources and attacker behavior and predicting topic metrics to train algorithms for attacker behavior prediction

2.6 Applications of Data Analysis in the Digital Operation

Applications of data analysis in power systems include support for online analysis, improving stability and reliability, accurate state estimation, event detection, load forecasting, etc. These applications can be described as follows:

- *Power outage management*: Power outages may be due to short circuits, station failures, and distribution line failures. Outage management is considered as one of the highest priorities of smart meter data analysis after billing. This system includes outage awareness and outage localization [18].
- *Eliminating technical and non-technical electrical loss*: Technical loss and detecting non-technical losses due to theft is one of the main concerns of power systems [53]. Smart meter data and power system data with machine learning methods can be used to detect electrical energy theft [54].
- *Increasing power system stability and reliability*: Stability and reliability are top priorities in power systems, which can address several issues such as event detection, voltage stability, and post-event analysis. Big data methods help improve reliability, stability, and power grid safety using computational analysis provided by real-time data mining [55].
- *Short-term load forecasting*: Load forecasting can be performed using machine learning methods based on intelligent data measurements, historical load data, and environmental data such as temperature and humidity. Load forecasting data related to consumers can be used to improve urban planning, reduce operating costs, increase quality, and decrease power losses [54].
- *Voltage stability analysis*: Voltage stability is the power system's ability to maintain the voltage of each bus in an acceptable range at any time, even after a fault. Voltage instability, on the other hand, occurs when a system fails due to increased demand or unexpected events. It results in a voltage decrease in the power grid that leads to an outage.

- Massive streaming PMU data make it possible to monitor dynamic behavior and stability characteristics of power systems. It provides the possibility of analyzing online voltage stability before reaching the point of voltage breakdown or blackout [55].
- *State estimation*: State estimation module receives various measurements (voltage, current, and power of phases) from grid substations and calculates the power system state using nonlinear estimations. Processing synchro-phasor measurements of buses is a powerful tool for performing state estimation using real-time measurement [55]. State estimation is used for applications such as operational resource planning, real-time system monitoring, and control.
- *Power system observability and advanced visualization*: Visualization tools combined with machine learning and big data analysis methods help operators make better decisions. Observability is possible when state variables are determined; therefore, when it is impossible to estimate the state of the grid, the power grid will not be observable.
- *Customer satisfaction*: With significant advances in smart meters installation, better fraud detection, power outage detection, smart real-time pricing schemes, and demand response, customer satisfaction is possible.
- *Line parameter calculation*: Accurate transmission line impedance parameters help improve the accuracy of relay settings and fault detection and location. These accurate parameters improve the rapid repair of systems. They also help improve transmission line modelling for system simulations, such as state estimation calculations. Measurements should be determined according to different loading conditions and ambient temperature to consider impedance changes, especially resistance to temperature [55].
- *Post-event analysis*: Post-event analysis is necessary to find the cause of events and helps us prevent these events again by taking corrective actions. Wide-area measurements are also among the necessities of post-event analysis. The data are crucial for reconstructing the sequence of events, leading to blackouts and shortening the analysis time. These analyses can help understand the cause of events and refine response strategies [55].
- *Frequency stability monitoring*: The essential indicator that may reflect the balance of system generation and load is frequency deviation, which also can illustrate system stability and equipment safety. PMUs measure the grid's frequency, which is the main indicator of the balance between generation and load in the power system [55].
- *DG integration*: Improving distributed generation integration in the power grid [56].
- *Analysis of power quality*: Data flow at high sample rates of electrical signals can be supported by big data. Therefore, it improves the power quality analysis [57].
- *Model validation*: New data-driven methods can be used to validate power plant models. Operators use PMU data to improve system transient and steady-state models. High-speed observations of power system status help model designers to tune accurate models for online and offline applications.

- *Renewable energy forecasting*: With respect to renewable wind power generation uncertainty, some obstacles are provided during electricity generation and distribution. Variation in wind speed causes fluctuations in the wind farm's output power, which leads to instability in the grid. Therefore, accurate wind power forecasting based on wind energy is needed to create operational strategies [54]. In [58], a method for short-term wind power forecasting using the deep learning method is proposed with unlabeled wind speed data.
- *Preventive maintenance and electrical device condition assessment*: Preventive maintenance requires accurate equipment condition data. This can be achieved using data analysis methods, device monitoring, and failure detection [59].
- *Faults and event identification*: The phasor measurement units can identify various events in the power system, such as faults and generation trips, load trips, and load changes. High-speed PMU sampling can identify the cause of fluctuations and help operators control the system at fault time [60].
- *Improving demand response management and dynamic pricing algorithms*: Data analysis can be in the consumption patterns of users and quickly determines customers' participation in a program. Consumer pattern analysis of millions of users makes it possible to visualize prices and maximize profits [61]. Figure 2.9 shows applications of data analysis in digital operation.

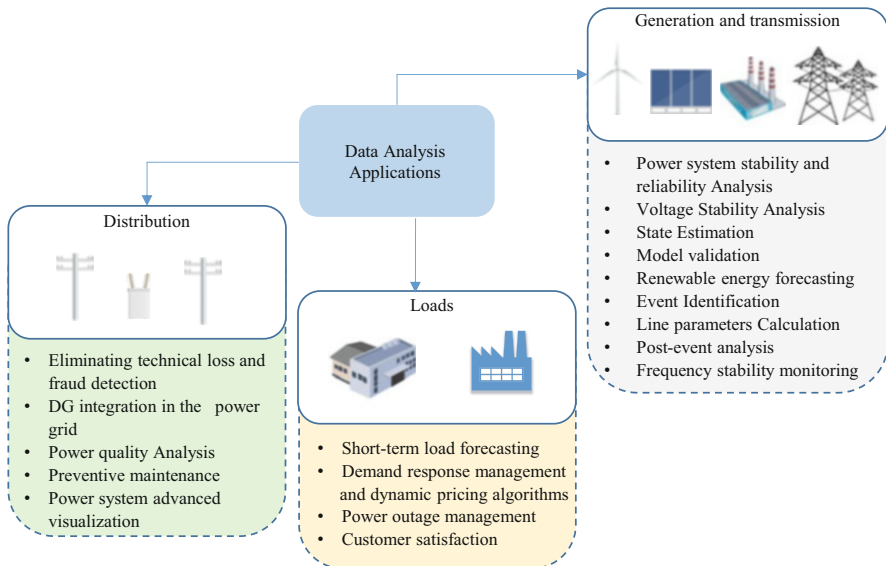


Fig. 2.9 Applications of data analysis in the digital operation

2.7 Conclusion

There is a significant increase in data generation in various power system resources. Massive streaming data analysis has motivated the use of near-real-time data processing systems. This chapter presents a comprehensive review of data analysis of power system digital operation, concepts, and literature. In addition, existing and previous research challenges and future research potential to solve existing challenges are also introduced. Big data analytics is described as a large-scale data analysis technique, and the hierarchical architecture of big data, including generation, acquisition, storage, and analysis of data, is introduced along with effective tools in each section. Concepts and algorithms of machine learning, data privacy, and security processing are also described. Finally, several applications such as improving network stability and reliability, more accurate system state estimation, data usage for fault detection, equipment monitoring, and asset maintenance were presented. Since data analysis technology is still in progress, there are challenges that need to be addressed, such as data optimization, data security, and privacy.

In this chapter, main achievements can be summarized as follows:

- Big data tools and architecture from the perspectives of data generation, storage, and processing are introduced.
- Applications of data analysis in the digital operation are provided.
- Research directions, literature review, and future challenges of big data are discussed.
- Cyber-physical models, attack identification, and data security in smart grids are summarized.
- Machine learning concepts, techniques, and different algorithms are introduced.

References

1. Raoufat ME, Tomsovic K, Djouadi SM (2016) Virtual actuators for wide-area damping control of power systems. *IEEE Trans Power Syst* 31(6):4703–4711
2. Usman MU, Omar Faruque M (2019) Applications of synchrophasor technologies in power systems. *J Modern Power Syst Clean Energy* 7(2):211–226
3. Asad Z, Rehman Chaudhry MA (2017) A two-way street: Green big data processing for a greener smart grid. *IEEE Syst J* 11(2):784–795
4. Marjani M et al (2017) Big IoT data analytics: architecture, opportunities, and open research challenges. *IEEE Access* 5:5247–5261
5. Huang C et al (2021) Smart meter pinging and reading through AMI two-way communication networks to monitor grid edge devices and DERs. *IEEE Trans Smart Grid* PP(99):1
6. Portelinha JFM, Oliveira DQ (2018) The role of Big Data in smart grid communications. In: *Big Data analytics in future power systems*. CRC Press, pp 37–53
7. Katz JS (2018) The role of Big Data and analytics in utility innovation. In: *Big Data application in power systems*. Elsevier, pp 43–56
8. Stimmel CL (2018) Emerging security and data privacy challenges for utilities: case studies and solutions. In: *Big Data application in power systems*. Elsevier, pp 29–42

9. Bessa RJ (2018) Future trends for big data application in power systems. In: Big data application in power systems. Elsevier, pp 223–242
10. Hu J, Vasilakos AV (2016) Energy big data analytics and security: challenges and opportunities. *IEEE Trans Smart Grid* 7(5):2423–2436
11. Sharifzadeh A, Ameli MT, Azad S (2021) Power system challenges and issues. In: Nazari-Heris M, Asadi S, Mohammadi-Ivatloo B, Abdar M, Jebelli H, Sadat-Mohammadi M (eds) Application of machine learning and deep learning methods to power system problems. Power systems. Springer, Cham. https://doi.org/10.1007/978-3-030-77696-1_1
12. Panda DK, Das S (2021) Smart grid architecture model for control, optimization and data analytics of future power networks with more renewable energy. *J Clean Prod* 301:126877
13. Farhoumandi M, Zhou Q, Shahidehpour M (2021) A review of machine learning applications in IoT-integrated modern power systems. *Electr J* 34(1):106879
14. Kezunovic M et al (2020) Big data analytics for future electricity grids. *Electr Power Syst Res* 189:106788
15. Völker B et al (2021) Watt's up at home? Smart meter data analytics from a consumer-centric perspective. *Energies* 14(3):719
16. Miraftebzadeh SM et al (2021) Advances in the application of machine learning techniques for power system analytics: a survey. *Energies* 14(16):4776
17. Li Y, Zhang M, Chen C (2022) A deep-learning intelligent system incorporating data augmentation for short-term voltage stability assessment of power systems. *Appl Energy* 308:118347
18. Wang Y et al (2018) Review of smart meter data analytics: applications, methodologies, and challenges. *IEEE Trans Smart Grid* 10(3):3125–3148
19. Musbah H et al (2022) Energy management using multi-criteria decision making and machine learning classification algorithms for intelligent system. *Electr Power Syst Res* 203:107645
20. Khalkho AM, Mohanta DK (2022) RBFNN assisted transient instability-based risk assessment of cyber-physical power system. *Int J Electr Power Energy Syst* 137:107787
21. Kumari A, Tanwar S (2020) Secure data analytics for smart grid systems in a sustainable smart city: challenges, solutions, and future directions. *Sustain Comput Inform Syst* 28:100427
22. Shi L, Dai Q, Ni Y (2018) Cyber-physical interactions in power systems: a review of models, methods, and applications. *Electr Power Syst Res* 163:396–412
23. Tu C et al (2017) Big data issues in smart grid—A review. *Renew Sust Energy Rev* 79:1099–1107
24. Moharm K (2019) State of the art in big data applications in microgrid: a review. *Adv Eng Inform* 42:100945
25. Zhou D et al (2016) Distributed data analytics platform for wide-area synchrophasor measurement systems. *IEEE Trans Smart Grid* 7(5):2397–2405
26. Chen L et al (2020) Robustness of cyber-physical power systems in cascading failure: survival of interdependent clusters. *Int J Electr Power Energy Syst* 114:105374
27. Ghorbanian M, Dolatabadi SH, Siano P (2019a) Big data issues in smart grids: a survey. *IEEE Syst J* 13(4):4158–4168
28. Moghaddass R, Wang J (2018) A hierarchical framework for smart grid anomaly detection using large-scale smart meter data. *IEEE Trans Smart Grid* 9(6):5820–5830
29. Hu H, Wen Y, Chua TS, Li X (2014) Toward scalable systems for big data analytics: a technology tutorial. *IEEE Access* 2:652–687
30. Wang K, Xu C, Zhang Y, Guo S, Zomaya A (2019) Robust big data analytics for electricity price forecasting in the smart grid. *IEEE Trans Big Data* 5(1):34–45
31. Wu J, Ota K, Dong M, Li J, Wang H (2017) Big data analysis based security situational awareness for smart grid. *IEEE Trans Big Data* 4(3):408–417
32. Jiang H, Wang K, Wang Y, Gao M, Zhang Y (2016) Energy big data: A survey. *IEEE Access* 4:3844–3861
33. Ali MS, Vecchio M, Pincheira M, Dolui K, Antonelli F, Rehmani MH (2019) Applications of blockchains in the Internet of Things: a comprehensive survey. *IEEE Commun Surv Tuts* 21(2):1676–1717

34. Daki H, El Hannani A, Aqqal A, Haidine A, Dahbi A (2017) Big data management in smart grid: concepts, requirements, and implementation. *J Big Data* 4(1):1–19
35. Wang K et al (2017) Wireless big data computing in smart grid. *IEEE Wireless Commun* 24(2): 58–64
36. He Y, Mendis GJ, Wei J (2017) Real-time detection of false data injection attacks in smart grid: a deep learning-based intelligent mechanism. *IEEE Trans Smart Grid* 8(5):2505–2516
37. Aman S, Simmhan Y, Prasanna VK (2015) Holistic measures for evaluating prediction models in smart grids. *IEEE Trans Knowl Data Eng* 27(2):475–488
38. Chin WL, Li W, Chen HH (2017) Energy big data security threats in IoT-based smart grid communications. *IEEE Commun Mag* 55(10):70–75
39. Zainab A et al (2021) Big data management in smart grids: technologies and challenges. *IEEE Access* 9:73046–73059
40. Ghorbanian M, Dolatabadi SH, Masjedi M, Siano P (2019b) Communication in smart grids: a comprehensive review on the existing and future communication and information infrastructures. *IEEE Syst J* PP(99):1–14
41. Liao D, Sun G, Yang G, Chang V (2018) Energy-efficient virtual content distribution network provisioning in cloud-based data centers. *Future Gener Comput Syst* 83:347–357
42. Akhavan-Hejazi H, Mohsenian-Rad H (2018) Power systems big data analytics: an assessment of paradigm shift barriers and prospects. *Energy Rep* 4:91–100
43. Wang M, Chow JH (2021) II data quality and privacy enhancement. In: *Advanced data analytics for power systems*, p 261
44. Mishra DP, Ray P (2018) Fault detection, location and classification of a transmission line. *Neural Comput & Applic* 30(5):1377–1424
45. Cheng L, Tao Y (2019) A new generation of AI: a review and perspective on machine learning technologies applied to smart energy and electric power systems. *Int J Energy Res* 43(6): 1928–1973
46. Chen K et al (2018) Learning-based data analytics: moving towards transparent power grids. *CSEE J Power Energy Syst* 4(1):67–82
47. Munshi AA, Mohamed A-RI, Yasser. (2017) Big data framework for analytics in smart grids. *Electr Power Syst Res* 151:369–380
48. Tanwar S, Parekh K, Evans R (2020) Blockchain-based electronic healthcare record system for healthcare 4.0 applications. *J Inform Secur Appl* 50:102407
49. Singh AP et al (2019) Storage and analysis of Synchrophasor data for event detection in Indian Power System Using Hadoop Ecosystem. In: *Data and communication networks*. Springer, Singapore, pp 291–304
50. Guo Y et al (2018) Complex power system status monitoring and evaluation using Big Data platform and machine learning algorithms: a review and a case study. *Complexity* 2018:1
51. Khan M et al (2014) Parallel detrended fluctuation analysis for fast event detection on massive PMU data. *IEEE Trans Smart Grid* 6(1):360–368
52. Chu L et al (2017) Massive streaming PMU data modelling and analytics in smart grid state evaluation based on multiple high-dimensional covariance test. *IEEE Tran Big Data* 4(1):55–64
53. Ruiguang M, Haiyan W, Quanming Z, Yuan L (2017) Technical research on the electric power big data platform of smart grid. In: *MATEC web of conferences*, vol 139. EDP Sciences, p 00217
54. Bhattarai BP et al (2019) Big data analytics in smart grids: state-of-the-art, challenges, opportunities, and future directions. *IET Smart Grid* 2(2):141–154
55. Liu Y, Lei W, Li J (2020) D-PMU based applications for emerging active distribution systems: a review. *Electr Power Syst Res* 179:106063
56. Cao Z, Lin J, Wan C, Song Y, Taylor G, Li M (2017) Hadoop-based framework for big data analysis of synchronized harmonics in active distribution network. *IET Gener Transm Distrib* 11(16):3930–3937

57. Mollaei N, Mousavi SH (2017) Application of a hadoop-based distributed system for offline processing of power quality disturbances. *Int J Power Electron Drive Syst(IJPEDS)* 8(2): 695–704
58. Khodayar M, Kaynak O, Khodayar ME (2017) Rough deep neural architecture for short-term wind speed forecasting. *IEEE Trans Indus Inform* 13(6):2770–2779
59. Zhang Y, Huang T, Bompard EF (2018) Big data analytics in smart grids: a review. *Energy Inform* 1(1):8
60. Madadi S et al (2018) Application of Big Data analysis to operation of smart power systems. In: *Big Data in engineering applications*. Springer, Singapore, pp 347–362
61. Chang L, Wang X, Mao M (2017) Forecast of schedulable capacity for thermostatically controlled loads with big data analysis. 2017 IEEE 8th international symposium on power electronics for distributed generation systems (PEDG), IEEE, pp 1–6
62. Husák M et al (2018) Survey of attack projection, prediction, and forecasting in cyber security. *IEEE Commun Surv Tutor* 21(1):640–660
63. Fang X et al (2019) A deep learning framework for predicting cyber attacks rates. *EURASIP J Inf Secur* 2019(1):1–11
64. Chadza T, Kyriakopoulos KG, Lambotharan S (2020) Analysis of hidden Markov model learning algorithms for the detection and prediction of multi-stage network attacks. *Futur Gener Comput Syst* 108:636–649
65. Zhang Y, Lin F, Wang K (2020) Robustness of short-term wind power forecasting against false data injection attacks. *Energies* 13(15):3780
66. Luo J, Hong T, Fang S-C (2018) Benchmarking robustness of load forecasting models under data integrity attacks. *Int J Forecast* 34(1):89–104
67. Doynikova E, Novikova E, Kotenko I (2020) Attacker behaviour forecasting using methods of intelligent data analysis: a comparative review and prospects. *Information* 11(3):168

Chapter 3

A New Stable Solar System for Electricity, Cooling, Heating, and Potable Water Production in Sunny Coastal Areas



Leyla Khani and Mousa Mohammadpourfard

Abstract Nowadays, more attention is paid to provide clean energy products with low environmental pollution in a decentralized way. Many coastal rural areas suffer from freshwater and electricity scarcity, especially in hot weather condition. Meanwhile, these regions have a great access to intense solar radiation and seawater. Hence, it seems logical to use the available solar energy in those places to provide necessities like power, heating, and cooling. A new solar cooling, power, heating, and freshwater production system is designed, evaluated, and optimized in this research. The proposed system is composed of several subsystems to generate each product with high efficiency and reliability. Solar energy is unavailable at night, so molten salt energy storage is used to establish the steady operation of the system. Then, the system is evaluated from thermodynamic and exergoeconomic viewpoints, and a parametric study is accomplished to study the effect on the system performance of key variables. In the end, the system is optimized to determine its best operating condition for different cases.

Keywords Goswami cycle · Solar energy · Optimization · Heat storage · Desalination · Multigeneration

3.1 Introduction

Nowadays, energy is an essential part of life and a primary requirement for economic and technical developments. Hence, energy consumption rate is rising rapidly, and it is predicted that the total energy necessity will grow by 25% until 2040 [1]. Fossil fuels are the main providers (nearly 80%) of present energy request [2]. However, it

L. Khani

Faculty of Chemical and Petroleum Engineering, University of Tabriz, Tabriz, Iran

M. Mohammadpourfard (✉)

Faculty of Chemical and Petroleum Engineering, University of Tabriz, Tabriz, Iran

Department of Energy Systems Engineering, Izmir Institute of Technology, Izmir, Turkey

e-mail: mohammadpour@tabrizu.ac.ir

should be considered that fossil fuel resources are limited, nonrenewable, and geographically unevenly distributed. This has led to some problems such as a decrease in available fossil fuel sources, the need to explore more reservoirs, an increase in fossil fuel prices, and political challenges. Yet, the utilization of fossil fuels leads to important problems: environmental pollution like greenhouse gas emissions, climate change, deforestation, polar ice melting, desertification, and associated health issues. Besides, current energy systems are not appropriately efficient, and almost 65–70% of fuel's chemical energy is lost in these systems. Thus, scientists are trying to find clean, efficient, and sustainable energy resources and conversion methods [3]. Among various suggestions, multigeneration systems and renewable energy sources seem significant [4].

Multigeneration systems are such systems which generate two or more types of energy products, e.g., electrical power, heating, hot water, cooling, freshwater, or material, from one fuel input [5]. These systems are usually designed by integrating separate thermodynamic systems through upper subsystem's waste recovery in the bottom ones [6]. Therefore, less fuel is needed in this case, and higher efficiency can be achieved [7]. Cost reduction [8], higher quality [9], less pollution [10], enhanced transmission [11], easier distribution [12], and reliability [13] are other benefits of the multigeneration systems, especially when renewable energy sources are selected as their fuel input.

As the main alternative of fossil fuels, renewable energy sources are going to provide more and more part of global energy demand, nearly 22% in 2035 [14]. The reduction in renewable energy costs, rule facilitation, and increase in their stability and durability are the main goals of researchers in this field. Among various types of renewable energies, solar energy has gained a lot of attention since it is the key source of available energy and its energy intensity is very significant. The utilization of solar energy is a good way to provide electrical power to remote areas in terms of cost, transportation, and maintenance. There are several applications for solar energy: power production, drying, cooking, hot water, and cooling [15]. Many areas benefit from high solar radiation and can convert it to their necessary products continuously, which decreases their dependency on fossil fuel resource utilization and transmission [16]. One of the important utilizations of solar energy is seawater desalination, as the reservoirs of freshwater are diminishing due to population growth, enhanced life standards, overconsumption, water pollution, and climate change [17]. Although 75% of the earth's surface is covered with water, less than 3% of it is freshwater [18]. Desalination is, in fact, the process of reducing salts in seawater to an acceptable range, making it suitable for drinking and human consumption [19]. This process requires a great amount of energy and is fortunately able to work with various energy sources such as solar energy. In this case, designed desalination system is a right solution for water shortage in remote areas with adequate solar radiation. Moreover, it can be integrated with other subsystems to generate other beneficial products that are necessary for those areas, as they are far from power and heating networks.

Renewable energy-based electrical power, freshwater, and refrigeration production systems have been studied in various papers, as summarized in Table 3.1.

Table 3.1 Literature review on electrical power, cooling, and potable water systems

References	Energy source	Proposed system	Products		
			Cooling	Power	Water
Sahoo et al. [20] Sahoo et al. [21]	Solar energy and biomass	Biomass-fired vapor compression cycle for power generation Preheating of working fluid by solar energy Heat recovery from the steam turbine for the desalination process	*	*	*
Ali et al. [22] Alsaman et al. [23] Elattar et al. [24] Fouda et al. [25] Ibrahim et al. [26] Su et al. [27]	Solar energy	Solar-based absorption refrigeration cycle and humidification-dehumidification process	*	×	*
Azhar et al. [28]	Solar energy, geothermal, and ocean heat	Power generation based on the ocean heat transfer cycle Three-stage flash based on geothermal and solar energy Absorption refrigeration cycle for cooling demand	*	*	*
Sadeghi et al. [29]	Hot environmental air and natural gas	Generation of superheated steam by hot air in the generator as the input to the steam turbine Humidification-dehumidification desalination process for freshwater production	×	*	*
Hogerwaard et al. [30]	Solar energy	Combined Brayton and Rankine cycle Multistage flash desalination cycle Absorption refrigeration cycle	*	*	*
Giwa et al. [31] Kabeel et al. [32]	Solar energy	Electricity production with photovoltaic cells Solar energy-based humidification-dehumidification cycle Heat transfer from the indoor air to refrigerant to cool the air Humidification-dehumidification cycle	*	*	*
Jabari et al. [33] Jabari et al. [34] Jabari et al. [35] Jabari et al. [36]	Solar energy and environmental air	Stirling cycle to generate electricity Air-to-air heat pump cycle to generate cooling and heating	*	*	*

(continued)

Table 3.1 (continued)

References	Energy source	Proposed system	Products		
			Cooling	Power	Water
Almutairi et al. [37] Catrini et al. [38] Gadhamshetty et al. [39]	Hot environmental air and natural gas	Brayton-Rankine combined cycle Distillation seawater desalination system Absorption refrigeration cycle Mechanical vapor compression	×	*	*
Antipova et al. [40] Delgado-Torres et al. [41] Gökçek [42] Nafey et al. [43] Rashidi et al. [44] Salcedo et al. [45]	Solar energy	Solar-based Rankine cycle and photovoltaic cells Reverse osmosis seawater desalination system	×	*	*

According to this table, a solar power, cooling, heating, and potable water generation system with energy storage has not been designed yet. This research addresses this important issue. Hence, a case study with real solar radiation data and power, cooling, heating, and freshwater demands is considered. A new system for generating electrical power, potable water, heating, and cooling based on solar energy is designed, analyzed, and optimized. The required equations for energy and exergoeconomic simulation of the system are applied together with an optimization algorithm. Then, the operation of the system under different conditions is assessed. Finally, the optimal conditions for the system performance in four optimization cases are determined.

3.2 System Description

The novel multigeneration system for electricity, cooling, heating, and freshwater is shown in Fig. 3.1. As can be seen from this figure, the proposed system consists of a solar energy collector, hot molten salt energy storage, cold molten salt energy storage, Goswami cycle, and a multistage flash seawater desalination process. Solar radiation energy is collected and transferred to the hot molten salt storage tank to make its temperature suitable for the other cycles. The excess solar energy is stored in the hot tank and used whenever the sun is not available, such as when it is cloudy or at night. This confirms the consistency of the system. The hot molten salt enters the superheater and boiler of the Goswami cycle [47]. In this cycle, the ammonia-water solution leaving the absorber is pumped and divided into streams 8A and 8B. 8A is sent directly to the rectifier, and 8B is heated in the recovery heat exchanger and mixed with streams 11, 19, and 20. The resulting mixture is sent to

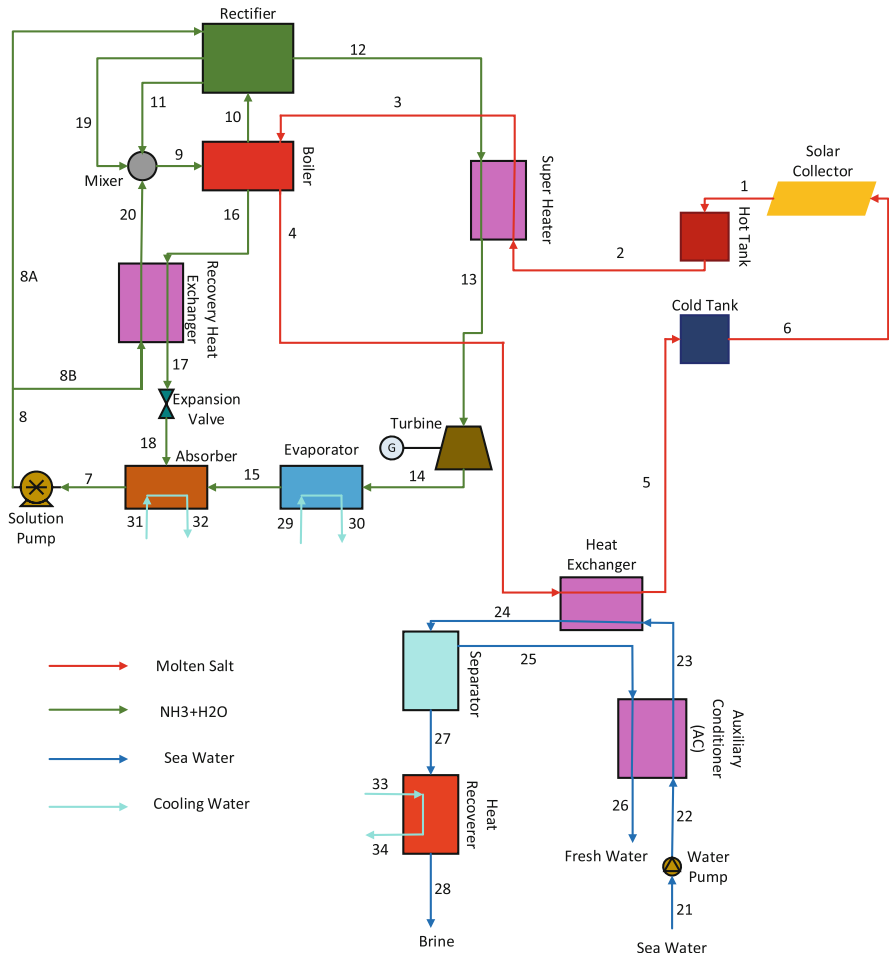


Fig. 3.1 Solar-based power, cooling, and freshwater trigenation system. (Reprinted from Khani et al. [46], copyright (2022), with permission from Elsevier)

the boiler, receives heat from the hot molten salt, and is separated into stream 10 (high ammonia concentration) and stream 16 (low ammonia concentration). Stream 16 flows back to the absorber through the recovery heat exchanger and expansion valve. Stream 10 is purified in the rectifier and heated in the superheater. It then generates electricity in the turbine and refrigeration in the evaporator. After the superheater and the boiler, the molten salt stream is used in the desalination subsystem to heat the pressurized seawater. The produced freshwater is separated from brine and cooled in the auxiliary conditioner and sent for storage/consumption. The brine is discharged after generating heat in the heat recovery unit.

3.3 Modeling Equations

In this section, mass, ammonia concentration (for Goswami cycle), and energy conservation equations are considered for each equipment. Also, the exergy and exergoeconomic relationships are applied. The obtained set of equations is solved with proper inputs in Engineering Equations Solver (EES) software, and thermodynamic and exergoeconomic properties of all existing streams are calculated. The following assumptions are considered:

- All components operate as steady-state control volumes, except the solar collector and the molten salt energy storage tanks.
- Potential and kinetic energy and exergy changes are neglected.
- Only the heat losses from the solar collector and molten salt storage tanks to the environment are of importance.

3.3.1 Thermodynamic Analysis

The mass and energy conservation laws for a component in steady state are as follows:

$$\sum \dot{m}_i = \sum \dot{m}_e \quad (3.1)$$

$$\dot{Q}_k - \dot{W}_k = \sum \dot{m}_e h_e - \sum \dot{m}_i h_i \quad (3.2)$$

in which:

\dot{m} : mass flow rate (kg/s)

e : outlet

i : inlet

\dot{Q} : heat transfer rate (kW)

\dot{W} : power (kW)

k : K^{th} component

h : specific enthalpy (kJ/kg)

Ammonia concentration for Goswami cycle is written as:

$$\sum \dot{m}_i x_i = \sum \dot{m}_e x_e \quad (3.3)$$

in which x is ammonia concentration.

Exergy is the maximum useful work that can be obtained when varying the system from its initial state to the dead state, if the system interacts just with the ambient. Also, exergy is the minimum essential work to take the system from the dead state to a desired state. Exergy analysis is useful in defining the place, cause,

and magnitude of energy loss and optimizing systems to better utilize finite energy sources. If electrical, magnetic, nuclear, and surface tension effects are neglected, the exergy of any material stream is computed as follows [48]:

$$\dot{E} = \dot{E}_{\text{ph}} + \dot{E}_{\text{ch}} \quad (3.4)$$

where:

\dot{E} : exergy rate (kW)
 ch: chemical
 ph: physical

Physical exergy is the maximum useful work gained when stream reaches thermal and mechanical equilibrium with the environment:

$$\dot{E}_{\text{ph}} = \sum \dot{m}_i [(h_i - h_i^0) - T_0 (s_i - s_i^0)] \quad (3.5)$$

where:

s : specific entropy (kJ/kg.K)
 T : temperature (K)
 0: environmental condition

Chemical exergy is the maximum work done by material while reaching chemical equilibrium with the environment. It can be calculated for an ideal gas mixture:

$$\dot{E}_{\text{ch}} = \sum \dot{m}_i e_i^{\text{ch}} + RT_0 \sum \dot{m}_i \ln y_i \quad (3.6)$$

in which:

\bar{e}^{ch} : standard chemical exergy of species (kJ/kmol)
 R : universal gas constant (kJ/kgK)
 y : mole fraction

For ammonia-water solution, chemical exergy is computed as follows:

$$\dot{E}_{\text{ch}} = \dot{m}_{\text{water}} e_{\text{water}}^{\text{ch}} + \dot{m}_{\text{ammonia}} e_{\text{ammonia}}^{\text{ch}} \quad (3.7)$$

The exergy destruction rate of a steady-state control volume is defined as [48]:

$$\dot{E}_D = \sum \left(1 - \frac{T_0}{T_j} \right) \dot{Q}_j - \dot{W}_{\text{cv}} + \sum \dot{E}_i - \sum \dot{E}_e \quad (3.8)$$

where D is destruction.

Equation (3.8) shows that the exergy is a destructible property due to the irreversible processes [48]. Thus, exergy analysis is an efficient tool for design, evaluation, and optimization of thermodynamic systems.

3.3.2 Exergoeconomic Analysis

There are several methods of economic evaluation of thermodynamic systems, of which exergoeconomics is considered. It combines exergy and economic principles. In other words, exergoeconomic analysis evaluates the cost of the exergy rate of each stream instead of the mass or energy flow. Consequently, the cost of the exergy destruction and products in the system equipment is calculated. The exergoeconomic balance for a steady-state control volume is defined as follows [49]:

$$\sum \dot{C}_e + \dot{C}_w = \sum \dot{C}_i + \dot{C}_q + \dot{Z} \quad (3.9)$$

$$\dot{C} = c\dot{E} \quad (3.10)$$

where:

c : cost per exergy unit (\$/GJ)

\dot{C} : cost rate (\$/hr)

\dot{Z} : capital cost rate (\$/hr)

q : heat

The exergoeconomic balance explains that the sum of the costs associated with exergy flows at the output equals the sum of the costs of the exergy streams at the input and the expenditure costs, as given in Eqs. (3.9) and (3.10). The expenditure cost is the cost of investment, operation, and maintenance of a control volume [50]:

$$\dot{Z} = \frac{Z \times \text{CRF} \times \varphi}{N} \quad (3.11)$$

$$\text{CRF} = \frac{i_r(1 + i_r)^n}{(1 + i_r)^n - 1} \quad (3.12)$$

where:

Z : component capital cost (\$)

CRF: capital recovery factor

N : system operating hours in a year

φ : maintenance factor

i_r : interest rate (%)

n : system lifetime (year)

The exergoeconomic equation, auxiliary relations, and purchase cost for each component are listed in Table 3.2.

Table 3.2 Exergoeconomic analysis of the system components

Component	Exergoeconomic equation	Auxiliary relation	Purchase cost
Solar collector [51]	$\dot{C}_6 + \dot{C}_q + \dot{Z}_{PTC} = \dot{C}_1$	$c_q = 0$	$Z_{PTC} = 150 \frac{\text{m}^2}{\text{m}^2}$
Cold tank [51]	$\dot{C}_5 + \dot{Z}_{CST} = \dot{C}_6$	—	$Z_{CST} = 35 \frac{\text{kWh}}{\text{kWh}}$
Hot tank [51]	$\dot{C}_1 + \dot{Z}_{HST} = \dot{C}_2$	—	$Z_{HST} = 35 \frac{\text{kWh}}{\text{kWh}}$
Solution pump [52, 53]	$\dot{C}_8 = \dot{C}_7 + \dot{C}_{w,SolutionPump} + \dot{Z}_{SolutionPump}$	$\frac{\dot{C}_{w,SolutionPump}}{W_{SolutionPump}} = \frac{\dot{C}_{w,Turbine}}{W_{Turbine}}$	$Z_{SolutionPump} = 2100 \left(\frac{W_{SolutionPump}}{10} \right)^{0.26} \left(\frac{1 - \eta_{SolutionPump}}{\eta_{SolutionPump}} \right)^{0.5}$
Rectifier [48, 52, 53]	$\dot{C}_{19} + \dot{C}_{11} + \dot{C}_{12} = \dot{C}_{8A} + \dot{C}_{10} + \dot{Z}_{Rectifier}$	$\frac{\dot{C}_{11} - \dot{C}_{10}}{E_{11} - E_{10}} = \frac{\dot{C}_{12} - \dot{C}_{10}}{E_{12} - E_{10}}$ $\frac{\dot{C}_{8A}}{E_{8A}} = \frac{\dot{C}_{19}}{E_{19}}, C_8 = C_{8A}$	$Z_{Rectifier} = 17000 \left(\frac{A_{Rectifier}}{100} \right)^{0.6}$
Mixer [54]	$\dot{C}_9 = \dot{C}_{11} + \dot{C}_{19} + \dot{C}_{20} + \dot{Z}_{Mixer}$	—	$Z_{Mixer} = 0$
Boiler [48, 52, 53]	$\dot{C}_{10} + \dot{C}_{16} + \dot{C}_4 = \dot{C}_9 + \dot{C}_3 + \dot{Z}_{Boiler}$	$\frac{\dot{C}_{10} - \dot{C}_9}{E_{10} - E_9} = \frac{\dot{C}_{16} - \dot{C}_9}{E_{16} - E_9},$ $\frac{\dot{C}_3}{E_3} = \frac{\dot{C}_4}{E_4}$	$Z_{Boiler} = 17500 \left(\frac{A_{Boiler}}{100} \right)^{0.6}$
Recovery heat exchanger [48, 52, 53]	$\dot{C}_{17} + \dot{C}_{20} = \dot{C}_{8B} + \dot{C}_{16} + \dot{Z}_{RecoveryHeatExchanger}$	$\frac{\dot{C}_{16}}{E_{16}} = \frac{\dot{C}_{17}}{E_{17}}, C_8 = C_{8B}$	$Z_{RecoveryHeatExchanger} = 12000 \left(\frac{A_{RecoveryHeatExchanger}}{100} \right)^{0.6}$
Expansion valve [55, 56]	$\dot{C}_{18} = \dot{C}_{17} + \dot{Z}_{ExpansionValve}$	—	$Z_{ExpansionValve} = 0$
Superheater [48, 52, 53]	$\dot{C}_{13} + \dot{C}_3 = \dot{C}_{12} + \dot{C}_2 + \dot{Z}_{Superheater}$	$\frac{\dot{C}_2}{E_2} = \frac{\dot{C}_3}{E_3}$	$Z_{Superheater} = 16000 \left(\frac{A_{Superheater}}{100} \right)^{0.6}$
Turbine [57]	$\dot{C}_{14} + \dot{C}_{w,Turbine} = \dot{C}_{13} + \dot{Z}_{Turbine}$	$\frac{\dot{C}_{13}}{E_{13}} = \frac{\dot{C}_{14}}{E_{14}}$	$Z_{Turbine} = 1.95(225 + 170\dot{W}_{Turbine})$
Evaporator [48, 52, 53]	$\dot{C}_{15} + \dot{C}_{30} = \dot{C}_{14} + \dot{C}_{29} + \dot{Z}_{Evaporator}$	$\frac{\dot{C}_{14}}{E_{14}} = \frac{\dot{C}_{15}}{E_{15}}, C_{29} = 0$	$Z_{Evaporator} = 16000 \left(\frac{A_{Evaporator}}{100} \right)^{0.6}$
Absorber [48, 52, 53]	$\dot{C}_7 + \dot{C}_{32} = \dot{C}_{15} + \dot{C}_{18} + \dot{C}_{31} + \dot{Z}_{Absorber}$	$\frac{\dot{C}_7}{E_7} = \frac{\dot{C}_{15} + \dot{C}_{18}}{E_{15} + E_{18}},$ $C_{31} = 0$	$Z_{Absorber} = 16500 \left(\frac{A_{Absorber}}{100} \right)^{0.6}$
Water pump [52, 53]	$\dot{C}_{22} = \dot{C}_{21} + \dot{C}_{w,WaterPump} + \dot{Z}_{WaterPump}$	$\frac{\dot{C}_{w,WaterPump}}{W_{WaterPump}} = \frac{\dot{C}_{w,Turbine}}{W_{Turbine}}$	$Z_{WaterPump} = 2100 \left(\frac{W_{WaterPump}}{10} \right)^{0.26} \left(\frac{1 - \eta_{WaterPump}}{\eta_{WaterPump}} \right)^{0.5}$
Auxiliary conditioner [48, 52, 53]	$\dot{C}_{23} + \dot{C}_{26} = \dot{C}_{22} + \dot{C}_{25} + \dot{Z}_{AuxiliaryConditioner}$	$C_{21} = 0$ $\frac{\dot{C}_{25}}{E_{25}} = \frac{\dot{C}_{26}}{E_{26}}$	$Z_{AuxiliaryConditioner} = 8000 \left(\frac{A_{AuxiliaryConditioner}}{100} \right)^{0.6}$

(continued)

Table 3.2 (continued)

Component	Exergoeconomic equation	Auxiliary relation	Purchase cost
Heat exchanger [48, 52, 53]	$\dot{C}_{24} + \dot{C}_5 = \dot{C}_{23} + \dot{C}_{24} + \dot{Z}_{\text{HeatExchanger}}$	$\frac{\dot{C}_4}{E_4} = \frac{\dot{C}_5}{E_5}$	$Z_{\text{HeatExchanger}} = 17000 \left(\frac{A_{\text{HeatExchanger}}}{100} \right)^{0.6}$
Separator [48]	$\dot{C}_{25} + \dot{C}_{27} = \dot{C}_{24} + \dot{Z}_{\text{Separator}}$	$\frac{\dot{C}_{24}}{E_{24}} = \frac{\dot{C}_{27}}{E_{27}}$	$Z_{\text{Separator}} = 0.98 (\eta_{25})^3$
Heat recoverer [48, 52, 53]	$\dot{C}_{28} + \dot{C}_{34} = \dot{C}_{27} + \dot{C}_{33} + \dot{Z}_{\text{HeatRecoverer}}$	$\frac{\dot{C}_{33}}{E_{33}} = \frac{\dot{C}_{34}}{E_{34}}$	$Z_{\text{HeatRecoverer}} = 17000 \left(\frac{A_{\text{HeatRecoverer}}}{100} \right)^{0.6}$

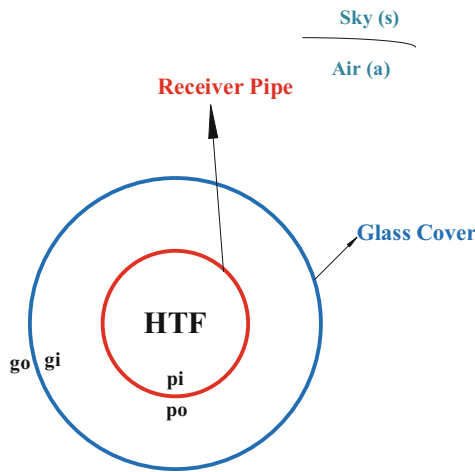
where:

- A: surface area (m²)
- CST: cold storage tank
- HST: hot storage tank
- PTC: parabolic trough collector
- η : energy efficiency

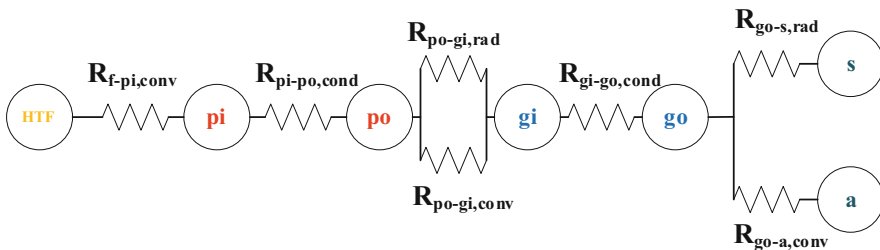
3.3.3 Solar Energy Collector (SEC)

The SEC consists of a parabolic reflector and a metal tube with a glass cover to decrease the thermal loss. Sunlight hits this parabolic reflector and gets reflected onto the receiver tube. The molten salt stream absorbs the solar energy. The thermal resistance method (TRM) [58] is used to model the thermal performance (TP) of the SEC. A cross-sectional view of the collector is shown in Fig. 3.2a. The thermal resistance model is also shown in Fig. 3.2b. The necessary equations for each resistance term are summarized in Table 3.3.

Finally, the energy balance is written for the receiver to calculate the energy transfer rate to the molten salt stream [58]:



(a) Cross-sectional view of receiver tube



(b) TRM [57]

Fig. 3.2 Schematic of SEC: (a) cross-sectional view of receiver tube, (b) TRM [58]. (Reprinted from Khani et al. [46], copyright (2022), with permission from Elsevier)

Table 3.3 Thermal resistance terms for the SEC [58, 59]

Heat transfer term	Equation
$\dot{q}_{\text{HTF-pi,conv}}$	$\frac{\left[1.82 \log \left(Re_{d_{\text{pi}}} \right) - 1.64 \right]^{-2}}{8 Pr_f \left(\frac{Re_{d_{\text{pi}}}}{1000} \right) + 1 + 12.7 \sqrt{\frac{f}{8}} (Pr_f^{2/3} - 1)} \left(\frac{Pr_f}{Pr_{\text{pi}}} \right)^{0.11} \left(\frac{k_f}{d_{\text{pi}}} \right) \pi d_{\text{pi}} (T_{\text{pi}} - T_f)$
$\dot{q}_{\text{pi-po,cond}}$	$\frac{2\pi k_{\text{pipe}} (T_{\text{pi}} - T_{\text{po}})}{\ln \left(\frac{d_{\text{po}}}{d_{\text{pi}}} \right)}$
$\dot{q}_{\text{po-gi,rad}}$	$\frac{\sigma \pi d_{\text{po}} (T_{\text{po}}^4 - T_{\text{gi}}^4)}{\frac{1}{\epsilon_{\text{po}}} + \frac{d_{\text{po}}}{\epsilon_{\text{gi}} d_{\text{gi}}}}$
$\dot{q}_{\text{po-gi,conv}}$	$\pi d_{\text{po}} \frac{k_{\text{std}}}{2 \ln \left(\frac{d_{\text{gi}}}{d_{\text{po}}} \right) + b\lambda \left(\frac{d_{\text{po}}}{d_{\text{gi}}} + 1 \right)} (T_{\text{po}} - T_{\text{gi}})$
$\dot{q}_{\text{gi-go,cond}}$	$\frac{2\pi k_g (T_{\text{gi}} - T_{\text{go}})}{\ln \left(\frac{d_{\text{go}}}{d_{\text{gi}}} \right)}$
$\dot{q}_{\text{go-s,rad}}$	$\sigma \epsilon_{\text{go}} \pi d_{\text{go}} (T_{\text{go}}^4 - T_s^4)$
$\dot{q}_{\text{go-a,conv}}$	$\pi d_{\text{go}} \frac{k_a}{d_{\text{go}}} C Re_{d_{\text{go}}}^m Pr_a^n \left(\frac{Pr_a}{Pr_{\text{go}}} \right)^{\frac{1}{4}} (T_{\text{go}} - T_a)$

In which:

d : diameter (m)

f : friction factor

gi : glass cover inner surface

go : glass cover outer surface

HTF: heat transfer fluid

K : thermal conductivity (W/mK)

pi : receiver pipe inner surface

po : receiver pipe outer surface

Pr : Prandtl number

Re : Reynolds number

σ : Stefan-Boltzmann constant (W/m²K)

λ : mean free path between collisions of a molecule (cm)

a : air

cond: conduction

conv: convection

f : fluid

rad: radiation

s : sky

$$\dot{Q}_u = \left(\dot{q}_{\text{po,SolAbs}} + \dot{q}_{\text{go,SolAbs}} - \dot{q}_{\text{heatloss}} \right) L_{\text{col}} \quad (3.13)$$

$$\dot{q}_{\text{heatloss}} = \dot{q}_{\text{go-a,conv}} + \dot{q}_{\text{go-s,rad}} \quad (3.14)$$

where:

L : length (m)

col: collector

$$\dot{Q}_u = \dot{m}_f c_{p,f} (T_{fo} - T_{fi}) \quad (3.15)$$

where c_p is specific heat capacity (kJ/kgK).

3.3.4 Molten Salt Heat Storage Tanks (MSHST)

The hot and cold MSHST are fully mixed [60]. As a result, each tank's temperature is uniformly time dependent and is defined by the following equations [51, 61]:

$$\left[(\rho V c_p)_I + (\rho V c_p)_{ST} \right] \frac{dT}{dt} = \dot{Q}_{in} - \dot{Q}_{loss} \quad (3.16)$$

$$\dot{Q}_{loss} = (UA)_{ST} (T_{ST} - T_0) \quad (3.17)$$

$$(UA)_{ST} = \left(\frac{k_i}{r_{ST1}} \right) \frac{1}{\ln \left(\frac{r_{SP2}}{r_{ST1}} \right)} (2\pi r_{ST1} L_{ST}) + \left(\frac{k_i}{\delta_i} (2\pi r_{ST1}^2) \right) \quad (3.18)$$

$$T_{ST,new} = T_{ST} + \frac{\Delta t}{(\rho V c_p)_I + (\rho V c_p)_{ST}} [\dot{Q}_{in} - \dot{Q}_{loss}] \quad (3.19)$$

in which:

r : radius (m)

t : time (s)

U : overall heat transfer coefficient (W/m²K)

V : volume (m³)

ρ : density (kg/m³)

ST: storage tank

The time interval is set as 1 hour, i.e., the properties of the molten salt and the tanks do not change in this period.

3.3.5 Performance Criteria

The electricity, cooling, heating, and potable water production rates are calculated as follows:

$$\dot{W}_{net} = \dot{W}_{Turbine} - \dot{W}_{SolutionPump} - \dot{W}_{WaterPump} \quad (3.20)$$

$$\dot{Q}_{cooling} = \dot{m}_{15} h_{15} - \dot{m}_{14} h_{14} \quad (3.21)$$

$$\dot{Q}_{\text{heating}} = \dot{m}_{34}h_{34} - \dot{m}_{33}h_{33} \quad (3.22)$$

$$\dot{Q}_{\text{freshwater}} = \dot{m}_{26}h_{26} - \dot{m}_{21}h_{21} \quad (3.23)$$

As is well-known, solar-based systems have time-dependent performance, but molten salt energy storage tanks enable the system constancy. Therefore, the energy and exergy efficiencies are defined as average daily values:

$$\eta = \frac{\sum_{t=1}^{24} \dot{W}_{\text{net}} + \dot{Q}_{\text{cooling}} + \dot{Q}_{\text{heating}} + \dot{Q}_{\text{freshwater}}}{\sum_{t=1}^{24} \dot{Q}_{\text{solar},t}} \quad (3.24)$$

$$\varepsilon = \frac{\sum_{t=1}^{24} \dot{W}_{\text{net}} + \dot{E}_{\text{cooling}} + \dot{E}_{\text{heating}} + \dot{E}_{\text{freshwater}}}{\sum_{t=1}^{24} \dot{E}_{\text{solar},t}} \quad (3.25)$$

\dot{Q}_{solar} and \dot{E}_{solar} are the total absorbed energy from the sun in the collector and its related exergy, respectively:

$$\dot{E}_{\text{solar}} = G_b A_a \left(1 + \frac{1}{3} \left(\frac{T_0}{T_{\text{sun}}} \right)^4 - \frac{4}{3} \left(\frac{T_0}{T_{\text{sun}}} \right) \right) \quad (3.26)$$

where G_b is solar radiation (W/m^2).

The total exergy destruction rate is the sum of the exergy destruction rates of all components.

$$\dot{E}_{D,\text{tot}} = \sum_k \dot{E}_{D,k} \quad (3.27)$$

The cost of producing drinking water, cooling, heating, and electrical energy together make up the total cost of the product:

$$c_{\text{tot}} = \frac{\dot{C}_{\dot{W}_{\text{net}}}}{\dot{W}_{\text{net}}} + \frac{\dot{C}_{\dot{Q}_{\text{cooling}}}}{\dot{Q}_{\text{cooling}}} + \frac{\dot{C}_{\dot{Q}_{\text{heating}}}}{\dot{Q}_{\text{heating}}} + \frac{\dot{C}_{\dot{Q}_{\text{freshwater}}}}{\dot{Q}_{\text{freshwater}}} \quad (3.28)$$

3.3.6 Optimization

Optimization of energy systems has attracted much attention recently, and its main objective is usually to minimize price or maximize efficiency. There are two types of optimization problems: single-objective optimization and multi-objective optimization. Single-objective optimization involves optimizing only one performance objective. In multi-objective optimization, on the other hand, more than one objective function is defined and optimized simultaneously. In this case, there are more than one answer to the problem that are equally good and acceptable. The genetic algorithm is widely used for engineering optimization problems. It is based on the theory of the evolution of generations: only the most tolerant members of a group live for generations. A comprehensive and parallel search is done in the problem space, and then the answers are compared to select the best one. So, it is more likely to get the globally optimal point [62].

Engineering Equations Solver (EES) is used to solve the resulting system of equations for mass, energy, exergy, and exergoeconomics. Then, four examples of the system's optimization are defined. The three single-objective optimization situations of maximizing energy efficiency, maximizing exergy efficiency, and minimizing total product cost are all solved by the general algebraic modeling system (GAMS). Finally, the EES and MATLAB software are coupled to undertake a multi-objective optimization process. The competing objective functions for this process are exergy efficiency and total product cost.

3.3.7 Verification

The simulation results for the Goswami cycle in this study are compared in Table 3.4 with the available data in [47], demonstrating respectable concordance between the results of the current work and earlier ones.

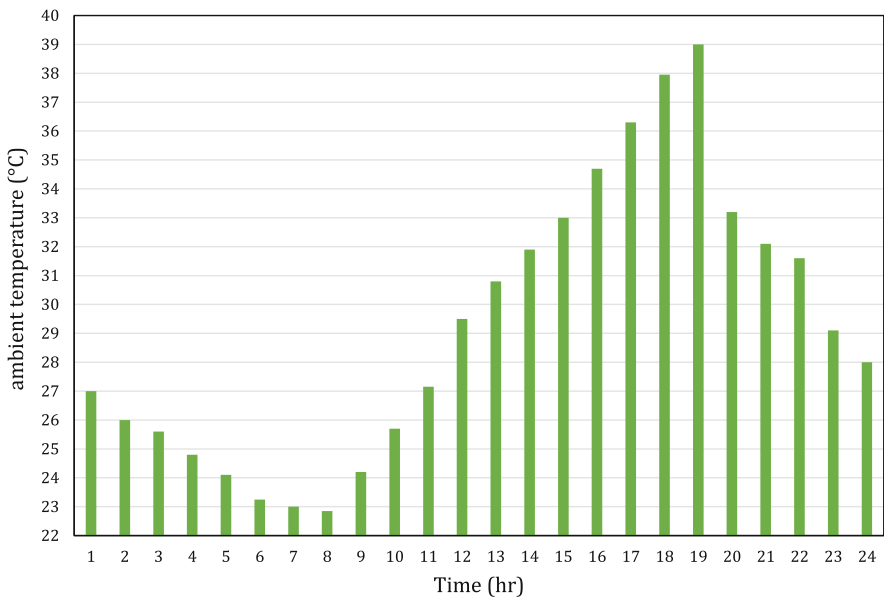
Moreover, When the output heat transfer fluid temperatures for various solar radiations in the current work are compared with those in reference [59] in Table 3.5, it is clear that the current study is highly accurate.

Table 3.4 Validation of Goswami cycle

Performance criteria	Ref. [47]	Present work
Turbine power (kW)	47.96	44.18
Pump power (kW)	3	2.771
Cooling load (kW)	3.85	3.361
Superheater duty (kW)	0	0
Energy efficiency (%)	14	16.18

Table 3.5 Validation of the solar energy collector

Radiation intensity (W/m ²)	Ambient temperature (°C)	Inlet temperature of heat transfer fluid (°C)	Outlet temperature of heat transfer fluid (°C)		Relative error (%)
			Present work	Ref. [59]	
933.7	21.2	102.2	123.7	121.65	1.68
968.2	22.4	151	170	170.15	0.088
982.3	24.3	197.5	218.5	216.51	0.92
909.5	26.2	250.7	267.1	265.84	0.47
937.9	28.8	297.8	315.3	312.97	0.74

**Fig. 3.3** The variation in ambient temperature during the day. (Reprinted from Khani et al. [46], copyright (2022), with permission from Elsevier)

3.4 Results and Discussion

To evaluate the performance of the designed system, a case study with realistic power and cooling requirements and hourly ambient temperature variations is considered, as shown in Figs. 3.3, 3.4, and 3.5, respectively. The required inputs are also listed in Table 3.6.

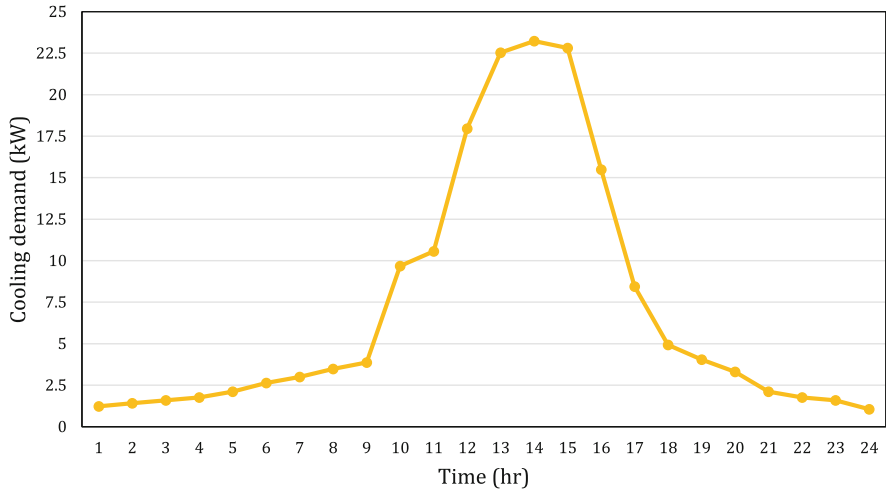


Fig. 3.4 The variation in cooling demand during the sample day. (Reprinted from Khani et al. [46], copyright (2022), with permission from Elsevier)

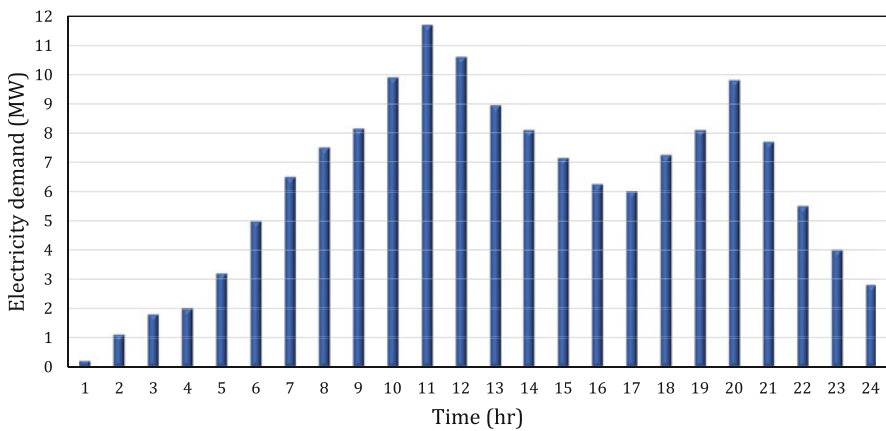


Fig. 3.5 The variation in electricity demand of the case study during the sample day. (Reprinted from Khani et al. [46], copyright (2022), with permission from Elsevier)

3.4.1 Base Case Study

The variations over time of the SEC outlet fluid temperature and the MSHST temperature are depicted in Fig. 3.6. As can be seen, the use of thermal energy storage tank has a positive effect on the reliability and stability of the system and compensates for the large hourly fluctuations in the ambient temperature and solar radiation.

Table 3.6 Used data for modeling of the system [47, 48, 58, 59, 63]

Parameter	Value
Ambient pressure (bar)	1
Ambient temperature (°C)	25
Pressure ratio for pump and turbine	10
Pressure loss in boiler (bar)	0.4
Pressure loss in superheater (bar)	0.2
Ammonia concentration at the rectifier exit	0.98
Boiler pressure (bar)	1.5
Absorber temperature	9.72
Pump and turbine adiabatic efficiency (%)	85
Superheating degree (°C)	0
Minimum approach temperature in heat exchangers (°C)	5
Interest rate (%)	12
Annual operating hours (hr/year)	8760
Year life	20
Operating and maintenance factor	1.06
Collector apparatus width (m)	5
Collector length (m)	7.8
Receiver outer diameter (m)	0.07
Receiver inner diameter (m)	0.066
Glass cover outer diameter (m)	0.0115
Glass cover inner diameter (m)	0.109
Receiver pipe thermal conductivity (W/mK)	54
Glass cover thermal conductivity (W/mK)	0.78
Glass cover emittance	0.86
Number of collectors	4

Figure 3.7 illustrates the variations of the input solar exergy rate and the exergy destruction of the solar collector during 24 hours. Both exergy rates reach their highest values around noon and become zero in the night hours, corresponding to the form of the radiation intensity.

3.4.2 Parametric Study

Figure 3.8 shows the influence of changing the pressure ratio in the Goswami cycle on the system performance. The system power output rate improves from 6.9 to 12.8 MW when the Goswami pressure ratio is increased from 5 to 14.5 as shown in Fig. 3.8a. This is because a larger production capacity in the Goswami cycle turbine is made possible by a higher pressure. However, when the pressure ratio is increased above 14.5, this trend reverses as the power consumption of the Goswami cycle exceeds the output of the turbine and reduces the net power generation of the system.

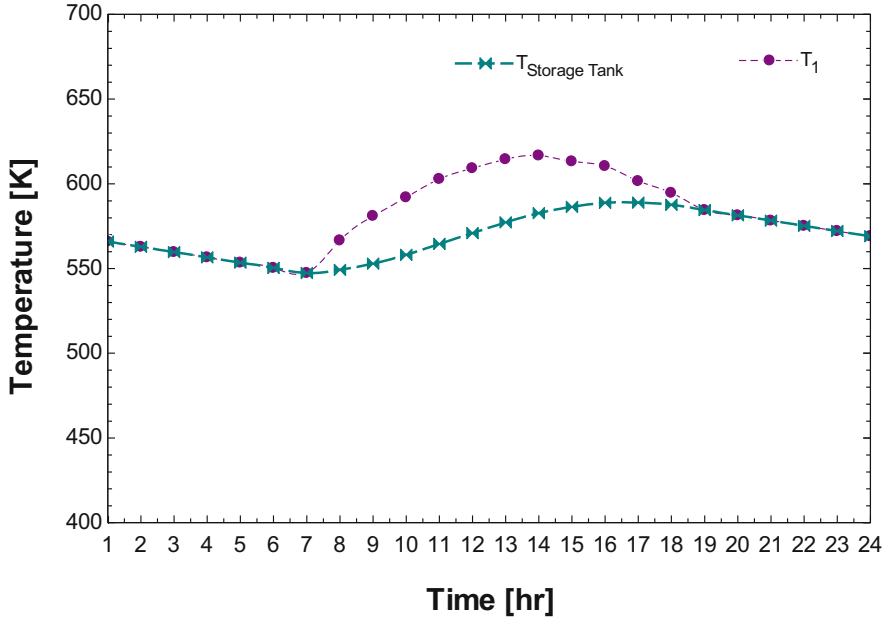


Fig. 3.6 The variation of temperatures of the MSHST and solar system outlet fluid during the day. (Reprinted from Khani et al. [46], copyright (2022), with permission from Elsevier)

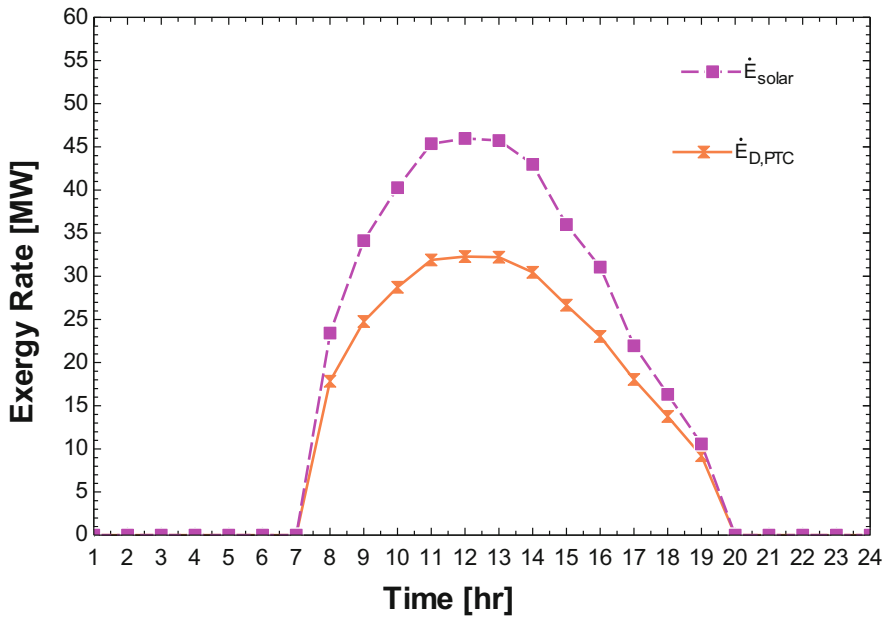


Fig. 3.7 Received solar exergy and its exergy destruction rates. (Reprinted from Khani et al. [46], copyright (2022), with permission from Elsevier)

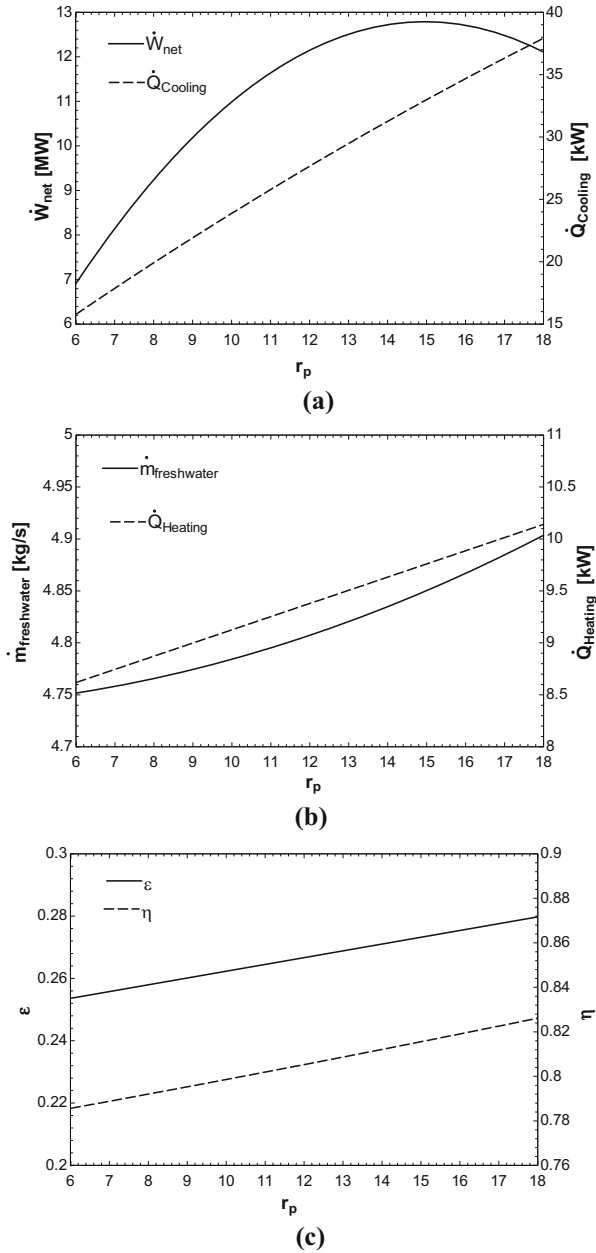


Fig. 3.8 Performance of the system as a result of adjusting the turbine pressure ratio: (a) net power and cooling, (b) freshwater and heating, (c) energy and exergy efficiencies, (d) total exergy destruction, (e) total product cost. (Reprinted from Khani et al. [46], copyright (2022), with permission from Elsevier)

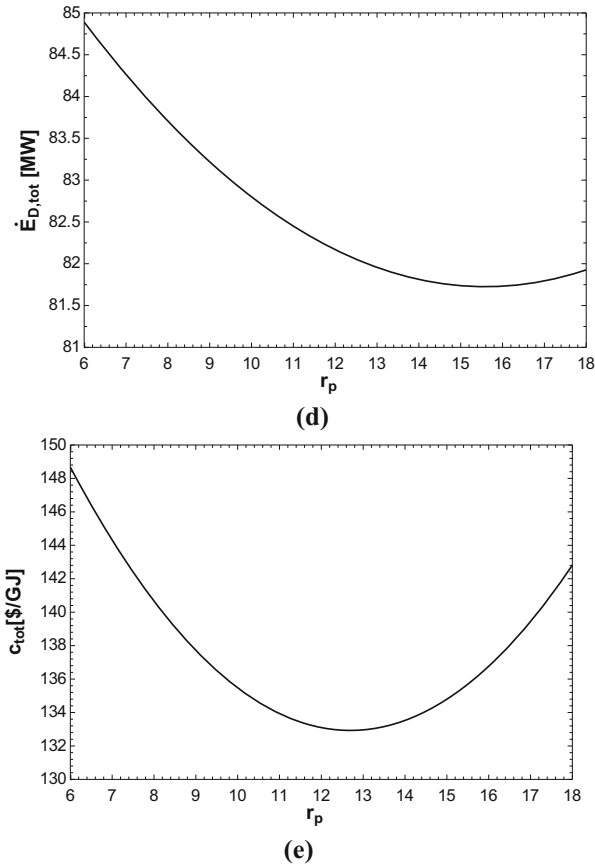


Fig. 3.8 (continued)

Also, the cooling of the evaporator incoming stream is directly affected by the pressure ratio and causes the amount of cooling produced to rise from 16 kW to 38 kW. Because there is more heat available to the desalination plant with a higher turbine pressure ratio, Fig. 3.8b shows that the mass flow of potable water and heating also increase. The variations in system energy and exergy efficiencies with turbine pressure ratio are shown in Fig. 3.8c. Both efficiencies improve by around 3.3% as the system pressure ratio rises. It is evident that the positive effects of freshwater production, cooling, and heating outweigh the negative effects of net electricity generation. The impact of the system pressure ratio on the rate of total exergy degradation is seen in Fig. 3.8d. At a pressure ratio of 15.7, the total exergy destruction has a minimum value of 81.74 MW. The rising system outputs are mostly responsible for the declining trend in energy destruction. As shown in Fig. 3.8a, the net power of the system drops over a particular pressure ratio; therefore, it is expected that the exergy destruction would also rise. The pressure ratio has a considerable influence on the price of the final product, as illustrated in

Fig. 3.8e; thus, the value of this parameter must be carefully chosen. The cost of the final product is reduced by 10.38 percent when the pressure ratio is raised from 6 to 12.6. This is because the system's beneficial products increase, which lowers their costs. The price of manufacturing the system products rises when the pressure ratio surpasses 12.6.

The effects of various ammonia concentrations at the rectifier's output on the system's operation are depicted in Fig. 3.9. According to Fig. 3.9a, the cooling capacity is closely correlated with this parameter because when x_{12} rises, the refrigerant flow rate in the evaporator also rises, increasing the cooling generation of the system. The net power generation, however, is on the decline and falls by 3.3 MW. A rise in x_{12} results in a drop in the turbine's output power and intake temperature, which has an adverse impact on system power. As seen in Fig. 3.9b, an adjustment to x_{12} has a favorable impact on the flow of freshwater and the generation of heat, mostly as a result of an increase in the saltwater input to the desalination system, owing to the rise in the heat it can get. The effect of x_{12} on the system's energy and exergy efficiencies is not the same, as shown in Fig. 3.9c. The system's energy efficiency rises as x_{12} rises, but its exergy efficiency falls. If Fig. 3.9a, b are additionally taken into account, the following may be explained: Energy efficiency rises because the rising trends in cooling, heating, and freshwater generation offset the falling trend in net power production. However, it should be emphasized that in terms of exergy efficiency, the rise in exergy value for cooling, heating, and drinking water cannot make up for the net power reduction; as a result, the system's exergy efficiency decreases. Figure 3.9d demonstrates that the x_{12} has a direct impact on the overall exergy destruction since it causes the system's useable exergy to decline. The total product cost with an increase in x_{12} initially achieves its lowest value of 131.2\$/GJ before rising to 150\$/GJ, as shown in Fig. 3.9e.

The impact of the system's superheating degree is depicted in Figs. 3.10a–e. As the superheating degree rises, Fig. 3.10a demonstrates that the system's net output power and refrigeration production both peak at particular superheating degree values. In reality, larger superheating degrees imply higher turbine intake temperatures, higher turbine production capacities, and higher evaporating capacities. A larger superheating degree than its peak values, however, has a negative impact on the system and lowers its cooling and power capability. Figure 3.10b illustrates the impact of the superheating degree on the flow of potable water and the production of heat, and in contrast to the previous figure, it shows a decreasing and growing trend. Solar energy is used to fuel the superheater in order to achieve higher superheating degrees. As a result, the desalination system's heat input declines, resulting in less water and less heating. This pattern flips over a certain point, increasing the quantity of heating and freshwater. Energy efficiency declines but the exergy efficiency increases when the superheating degree rises, as seen in Fig. 3.10c. By taking into account the explanations in Fig. 3.10a, b, these tendencies are easily comprehended. Figure 3.10d shows that the total energy destruction decreases by 0.3 MW as the superheating degree rises from 0 to 10 K. It should be noted that the reason for this decrease is the increase in product exergy rates leaving the system. Figure 3.10e

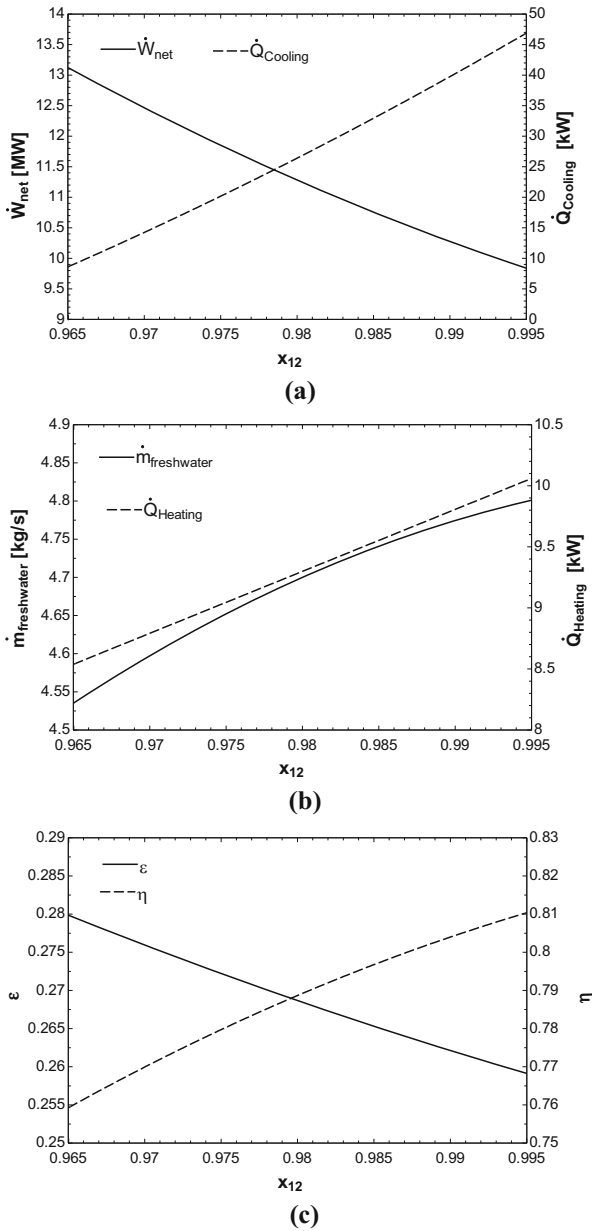
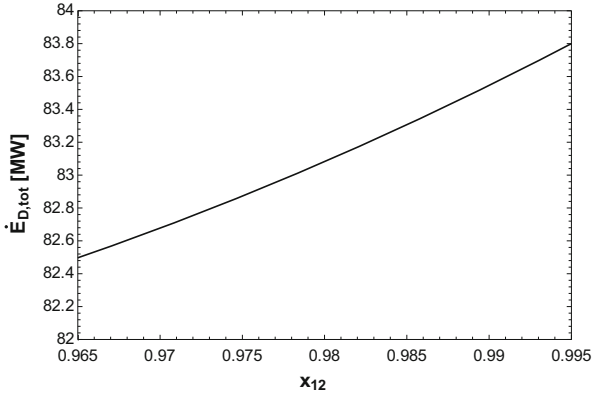
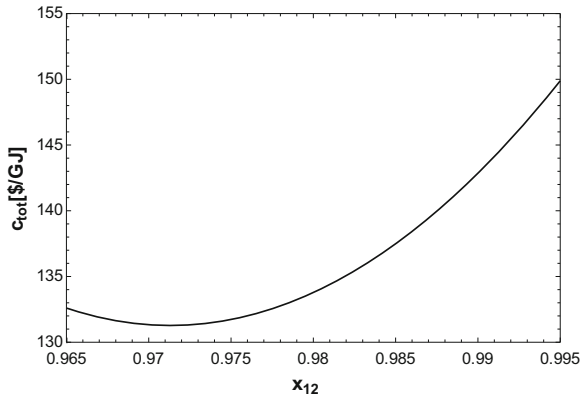


Fig. 3.9 The system performance variation in versus ammonia concentration in the rectifier outlet: (a) net power and cooling, (b) freshwater and heating, (c) energy and exergy efficiencies, (d) total exergy destruction, (e) total product cost. (Reprinted from Khani et al. [46], copyright (2022), with permission from Elsevier)



(d)



(e)

Fig. 3.9 (continued)

shows the effect of the superheating degree on the total product cost. By increasing the superheating degree from 0 to 8.3 K, this cost is reduced by 5.5 \$/GJ.

The differences in system functioning brought on by the change in the minimum approach temperature in the heat exchangers are shown in Fig. 3.11. According to Fig. 3.11a, the output power first rises to 11.7 MW when the minimum approach temperature rises before falling as a result of changes in turbine power. On the other side, 84.62 percent less system cooling is provided. As revealed in Fig. 3.11b, the freshwater flow rate decreases to its minimum and then increases to 4.9 kg/s. However, the heat production rate shows an opposite trend. Additionally, Fig. 3.11c shows that the energy efficiency trend is the reverse of the exergy efficiencies. Energy efficiency first declines and subsequently increases as the minimum approach temperature rises. On the other side, exergy efficiency shows a counterintuitive tendency. Furthermore, Fig. 3.11d shows that the total exergy destruction changes in an increasing process from 83.02 to 83.04 MW when the

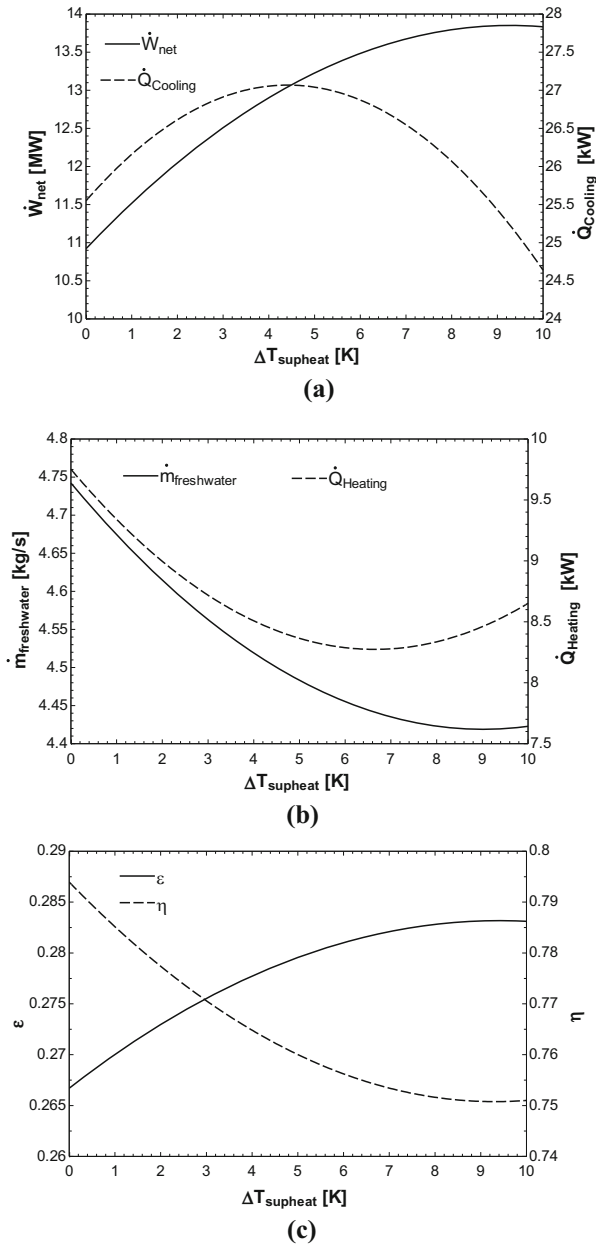


Fig. 3.10 Variation of performance of the proposed system in versus superheating degree: (a) net power and cooling, (b) freshwater and heating, (c) energy and exergy efficiencies, (d) total exergy destruction, (e) total product cost. (Reprinted from Khani et al. [46], copyright (2022), with permission from Elsevier)

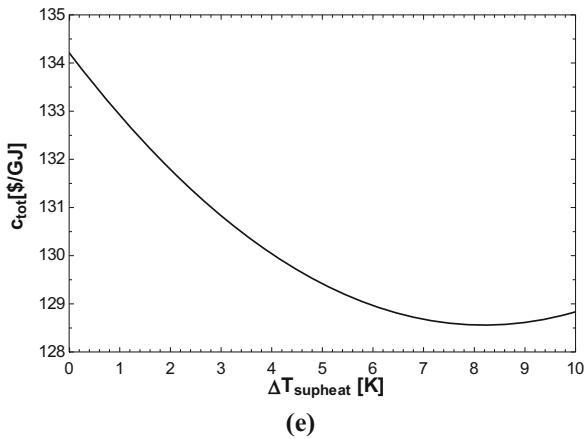
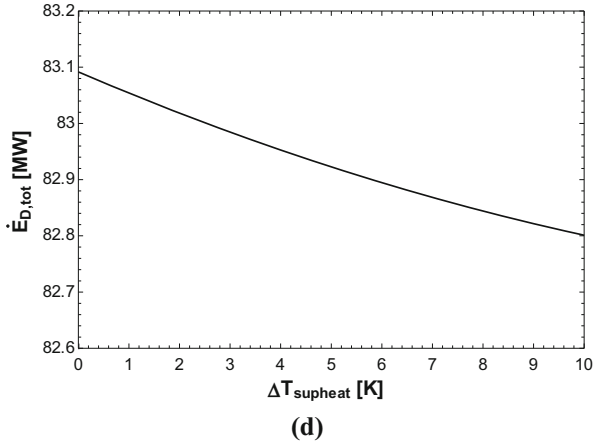


Fig. 3.10 (continued)

minimum approach temperature rises from 3 to 15 K. The overall cost of the products increases from 129 to 167 \$/GJ, as shown by Fig. 3.11e.

3.4.3 Optimization Results

The aforementioned parametric study demonstrates that four variables have an impact on how the system operates: the pressure ratio in the Goswami cycle, the ammonia concentration at the rectifier's outlet, the degree of superheating, and the minimum approach temperature in the heat exchangers. The decision variables' upper and lower bounds are as follows:

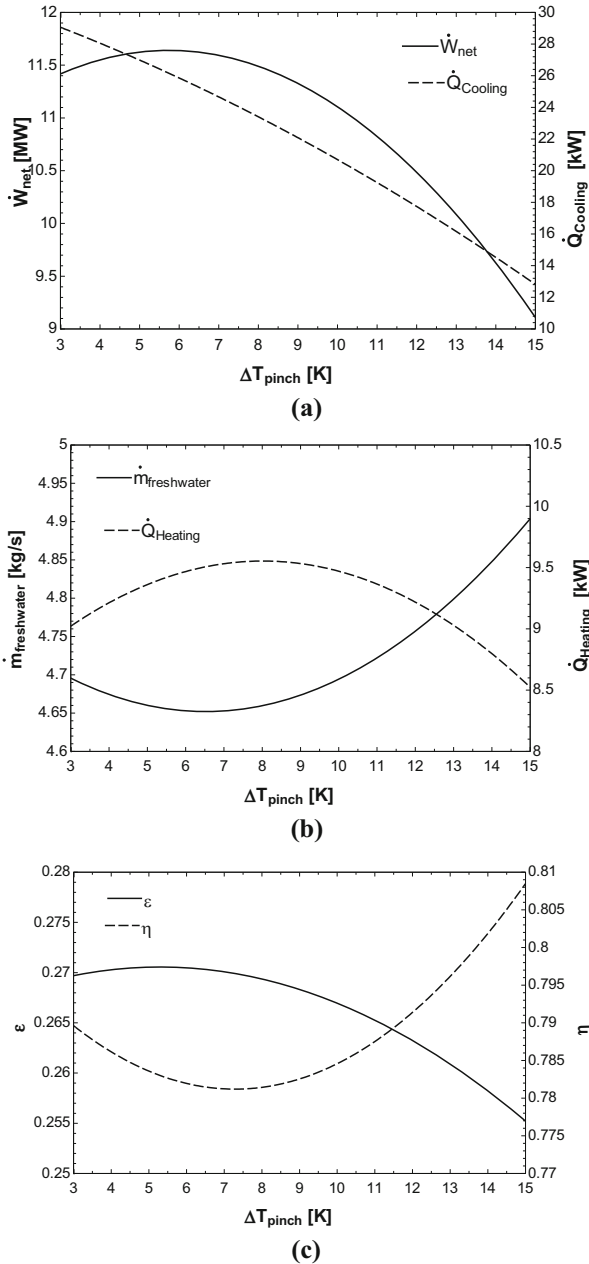


Fig. 3.11 The effect of variation in the minimum approach temperature of the heat exchangers on the system performance: (a) net power and cooling, (b) freshwater and heating, (c) energy and exergy efficiencies, (d) total exergy destruction, (e) total product cost. (Reprinted from Khani et al. [46], copyright (2022), with permission from Elsevier)

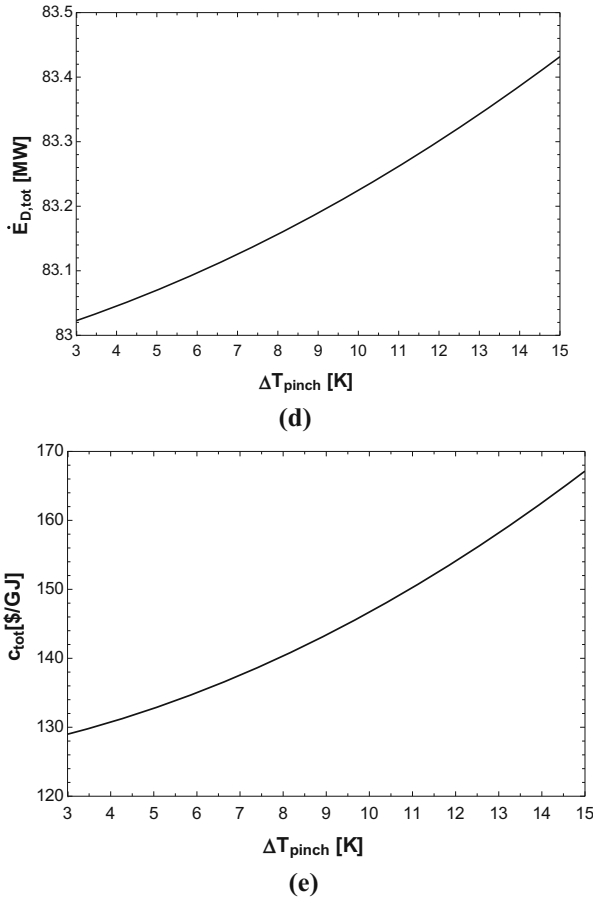


Fig. 3.11 (continued)

$$6 \leq r_p \leq 18 \quad (3.29)$$

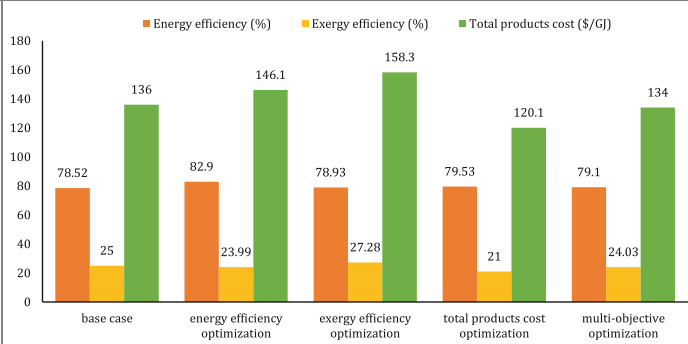
$$0.965 \leq x_{12} \leq 0.995 \quad (3.30)$$

$$0 \leq \Delta T_{\text{supheat}} \leq 10 \quad (3.31)$$

$$3 \leq \Delta T_{\text{pinch}} \leq 15 \quad (3.32)$$

Table 3.7 provides a summary of the findings for the base case, the three single-objective optimization instances, and the two-objective optimization case. The exergy efficiency in the exergy optimization instance, as shown in the table, is 27.28 percent, which is 3.29 percent and 6.28 percent greater than the values for the other single-objective optimization modes, energy efficiency and total product cost, respectively. For energy efficiency optimization, the maximum value of 82.9 percent is reached. By optimizing the cost function, the lowest cost of all items is

Table 3.7 The results of the optimization scenarios



Goswami turbine pressure ratio	10	6.98	14.53	17.06	15.8
Minimum approach temperature in heat exchangers (K)	5	3.596	14.71	3	10
Superheating degree (K)	0	6.261	6.437	0.2495	4.5
Ammonia concentration in the rectifier exit	0.98	0.992	0.9723	0.965	0.971
Net output power (MW)	11.52	7.027	11.56	13.74	12
Total exergy destruction (MW)	83.07	84.52	82.32	80.73	81.05
Cooling capacity (kW)	26.8	25.19	10.1	23.81	15.74
Heating production (kW)	9.31	10.11	9.35	9.4	10.05
Freshwater mass flow rate (kg/s)	4.67	5.03	4.75	4.71	4.72

reached, which is 120.1 \$/GJ. The single-objective optimization of exergy efficiency yields the greatest overall product cost, which is 158.3 \$/GJ. On the other side, when the cost of the entire product is optimized, the exergy efficiency is at its lowest. It can be concluded that in order to get the highest exergy efficiency, one must select more costly, consequently more expensive, equipment and operating conditions. This raises the cost of the system. Additionally, selecting less expensive tools and circumstances lowers exergy efficiency.

If we compare the outcomes of single-objective optimization to those of multi-objective optimization, we find that the values achieved in multi-objective optimization fall within the realm of single-objective optimization outcomes. Exergy efficiency and total product cost, as was previously said, are incompatible, and improving one results in a decline in the other. It is therefore difficult to establish

an operating situation where the exergy efficiency and the overall cost of the items are at their highest levels. The degree to which both objective functions are met therefore defines the working condition for multi-objective optimization.

3.5 Conclusions

In this study, a multistage seawater desalination system is coupled with a Goswami power and cooling cycle to provide a solar-assisted power, cooling, and freshwater tri-generation process. To maintain consistent system performance despite changing solar radiation, a molten salt heat storage mechanism is also installed. The system components are subjected to the laws of thermodynamics and exergoeconomics. Analysis is done on the sensitivity of the system performance to the primary key parameters. The optimal operating scenarios are then ascertained by simulating three single-objective optimization cases (i.e., maximizing energy efficiency, maximizing exergy efficiency, and minimizing total products cost) and a multi-objective optimization case:

- For certain values of turbine pressure ratio, the net power generation of the system is maximized, but the total exergy destruction rate and the total products cost are minimized. In addition, the cooling capacity, heating capacity, freshwater flow rate, and energy and exergy efficiency increase as the turbine pressure ratio increases.
- As the ammonia concentration at the rectifier's outlet rises, so do the cooling capacity, heat production, freshwater flow rate, energy efficiency, and total exergy destruction. However, under these operating circumstances, the net power and exergy efficiency decline. Finally, for a given x_{12} , the overall cost of the items is low.
- Both the net output power and the cooling generation reach their maximum levels as the superheating degree rises, but the potable water flow rate, heating, and the total products cost are minimal for certain values of the superheating degree. In addition, system energy efficiency and the total exergy destruction decrease, while exergy efficiency increases.
- The net power, heating rate, and energy efficiency finally achieve their maximum values as the minimum approach temperature rises. In contrast, there is a lowering to growing trend in freshwater rate and energy efficiency. Additionally, although the amount of energy destroyed and the overall cost of all items rise, cooling capacity declines.
- The multi-objective optimization scenario's outcomes are in between the single-objective optimizations' operational circumstances. This is because exergy efficiency and total product cost are in opposition to one another, and improving one causes the other to degrade.

References

1. Santamouris M (2019) Energy consumption and environmental quality of the building sector. <https://doi.org/10.1016/b978-0-12-811417-9.00002-7>
2. Kumar V, Shrivastava RL, Untawale SP (2015) Solar energy: review of potential green & clean energy for coastal and offshore applications. *Aquat Proc* 4:473–480. <https://doi.org/10.1016/j.aqpro.2015.02.062>
3. Mossi Idrissa AK, Goni BK (2019) Advanced exergy analysis of a combined Brayton/Brayton power cycle. *Energy* 166:724–737. <https://doi.org/10.1016/j.energy.2018.10.117>
4. Mirzaee M, Zare R, Sadeghzadeh M, Maddah H, Ahmadi MH, Acıkkalp E et al (2019) Thermodynamic analyses of different scenarios in a CCHP system with micro turbine – absorption chiller, and heat exchanger. *Energy Convers Manag* 198:111919. <https://doi.org/10.1016/j.enconman.2019.111919>
5. Dinçer İ, Zamfirescu C (2012) Integrated multigeneration energy systems BT - sustainable energy systems and applications. In: Dinçer İ, Zamfirescu C (eds) . Springer US, Boston, MA, pp 479–517. https://doi.org/10.1007/978-0-387-95861-3_12
6. Bicer Y, Dincer I (2016) Analysis and performance evaluation of a renewable energy based multigeneration system. *Energy* 94:623–632. <https://doi.org/10.1016/J.ENERGY.2015.10.142>
7. Ahmadi P, Dincer I, Rosen MA (2013a) Thermodynamic modeling and multi-objective evolutionary-based optimization of a new multigeneration energy system. *Energy Convers Manag* 76:282–300. <https://doi.org/10.1016/j.enconman.2013.07.049>
8. Nazerifard R, Khani L, Mohammadpourfard M, Mohammadi-Ivatloo B, Akkurt GG (2021) Design and thermodynamic analysis of a novel methanol, hydrogen, and power trigeneration system based on renewable energy and flue gas carbon dioxide. *Energy Convers Manag* 233: 113922. <https://doi.org/10.1016/j.enconman.2021.113922>
9. Ahmadi P, Dincer I, Rosen MA (2013b) Development and assessment of an integrated biomass-based multi-generation energy system. *Energy* 56:155–166. <https://doi.org/10.1016/j.energy.2013.04.024>
10. Ishaq H, Dincer I, Naterer GF (2019) Multigeneration system exergy analysis and thermal management of an industrial glassmaking process linked with a Cu–Cl cycle for hydrogen production. *Int J Hydrog Energy* 44:9791–9801. <https://doi.org/10.1016/j.ijhydene.2018.12.140>
11. Pirmohamadi A, Ghazi M, Nikian M (2019) Optimal design of cogeneration systems in total site using exergy approach. *Energy* 166:1291–1302. <https://doi.org/10.1016/j.energy.2018.10.167>
12. Ozturk M, Dincer I (2013) Thermodynamic analysis of a solar-based multi-generation system with hydrogen production. *Appl Therm Eng* 51:1235–1244. <https://doi.org/10.1016/j.applthermaleng.2012.11.042>
13. Dincer I, Rosen MA, Ahmadi P (2017) Modeling and optimization of multigeneration energy systems. In: *Optim. Energy Syst.* Wiley, Chichester, UK, pp 398–446. <https://doi.org/10.1002/9781118894484.ch11>
14. Gruenspecht, H., & Administrator A. Key findings in the IEO2011 reference case. 2011
15. Kannan N, Vakeesan D (2016) Solar energy for future world: - a review. *Renew Sust Energ Rev* 62:1092–1105. <https://doi.org/10.1016/J.RSER.2016.05.022>
16. Najafi G, Ghobadian B, Mamat R, Yusaf T, Azmi WH (2015) Solar energy in Iran: current state and outlook. *Renew Sust Energ Rev* 49:931–942. <https://doi.org/10.1016/J.RSER.2015.04.056>
17. *Future_Challenges_of_Providing_High_Qual* n.d.
18. Organisation WH (2011) Guidelines for drinking water quality
19. Brandt MJ, Johnson KM, Elphinston AJ, Ratnayaka DD (2017) Chapter 1 - The demand for potable water. In: Brandt MJ, Johnson KM, Elphinston AJ, Ratnayaka DDBT-TWS, Seventh E (eds) . Butterworth-Heinemann, Boston, pp 1–36. <https://doi.org/10.1016/B978-0-08-100025-0.00001-6>

20. Sahoo U, Kumar R, Pant PC, Chaudhury R (2015) Scope and sustainability of hybrid solar-biomass power plant with cooling, desalination in polygeneration process in India. *Renew Sust Energy Rev* 51:304–316. <https://doi.org/10.1016/J.RSER.2015.06.004>
21. Sahoo U, Kumar R, Pant PC, Chaudhary R (2017) Development of an innovative polygeneration process in hybrid solar-biomass system for combined power, cooling and desalination. *Appl Therm Eng* 120:560–567. <https://doi.org/10.1016/J.APPLTHERMALENG.2017.04.034>
22. Ali SM, Chakraborty A (2016) Adsorption assisted double stage cooling and desalination employing silica gel + water and AQSOA-Z02 + water systems. *Energy Convers Manag* 117: 193–205. <https://doi.org/10.1016/J.ENCONMAN.2016.03.007>
23. Alsaman AS, Askalany AA, Harby K, Ahmed MS (2017) Performance evaluation of a solar-driven adsorption desalination-cooling system. *Energy* 128:196–207. <https://doi.org/10.1016/J.ENERGY.2017.04.010>
24. Elattar HF, Fouda A, Nada SA (2016) Performance investigation of a novel solar hybrid air conditioning and humidification–dehumidification water desalination system. *Desalination* 382: 28–42. <https://doi.org/10.1016/J.DESAL.2015.12.023>
25. Fouda A, Nada SA, Elattar HF (2016) An integrated A/C and HDH water desalination system assisted by solar energy: transient analysis and economical study. *Appl Therm Eng* 108:1320–1335. <https://doi.org/10.1016/J.APPLTHERMALENG.2016.08.026>
26. Ibrahim AGM, Dincer I (2015) Experimental performance evaluation of a combined solar system to produce cooling and potable water. *Sol Energy* 122:1066–1079. <https://doi.org/10.1016/J.SOLENER.2015.10.033>
27. Su B, Han W, Jin H (2017) An innovative solar-powered absorption refrigeration system combined with liquid desiccant dehumidification for cooling and water. *Energy Convers Manag* 153:515–525. <https://doi.org/10.1016/J.ENCONMAN.2017.10.028>
28. Azhar MS, Rizvi G, Dincer I (2017) Integration of renewable energy based multigeneration system with desalination. *Desalination* 404:72–78. <https://doi.org/10.1016/J.DESAL.2016.09.034>
29. Sadeghi M, Yari M, Mahmoudi SMS, Jafari M (2017) Thermodynamic analysis and optimization of a novel combined power and ejector refrigeration cycle – desalination system. *Appl Energy* 208:239–251. <https://doi.org/10.1016/J.APENERGY.2017.10.047>
30. Hogerwaard J, Dincer I, Naterer GF (2017) Solar energy based integrated system for power generation, refrigeration and desalination. *Appl Therm Eng* 121:1059–1069. <https://doi.org/10.1016/J.APPLTHERMALENG.2017.03.116>
31. Giwa A, Fath H, Hasan SW (2016) Humidification–dehumidification desalination process driven by photovoltaic thermal energy recovery (PV-HDH) for small-scale sustainable water and power production. *Desalination* 377:163–171. <https://doi.org/10.1016/J.DESAL.2015.09.018>
32. Kabeel AE, Abdelgaied M, Zakaria Y (2017) Performance evaluation of a solar energy assisted hybrid desiccant air conditioner integrated with HDH desalination system. *Energy Convers Manag* 150:382–391. <https://doi.org/10.1016/J.ENCONMAN.2017.08.032>
33. Jabari F, Nojavan S, Mohammadi Ivatloo B, Sharifian MBB (2016a) Optimal short-term scheduling of a novel tri-generation system in the presence of demand response programs and battery storage system. *Energy Convers Manag* 122:95–108. <https://doi.org/10.1016/J.ENCONMAN.2016.05.056>
34. Jabari F, Nojavan S, Mohammadi IB (2016b) Designing and optimizing a novel advanced adiabatic compressed air energy storage and air source heat pump based μ -Combined Cooling, heating and power system. *Energy* 116:64–77. <https://doi.org/10.1016/J.ENERGY.2016.09.106>
35. Jabari F, Mohammadi-Ivatloo B, Rasouli M (2017) Optimal planning of a micro-combined cooling, heating and power system using air-source heat pumps for residential buildings BT - energy harvesting and energy efficiency: technology, methods, and applications. In: Bizon N, Mahdavi Tabatabaei N, Blaabjerg F, Kurt E (eds) . Springer International Publishing, Cham, pp 423–455. https://doi.org/10.1007/978-3-319-49875-1_15

36. Jabari F, Mohammadi-Ivatloo B, Li G, Mehrjerdi H (2018) Design and performance investigation of a novel absorption ice-making system using waste heat recovery from flue gases of air to air heat pump. *Appl Therm Eng* 130:782–792. <https://doi.org/10.1016/J.APPLTHERMALENG.2017.11.015>
37. Almutairi A, Pilidis P, Al-Mutawa N, Al-Weshahi M (2016) Energetic and exergetic analysis of cogeneration power combined cycle and ME-TVC-MED water desalination plant: Part-1 operation and performance. *Appl Therm Eng* 103:77–91. <https://doi.org/10.1016/J.APPLTHERMALENG.2016.02.121>
38. Catrini P, Cipollina A, Micale G, Piacentino A, Tamburini A (2017) Exergy analysis and thermoeconomic cost accounting of a combined heat and power steam cycle integrated with a multi effect distillation-thermal vapour compression desalination plant. *Energy Convers Manag* 149:950–965. <https://doi.org/10.1016/J.ENCONMAN.2017.04.032>
39. Gadhamshetty V, Gude VG, Nirmalakhandan N (2014) Thermal energy storage system for energy conservation and water desalination in power plants. *Energy* 66:938–949. <https://doi.org/10.1016/J.ENERGY.2014.01.046>
40. Antipova E, Boer D, Cabeza LF, Guillén-Gosálbez G, Jiménez L (2013) Multi-objective design of reverse osmosis plants integrated with solar Rankine cycles and thermal energy storage. *Appl Energy* 102:1137–1147. <https://doi.org/10.1016/J.APENERGY.2012.06.038>
41. Delgado-Torres AM, García-Rodríguez L (2012) Design recommendations for solar organic Rankine cycle (ORC)-powered reverse osmosis (RO) desalination. *Renew Sust Energy Rev* 16:44–53. <https://doi.org/10.1016/J.RSER.2011.07.135>
42. Gökçek M (2018) Integration of hybrid power (wind-photovoltaic-diesel-battery) and seawater reverse osmosis systems for small-scale desalination applications. *Desalination* 435:210–220. <https://doi.org/10.1016/J.DESAL.2017.07.006>
43. Nafey AS, Sharaf MA (2010) Combined solar organic Rankine cycle with reverse osmosis desalination process: energy, exergy, and cost evaluations. *Renew Energy* 35:2571–2580. <https://doi.org/10.1016/J.RENENE.2010.03.034>
44. Rashidi H, Khorshidi J (2018) Exergoeconomic analysis and optimization of a solar based multigeneration system using multiobjective differential evolution algorithm. *J Clean Prod* 170:978–990. <https://doi.org/10.1016/J.JCLEPRO.2017.09.201>
45. Salcedo R, Antipova E, Boer D, Jiménez L, Guillén-Gosálbez G (2012) Multi-objective optimization of solar Rankine cycles coupled with reverse osmosis desalination considering economic and life cycle environmental concerns. *Desalination* 286:358–371. <https://doi.org/10.1016/J.DESAL.2011.11.050>
46. Khani L, Jabari F, Mohammadpourfard M, Mohammadi-ivatloo B (2021) Design, evaluation, and optimization of an efficient solar-based multi-generation system with an energy storage option for Iran's summer peak demand. *Energy Convers Manag* 242:114324
47. Demirkaya G, Vasquez Padilla R, Goswami DY, Stefanakos E, Rahman MM (2011) Analysis of a combined power and cooling cycle for low-grade heat sources. *Int J Energy Res* 35:1145–1157. <https://doi.org/10.1002/er.1750>
48. Seshadri K (1996) Thermal design and optimization, vol 21. [https://doi.org/10.1016/s0360-5442\(96\)90000-6](https://doi.org/10.1016/s0360-5442(96)90000-6)
49. Pirmohamadi A, Ghaebi H, Ziapour BM, Ebadollahi M (2021) Exergoeconomic analysis of a novel hybrid system by integrating the Kalina and Heat pump cycles with a nitrogen closed Brayton system. *Energy Rep* 7:546–564. <https://doi.org/10.1016/j.egyr.2021.01.009>
50. Lazzaretto A, Tsatsaronis G (2006) SPECO: a systematic and general methodology for calculating efficiencies and costs in thermal systems. *Energy* 31:1257–1289. <https://doi.org/10.1016/j.energy.2005.03.011>
51. Ashouri M, Khoshkar Vandani AM, Mehrpooya M, Ahmadi MH, Abdollahpour A (2015) Techno-economic assessment of a Kalina cycle driven by a parabolic Trough solar collector. *Energy Convers Manag* 105:1328–1339. <https://doi.org/10.1016/j.enconman.2015.09.015>

52. Misra RD, Sahoo PK, Gupta A (2006) Thermoeconomic evaluation and optimization of an aqua-ammonia vapour-absorption refrigeration system. *Int J Refrig* 29:47–59. <https://doi.org/10.1016/j.ijrefrig.2005.05.015>
53. Misra RD, Sahoo PK, Sahoo S, Gupta A (2003) Thermoeconomic optimization of a single effect water/LiBr vapour absorption refrigeration system. *Int J Refrig* 26:158–169. [https://doi.org/10.1016/S0140-7007\(02\)00086-5](https://doi.org/10.1016/S0140-7007(02)00086-5)
54. Vieira LS, Donatelli JL, Cruz ME (2009) Exergoeconomic improvement of a complex cogeneration system integrated with a professional process simulator. *Energy Convers Manag* 50: 1955–1967. <https://doi.org/10.1016/j.enconman.2009.04.020>
55. Al-Otaibi DA, Dincer I, Kalyon M (2004) Thermoeconomic optimization of vapor-compression refrigeration systems. *Int Commun Heat Mass Transf* 31:95–107. [https://doi.org/10.1016/S0735-1933\(03\)00205-7](https://doi.org/10.1016/S0735-1933(03)00205-7)
56. Gebreslassie BH, Guillén-Gosálbez G, Jiménez L, Boer D (2009) Design of environmentally conscious absorption cooling systems via multi-objective optimization and life cycle assessment. *Appl Energy* 86:1712–1722. <https://doi.org/10.1016/j.apenergy.2008.11.019>
57. Quoilin S, Declaye S, Tchanche BF, Lemort V (2011) Thermo-economic optimization of waste heat recovery Organic Rankine Cycles. *Appl Therm Eng* 31:2885–2893. <https://doi.org/10.1016/j.applthermaleng.2011.05.014>
58. Kalogirou SA (2012) A detailed thermal model of a parabolic trough collector receiver. *Energy* 48:298–306. <https://doi.org/10.1016/j.energy.2012.06.023>
59. Behar O, Khellaf A, Mohammedi K (2015) A novel parabolic trough solar collector model – validation with experimental data and comparison to Engineering Equation Solver (EES). *Energy Convers Manag* 106:268–281. <https://doi.org/10.1016/j.enconman.2015.09.045>
60. Zolfagharnasab MH, Aghanajafi C, Kavian S, Heydarian N, Ahmadi MH (2020) Novel analysis of second law and irreversibility for a solar power plant using heliostat field and molten salt. *Energy Sci Eng* 8:4136–4153. <https://doi.org/10.1002/ese3.802>
61. Sukhatme K, Sukhatme SP (1996) *Solar energy: principles of thermal collection and storage*. Tata McGraw-Hill
62. Link H, Weuster-Botz D (2011) 2.17 - medium formulation and development. In: Moo-Young MBT-CB, Third E (eds) . Pergamon, Oxford, p 199–213. <https://doi.org/10.1016/B978-0-444-64046-8.00074-4>
63. Vidal A, Best R, Rivero R, Cervantes J (2006) Analysis of a combined power and refrigeration cycle by the exergy method. *Energy* 31:3401–3414. <https://doi.org/10.1016/j.energy.2006.03.001>

Chapter 4

Investigation of a New Methanol, Hydrogen, and Electricity Production System Based on Carbon Capture and Utilization



Leyla Khani and Mousa Mohammadpourfard

Abstract It is well-known that clean energy transition requires low carbon emission. The increase in population, economic development, and human welfare demands has led to a rise in energy consumption, mainly supplied by fossil fuels. However, burning fossil fuels produces carbon dioxide, which is a greenhouse gas and a contributor to environmental problems. Therefore, carbon capture and conversion to different products have gained attention. On the other hand, combining two or more different thermodynamic systems for simultaneous production of various demands from one energy source looks reasonable. In this regard, a new trigeneration system is proposed to decrease atmospheric carbon dioxide emission and produce methanol, hydrogen, and power. A flue gas stream with a defined composition, solar energy, and atmospheric air are the system's inlets. Then, mass, energy, and exergy balance equations are applied for each subsystem to investigate the system's thermodynamic performance. Also, the effect of changing operating parameters on the performance of each subsystem is studied.

Keywords Carbon dioxide capture · Methanol · Direct methanol fuel cell · Multigeneration system · Exergy · Waste utilization

4.1 Introduction

Global energy consumption has increased in recent years due to population growth, rapid economic development, and improved living conditions. About 85% of energy demand is met by burning fossil fuels [1]. Although fossil fuel-based power plants have advanced technologies and are widely used worldwide, burning fossil fuels

L. Khani

Faculty of Chemical and Petroleum Engineering, University of Tabriz, Tabriz, Iran

M. Mohammadpourfard (✉)

Faculty of Chemical and Petroleum Engineering, University of Tabriz, Tabriz, Iran

Department of Energy Systems Engineering, Izmir Institute of Technology, Izmir, Turkey

e-mail: mohammadpour@tabrizu.ac.ir

releases large amounts of greenhouse gas emissions including carbon dioxide, which leads to environmental problems such as global warming, climate change, deforestation, and flooding. It is estimated that 7 Gt of carbon dioxide is released into the atmosphere [2], which is really worrying. Therefore, it seems essential to reduce the production and emission of carbon dioxide. Various solutions have been proposed, of which carbon capture and storage (CCS) has gained attention, especially when the captured carbon is converted into valuable products such as methanol, dimethyl ether, and methane [3].

The reaction of carbon dioxide and hydrogen in a catalytic regenerative converter produces methanol. Methanol has high energy density, is easy to store and transport, and has low toxicity and little impact on the environment [4]. In addition, other valuable substances can be obtained from methanol, such as acetic acid, formaldehyde, methyl tertiary-butyl ether, and dimethyl ether [5]. Methanol can also be blended with gasoline to increase its octane number or used as fuel for fuel cells [6]. Therefore, conversion of emitted carbon dioxide to methanol has been studied under various conditions [7]. The hydrogen required for conversion of carbon dioxide to methanol can be provided in several ways, and one of them is solar water splitting. In this case, no pollution is produced, and excess hydrogen can be stored for further use or sale or even as a storage medium for solar energy.

Another disadvantage of fossil fuels is their finite nature, which leads to price instability and energy insecurity. Moreover, conventional thermodynamic systems have an efficiency of about 35–40%, which means that two-thirds of the chemical energy of the fuel is lost. Researchers are therefore trying to develop more efficient systems to convert most of the fuel's energy into useful products. Multigeneration systems are one of the proposed solutions that combine two or more systems to simultaneously generate products such as electricity, heating, cooling, and freshwater from one fuel source. As a result, they have many advantages such as high efficiency, reliability, low cost, and less pollution [8].

The effects of employing various waste heat sources on a system for creating methanol from collected carbon dioxide were investigated by Migrand et al. [9]. They showed that the efficiency of energy production from renewable sources is up to 59%. Nevertheless, fossil fuels should be used to meet almost 3.6% of the energy demand of the system. Boretti [10] examined a system that uses hydrogen as a feedstock and flue gas from an oxyfuel combustion plant to create methanol. He arrived at the conclusion that methanol has a higher conversion efficiency than gasoline and can be a good choice for high power concentration. A technique for producing hydrogen and methanol from wind energy was developed by Sayah et al. [11]. According to their findings, the implementation of their method in Iran might result in a rise in the use of renewable energy sources, natural gas consumption, and CO₂ emissions. Esmaili et al. [12] conducted a research on a solar-powered system for producing methanol and hydrogen. By studying the effects of different operating parameters, they demonstrated that the intensity of sunlight affects system efficiency. Under equilibrium settings, Leonzio et al. [13] examined three distinct methanol reactor designs: a once-through reactor, a reactor that recycles unconverted gases, and a reactor with a water-permeable membrane. The feed streams were only

pure carbon dioxide and hydrogen. They demonstrated that the highest carbon conversion of 69% could be reached when a reactor with recycling of unconverted gases was employed to produce methanol. A carbon to methanol conversion system was subjected to an evaluation by Atsonios et al. [14] of the effects of various design and operational factors. They came to the conclusion that the most crucial factor is the cost of producing hydrogen. When various renewable energy sources are employed, Rivarolo et al. [15] investigated the thermoeconomic performance of high-pressure reactors for the manufacture of methanol. According to their findings, the plant based on biogas has the best economic performance, and buying carbon dioxide results in reduced investment expenses. The performance of a plant that generates electricity, methanol, and hydrogen was examined from a thermodynamic, thermoeconomic, and environmental perspective by Nami et al. [16]. A geothermally driven organic Rankine cycle, a proton exchange membrane electrolyzer (PEME), an S-Graz cycle with oxyfuel combustion, and a methanol synthesis unit were the components of their planned facility. They pointed out that the S-Graz cycle is the most investment-intensive part of the system, and the cost per unit product was estimated to be about 24.88 \$/GJ. In order to manufacture methanol from carbon dioxide hydrogenation, Kiatphuegorn et al. [17] investigated the impact of an external magnetic field on the performance of a packed bed reactor. Catalysts supported on copper-iron were placed throughout the reactor. Their findings demonstrated that the use of a magnetic field enhanced methanol synthesis, carbon dioxide conversion, and reactor efficiency. A post-combustion carbon capture system was examined by Luu et al. [18] for better gas recovery and methanol production from a coal-fired power plant's flue gas. They asserted that their suggested method, which relied on natural gas with a high carbon dioxide concentration, might function effectively. The use of hydrogen from the formation of sodium methoxide (NaOCH_3) in the carbon dioxide hydrogenation reaction was looked into by Charoensuppanimit et al. [19]. They claimed that the optimum choice was an adiabatic packed bed reactor. Ghosh et al. [20] assessed three process designs for producing methanol from carbon dioxide produced in a biogas plant. They showed that all these designs can satisfy the need for energy, but the two-reactor concept with the fiber catalyst has the maximum efficiency and methanol production. In order to change the syngas concentration in the process of producing methanol from landfill gas, Gao et al. [21] suggested either adding more hydrogen or absorbing more carbon dioxide. They came to the conclusion that the first alternative is more inexpensive and more energy-efficient. In a novel methanol manufacturing method, Alsayegh et al. [22] investigated how safely collected carbon dioxide diluted the hydrogen generated by photovoltaic water splitting and aided the hydrogenation reaction. The methanol produced in this situation is more expensive than the usual one, according to their economic analysis. In their simulation of a plant, Matzen et al. [23] used electrolytic hydrogen produced by wind energy to produce methanol and dimethyl ether while capturing carbon dioxide produced by the fermentation of ethanol ($\text{C}_2\text{H}_5\text{OH}$). They said that although the manufacturing of methanol has a lesser environmental effect than the production of dimethyl ether, the advantages are negated by the burning of methanol.

In this work, a novel system for the production of methanol, hydrogen, and electric power is designed and evaluated from a thermodynamic point of view. First, flue gas from a refinery furnace is fed into an organic Rankine cycle (ORC) to generate electricity and control the temperature for carbon capture and methanol production. Hydrogen is produced from water in the proton exchange membrane electrolyzer using solar energy and divided into two parts: one for the conversion reaction of carbon to methanol and the other for storage, sale, and use during cloudy or nighttime periods. Then, a direct methanol fuel cell is integrated to generate electricity from a certain amount of the methanol produced. Heat integration is implemented into the system, with special attention to reducing external energy requirement. In the next step, mass and energy conversion laws are established for each component, as well as exergy relations at steady state. Aspen HYSYS and Engineering Equation Solver (EES) software tools are used to model the energy and exergy performance of the system. Finally, the operation of the system under various conditions is studied.

4.2 System Description

The schematic diagram of the proposed system for the production of electricity, hydrogen, and methanol can be seen in Fig. 4.1. According to this figure, the system consists of the following subsystems: an ORC, a carbon dioxide capture unit (CC), a

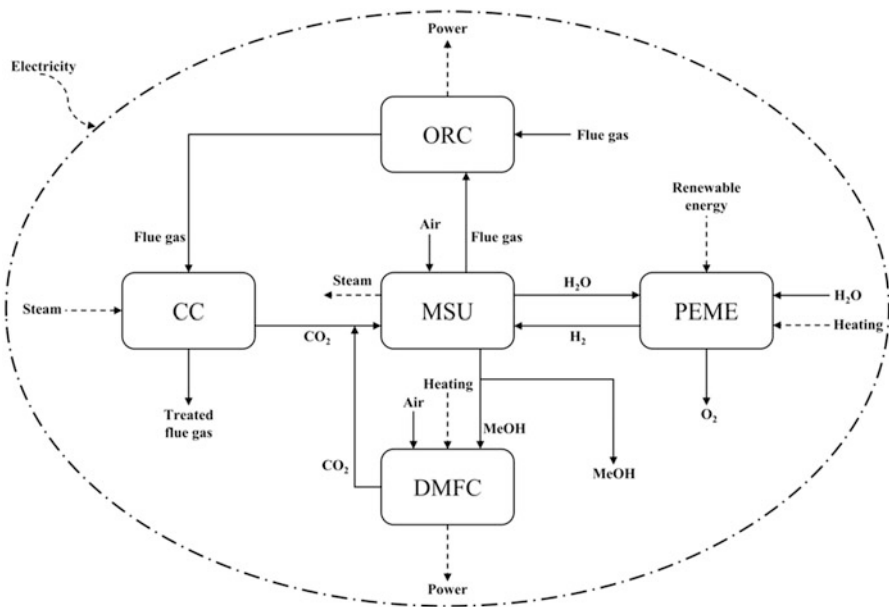


Fig. 4.1 An overview of the whole system. (Reprinted from Nazerifard et al. [24], copyright (2022), with permission from Elsevier)

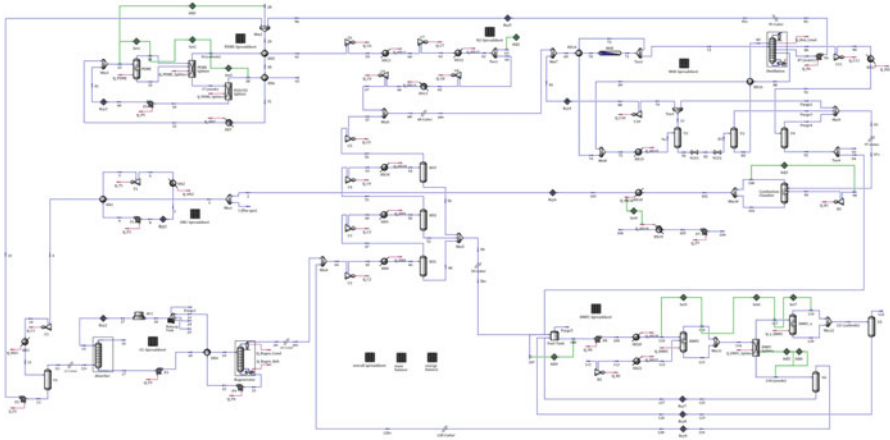


Fig. 4.2 Configuration of the system in Aspen HYSYS. (Reprinted from Nazerifard et al. [24], copyright (2022), with permission from Elsevier)

PEME, a methanol synthesis unit (MSU), and a DMFC. The complete arrangement of the system in the Aspen HYSYS simulation environment is shown in Fig. 4.2. The input materials are flue gas from a refinery furnace, water, solar energy, and air.

The ORC is used to generate electricity from high-temperature flue gasses and to adjust the temperature for the carbon capture system. Then the flue gas is fed into the carbon dioxide capture plant; 91% of the carbon dioxide content is captured and fed into the methanol synthesis plant. The hydrogen required for methanol synthesis is generated in the solar-based proton exchange membrane electrolyzer by the water splitting reaction. Part of the hydrogen is sent to the MSU, and the other part is stored for use or sale. In the MSU, carbon dioxide reacts with hydrogen to produce methanol and water. The water is sent to the electrolyzer, while the methanol is divided into two parts: Part of the methanol is used in a DMFC stack to generate electricity, and the rest is stored as liquid fuel. The gas released from the MSU is combusted to provide heat for pressurized steam generation.

The system is modeled using the following assumptions:

- The system operates in a steady state.
- The pipeline pressure fluctuations are disregarded.
- Heat transfer from the piping and apparatus is neglected.
- The system uses cooling water at a temperature and pressure of 25 °C and 3 bar.
- The efficiency of all pumps, compressors, and turbines is assumed to be 85%.
- The changes in potential and kinetic energy and exergy are negligible.
- 25 °C and 1 atm are the ambient temperature and pressure, respectively.

To design and simulate the system, Aspen HYSYS v8.8 with three separate fluid packages is employed. For carbon capture and methanol synthesis, the Acid Gas and Extended NRTL fluid packages are employed, respectively. The Peng-Robinson fluid package is used for the other units.

Table 4.1 Molar composition of the system's input flue gas

Composition	Molar fraction
N ₂	0.782
O ₂	0.021
H ₂ O	0.074
CO ₂	0.123

Table 4.2 Some of Refrig-600's physical characteristics

Parameter	Value	Unit
Molecular weight	58.12	g/mol
Critical temperature	151.98	°C
Critical pressure	3.80	MPa
Latent heat of vaporization at b.p.	366.35	J/g
Flammable limits in air	1.8–8.4	%vol

The flue gas from traditional refinery furnaces, which have a temperature of 220 °C and a flow rate of 250,194 m³/h with the composition shown in Table 4.1, is taken into consideration for carbon capture.

4.2.1 Organic Rankine Cycle

As mentioned earlier, the flue gas emitted from a refinery is fed into the organic Rankine cycle so that its temperature and energy content decrease and electric power is generated. Rankine cycles are less efficient, less complicated, and less suited for waste heat recovery than organic Rankine cycles [25, 26]. Due to its high critical temperature, improved performance, increased efficiency, and other thermal, economic, safety, and environmental benefits, Refrig-600 was chosen as the working fluid for ORC. Table 4.2 [27] is a list of Refrig-600's physical characteristics.

The schematic diagram of ORC in Aspen HYSYS is shown in Fig. 4.3. Flue gas from the purge stream boiler and the refinery furnace stack are combined and routed to the shell side of the ORC evaporator (HX1). The flue gas heats Refrig-600, causing it to become overheated. At 110 °C, it next passes through the expander (T1) and produces power. After that, it is liquefied in the cooler (HX2), and the cycle is completed. The net power and the thermal efficiency of ORC can be defined as follows:

$$W_{\text{net,ORC}} = W_{\text{T1}} - W_{\text{P1}} \quad (4.1)$$

$$\eta_{\text{ORC}} = \frac{W_{\text{net,ORC}}}{Q_{\text{HX1}}} \quad (4.2)$$

where:

W: power (kW)

P: pump

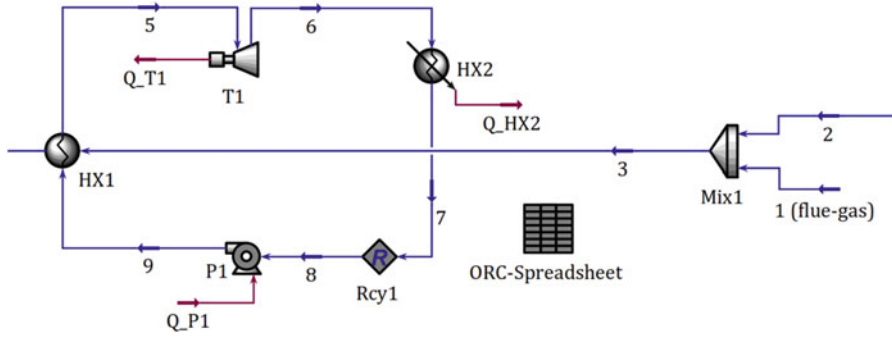


Fig. 4.3 Schematic of ORC in Aspen HYSYS. (Reprinted from Nazerifard et al. [24], copyright (2022), with permission from Elsevier)

T: turbine

ORC: organic Rankine cycle

η : efficiency

Q : heat (kW)

HX: heat exchanger

4.2.2 Carbon Capture Unit

In this plant, an amine solution absorbs carbon dioxide from the flue gas. The carbon capture system in Aspen HYSYS is shown in Fig. 4.4 based on Ref. [28]. The rate of carbon dioxide capture is 90.74%, and it is anticipated that at a temperature of 35 °C and a pressure of 1.7 bar, roughly 29.97 t/h of CO₂ will be generated.

As can be seen in Fig. 4.4, the flue gas exiting the ORC evaporator enters the compressor C1. It is then cooled to a temperature of 45 °C. As a result, 445.50 kg/h of the water vapor contained in the flue gas is condensed, separated in separator V1, and pumped through P2 to the electrolysis unit for hydrogen production. Stream 12 is introduced at the absorber column's bottom, and a lean aqueous solvent containing 30 weight percent MEA (HOCH₂CH₂NH₂) is introduced at the top. In the absorber column, the MEA moves to the bottom, while the flue gas rises to the top. The reactions taking place in the absorber column are as follows [28]:



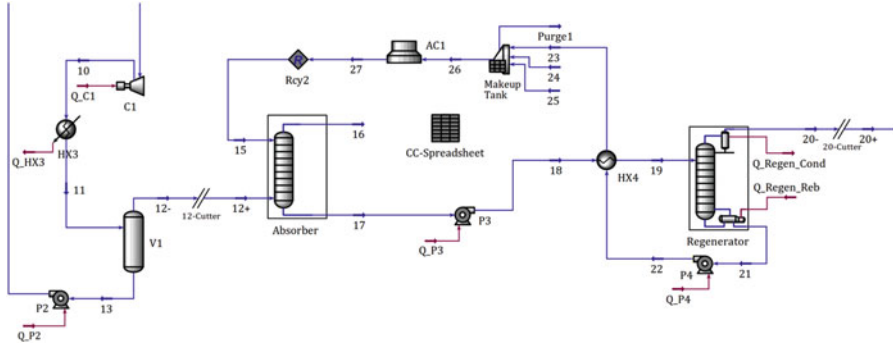
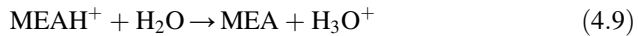
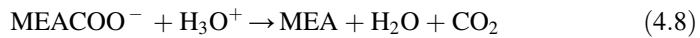


Fig. 4.4 Simulated carbon capture unit in Aspen HYSYS. (Reprinted from Nazerifard et al. [24], copyright (2022), with permission from Elsevier)



Thus, MEA chemically absorbs the carbon dioxide and separates it from the exhaust gas. Low carbon dioxide content flue gas is produced and discharged into the atmosphere. Rich solvent (stream 17) exits the column at the bottom and enters the internal lean/rich heat exchanger after being pumped to a pressure of 2.5 bar (HX4). The pressured rich solvent is heated using the hot regenerated lean MEA that comes from the bottom of the regeneration column. The hot, rich solvent then moves into the regenerator where it is heated by the vapor from the reboiler to desorb its CO₂. Lean MEA, which is the final result of the regeneration column at the bottom, moves through the following units and returns to the absorber column after being cooled in the lean/rich exchanger (HX4), mixing with water and MEA make-ups, and cooling to 45 °C in the air cooler (AC1). This compensates for the MEA loss brought on by evaporation and heat degradation [29]. In contrast, a combination of CO₂ and H₂O from the regeneration column’s overhead product is cooled to 35 °C in the condenser. A portion of the water vapor condenses during this process and, with a reflux ratio of 1.23, returns to the regeneration column. The primary design data for absorber and regenerator columns are shown in Table 4.3.

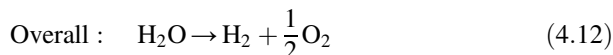
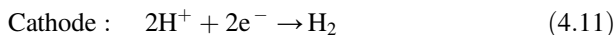
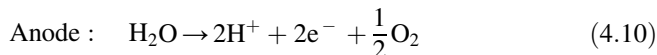
4.2.3 Water Electrolyzer Subsystem

The electrolysis method is the most popular way to create hydrogen from water. The three types of electrolyzers—alkaline water electrolyzer (AE), proton exchange

Table 4.3 Absorber and regenerator column design features

Parameter	Absorber	Regenerator	Unit
Column diameter	6	3	m
Column height	12.19	12.19	m
Packing type	IMTP – metal (50 mm)	IMTP – metal (50 mm)	–
Reflux ratio	–	1.23	–

membrane water electrolyzer (PEME), and solid oxide water electrolyzer (SOE)—can each divide water using the same fundamental concept. Not yet in commercial usage, the SOE is still in the research and development phase [30]. Despite the alkaline electrolyzer’s established technology, the PEME’s benefits, including its small size [31], greater gas purity [32], and higher current density and efficiency [33], make it a desirable and reasonably priced option for producing hydrogen. For water splitting in this work, a low-pressure PEME is taken into consideration. The following are the overall and half-cell reactions that take place in the PEME:



The Aspen HYSYS program does not include a built-in module for PEME; thus, some process equipment is put together to mimic PEME. The PEME subsystem’s process flow diagram in the Aspen HYSYS environment is shown in Fig. 4.5. It has a component splitter for separating the anode and cathode flows, a conversion reactor for the electrolysis reaction, three SET logical operations (Set1, Set2, and Set3) for stream temperature control, and a component splitter for separating H₂O and O₂ on the anode side.

According to Fig. 4.5, the inlet water of the PEME is a mixture of three streams: fresh water (stream 28), water separated from the flue gas by partial dehumidification (stream 14), and water produced in the methanol synthesis unit (stream 96). It is worth noting that the operating temperature of the PEME is constant at 80 °C. The incoming water stream is warmed with the hydrogen and oxygen streams, leaving the electrolyzer for heat integration and to boost system efficiency, and is subsequently heated to the PEME temperature in HX7. It is blended with the unconverted water in the PEME outflow before entering the PEME (stream 41). The electrochemical water splitting process occurs in the PEME reactor. The electrolyzer splitter is then supplied with hydrogen, oxygen, and unconverted water to separate the cathode stream from the anode stream. At a temperature of 80 °C, the cathode stream (stream 36) contains pure hydrogen. This hydrogen is cooled to 35 °C in HX5 before entering the compression stage of the methanol synthesis unit. A different splitter is used to purify the oxygen (stream 38) and recycle the unreacted water from

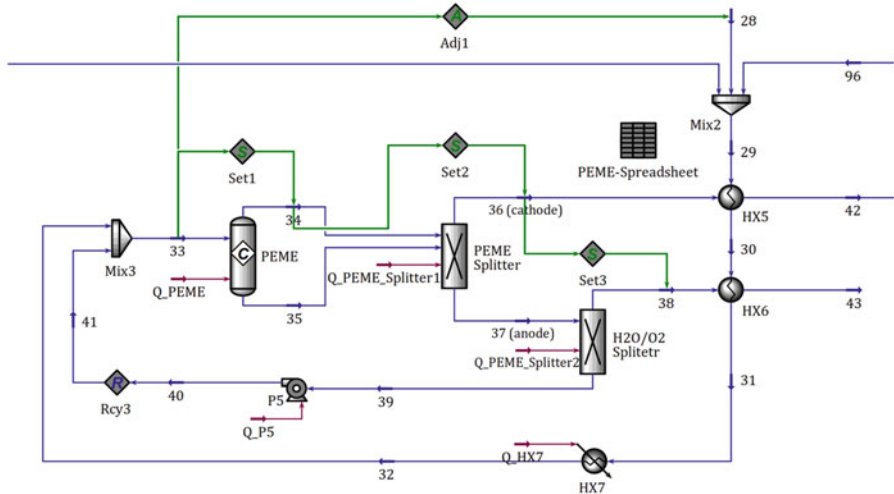


Fig. 4.5 Process flow diagram of simulated PEME subsystem in Aspen HYSYS. (Reprinted from Nazerifard et al. [24], copyright (2022), with permission from Elsevier)

the anode-side stream. The pure oxygen is cooled in HX6 and stored as a valuable by-product that can be sold. After a pump increases pressure, the unconverted water is returned to the electrolyzer.

The molar flow rates of water consumed, hydrogen created, and oxygen produced, according to Faraday’s law, are as follows:

$$\dot{N}_{PEME,H_2O}^{cons} = \frac{I}{2F} \tag{4.13}$$

$$\dot{N}_{PEME,H_2}^{prod} = \frac{I}{2F} \tag{4.14}$$

$$\dot{N}_{PEME,O_2}^{prod} = \frac{I}{4F} \tag{4.15}$$

where:

\dot{N} : molar flow rate (mol/s)

I : current (A)

F : faraday number (A.s/mol)

PEME: proton exchange membrane electrolyzer

prod: production

cons: consumption

Stoichiometric calculations may be used to determine how much hydrogen is needed for the production of methanol (using Adj2). The PEME subsystem in this plant is built to generate 25 t/h of hydrogen. The unit that produces hydrogen uses around 17.5% of it to create methanol. The remaining hydrogen is either saved for

use in overcast or dark conditions or for other pressing demands or it can be sold for a profit.

Electrolysis of water requires a lot of energy. Therefore, it is important to calculate the PEME's voltage and the necessary power. PEME's essential power is determined using the equation shown below:

$$W_{\text{PEME,stack}} = V_{\text{stack}} \cdot I = V_{\text{cell}} \cdot N \cdot i \cdot A_{\text{cell}} \quad (4.16)$$

in which:

V : voltage (V)

A_{cell} : cell area (m^2)

I : current density (A/m^2)

N : number of cells in the stack

The cell voltage for PEME can be expressed as:

$$V_{\text{cell}} = U_{\text{rev}} + v_{\text{act,a}} + v_{\text{act,c}} + v_{\text{ohm}} + v_{\text{conc}} \quad (4.17)$$

where:

U_{rev} : cell reversible potential (V)

V : overpotential (V)

Act: activation

a: anode

c: cathode

ohm: ohmic

conc: concentration

The concentration overpotential can be disregarded at low current densities [33]. The Nernst equation [34] may be used to calculate the reversible or open circuit potential:

$$U_{\text{rev}} = U_{\text{rev}}^0 + \frac{RT}{nF} \ln \left(\frac{p_{\text{H}_2} \cdot \sqrt{p_{\text{O}_2}}}{a_{\text{H}_2\text{O}}} \right) \quad (4.18)$$

$$U_{\text{rev}}^0 = 1.229 - 0.9 \times 10^{-3} (T - 298.15) \quad (4.19)$$

in which:

0: standard condition

R : universal gas constant ($\text{J}/\text{mol} \cdot \text{K}$)

T : temperature (K)

n : number of transferred electrons

p : pressure (Pa)

$a_{\text{H}_2\text{O}}$ is 1 for the liquid state, while n is 2 for the water splitting process.

By condensing the Butler-Volmer equation, it is possible to compute the anode and cathode's activation overpotential [35]:

$$v_{act,i} = \frac{RT}{\alpha_i F} \sinh^{-1} \left(\frac{i}{2i_{0,i}} \right), \quad i = a, c \quad (4.20)$$

$$i_{0,i} = i_i^{ref} \exp \left(\frac{-E_{act,i}}{RT} \right), \quad i = a, c \quad (4.21)$$

where:

α : charge transfer coefficient

i_0 : exchange current density (A/m^2)

i^{ref} : pre-exponential factor (A/m^2)

E_{act} : activation energy (J/mol)

where the charge transfer coefficient is equal to 1 for both the anode and cathode ($\alpha_a = \alpha_c = 1$).

Ohm's law may be used to determine the ohmic overpotential, which is mostly caused by the membrane's resistance to proton flow [36]:

$$v_{ohm} = R_{mem} \cdot i = \frac{\delta_{mem}}{\sigma_{mem}} \cdot i \quad (4.22)$$

$$\sigma_{mem} = (0.5139\lambda - 0.326) \exp \left[1268 \left(\frac{1}{303.15} - \frac{1}{T} \right) \right] \quad (4.23)$$

$$\lambda = \frac{(-2.89556 + 0.016T) + 1.625}{0.1875} \quad (4.24)$$

in which:

R_{mem} : Membrane resistance (Ω/m^2)

δ : Thickness (m)

mem: Membrane

σ : Protonic conductivity (S/m)

λ : Water content ($mol_{H_2O}/mol_{SO_3^{-1}}$)

Table 4.4 lists the values of the constant parameters that were employed in the PEME modeling.

Calculate the electrolyzer subsystem's efficiency, or the ratio of hydrogen energy generated to total power used in the PEME stack, in order to assess its performance:

$$\eta_{PEME} = \frac{\dot{M}_{H_2} \cdot HHV_{H_2}}{W_{net}} \quad (4.25)$$

Table 4.4 Parameters used for PEME modeling

Parameter	Value	Unit	Ref.
T	80	°C	–
$p_{H_2} = p_{O_2}$	1.5	bar	–
i_a^{ref}	1744271.56	A/m ²	[35]
i_c^{ref}	4597.14	A/m ²	[35]
$E_{\text{act, a}}$	76	kJ/mol	[35]
$E_{\text{act, c}}$	18	kJ/mol	[35]
δ_{mem}	50	μm	[35]

$$W_{\text{net}} = W_{\text{PEME,stack}} + Q_{\text{HX7}} + W_{\text{P5}} \quad (4.26)$$

where:

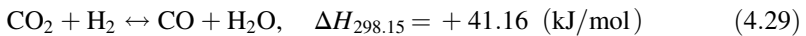
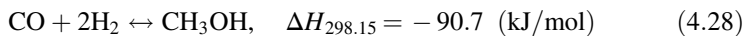
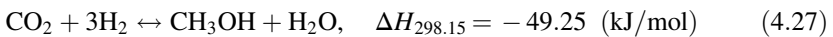
\dot{M} : Mass flow rate (kg/s)

HHV: Higher heating value (J/kg)

The higher heating value of hydrogen and equals 141.88 MJ/kg.

4.2.4 Methanol Synthesis Unit

In general, there are two ways to create methanol from carbon dioxide: (1) direct or one-step synthesis, in which CO₂ and H₂ react directly to create methanol, and (2) indirect or two-step synthesis, in which CO₂ is first changed into CO by the reverse water gas shift (RWGS), and then methanol is created. The direct technique has been demonstrated to be more economical and energy-efficient [37]. As a result, this study takes into account the direct way of producing methanol from carbon dioxide. The exothermic synthesis of methanol involves the simultaneous occurrence of the following events in the reactor [7]:



The desired hydrogenation of CO₂ and CO into methanol occurs in the first two processes, and the unwanted reverse water gas shift occurs in the third (undesirable). Le Chatelier's principle states that rising pressure and dropping temperature benefit the methanol synthesis process.

This work's suggested methanol synthesis unit is based on Van-Dal and Bouallou [38]. Their research suggests that the three basic steps of methanol synthesis are compression, reaction, and separation. Figure 4.6 displays the Aspen HYSYS-simulated methanol synthesis subsystem.

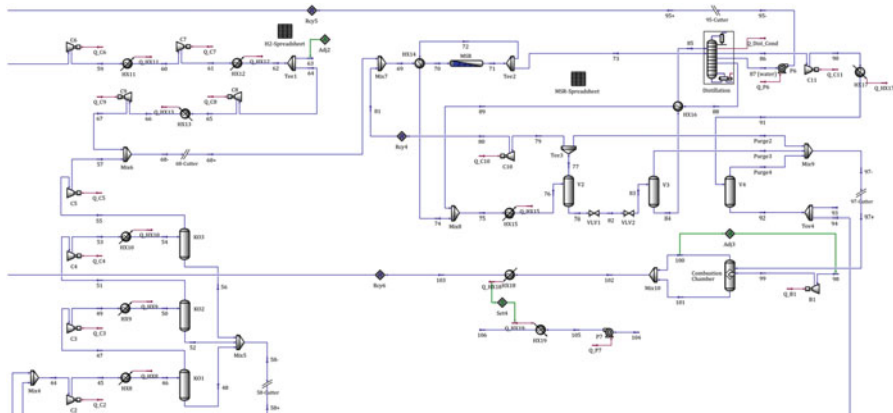


Fig. 4.6 Simulated methanol synthesis subsystem in Aspen HYSYS. (Reprinted from Nazerifard et al. [24], copyright (2022), with permission from Elsevier)

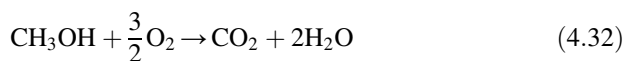
The intended output of this operation is 518.88 t/day of methanol. CO_2 and H_2 are first compressed to 78 bar. The CO_2 stream (stream 44) contains a combination of CO_2 that was created in the DMFC subsystem and CO_2 that was collected from the flue gas. It is delivered at 34.8 °C and 1.013 bar. The pressure of the carbon dioxide is increased using a set of four compressors that are intercooled to 35 °C by cooling water. With a pressure ratio of around 3.16 and an adiabatic efficiency of 85%, these compressors (C2, C3, C4, and C5) are categorized as reciprocating compressors. Since there is water vapor in the CO_2 stream, some of it is condensed after each intercooling and separated using knockout drums (KO1, KO2, and KO3). In the DMFC subsystem, these condensed streams are combined and used. A similar process is used to compress H_2 (stream 42), which is compressed by four reciprocating compressors (C6, C7, C8, and C9) with intercooling to 35 °C from 1 pressure and 35 °C to 78 bar. These compressors have an adiabatic efficiency of 85% and a pressure ratio of roughly 3.17. After cooling in HX12, the second compressor's output is split into two streams. While one of these streams, stream 64, is utilized to create methanol, stream 63 is sent to storage tanks.

These compressors' outputs are combined, and after mixing with the recycled stream (stream 81), they are heated to 210 °C before a part of the reactor's exit (stream 72), which is in HX14, enters the reactor. The gases react over 15,975 kg of commercial $\text{Cu/ZnO/Al}_2\text{O}_3$ catalysts in a fixed bed adiabatic plug flow reactor (MSR) using the reaction kinetics given in [38] for reactions (4.27) to (4.29). The pressure decrease in the reactor was calculated using the Ergun equation. Because of the exothermic nature of the reaction, the reactor's output (stream 71), which includes hydrogen, carbon dioxide, methanol, water, and carbon monoxide, reaches a temperature of 287.9 °C. This stream is divided into two streams: Stream 73 serves as the hot stream in the distillation column reboiler and in HX16, while Stream 72 is utilized to pre-heat the reactor feed in HX14. These two streams are

heated together until their combined temperature is 83 °C, at which point they are once more blended.

Additionally, utilizing the cooling water, stream 75 in HX15 cools to 35 °C. Methanol and water are liquefied in this manner. The flash drum (V2) is where this two-phase stream goes to be separated from the unreacted gas and turn into liquid methanol and water. One percent of the unreacted gases are expelled to prevent the buildup of inert gases and reaction by-products in the reaction loop, while the other 99% are repressurized by the centrifugal compressor (C10) and cycled to mix with new input from the reactor intake. Two valves reduce the effluent flow from the flash drum's bottom to 1.6 bar before it enters another flash drum (V3). Drum V3's liquid phase, which is a combination of methanol and water, is supplied to the distillation column after the gas phase of the drum is purged and heated to 80 °C in HX16. There are 40 trays in the distillation column (feeding starts at tray 25 from the top), along with a partial condenser and a reboiler. The column's reflux ratio is 1.42, resulting in 75 ppmwt of water in the overhead product and 50 ppbwt of methanol in the bottom stream. Methanol is 99.86 wt% pure in the vapor state and is present in the overhead product stream. Its temperature is 64.1 °C; however, it must be lowered to 35 °C in order to turn into liquid. As a result, it is compressed to 1.2 bar using a centrifugal compressor (C11) and then cooled in HX17 using cooling water. After that, the residual inert and unreacted gases are separated in the flash drum (V4). Pure water, the final by-product of the distillation process, is pumped through P6 to the pressure required by the water electrolyzer subsystem.

In order to improve the performance of the methanol synthesis subsystem, it is preferable to reuse the purge streams that include valuable H₂, methanol, and CO. In order to produce steam, the purge streams from V2, V3, and V4 are combined and burnt in the boiler with air. The upstream carbon capture system or other applications may utilize this steam. A conversion reactor with combustion is how the boiler is modeled. For heat transmission between combustion gases and boiler feed water (BFW), two heat exchangers are taken into consideration. To make the flame's temperature 1250 °C, adjust the air inlet to the boiler using Adj3. A high-pressure stream of steam at 380 °C and 42 bar is produced by the combustor's exhaust as it enters the HX18 at a rate of 8547 kg per hour. With Set4, the boiler's efficiency is set at 85%. In order for the CO₂ content of the boiler flue gas (stream 2) to be captured in the carbon capture system, it is combined with the system feed (stream 1). The following is how the combustion processes in the boiler happen:



Kinetics of reactions. In this work, methanol synthesis and RWGS rate estimates are performed using the modified kinetic model from [38]. Temperatures are in K, and pressures are in Pa. These are the equations.

$$r_{\text{CH}_3\text{OH}} = \frac{k_1 p_{\text{CO}_2} p_{\text{H}_2} - k_6 \frac{p_{\text{H}_2\text{O}} p_{\text{CH}_3\text{OH}}}{p_{\text{H}_2}^2}}{\left(1 + k_2 \frac{p_{\text{H}_2\text{O}}}{p_{\text{H}_2}} + k_3 \sqrt{p_{\text{H}_2}} + k_4 p_{\text{H}_2\text{O}}\right)^3} \left[\frac{\text{kmol}}{\text{kg}_{\text{cat}}\text{s}} \right] \quad (4.33)$$

$$r_{\text{RWGS}} = \frac{k_5 p_{\text{CO}_2} - k_7 \frac{p_{\text{H}_2\text{O}} p_{\text{CO}}}{p_{\text{H}_2}}}{1 + k_2 \frac{p_{\text{H}_2\text{O}}}{p_{\text{H}_2}} + k_3 \sqrt{p_{\text{H}_2}} + k_4 p_{\text{H}_2\text{O}}} \left[\frac{\text{kmol}}{\text{kg}_{\text{cat}}\text{s}} \right] \quad (4.34)$$

$$\ln k_i = A_i + \frac{B_i}{T}, \quad i = 1, 7 \quad (4.35)$$

where:

r : reaction rate (kmol/kgcat.s)

k : reaction rate constant

A : kinetic constant

B : kinetic constant

Tables 4.5 and 4.6, respectively, include the constants for these equations and information on the characteristics of the catalyst particles [38].

Multiple parameters may be used to assess the methanol synthesis subsystem's thermodynamic performance. The conversion of carbon dioxide is one of these factors, and it may be computed in two different ways: for the reactor and the entire MSU.

Table 4.5 Constants of the kinetic model

Index (i)	A	B
1	-29.87	4811.2
2	8.147	0
3	-6.452	2068.4
4	-34.95	14928.9
5	4.804	-11797.5
6	17.55	-2249.8
7	0.131	-7023.5

Table 4.6 Characteristics of catalyst particles

Parameter	Value	Unit
Density	1775	kg/m ³
Diameter	5.5	mm
Fixed bed porosity	0.5	-

$$X_{\text{CO}_2,i}(\%) = \left(\frac{\dot{N}_{\text{CO}_2}^{\text{in}} - \dot{N}_{\text{CO}_2}^{\text{out}}}{\dot{N}_{\text{CO}_2}^{\text{in}}} \right)_i \times 100, \quad i = \text{reactor, unit} \quad (4.36)$$

in which:

X : conversion (%)

in: inlet

out: outlet

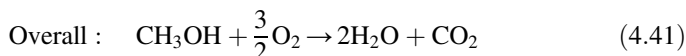
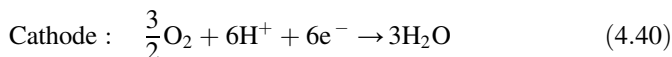
The two additional thermodynamic measurements for MSU are methanol selectivity and methanol yield. The portion of ingested carbon dioxide that is converted to methanol and not to other byproducts is known as methanol selectivity. The amount of methanol generated in the MSR to the amount of CO_2 used as feedstock is known as the “methanol yield.”

$$\text{Selectivity}_{\text{CO}_2}(\%) = \left(\frac{\dot{N}_{\text{MeOH}}^{\text{out}} - \dot{N}_{\text{MeOH}}^{\text{in}}}{\dot{N}_{\text{CO}_2}^{\text{in}} - \dot{N}_{\text{CO}_2}^{\text{out}}} \right) \times 100 \quad (4.37)$$

$$\text{Yield}_{\text{CO}_2}(\%) = \left(\frac{\dot{N}_{\text{MeOH}}^{\text{out}} - \dot{N}_{\text{MeOH}}^{\text{in}}}{\dot{N}_{\text{CO}_2}^{\text{in}}} \right) \times 100 \quad (4.38)$$

4.2.5 Direct Methanol Fuel Cell Subsystem

Stable power may be created using a portion of the methanol produced. Using a DMFC, in which a liquid methanol solution is delivered directly into the stack as fuel, is the simplest method. The crossing of the methanol from the membrane in this situation is the most critical issue and cannot be prevented. The methanol can dissolve even in the most typical electrolyte employed in this kind of fuel cell. This phenomenon reduces the DMFC’s effectiveness and efficiency [39, 40]. The DMFC’s anode and cathode electrode electrochemical reactions, as well as the total reaction, are as follows:



Species in the DMFC can be classified according to their consumption and production rates using Faraday’s law:

$$\dot{N}_{\text{DMFC,MeOH,a}}^{\text{cons}} = \dot{N}_{\text{DMFC,H}_2\text{O,a}}^{\text{cons}} = \dot{N}_{\text{DMFC,CO}_2,\text{a}}^{\text{prod}} = \frac{I}{6F} \quad (4.42)$$

$$\dot{N}_{\text{DMFC,O}_2,\text{c}}^{\text{cons}} = \frac{I + I_{\text{xover}}}{4F} \quad (4.43)$$

$$\dot{N}_{\text{DMFC,H}_2\text{O,c}}^{\text{prod}} = \frac{3I + 2I_{\text{xover}}}{6F} \quad (4.44)$$

$$\dot{N}_{\text{DMFC,MeOH,c}}^{\text{cons}} = \frac{I_{\text{xover}}}{6F} \quad (4.45)$$

where:

cons: consumption

DMFC: direct methanol fuel cell

I_{xover} : crossover current (A)

It is important to note that the methanol that crosses the membrane from the anode to the cathode is entirely burned there. Electro-osmotic drag (EOD) and diffusion are the causes of this methanol transport across the membrane. The following may be inferred from this:

$$\dot{N}_{\text{DMFC,MeOH,c}}^{\text{cons}} = \dot{N}_{\text{MeOH,mem}}^{\text{cross}} \quad (4.46)$$

$$\begin{aligned} \dot{N}_{\text{MeOH,mem}}^{\text{cross}} &= \dot{N}_{\text{MeOH,mem}}^{\text{eod}} + \dot{N}_{\text{MeOH,mem}}^{\text{diff}} = n_{\text{d,MeOH}} \frac{I}{F} \\ &+ D_{\text{MeOH,mem}}^{\text{eff}} \frac{C_{\text{MeOH}}|_{\text{acl}}}{\delta_{\text{mem}}} \cdot N \cdot A_{\text{cell}} \end{aligned} \quad (4.47)$$

where:

D : diffusivity (m^2/s)

C : molar concentration (mol/m^3)

n_{d} : drag coefficient

acl: anode catalyst layer

eff: effective

diff: diffusion

cross: crossover

EOD: electro-osmotic drag

The relationship between the EOD coefficient of water, the concentration of water and methanol in the anode catalyst layer, and the EOD coefficient of methanol is described in [41]:

$$n_{\text{d,MeOH}} = n_{\text{d,H}_2\text{O}} \frac{C_{\text{MeOH}}}{C_{\text{H}_2\text{O}}} |_{\text{acl}} \quad (4.48)$$

$$n_{d,H_2O} = 1.6767 + 0.0155 \times (T - 273.15) + 8.9074 \times 10^{-5} \times (T - 273.15)^2 \quad (4.49)$$

Moreover, the Bruggeman correlation is used to calculate the effective diffusion coefficient [41]:

$$D_{MeOH,mem}^{eff} = \varepsilon^{1.5} D_{MeOH,mem} \quad (4.50)$$

$$D_{MeOH,mem} = 4.9 \times 10^{-10} \exp\left[2436\left(\frac{1}{333.15} - \frac{1}{T}\right)\right] \quad (4.51)$$

where ε is porosity.

The electrical power generated by the DMFC stack can be expressed as follows:

$$W_{DMFC,stack} = V_{stack} \cdot I = V_{cell} \cdot N \cdot i \cdot A_{cell} \quad (4.52)$$

When all overpotentials are removed from the thermodynamic equilibrium voltage, the resulting voltage, V_{cell} , is obtained:

$$V_{cell} = U_{rev} - v_{kin,a} - v_{kin,c} - v_{ohm} - v_{cont} \quad (4.53)$$

where:

kin: kinetic loss

cont: contact

The electrochemical reaction rate on the anode side is determined using the kinetics of the methanol oxidation reaction (MOR) by Meyers and Newman [42]. On the other hand, the oxygen reduction process (ORR) on the cathode side is modeled using first-order Tafel-based kinetics [43]. For both the anode and the cathode, the charge transfer coefficient is equal to 0.5 ($\alpha_a = \alpha_c = 0.5$):

$$\text{Anode MOR : } i = i_{0,a} \frac{C_{MeOH}|_{acl} \exp\left(\frac{\alpha_a F}{RT} v_{kin,a}\right)}{C_{MeOH}|_{acl} + K_{reac} \exp\left(\frac{\alpha_a F}{RT} v_{kin,a}\right)} \quad (4.54)$$

$$\text{Cathode ORR : } i + i_{xover} = i_{0,c} \left(\frac{C_{O_2}|_{ccl}}{C_{O_2}^{ref}}\right) \exp\left(\frac{\alpha_c F}{RT} v_{kin,c}\right) \quad (4.55)$$

where:

i_{xover} : crossover current density (A/m²)

K_{reac} : reaction rate constant (mol/m³)

ccl: cathode catalyst layer

According to [44], the anode and cathode sides' exchange current densities are as follows:

$$i_{0,i} = i_i^{\text{ref}} \exp \left[\frac{E_{\text{act},i}}{R} \left(\frac{1}{353.15} - \frac{1}{T} \right) \right], \quad i = a, c \quad (4.56)$$

The quantities of the kinetic losses caused by the MOR and the ORR are derived by rearranging Eqs. (4.54) and (4.55):

$$v_{\text{kin},a} = \frac{RT}{\alpha_a F} \ln \left(\frac{i C_{\text{MeOH}}|_{\text{acl}}}{i_{0,a} C_{\text{MeOH}}|_{\text{acl}} - i K_{\text{reac}}} \right) \quad (4.57)$$

$$v_{\text{kin},c} = \frac{RT}{\alpha_c F} \ln \left[\frac{i + i_{\text{xover}}}{i_{0,c}} \left(\frac{C_{\text{O}_2}^{\text{ref}}}{C_{\text{O}_2}|_{\text{ccl}}} \right) \right] \quad (4.58)$$

According to the electrolyzer subsystem's description, Eq. (4.22), which can be found here, may be used to compute the membrane's ohmic overpotential.

$$\sigma_{\text{mem}} = (0.5139\lambda - 0.326) \exp \left[1268 \left(\frac{1}{333.15} - \frac{1}{T} \right) \right] \quad (4.59)$$

Finally, the following equation may be used to get the contact resistance overpotential:

$$v_{\text{cont}} = i R_{\text{cont}} \quad (4.60)$$

where R_{cont} is contact resistance (Ωm^2).

The cell efficiency of the DMFC is the product of three types of efficiencies—the theoretical efficiency (η_{th}), the voltage efficiency (η_{volt}), and the fuel efficiency (η_{fuel}):

$$\eta_{\text{cell}} = \eta_{\text{th}} \eta_{\text{volt}} \eta_{\text{fuel}} \quad (4.61)$$

$$\eta_{\text{th}} = \frac{\Delta G}{\Delta H} \quad (4.62)$$

$$\eta_{\text{volt}} = \frac{V_{\text{cell}}}{U_{\text{rev}}} \quad (4.63)$$

$$\eta_{\text{fuel}} = \frac{i}{i + i_{\text{xover}}} \quad (4.64)$$

where:

th: theoretical

ΔG : gibbs free energy change (J)

ΔH : enthalpy change (J)

The following equation should be used to calculate the overall stack efficiency:

$$\eta_{DMFC} = \frac{W_{DMFC,stack}}{W_{net}} \tag{4.65}$$

$$W_{net} = \dot{M}_{MeOH} \cdot HHV_{MeOH} + Q_{HX20} + Q_{HX21} + W_{P8} + W_{B2} \tag{4.66}$$

For methanol, the HHV value is 22.7 MJ/kg. The values of the constant parameters used to simulate the DMFC in Aspen HYSYS are listed in Table 4.7.

The fuel cell is not an Aspen HYSYS standard specified component, similar to the PEME. As a result, the DMFC is being created with a set of integrated process tools that can produce a comparable process. The DMFC-specific flowsheet is depicted in Fig. 4.7. Two conversion reactors make up the developed model: the first is for the overall reaction, and the second is for the reaction that takes place on the cathode side as a result of the methanol crossover. The DMFC stack also includes a component splitter to divide the anode and cathode sides, three SET logical operations (Set5, Set6, and Set7) to modify the temperature of the streams, and two adjust

Table 4.7 Parameters used for DMFC simulation

Parameter	value	Unit	Ref.
T	50	°C	–
p	1	Atm	–
ϵ	0.5	–	[39]
i_a^{ref}	94.25	A/m ²	[44]
i_c^{ref}	0.0422	A/m ²	[44]
$E_{act, a}$	35,570	J/Mol	[44]
$E_{act, c}$	73,200	J/Mol	[44]
K_{reac}	0.2	1/s	[45]
$C_{O_2}^{ref}$	0.472	mol/m ³	[41]
δ_{mem}	50	µm	[39]
R_{cont}	0.45×10^{-4}	Ωm ²	[46]

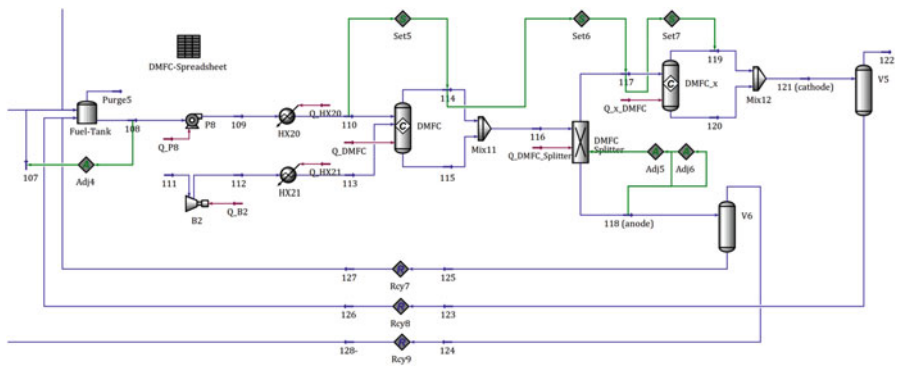


Fig. 4.7 Process flow diagram of simulated DMFC subsystem in Aspen HYSYS. (Reprinted from Nazerifard et al. [24], copyright (2022), with permission from Elsevier)

logical operations (Adj5 and Adj6) to modify the split percentage between the anode and cathode streams.

As displayed, the methanol stream is delivered to the DMFC subsystem at a rate of 3277.71 kg/h, or nearly 15% of the total methanol generated in the MSU. The DMFC stack's methanol inflow concentration is thought to be 2 M. Thus, five streams—Stream 94, the main methanol from the MSU; Stream 58, the liquid outlet from the CO₂ compression knockout drums; Streams 126 and 127, the liquid outlets from the flash drums of the DMFC cathode and anode sides, respectively; and Stream 107, pure water—are combined in a fuel tank to dilute pure methanol. Adj4 is used to change the pure water inlet's flow rate so that the fuel tank outflow stream's concentration achieves the appropriate level.

In order to make up for the pressure decrease in the following heat exchanger, the treated fuel is injected into the pump (P8). The necessary air is extracted from the environment on the cathode side using the blower. These two streams are heated in HX20 and HX21 to 50 °C (the working temperature of the DMFC), at which point they enter the fuel cell stack. The DMFC splitter receives the reactor output streams and separates them into anode and cathode streams. The splitter's splitter fractions are adjusted by Adj4 and Adj5 to balance the species' consumption and output rates. The unreacted methanol, water, and generated CO₂ from the anode stream (stream 118) are sent into the flash drum (V6) where the liquid and gaseous phases are separated. The gaseous phase, which mostly consists of carbon dioxide (stream 128), is returned to the intake of the CO₂ compressors in the MSU, while the liquid phase is returned to the fuel tank. The cathode stream (stream 117) is made up of crossed methanol, production water, and air. Equation (41) states that this methanol reacts fully on the cathode side. The flash drum (V5) receives the output stream from the cathode side (stream 121), which is then routed to the fuel tank in its liquid phase (stream 126) and vented to the atmosphere in its gaseous phase.

4.3 System Analysis

All equations from the preceding section are applied using the laws of mass and energy conservation after placing the subsystems in the overall multigenerational system with the best possible heat and mass interaction. Additionally, each subsystem is subjected to the exergy analysis that is derived from the second law of thermodynamics. The assessment of the energy and exergy efficiencies also guarantees a thorough examination of the suggested system.

Exergy is a term that is first introduced by the second law of thermodynamics. When a system changes from its starting condition to a dead state and participates exclusively in heat and work exchanges with its environment, it can perform as much work as possible, or exergy. Exergy, then, is the minimal effort necessary to change a system from a dead state to a selected state. The amount and source of energy losses are thus determined using exergy analysis, which is not achievable with energy analysis. Exergy analysis has gotten a lot of interest since energy resources are few

and need to be used as efficiently as possible. In order to minimize energy waste, it may be used to design new systems and optimize ones that already exist. The exergy of a stream is the total of its physical and chemical exergies if electrical, magnetic, nuclear, and surface tension effects, as well as kinetic and potential exergy variations, are ignored:

$$\dot{E} = \dot{E}_{\text{ph}} + \dot{E}_{\text{ch}} \quad (4.67)$$

where:

\dot{E} : exergy flow rate (J/mol)

ph: physical

ch: chemical

The amount of effort that can be done by a stream to reversibly change from its starting condition to its finite dead state or ambient state is called its physical exergy:

$$\dot{E}_{\text{ph}} = \sum \dot{N}_i \left[(\bar{h}_i - \bar{h}_i^{\text{amb}}) - T_{\text{amb}} (\bar{s}_i - \bar{s}_i^{\text{amb}}) \right] \quad (4.68)$$

where:

\bar{h} : specific molar enthalpy (J/mol)

amb: ambient

\bar{s} : specific molar entropy (J/mol)

The maximal work accomplished by a stream as it transitions from a restricted dead state to the genuine dead state is known as chemical exergy. The chemical exergy is computed as follows for an ideal gas mixture:

$$\dot{E}_{\text{ch}} = \sum \dot{N}_i \bar{e}_i^{\text{ch}} + RT_{\text{amb}} \sum \dot{N}_i \ln y_i \quad (4.69)$$

where:

\bar{e} : standard molar exergy (J/mol)

y: molar fraction

The exergy balance of a component under steady-state conditions can be described as follows:

$$\dot{E}_{\text{des,k}} = \sum_j \left(1 - \frac{T_{\text{amb}}}{T_j} \right) Q_j - W_{\text{cv}} + \sum_{\text{in}} \dot{E}_{\text{in}} - \sum_{\text{out}} \dot{E}_{\text{out}} \quad (4.70)$$

in which:

des: destruction

cv: control volume

k: k^{th} component

The above equation states that the input exergy of the system is greater than its output exergy because the irreversibilities cause some exergy destruction.

All of the subsystems cooperate, as seen in Fig. 4.1, to generate the desired products with the greatest amount of heat and material recovery. The entire system may be viewed as a control volume that is in a steady state of operation. In this instance, the ratio of all valuable outputs to all helpful inputs may be used to determine the energy efficiency of the entire system. The power of the ORC turbine, the DMFC's generated electricity, the stored hydrogen in stream 63, the produced methanol in stream 93, and the created steam are the system's outputs. The inputs to the entire system include the power used by all pumps and compressors, the power needed for the water electrolyzer, and the steam used for heating. As a result, the suggested multigeneration system's energy efficiency may be described as follows:

$$\eta_{\text{overall}} = \frac{W_{\text{T1}} + W_{\text{DMFC,stack}} + \dot{M}_{\text{H}_2} \cdot \text{HHV}_{\text{H}_2} + \dot{M}_{\text{MeOH}} \cdot \text{HHV}_{\text{MeOH}} + Q_{\text{steam}}^{\text{prod}}}{W_{\text{C}}^{\text{tot}} + W_{\text{P}}^{\text{tot}} + W_{\text{PEME,stack}} + Q_{\text{steam}}^{\text{cons}}} \quad (4.71)$$

Likewise, exergy efficiency is defined as:

$$\eta_{\text{exergy}} = \frac{W_{\text{T1}} + W_{\text{DMFC,stack}} + \dot{N}_{\text{H}_2} \cdot \bar{e}_{\text{H}_2}^{\text{ch}} + \dot{N}_{\text{MeOH}} \cdot \bar{e}_{\text{MeOH}}^{\text{ch}} + Q_{\text{steam}}^{\text{prod}} \left(1 - \frac{T_{\text{amb}}}{T_{\text{b,steam}}^{\text{prod}}} \right)}{W_{\text{C}}^{\text{tot}} + W_{\text{P}}^{\text{tot}} + W_{\text{PEME,stack}} + Q_{\text{steam}}^{\text{cons}} \left(1 - \frac{T_{\text{amb}}}{T_{\text{b,steam}}^{\text{cons}}} \right)} \quad (4.72)$$

4.4 Results and Discussion

The trigeneration system suggested in this study is first contrasted with other systems using various fuels or prime movers and exhibits comparatively superior performance in Table 4.8.

4.4.1 Base Case

The system's mass and energy balances are presented in Tables 4.9 and 4.10, respectively. Table 4.9 shows that the electrolyzer produces a significant amount of oxygen by water splitting. The electrolyzer also accounts for the majority of the system power's electricity usage, as shown in Table 4.10. The ORC power usage, on the other hand, is the least. In addition, Table 4.11 displays the stream conditions.

The primary performance indicators for the subsystems and the entire system are listed in Table 4.12. Under base case circumstances, the system has energy and exergy efficiencies of 66.84% and 55.10%, respectively.

Table 4.8 Analysis of existing systems and the planned trigeneration system plant

Case study	System type	Fuel	Application	Advantageous	Drawbacks	Efficiencies
Present work	Trigeneration methanol, hydrogen, and power system	Flue gas and solar energy	Commercial application Small industries	Reduction in emitted CO ₂ Additional power generation methanol and hydrogen production by carbon capture	Solar panels may be expensive The system is bulky	Energy efficiency = 66.84% Exergy efficiency = 55.10%
Boretti [10]	Methanol production system	Carbon dioxide from oxy-fuel combustion and solar/wind renewable energy	Industrial use	Reduction in environmental carbon pollutant Methanol seems a better, safer, and easier option than hydrogen for transportation, distribution, and small/high power density utilization	A significant amount of renewable energy is necessary	–
Sayah et al. [11]	Methanol production system	Flue gas and wind energy	Commercial application	Zero carbon emission Methanol production Compatibility with Iran condition Can compete with conventional methanol synthesis options Lowering methanol and steam intensity Lower cost	The detailed cost estimation depends on the energy source A separate unit for methanol synthesis affects the product cost	–
Esmaili et al. [12]	Hydrogen and methanol production system	Carbon dioxide and solar energy	Commercial and industrial applications	Zero carbon emission Compact structure Improved efficiency	Heat and water management should be considered Dependent on solar radiation	Energy and exergy efficiencies = 55–90%

(continued)

Table 4.8 (continued)

Case study	System type	Fuel	Application	Advantageous	Drawbacks	Efficiencies
Atsonios et al. [14]	Methanol production system	Flue gas and electricity from the grid or renewable energy source	Commercial application	Lowering carbon dioxide emission Additional power generation with a power-to-fuel integrated system	Hydrogen production cost has a significant impact Carbon dioxide-based fuels do not share much in the global market	–
Rivarolo et al. [15]	Methanol production system	Solar/wind/hydroelectric energy and biogas/external plant carbon dioxide	Industrial application	Zero carbon emission No fossil fuel consumption for hydrogen generation Biogas configuration has the best performance	The presented configurations do not seem viable yet If any interruption happens in providing renewable energy, the necessary power should be extracted from the grid The renewable sources are not available throughout the year	–
Nami et al. [16]	Methanol, hydrogen, and power production system	Carbon dioxide from the S-Graz cycle and renewable hydrogen	Industrial application	Zero-emission Good equipment integration	The cost is the main factor	–
Alsayegh et al. [22]	Methanol production system	Carbon dioxide and solar energy	Industrial application	Simplicity Zero carbon emission	Special attention should be paid to heat and hydrogen to carbon ratio management Further research and investigations are needed	Energy efficiency = 28.18%
Matzen et al. [23]	Methanol and dimethyl ether cogeneration system	Carbon dioxide from the ethanol fermentation process and wind-based hydrogen	Commercial application	Lower carbon dioxide emission Renewable energy usage	Its feasibility is under doubt System complexity	–

Table 4.9 Mass balance

Component	In (t/h)	Out (t/h)
CO ₂	31.38	5.66
H ₂	0	20.61
MeOH	0	18.34
H ₂ O	249.5	44.4
CO	0	0.0004
O ₂	28.41	219.86

Table 4.10 Energy balance

Unit	Input energy (MW)			Output energy (MW)		
	Electrical	Thermal	Chemical	Electrical	Thermal	Chemical
ORC	0.047	–	–	1.132	–	–
CC	3.926	31.56	–	–	–	–
PEME	1320	7.945	–	–	–	985.28
MSU	37.28	–	173.015	–	6.329	136.33
DMFC	0.56	0.202	20.668	1.819	–	–

The contribution of each subsystem to the overall exergy destruction rate is shown in Fig. 4.8. As can be observed, the PEME subsystem, mostly because of its enormous power consumption, has the biggest effect on the system's exergy destruction. Since there is no reaction in this subsystem, the ORC share is minimal.

4.4.2 Parametric Study

For various values of the turbine inlet temperature, Fig. 4.9 illustrates the impact of adjusting the turbine intake pressure on the ORC efficiency. It is important to note that the exhaust gas from the evaporator has a consistent temperature at its exit. As observed in this graph, an increase in turbine intake pressure results in an increase in ORC efficiency at a fixed turbine inlet temperature. The input energy to ORC, QHX1, is constant since the temperature of the flue gas doesn't fluctuate. Greater pump power usage and turbine power output result from higher turbine inlet pressure. The end result is an improvement in the ORC's net power output and, as a result, in ORC efficiency. Additionally, at a given turbine intake pressure, ORC efficiency falls as the turbine inlet temperature rises. Because the energy supplied by the ORC cycle is constant, the flow rate of the cycle drops as the temperature of the turbine inlet increases. As a result, choosing a greater turbine inlet temperature reduces the power produced by the turbine, the ORC net power, and the cycle efficiency.

Figure 4.10 displays the temperature and molar CO₂ flow rate curves for the gas phase within the absorber column. As anticipated, the carbon capture process causes the CO₂ flow rate to decrease as the height of the absorber column increases. As carbon capture reaches its maximum value and equilibrium state in the upper stages,

Table 4.11 Stream’s conditions

<i>St. no.</i>	<i>1</i>	<i>2</i>	<i>3</i>	<i>4</i>	<i>5</i>	<i>6</i>	<i>7</i>	<i>8</i>	<i>9</i>
<i>m (t/h)</i>	170	20.45	190.45	190.45	72.85	72.85	72.85	72.85	72.85
<i>T (°C)</i>	220	220	220	50	110	67.67	30	30	30.73
<i>P (bar)</i>	0.95	0.95	0.95	0.75	14	3.2	3	3	14.2
<i>St. no.</i>	<i>10</i>	<i>11</i>	<i>12</i>	<i>13</i>	<i>14</i>	<i>15</i>	<i>16</i>	<i>17</i>	<i>18</i>
<i>m (t/h)</i>	190.45	190.45	190	0.45	0.45	472.5	179.3	483.2	483.2
<i>T (°C)</i>	119.2	45	45	45	45.01	45	65.46	49.93	49.96
<i>P (bar)</i>	1.4	1.2	1.2	1.2	3	1.4	1	1.1	2.5
<i>St. no.</i>	<i>19</i>	<i>20</i>	<i>21</i>	<i>22</i>	<i>23</i>	<i>24</i>	<i>25</i>	<i>26</i>	<i>27</i>
<i>m (t/h)</i>	483.2	30.41	452.8	452.8	452.8	19.67	0.03	472.5	472.5
<i>T (°C)</i>	105	35.17	120.5	120.6	57.65	57.65	57.65	60.01	45
<i>P (bar)</i>	2	1.7	1.9	2.4	1.9	1.9	1.9	1.9	1.4
<i>St. no.</i>	<i>28</i>	<i>29</i>	<i>30</i>	<i>31</i>	<i>32</i>	<i>33</i>	<i>34</i>	<i>35</i>	<i>36</i>
<i>m (t/h)</i>	210.4	223.4	223.4	223.4	223.4	279.2	279.2	0	25
<i>T (°C)</i>	25	29.37	45.88	50.46	80	80	80	80	80
<i>P (bar)</i>	3	3	2.5	2	1.5	1.5	1.5	1.5	1.5
<i>St. no.</i>	<i>37</i>	<i>38</i>	<i>39</i>	<i>40</i>	<i>41</i>	<i>42</i>	<i>43</i>	<i>44</i>	<i>45</i>
<i>m (t/h)</i>	254.2	198.4	55.8	55.8	55.8	25	198.4	32.53	32.53
<i>T (°C)</i>	80	80	80	80	80.01	35	55.88	34.79	133.7
<i>P (bar)</i>	1.5	1.5	1.5	1.5	1.55	1	1	1.013	3.2
<i>St. no.</i>	<i>46</i>	<i>47</i>	<i>48</i>	<i>49</i>	<i>50</i>	<i>51</i>	<i>52</i>	<i>53</i>	<i>54</i>
<i>m (t/h)</i>	32.53	32.26	0.27	32.26	32.26	32.07	0.19	32.07	32.07
<i>T (°C)</i>	35	35	35	134.4	35	35	35	136.3	35
<i>P (bar)</i>	2.7	2.7	2.7	8.54	8.04	8.04	8.04	25.4	24.9
<i>St. no.</i>	<i>55</i>	<i>56</i>	<i>57</i>	<i>58</i>	<i>59</i>	<i>60</i>	<i>61</i>	<i>62</i>	<i>63</i>
<i>m (t/h)</i>	32.01	0.06	32.01	0.52	25	25	25	25	20.61
<i>T (°C)</i>	35	35	140.5	35	179.4	35	179.5	35	35
<i>P (bar)</i>	24.9	24.9	78	2.7	3.17	2.67	8.46	7.96	7.96
<i>St. no.</i>	<i>64</i>	<i>65</i>	<i>66</i>	<i>67</i>	<i>68</i>	<i>69</i>	<i>70</i>	<i>71</i>	<i>72</i>
<i>m (t/h)</i>	4.39	4.39	4.39	4.39	36.4	170.4	170.4	170.4	93.71
<i>T (°C)</i>	35	179.6	35	179.2	156.5	61.03	210	287.9	287.9
<i>P (bar)</i>	7.96	25.25	24.75	78	78	78	77.5	76.47	76.47
<i>St. no.</i>	<i>73</i>	<i>74</i>	<i>75</i>	<i>76</i>	<i>77</i>	<i>78</i>	<i>79</i>	<i>80</i>	<i>81</i>
<i>m (t/h)</i>	76.69	93.71	170.4	170.4	135.9	34.5	134.5	134.5	134.5
<i>T (°C)</i>	287.9	82.62	83.25	35	35	35	35	39.7	39.7
<i>P (bar)</i>	76.47	74.97	74.97	74.47	74.47	74.47	74.47	78	78
<i>St. no.</i>	<i>82</i>	<i>83</i>	<i>84</i>	<i>85</i>	<i>86</i>	<i>87</i>	<i>88</i>	<i>89</i>	<i>90</i>
<i>m (t/h)</i>	34.5	34.5	34.18	34.18	21.66	12.52	76.69	76.69	21.66
<i>T (°C)</i>	35.26	34.66	34.66	80	64.13	101.8	151.5	84.08	77.2
<i>P (bar)</i>	12	1.6	1.6	1.1	1	1.08	75.97	75.47	1.2
<i>St. no.</i>	<i>91</i>	<i>92</i>	<i>93</i>	<i>94</i>	<i>95</i>	<i>96</i>	<i>97</i>	<i>98</i>	<i>99</i>
<i>m (t/h)</i>	21.66	21.64	18.36	3.28	12.52	12.52	1.74	18.71	18.71
<i>T (°C)</i>	35	35	35	35	101.8	101.8	30.51	25	33.31

(continued)

Table 4.11 (continued)

<i>P</i> (bar)	1	1	1	1	3	3	1	1.013	1.1
<i>St. no.</i>	100	101	102	103	104	105	106	107	108
<i>m</i> (t/h)	20.45	0	20.45	20.45	8.55	8.55	8.55	3.18	53.94
<i>T</i> (°C)	1250	1250	1250	220	120	120.5	380	25	47.57
<i>P</i> (bar)	1	1	1	0.95	2	43	42	2	1
<i>St. no.</i>	109	110	111	112	113	114	115	116	117
<i>m</i> (t/h)	53.94	53.94	86.55	86.55	86.55	95.33	45.16	140.5	101.8
<i>T</i> (°C)	47.58	50	25	48.01	50	50	50	50	50
<i>P</i> (bar)	1.313	1.013	1.013	1.267	1.013	1.013	1.013	1.013	1.013
<i>St. no.</i>	118	119	120	121	122	123	124	125	126
<i>m</i> (t/h)	38.74	91.46	10.29	101.8	91.46	10.29	2.13	36.61	10.29
<i>T</i> (°C)	50	50	50	50	50	50	50	50	50
<i>P</i> (bar)	1.013	1.013	1.013	1.013	1.013	1.013	1.013	1.013	1.013
<i>St. no.</i>	127	128			<i>Purge1</i>	<i>Purge2</i>	<i>Purge3</i>	<i>Purge4</i>	<i>Purge5</i>
<i>m</i> (t/h)	36.61	2.13			0	1.4	0.32	0.02	0
<i>T</i> (°C)	50	50			60.01	35	34.66	35	47.57
<i>P</i> (bar)	1.013	1.013			1.9	74.47	1.6	1	1

the absorption rate slows from being rapid in the lower stages. In the interim, the temperature initially rises, reaches its peak in stage 4 (73.97 °C), and then starts to fall. The liquid to gas ratio, solvent characteristics, heat of absorption, column height, and carbon content in the flue gas are only a few of the factors that affect the form of the temperature profile and its peak value [47].

The V-i curve of PEME in this study is compared with the information presented in [48] and is displayed in Fig. 4.11 to guarantee that the simulation of PEME in the Aspen HYSYS program is carried out accurately. The highest relative error is 1.4%, and this result shows that the two are in good agreement with one another. So, this work's PEME simulation block can successfully forecast the electrolyzer's performance.

Figure 4.12 shows the PEME's heat demand, or TΔS, and the heat it produces as a result of irreversibilities, or overpotentials. Since the activation and ohmic overpotential terms are directly connected to the current density of the electrolyzer in this figure, it can be seen that the heat created rises with current density (Eqs. 4.20 and 4.22). It should be observed that the PEME's heat consumption is lower than its heat production for all levels of current density. As a result, it is not necessary to introduce more heat from an outside source, and any extra heat should be released to keep the PEME at a constant temperature.

The electrolyzer's electrical power consumption and hydrogen energy output are affected by current density, as shown in Fig. 4.13. It is evident that as the current density of the electrolyzer rises, so do the energy input and output. The pace of rise in energy consumption, however, is substantially greater than the rate of hydrogen production. As seen in Fig. 4.14, this results in a decline in PEME energy efficiency. When $i > 1000 \text{ A/m}^2$, the energy efficiency falls off more quickly. There is thereafter

Table 4.12 Performance parameters of the subsystems and overall system

Parameter	Value
<i>ORC</i>	
$W_{\text{net,ORC}}$ (kW)	1085
η_{ORC} (%)	11.15
<i>CC</i>	
CO_2 recovery (%)	90.74
Reboiler duty (GJ/t _{CO₂})	3.79
Lean loading (mol CO ₂ /mol MEA)	0.203
Rich loading (mol CO ₂ /mol MEA)	0.496
pH _{lean}	9.79
pH _{rich}	8.52
<i>PEME</i>	
Current density (A/m ²)	7186
Voltage (V)	1.986
Power (MW)	1320
η_{PEME} (%)	74.20
<i>MSU</i>	
CO_2 conversion in the reactor (%)	21.30
CO_2 conversion in the unit (%)	94.84
Methanol selectivity (%)	97.70
Methanol yield (%)	20.81
Methanol production (t/d)	518.88
<i>DMFC</i>	
Current density (A/m ²)	2082
Voltage (V)	0.25
Power (MW)	1.82
η_{cell} (%)	8.83
η_{DMFC} (%)	8.49
Overall energy efficiency (%)	66.84
Overall exergy efficiency (%)	55.10

a linear drop. The electrolysis voltage rises as current density rises, as seen in Fig. 4.14. According to Eqs. (4.20) and (4.22), this tendency results from the overpotentials' direct response to rising current density. These equations predict that when cell temperature rises, overpotentials diminish, causing the cell's potential to fall and its efficiency to rise. For instance, the electrolyzer becomes 2.6% more efficient when the temperature rises from 40 to 80 °C at $i = 4400 \text{ A/m}^2$.

The fluctuations in methanol concentration, CO_2 conversion, and temperature profiles over the axial reactor distance at five different input temperatures are depicted in Figs. 4.15, 4.16, and 4.17. Initially, a hydrogenation process transforms carbon dioxide into methanol, and then a reverse water-gas shifting reaction transforms it into carbon monoxide. Figures 4.15 and 4.16 demonstrate the effects of these processes on methanol concentration and carbon dioxide conversion, respectively. The hydrogenation reaction is exothermic, as stated in Eqs. (4.27)–(4.29), but

Fig. 4.8 Portion of each subsystem in total exergy destruction. (Reprinted from Nazerifard et al. [24], copyright (2022), with permission from Elsevier)

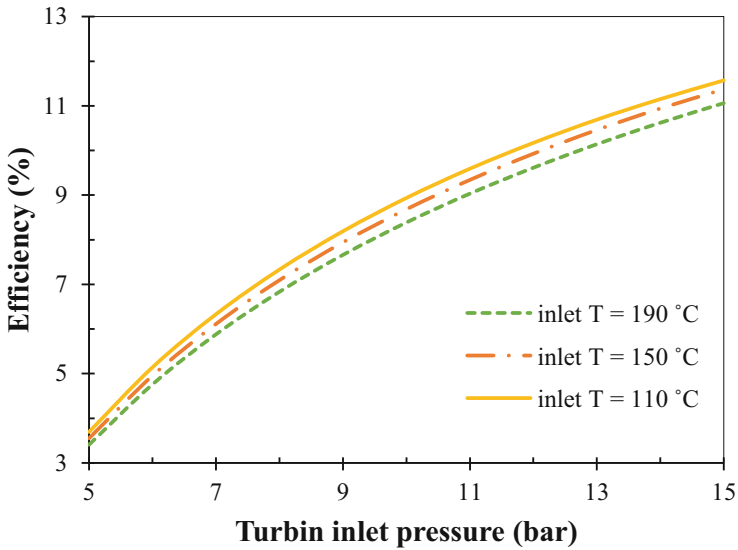
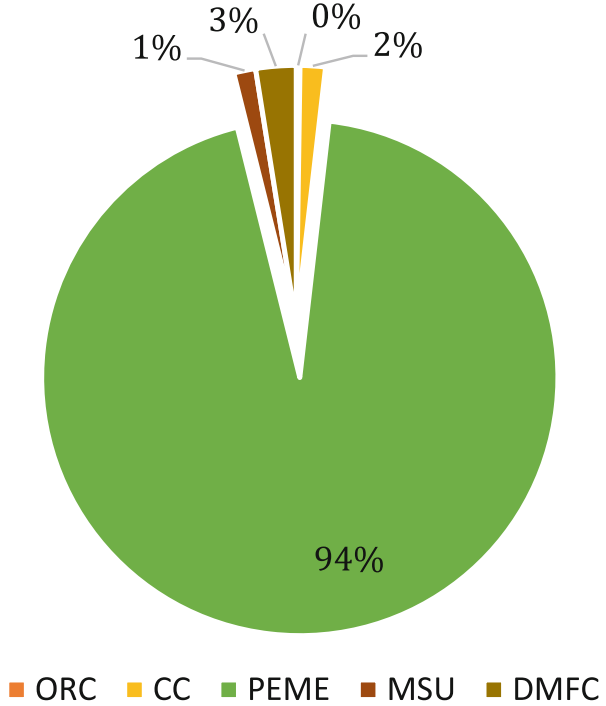


Fig. 4.9 At various turbine intake temperatures, the impact of turbine inlet pressure on ORC efficiency may be observed. (Reprinted from Nazerifard et al. [24], copyright (2022), with permission from Elsevier)

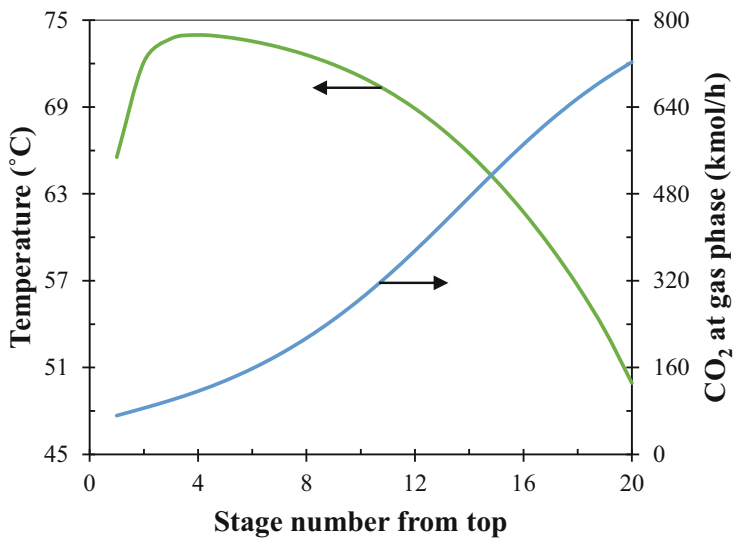


Fig. 4.10 Profiles of temperature and gas-phase CO₂ molar flowrate inside the absorber column. (Reprinted from Nazerifard et al. [24], copyright (2022), with permission from Elsevier)

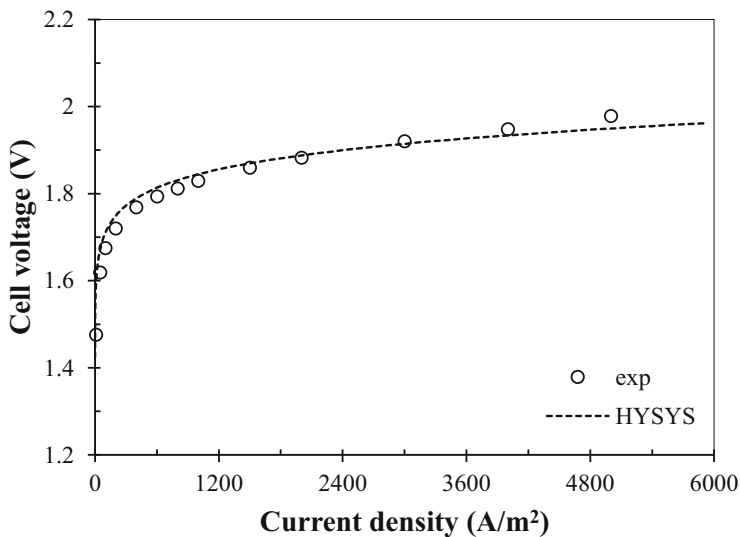


Fig. 4.11 Simulation results of PEME from present work versus experimental data. (Reprinted from Nazerifard et al. [24], copyright (2022), with permission from Elsevier)

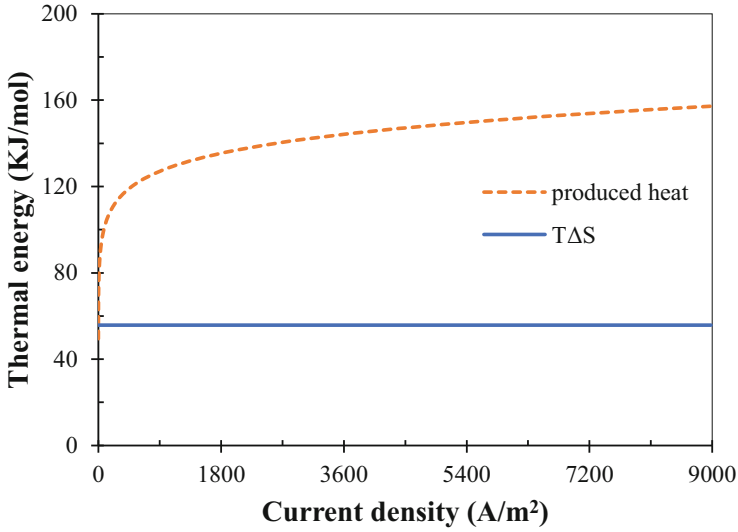


Fig. 4.12 Comparison between heat demand and produced heat of PEME at 80 °C. (Reprinted from Nazerifard et al. [24], copyright (2022), with permission from Elsevier)

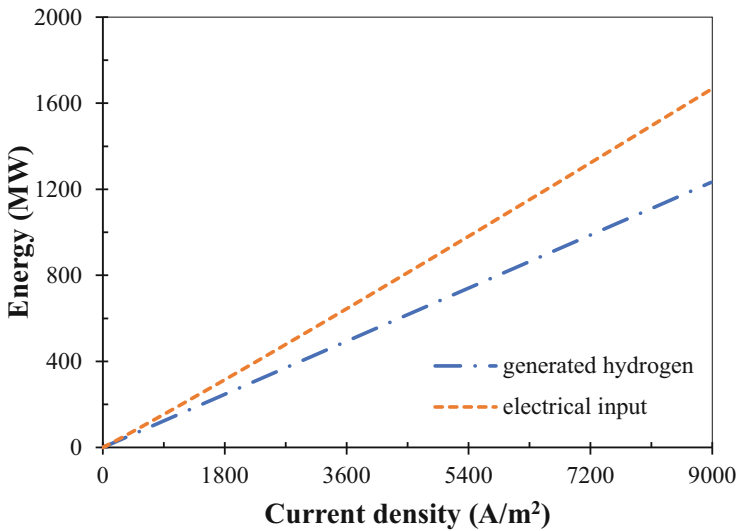


Fig. 4.13 Effect of electrolyzer current density on electrical input power and generated hydrogen energy at 80 °C. (Reprinted from Nazerifard et al. [24], copyright (2022), with permission from Elsevier)

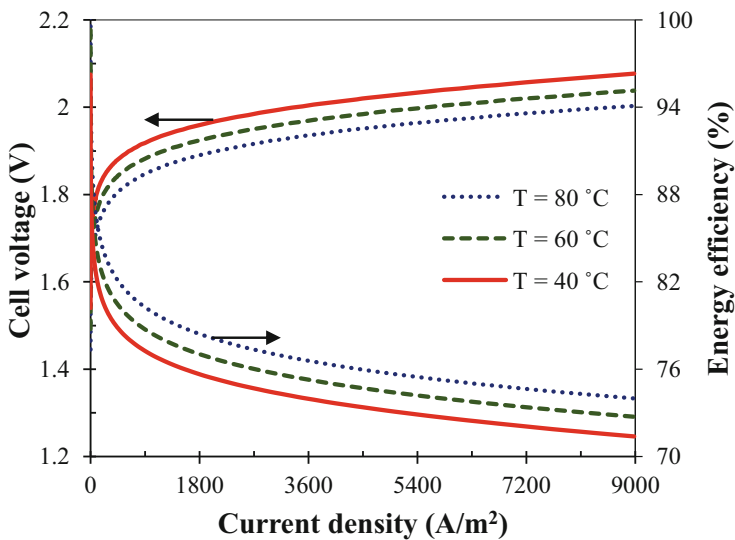


Fig. 4.14 Effect of temperature on electrolyzer voltage and energy efficiency. (Reprinted from Nazerifard et al. [24], copyright (2022), with permission from Elsevier)

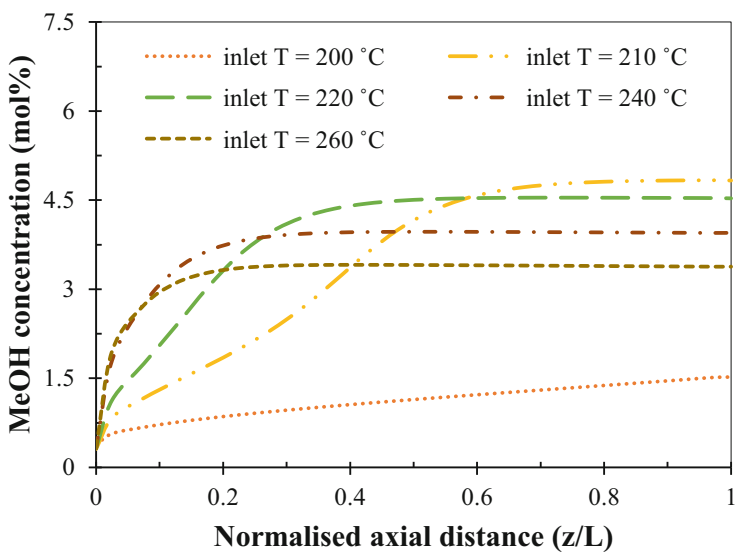


Fig. 4.15 Effect of reactor inlet temperature on the methanol concentration profile at 75 bar. (Reprinted from Nazerifard et al. [24], copyright (2022), with permission from Elsevier)

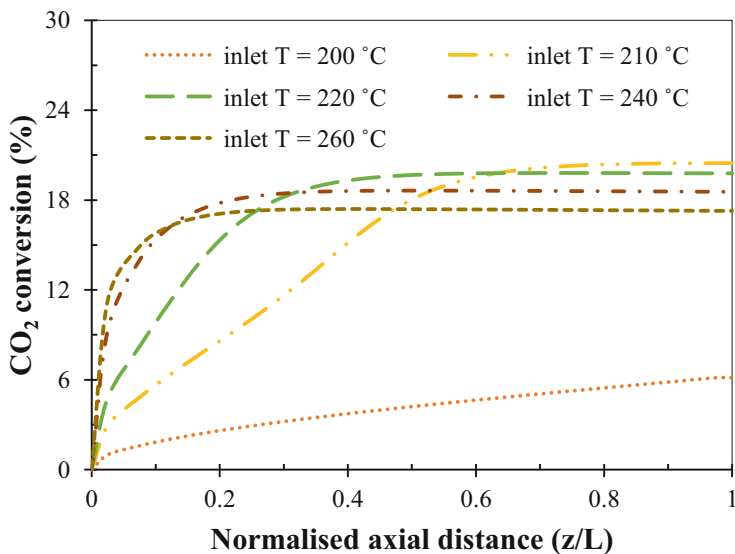


Fig. 4.16 Effect of reactor inlet temperature on CO₂ conversion profile at 75 bar. (Reprinted from Nazerifard et al. [24], copyright (2022), with permission from Elsevier)

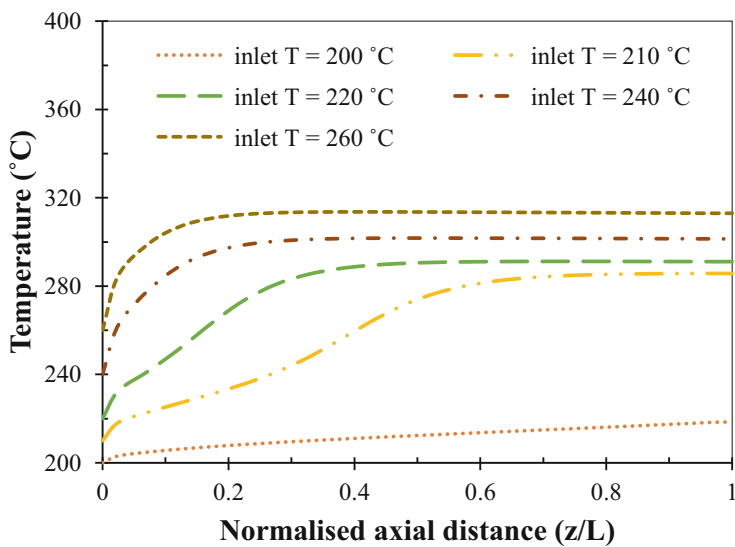


Fig. 4.17 Effect of reactor inlet temperature on temperature profile at 75 bar. (Reprinted from Nazerifard et al. [24], copyright (2022), with permission from Elsevier)

the reverse shifting reaction is endothermic. The total thermal effect is shown by the rise in reactor temperature in Fig. 4.17 because the rate of the hydrogenation reaction is larger than that of the RWGS reaction. The CO_2 concentration falls as the stream passes through the reactor, and both processes come to a stop at a specific distance from the reactor entrance. The reactor temperature, methanol concentration, and CO_2 conversion are all at their peak values at this time. The intake temperature has a significant impact on the equilibrium point's position and properties. The equilibrium distance from the reactor intake decreases as a greater inlet temperature causes the equilibrium state to occur earlier, as seen in Figs. 4.15, 4.16, and 4.17. The kinetic rate of both processes is enhanced by a high input temperature, which accounts for this. The reactions are so kinetically restricted at an intake temperature of $200\text{ }^\circ\text{C}$ that no equilibrium state is established in the reactor. Both processes go forward quickly at an inlet temperature of $210\text{ }^\circ\text{C}$, achieving a maximum equilibrium concentration of methanol and a maximum CO_2 conversion. The RWGS reaches equilibrium sooner and subsequently progresses in the opposite direction, leading to a lower equilibrium methanol concentration and CO_2 conversion if the reactor input temperature is higher than $210\text{ }^\circ\text{C}$. In other words, a low intake temperature is preferred by the exothermic nature of CO_2 hydrogenation. On the other side, extremely low temperatures cause the reactions' kinetic to slow down. As a result, there is an ideal inlet temperature, which in this case is $210\text{ }^\circ\text{C}$, that fulfills both of these opposing factors. According to Fig. 4.17, the greater the inflow temperature, the higher the reactor temperature will be.

The correlation between intake temperature and pressure and carbon dioxide conversion is shown in Fig. 4.18. The processes in the reactor have not achieved an equilibrium state at $200\text{ }^\circ\text{C}$, as indicated in Figs. 4.15, 4.16, and 4.17. As a result, as the temperature rises, the rate of reactions rises as well, increasing the conversion of CO_2 . These numbers indicate that the processes attain equilibrium at temperatures of $210\text{ }^\circ\text{C}$ or above. Therefore, Le Chatelier's concept is applicable in these circumstances. As a result of the exothermic nature of the methanol synthesis process, the conversion of CO_2 declines with rising temperature. When the temperature rises from 200 to $275\text{ }^\circ\text{C}$ and the pressure remains constant, the CO_2 conversion first reaches a maximum value before linearly declining. Maximum CO_2 conversion occurs at a temperature of around $210\text{ }^\circ\text{C}$ and depends on the reactor input pressure. The relationship between the reactor intake temperature and the impact of a change in input pressure on CO_2 conversion is also seen in Fig. 4.18. In other words, the CO_2 conversion degrades as the input pressure rises if the reactor's inlet temperature is below $210\text{ }^\circ\text{C}$ (the maximum point). CO_2 conversion and inlet pressure are connected, nevertheless, if the input temperature is greater than $210\text{ }^\circ\text{C}$. The hydrogenation processes (Eqs. 4.27 and 4.28) proceed in accordance with Le Chatelier's principle as the input pressure rises. As a result, the production of methanol increases and the CO_2 conversion rate rises. Additionally, at higher temperatures, the reliance of CO_2 conversion on pressure is more prominent. For instance, the CO_2 conversion decreases by 1.583% when the pressure is increased from 50 to 80 bar at $200\text{ }^\circ\text{C}$ while increasing by 5.097% at $250\text{ }^\circ\text{C}$.

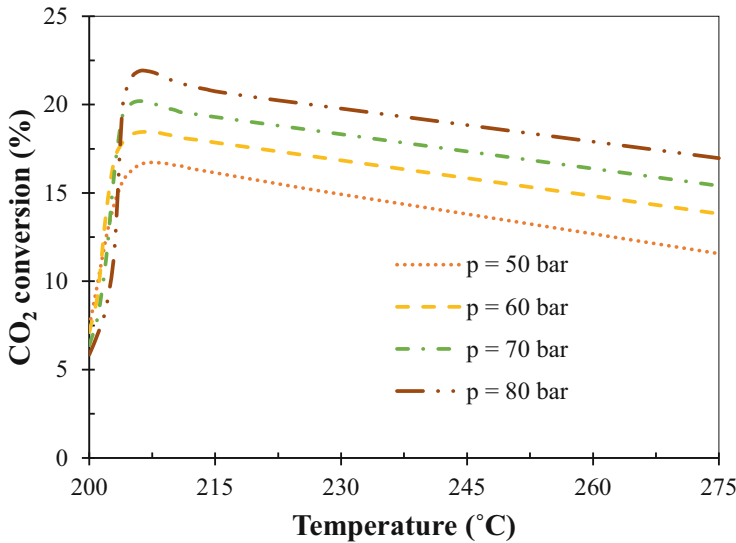


Fig. 4.18 Effect of reactor inlet temperature and pressure on CO₂ conversion. (Reprinted from Nazerifard et al. [24], copyright (2022), with permission from Elsevier)

To confirm the simulation of the DMFC in this study, the generated results for the DMFC are compared with the experimental data in [49] in the form of a cell voltage-current density plot under the identical operating circumstances. The two exhibit good agreement, as seen in Fig. 4.19, and the resulting model is quite good for forecasting DMFC behavior. The kinetic equations of MOR and ORR, Eqs. (4.54) and (4.55), and their parameters, Eq. (4.56), are responsible for the variation at low current density levels. On the other side, the variation at high current density results from the liquid fuel's restricted reaction and diffusion rates, as well as the simulation code's disregard for two-phase effects.

Figure 4.20 shows how changing the DMFC current density affects the overpotentials and cell voltage. According to the calculation, the thermodynamic equilibrium voltage, or the cell voltage at zero current density, is 1.214 V, which is significantly greater than the open circuit value. This is brought on by the fuel cell's methanol crossover phenomena and a substantial cathode overpotential that exists even when no current is being provided. There are no additional overpotentials when there is no current density. Due to two opposing factors—methanol crossover and the actual performance of the DMFC—the cathode overpotential displays a roughly constant trend as the DMFC current density rises. The other overpotentials start to rise with current density, as seen in Fig. 4.20. When taking into account Eqs. (4.22), (4.57), (4.58), and (4.60), this procedure is anticipated. The anode overpotential is increasing at a rapid pace, yet the membrane's ohmic overpotential is minimal at all current densities. Finally, a reduction in cell voltage is brought on by an increase in overpotentials with current density.

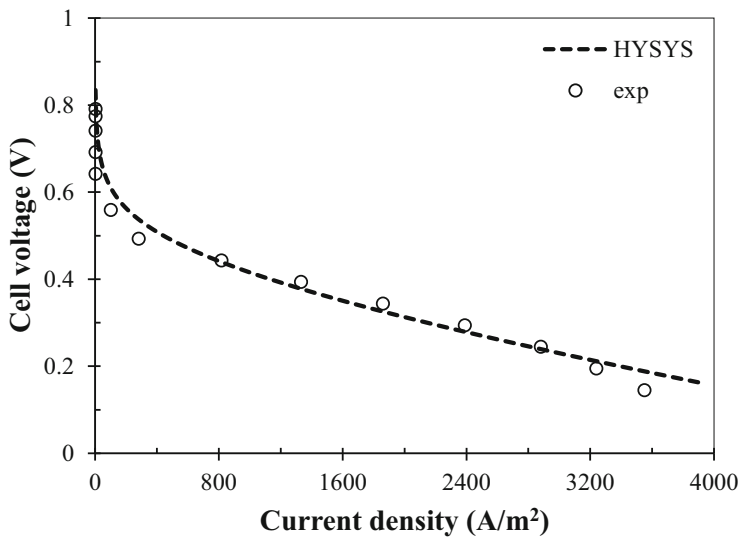


Fig. 4.19 Comparison between simulation results of DMFC with Aspen HYSYS and experimental data. (Reprinted from Nazerifard et al. [24], copyright (2022), with permission from Elsevier)

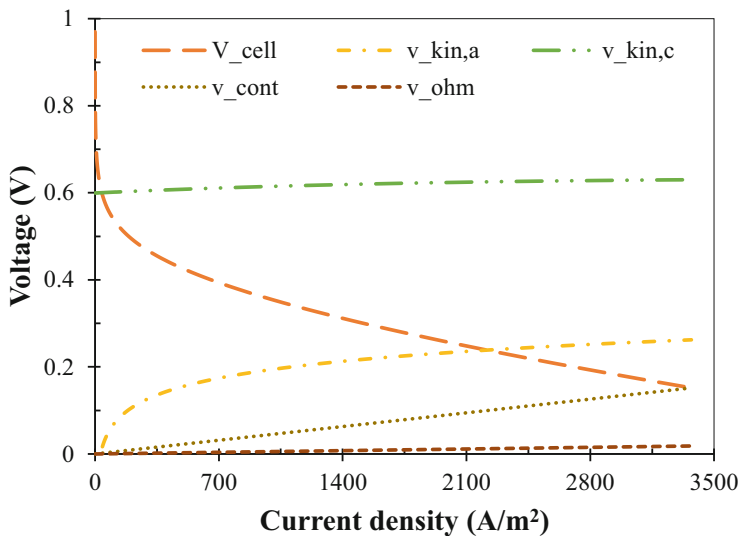


Fig. 4.20 Effect of DMFC current density on cell voltage and overpotentials. (Reprinted from Nazerifard et al. [24], copyright (2022), with permission from Elsevier)

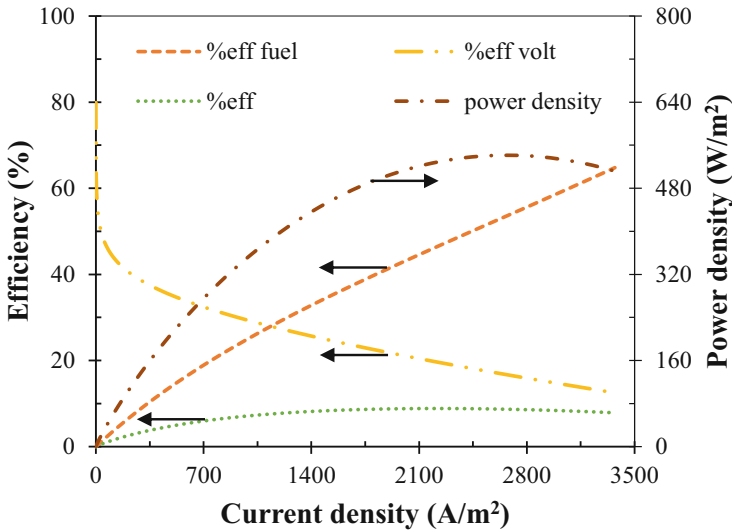


Fig. 4.21 Effect of DMFC current density on efficiencies and power density. (Reprinted from Nazerifard et al. [24], copyright (2022), with permission from Elsevier)

Figure 4.21 displays the DMFC efficiency and power density curves as a function of current density. The voltage efficiency of the cell declines as methanol usage rises (Eq. 4.63), whereas the fuel efficiency increases (Eq. 4.64). Fuel efficiency has a major role in cell efficiency at low current densities, but voltage efficiency plays a major role at high current densities. As a result, as seen in Fig. 4.21, the cell efficiency curve has a maximum value. The power density of the DMFC rises with the current density first increases to its maximum value and subsequently falls. According to Eq. (4.52), current density and cell voltage are two opposing factors that affect the fuel cell's power density. The influence of rising DMCF current density is more pronounced at low current densities, but at high current densities, the power density is mostly determined by the rate at which cell voltage is reducing.

The variations in cell voltage and power density with current density at various operating temperatures are shown in Fig. 4.22. This graph demonstrates how increasing the fuel cell's operating temperature raises its voltage and power density because a higher temperature enhances the reactant's transport characteristics and the electrochemical reaction's kinetics. However, because methanol crossover rises with operating temperature, it has a detrimental influence on the limiting current density.

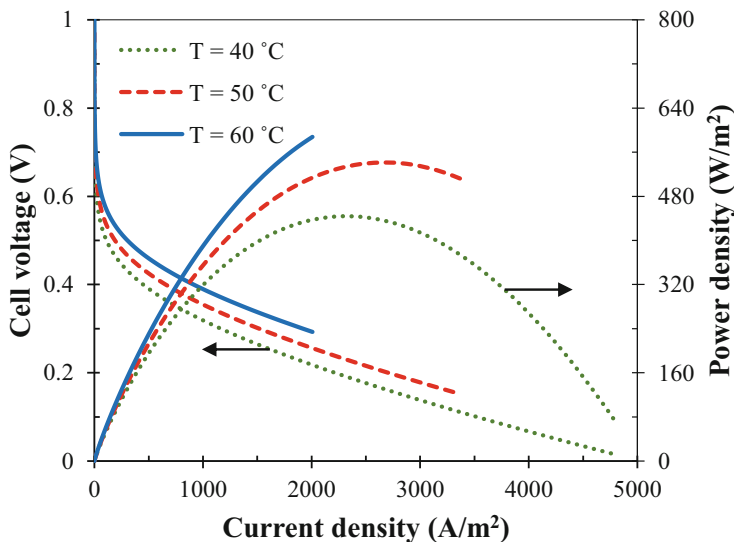


Fig. 4.22 Effect of DMFC current density and operating temperature on cell voltage and power density. (Reprinted from Nazerifard et al. [24], copyright (2022), with permission from Elsevier)

4.5 Conclusions

In this study, a novel trigeneration system is constructed and thermodynamically investigated. It consists of an organic Rankine cycle, a carbon capture unit, a proton exchange membrane electrolyzer, a methanol synthesis unit, and a direct methanol fuel cell. By collecting the majority of the carbon dioxide present in the flue gas and turning it into methanol, hydrogen, and energy, the suggested system lowers the rate of carbon dioxide emissions. The organic Rankine cycle regulates the carbon flue gas temperature for carbon capture system. The electrolyzer receives the necessary energy from solar radiation, and it also generates the necessary hydrogen for the methanol synthesis unit. The following can be used to summarize the key findings of the current work:

- Due to its significant power consumption, electrochemical processes, and heat exchange, the electrolyzer system contributes the most to the overall exergy destruction rate. On the other hand, because no reaction takes place in the organic Rankine cycle, its influence on the overall loss of exergy is insignificant.
- The system's estimated energy and exergy efficiencies are 66.84% and 55.10%, respectively.
- Increasing the ORC turbine inlet pressure increases the efficiency, while increasing the turbine inlet temperature degrades efficiency.

- The carbon capture rate is high in the lower stages of the absorber column in the carbon capture unit. After that, it slows down. As the stream moves through the absorber column, the temperature peaks in the fourth stage.
- As the current density of the electrolyzer increases, the cell voltage increases, but the energy efficiency decreases.
- The methanol concentration, CO₂ conversion, and temperature profiles over the reactor length are all significantly influenced by the reactor input temperature. The temperature at the reactor's input determines even how much pressure the reactor exerts to convert carbon.
- The cell efficiency and power density of the direct methanol fuel cell rise to their maximum levels and subsequently fall as the current density rises.
- Although the fuel cell's operating temperature is greater, this has a favorable impact on cell voltage and power density while reducing the fuel cell's current density.

References

1. Choi W-J, Seo J-B, Jang S-Y, Jung J-H, Oh K-J (2009) Removal characteristics of CO₂ using aqueous MEA/AMP solutions in the absorption and regeneration process. *J Environ Sci* 21: 907–913
2. Bryant S (2007) Geologic CO₂ storage—can the oil and gas industry help save the planet? *J Pet Technol* 59:98–105
3. Ribeiro AM, Santos JC, Rodrigues AE (2010) PSA design for stoichiometric adjustment of bio-syngas for methanol production and co-capture of carbon dioxide. *Chem Eng J* 163:355–363
4. Peters M, Köhler B, Kuckshinrichs W, Leitner W, Markewitz P, Müller TE (2011) Chemical technologies for exploiting and recycling carbon dioxide into the value chain. *ChemSusChem* 4: 1216–1240
5. Quadrelli EA, Centi G, Duplan JL, Perathoner S (2011) Carbon dioxide recycling: emerging large-scale technologies with industrial potential. *ChemSusChem* 4:1194–1215
6. Olajire AA (2013) Valorization of greenhouse carbon dioxide emissions into value-added products by catalytic processes. *Journal of CO2 Utilization* 3:74–92
7. Riaz A, Zahedi G, Klemeš JJ (2013) A review of cleaner production methods for the manufacture of methanol. *J Clean Prod* 57:19–37
8. Dincer I, Rosen MA, Ahmadi P (2017) Modeling and optimization of multigeneration energy systems. In: *Optimization of energy systems*. John Wiley & Sons Ltd, Chichester, pp 398–446
9. Mignard D, Sahibzada M, Duthie J, Whittington H (2003) Methanol synthesis from flue-gas CO₂ and renewable electricity: a feasibility study. *Int J Hydrog Energy* 28:455–464
10. Boretti A (2013) Renewable hydrogen to recycle CO₂ to methanol. *Int J Hydrog Energy* 38: 1806–1812
11. Sayah AK, Sayah AK (2011) Wind-hydrogen utilization for methanol production: an economy assessment in Iran. *Renew Sust Energy Rev* 15:3570–3574
12. Esmaili P, Dincer I, Naterer G (2015) Development and analysis of an integrated photovoltaic system for hydrogen and methanol production. *Int J Hydrog Energy* 40:11140–11153
13. Leonzio G, Zondervan E, Foscolo PU (2019) Methanol production by CO₂ hydrogenation: analysis and simulation of reactor performance. *Int J Hydrog Energy* 44:7915–7933
14. Atsonios K, Panopoulos KD, Kakaras E (2016) Investigation of technical and economic aspects for methanol production through CO₂ hydrogenation. *Int J Hydrog Energy* 41:2202–2214

15. Rivarolo M, Bellotti D, Magistri L, Massardo A (2016) Feasibility study of methanol production from different renewable sources and thermo-economic analysis. *Int J Hydrog Energy* 41: 2105–2116
16. Nami H, Ranjbar F, Yari M (2019) Methanol synthesis from renewable H₂ and captured CO₂ from S-Graz cycle—energy, exergy, exergoeconomic and exergoenvironmental (4E) analysis. *Int J Hydrog Energy* 44:26128–26147
17. Kiatphuengporn S, Donphai W, Jantaratana P, Yigit N, Föttinger K, Rupprechter G et al (2017) Cleaner production of methanol from carbon dioxide over copper and iron supported MCM-41 catalysts using innovative integrated magnetic field-packed bed reactor. *J Clean Prod* 142: 1222–1233
18. Luu MT, Milani D, Abbas A (2016) Analysis of CO₂ utilization for methanol synthesis integrated with enhanced gas recovery. *J Clean Prod* 112:3540–3554
19. Charoensuppanimit P, Kitsahawong K, Kim-Lohsoontorn P, Assabumrungrat S (2019) Incorporation of hydrogen by-product from NaOCH₃ production for methanol synthesis via CO₂ hydrogenation: process analysis and economic evaluation. *J Clean Prod* 212:893–909
20. Ghosh S, Uday V, Giri A, Srinivas S (2019) Biogas to methanol: a comparison of conversion processes involving direct carbon dioxide hydrogenation and via reverse water gas shift reaction. *J Clean Prod* 217:615–626
21. Gao R, Zhang C, Lee Y-J, Kwak G, Jun K-W, Kim SK et al (2020) Sustainable production of methanol using landfill gas via carbon dioxide reforming and hydrogenation: process development and techno-economic analysis. *J Clean Prod* 272:122552
22. Alsayegh S, Johnson J, Ohs B, Wessling M (2019) Methanol production via direct carbon dioxide hydrogenation using hydrogen from photocatalytic water splitting: process development and techno-economic analysis. *J Clean Prod* 208:1446–1458
23. Matzen M, Demirel Y (2016) Methanol and dimethyl ether from renewable hydrogen and carbon dioxide: alternative fuels production and life-cycle assessment. *J Clean Prod* 139:1068–1077
24. Nazerifard R et al (2021) Design and thermodynamic analysis of a novel methanol, hydrogen, and power trigeneration system based on renewable energy and flue gas carbon dioxide. *Energy Convers Manag* 233:113922
25. Abam FI, Briggs TA, Ekwe EB, Kanu C, Effiom SO, Ndukwu M et al (2019) Exergy analysis of a novel low-heat recovery organic Rankine cycle (ORC) for combined cooling and power generation. *Energy Sources Part A: Recovery Util Environ Eff* 41:1649–1662
26. Zhou N, Wang X, Chen Z, Wang Z (2013) Experimental study on organic Rankine cycle for waste heat recovery from low-temperature flue gas. *Energy* 55:216–225
27. Guo C, Du X, Yang L, Yang Y (2015) Organic Rankine cycle for power recovery of exhaust flue gas. *Appl Therm Eng* 75:135–144
28. Laribi S, Dubois L, De Weireld G, Thomas D (2019) Study of the post-combustion CO₂ capture process by absorption-regeneration using amine solvents applied to cement plant flue gases with high CO₂ contents. *International Journal of Greenhouse Gas Control* 90:102799
29. Léonard G (2013) Optimal design of a CO₂ capture unit with assessment of solvent degradation. Université de Liège, Liège
30. Ursua A, Gandia LM, Sanchis P (2011) Hydrogen production from water electrolysis: current status and future trends. *Proc IEEE* 100:410–426
31. Millet P, Mbemba N, Grigoriev S, Fateev V, Aukaaloo A, Etiévant C (2011) Electrochemical performances of PEM water electrolysis cells and perspectives. *Int J Hydrog Energy* 36:4134–4142
32. Jamali Ghahderijani M, Ommi F (2016) One-dimensional Electrolyzer modeling and system sizing for solar hydrogen production: an economic approach. *J Renew Energy Environ* 3:31–43
33. García-Valverde R, Espinosa N, Urbina A (2012) Simple PEM water electrolyser model and experimental validation. *Int J Hydrog Energy* 37:1927–1938
34. Awasthi A, Scott K, Basu S (2011) Dynamic modeling and simulation of a proton exchange membrane electrolyzer for hydrogen production. *Int J Hydrog Energy* 36:14779–14786

35. Ni M, Leung MK, Leung DY (2008) Energy and exergy analysis of hydrogen production by a proton exchange membrane (PEM) electrolyzer plant. *Energy Convers Manag* 49:2748–2756
36. Ruuskanen V, Koponen J, Huoman K, Kosonen A, Niemelä M, Ahola J (2017) PEM water electrolyzer model for a power-hardware-in-loop simulator. *Int J Hydrog Energy* 42:10775–10784
37. Anicic B, Trop P, Goricanec D (2014) Comparison between two methods of methanol production from carbon dioxide. *Energy* 77:279–289
38. Van-Dal ÉS, Bouallou C (2013) Design and simulation of a methanol production plant from CO₂ hydrogenation. *J Clean Prod* 57:38–45
39. Ko J, Chippar P, Ju H (2010) A one-dimensional, two-phase model for direct methanol fuel cells—part I: model development and parametric study. *Energy* 35:2149–2159
40. Yin K-M (2008) A theoretical model of the membrane electrode assembly of liquid feed direct methanol fuel cell with consideration of water and methanol crossover. *J Power Sources* 179:700–710
41. Sharifi S, Rahimi R, Mohebbi-Kalhari D, Colpan CO (2018) Numerical investigation of methanol crossover through the membrane in a direct methanol fuel cell. *Iran J Hydrog Fuel Cell* 5:21–33
42. Meyers JP, Newman J (2002) Simulation of the direct methanol fuel cell: II. Modeling and data analysis of transport and kinetic phenomena. *J Electrochem Soc* 149:A718
43. Bernardi DM, Verbrugge MW (1991) Mathematical model of a gas diffusion electrode bonded to a polymer electrolyte. *AIChE J* 37:1151–1163
44. Wang Z, Wang C (2003) Mathematical modeling of liquid-feed direct methanol fuel cells. *J Electrochem Soc* 150:A508
45. Lee J, Lee S, Han D, Gwak G, Ju H (2017) Numerical modeling and simulations of active direct methanol fuel cell (DMFC) systems under various ambient temperatures and operating conditions. *Int J Hydrog Energy* 42:1736–1750
46. Xu C, Faghri A (2011) Analysis of an active tubular liquid-feed direct methanol fuel cell. *J Power Sources* 196:6332–6346
47. Kvamsdal HM, Rochelle GT (2008) Effects of the temperature bulge in CO₂ absorption from flue gas by aqueous monoethanolamine. *Ind Eng Chem Res* 47:867–875
48. Ioroi T, Yasuda K, Siroma Z, Fujiwara N, Miyazaki Y (2002) Thin film electrocatalyst layer for unitized regenerative polymer electrolyte fuel cells. *J Power Sources* 112:583–587
49. Ge J, Liu H (2005) Experimental studies of a direct methanol fuel cell. *J Power Sources* 142:56–69

Chapter 5

Protection and Monitoring of Digital Energy Systems Operation



Reza Jalilzadeh Hamidi and Ananta Bijoy Bhadra

Abstract Digital transition of energy systems encloses all major parts of the electric grids, including power system protection and monitoring. This chapter first accurately reviews the basics of smart microgrid protection since the definitions vary from a reference to another. Then it focuses on the fault responses of inverter-based resources (IBRs), as those are emerging technologies that will be playing the great role of interfacing primary energy resources and the grid. In particular, for materialization of net-zero carbon emission in electricity generation, the use of IBRs is indispensable. However, the non-universal and software-defined IBR fault responses make conventional relays such as overcurrent, directional, and distance relays inapplicable in heavily IBR-based grids. Therefore, the discrepancy between conventional and IBR fault responses is elaborated, and possible solutions to the looming protection issues are discussed. The shortcomings and merits of each solution are also discussed.

Keywords Autonomous grid · Fault current · Fault level · Fault response · IBR · Inverter · Source-independent protection

5.1 Introduction

Digital energy systems are technologies and schemes that utilize digital computers together with digital models to manage the increasingly sophisticated modern energy systems. The emergence of digital energy system (DES) will have profound impression on the betterment of energy resiliency, cost-effectiveness, transparency, quality of service, and consequently both customer and provider satisfaction [1, 2]. One of the major aims of DESs is to develop highly sophisticated and complex protection and monitoring schemes to respond to smart microgrid needs, utilizing communications, uncertainty analysis, and intelligent management capabilities [3, 4].

R. J. Hamidi (✉) · A. B. Bhadra
Georgia Southern University, ECE Department, Statesboro, GA, USA
e-mail: rhamidi@georgiasouthern.edu; ananta.bijoy@ieee.org

The addition of distributed energy resources (DERs) either uncertain renewable-based or dispatchable [5], integration of energy storage systems (ESSs), and the emergence of new types of power electronic-based loads, adaptive power network topology, DC grids, and so on necessitate the development of new methods for recognition of faults and protection coordination [6–9]. These developments are necessary to safeguard the power grid against new phenomena and new components [9–11] as well as providing real-time monitoring.

This chapter will provide an insight into the protection and monitoring needs of advanced power grids and then delivers some of the most up-to-date developments in response to the arising issues and needs.

5.2 Overview of Protection Key Points and Definitions

This section briefly, but precisely, reviews the basics of protection. This is necessary since there are some discrepancies in different resources and technical texts. Therefore, providing a precise definition of the fundamentals helps understanding from the readers.

- Protection zone: with reference to Fig. 5.1a, protection zone is a part of a power grid that is protected by a certain protective scheme. Whenever a fault happens in a specific zone, only the faulty zone will be disconnected by the circuit breakers surrounding that zone, and the rest of the system keeps functioning. Conversely, the protective devices supporting a particular zone stay restrained in case of faults outside their own zone.
- Unit protection: following this scheme, the protective relays operate in case of abnormal conditions inside the protection zone, while the relays stay stable for abnormal conditions outside the zone. The circumference of the zone is limited by the measuring devices connected to the relays. For example, and with reference to Fig. 5.1a, a unit protection, which is differential protection, protects a transformer, and the zone is the span between two CTs. It is worth noting that the

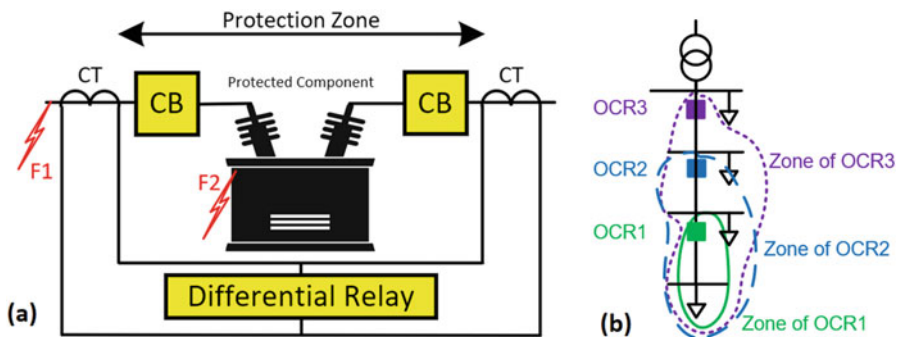


Fig. 5.1 A typical unit protection, (a); a typical non-unit protection, (b)

CBs are generally placed in a way that their failure is detected by the closest CT to them, or in other words, CBs are placed toward the protected component. Therefore, CBs are normally placed inside the protection zone. In Fig. 5.1a, the differential relay should react to F2 that is inside the zone, but it should remain restrained against F1 that falls outside the zone. In unit protection, coordination between relays is not needed.

- Non-unit protection: converse to the unit protection, non-unit relays’ protection zones extend well beyond their measuring components and often cover large portions of power grids. One of the typical examples in this area is overcurrent relays (OCRs). As shown in Fig. 5.1b, each upper OCR overlaps the zones of the lower ones. In non-unit protection, relay-to-relay coordination should be done with extra care following the general protection scheme selected for the grid.
- Overlapping zones: with reference to Fig. 5.1b, when some protection zones intersect, the intersection is an overlapping zone. This can be deliberately done for providing backup protection, or it happens unintentionally that often leads to coordination issues.
- Graded coordination: when relays’ zones overlap, the closest relay to the fault should react first as the “main” relay to keep the de-energization of the grid as minimal as possible. If it fails to disconnect the faulty zone for any reasons, then the “backup” one should now react. Therefore, non-unit relays are coordinated as the main and backup one(s). This coordination procedure is done by putting the characteristic curves of the backup ones above the main one. For example, as for OCRs, grading can be done considering both time and current, which is called time-current-graded coordination, as shown in Fig. 5.2a. The coordination can be done with respect to time only; that is called time-graded coordination, as depicted in Fig. 5.2b, or as Fig. 5.2c shows, the coordination can be current-graded (e.g., instantaneous function) [7, 12].

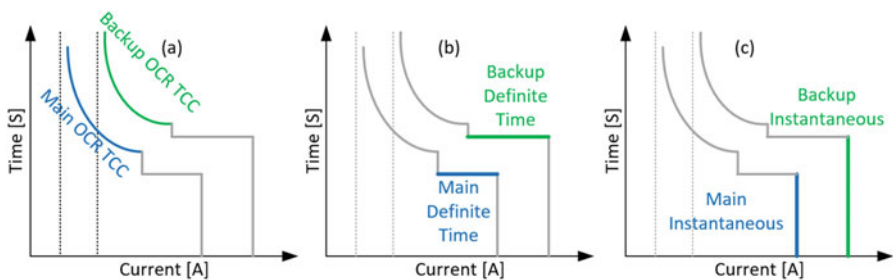


Fig. 5.2 Different ways for graded coordination: (a) Time-current-graded coordination; (b) time-graded coordination; (c) current-graded coordination

5.3 Overview of Microgrid Protection Bottlenecks

5.3.1 Loss of Coordination

- As DERs participate in fault currents and increase their levels, DERs disturb the time-current and current graded coordination of non-unit protective devices. However, this has no effect on time-graded coordination.

Solutions: (i) Re-coordination of time-current- or current-graded coordination schemes [13]; (ii) using only time-graded coordination [14]; (iii) addition of fault current limiters (FCLs) to the system [15].

- The second problem arising from DERs is that they change the power flow in distribution grids, which conventionally flows upstream to downstream. However, when DERs are added toward the end of feeders, then power-flow direction can be reversed downstream to upstream.

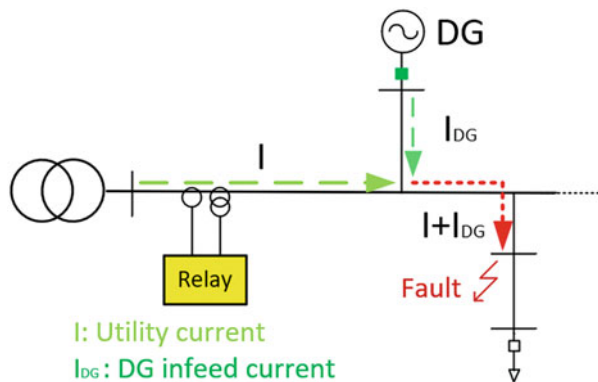
Solution: (i) Adaptively readjustments of the settings of OCRs; (ii) addition of directional elements to OCRs to prevent them from tripping in case of upstream faults.

5.3.2 Protection Under-reaching, Desensitization, or Blinding

With respect to Fig. 5.3, when infeed DERs are added to the grid, the responsible relays sense a fault current lower than the actual fault current passing through the faulty feeder. Therefore, the relays may not react in time, and the system gets damaged [16, 17]. In severe cases, the built-up voltage across the fault resistance and the feeder can decrease the contribution of the main grid to the fault causing blindness of the feeder's relay [17].

Solution: The solution to this issue is to add a protective relay at the distributed generation (DG) location.

Fig. 5.3 Interconnection of a DG as an infeed



5.3.3 False Tripping (Nuisance and Sympathetic)

Due to the contribution of DERs to the faults, there are currents flowing throughout the grid during the fault that may cause unwanted tripping of some of the relays in the grid. If a relay reacts to a fault outside its protection zone, it is generally called “false tripping,” which can be divided into two major categories.

- *Sympathetic Tripping*

When healthy feeders become disconnected due to a fault in the other feeder, sympathetic tripping happens. For example, in Fig. 5.4a, if there is any of R1 or R2 trips for F1 because of the currents fed by the DG units, a sympathetic trip occurred [18].

Solution: Directional blockers should be added to R1 and R2.

- *Nuisance Tripping*

With reference to Fig. 5.4b, there are two protection schemes for the faulty feeder with DERs: (a) all the DERs should be disconnected (the present-time scheme suggested by [19]). (b) Only the fault location should be disconnected, and the rest of the system continues working in the islanding mode (the preferable scheme). If the first scheme is selected for the grid, and if R2 disconnects F2 before both R_{DG1} and R_{DG2} , nuisance tripping will happen.

Solution: it is suggested that the system is equipped with transfer trip relays that disconnect R_{DG1} or R_{DG2} when R1 or R2 detects a fault [20].

5.3.4 Auto-reclosers

As some faults are temporary (e.g., caused by lightning), the system can be kept from outages with the use of auto-reclosers. A typical operation sequence of

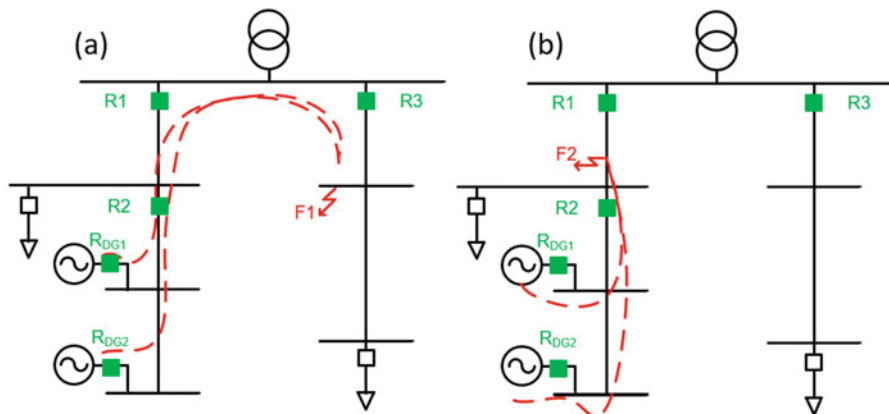


Fig. 5.4 False trips. (a) Sympathetic tripping. (b) Nuisance tripping

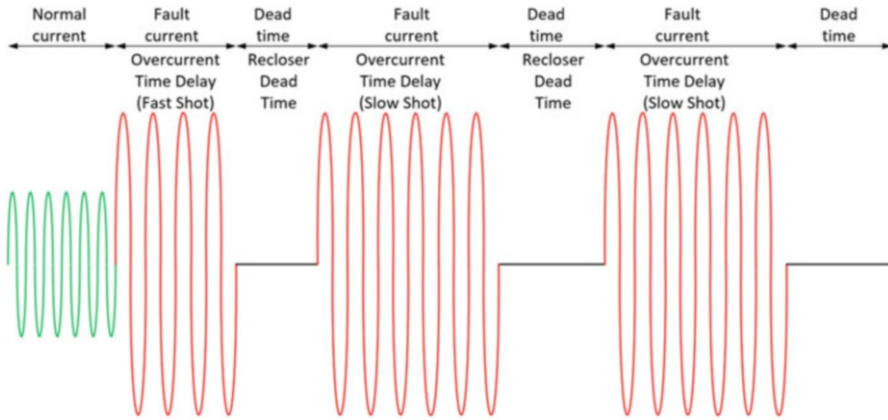


Fig. 5.5 A typical operation sequence of auto-reclosers

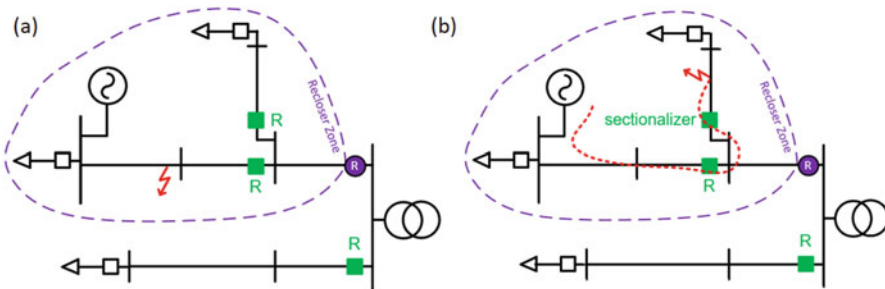


Fig. 5.6 Auto-recloser issues. (a) Auto-recloser protection zone. (b) The sectionnalizer issue arising from DERs

auto-reclosers is shown in Fig. 5.5. However, the number of fast and slow shots, as well as dead times, is selected based on the protection scheme and the grid specifications.

An auto-recloser is installed in a power grid well upstream, and its protection zone covers a large portion of the system as Fig. 5.6a shows. If a temporary fault happens, the recloser de-energizes the system with a short delay as the fast shot in Fig. 5.5 shows. The dead time should give the arc enough time to quench, and when the recloser reconnects after the deadtime, there is no longer any fault in the system. However, if the fault is permanent (e.g., a dropped bare conductor or broken insulator), after several dead shots, the fault still exists, and the recloser does not reconnect anymore. In setting the recloser, there are two major schemes to follow:

- (i) Fuse blowing scheme: the recloser gives fuses enough time to blow and clear the fault during recloser's slow shots.
- (ii) Fuse saving scheme: the recloser does not let fuses blow by having no slow shots.

As Fig. 5.6b depicts, when a recloser disconnects a system with DERs connected to it, (i) the contribution of the DER to the fault may not let the arc quench. (ii) The asynchronous reclosing may result in high currents in the grid.

Solution: for the first issue, the dead time of the recloser should be increased such that the protective systems of all DERs in the recloser zone trip. As for the second issue, a synchronous relay should block asynchronous reclosures.

5.3.5 Sectionalizers

Sectionalizers are devices that are used together with reclosers to disconnect the faulted feeders. When an upper recloser interrupt the fault currents, a lower sectionalizer counts high currents (caused by a fault along their feeder) after the dead times. If a specific number of unsuccessful reclosures occurs, the sectionalizer disconnects the faulty feeder during the next dead time.

As Fig. 5.6b shows, the problem arises from the contribution of DERs to the fault that does not allow the sectionalizer to count the high currents and dead times since a fault current continuously flows from the DER without any interruption during the recloser's dead times.

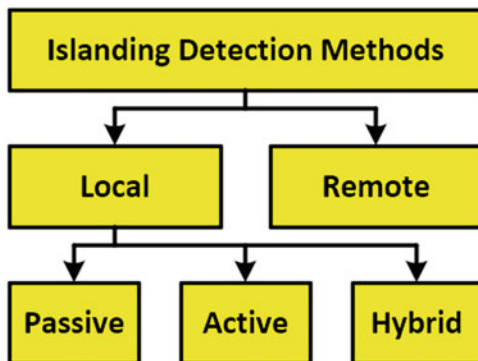
5.3.6 Unintentional Islanding

Different contingencies, in particular false tripping, may result in undesirable islanding in that a part of the microgrid stays energized by DERs while it is disconnected from the rest of the grid. Islanding operation of the grids requires advanced frequency, voltage, load-sharing control systems, as well as sophisticated monitoring systems. Therefore, in most of the practical grids, a part of the system should not be allowed to continue working in islanding mode [20]. There is a significant body of research looking into islanding detection.

Based on IEEE Standard 1547, DERs must be switched out from the grid in 2 s after the occurrence of islanding [19]. To this end, reliable islanding detection methods are required. Major types of islanding detection methods have been developed as shown in Fig. 5.7 [21, 22]. (i) Remote methods utilize both the local and far measurements through communication systems for detection of islanding. (ii) Local methods only rely on local measurements at the location of the DERs, and they do not use communications.

- Passive islanding detection methods rely on measuring electrical parameters of the grid such as voltage displacement, frequency deviation, rate of change of frequency or voltage (ROCOF or ROCOV), rate of change of frequency with respect to power (df/dp), and total harmonic distortion together with voltage

Fig. 5.7 General classification of islanding detection methods



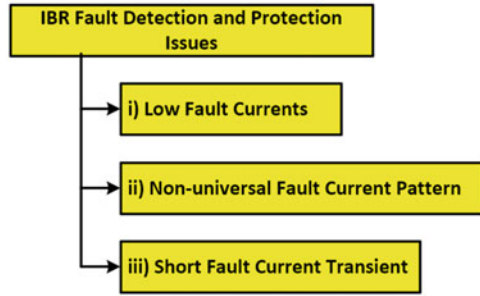
unbalances. However, large non-detection zones and false tripping are major downsides of passive methods.

- In active methods, some external signals are injected into the grid. Then, the grid's response to the signal is observed at the location of DERs and premised on the system response, a probable islanding is detected. However, power quality issues due to the injected signal and also comparatively longer times to detect the islanding detract from active methods.
- Hybrid methods have been developed to improve the shortcomings of passive and active methods. This classification not only injects a noise into the system, but it also concurrently monitors the electrical parameters throughout the grid for the betterment of islanding detection.

5.3.7 Heavily Power Electronic-Based Grids

In conventional power grids, which are mainly supplied by synchronous or induction generators, the fault contribution and during-the-fault current patterns of conventional generators are well-known. However, the contribution of the power-electronic-based sources is unpredictable, software-defined, and incomparable with the conventional generators [20, 23]. The protection issues caused by inverter-based resources (IBRs) are summarized in Fig. 5.8, and then, each one is described.

Fig. 5.8 Main protection issues of IBRs



- (i) In conventional systems, a fault is detected by fault-current features; this is the most basic and widely used method for detection of faults in power systems. The steady-state fault current is reversely proportional to the driving-point impedance (diagonal elements of the impedance matrix, also referred to as Z-bus) of the fault location. However, in the case of heavily or 100% inverter-based grids, the size and pattern of fault currents do not follow the abovementioned well-known patterns [19, 20, 23, 24]. The differences are as follows:
- **Magnitude:** IBRs generate fault currents in the order of 1.00–1.2 p.u. (in less common ones, the fault current can increase to 1.5 p.u.), while conventional generators typically generate fault currents as large as 3–5 p.u [25]. This can be found in Figs. 5.9 and 5.10.
 - **Fault current phase Angle:** In conventional systems, fault currents lag voltage. However, in the case of IBRs, the fault currents can be capacitive, inductive, or even resistive [23, 25].
 - **Sequence:** The negative and zero current sequences are negligible depending on the control system of the IBR, whereas those sequences can be high in case of unsymmetrical faults in conventional systems [19, 23, 24]. Figure 5.9b depicts this.
 - **Fault current direction:** the directional elements find direction of fault currents by comparing the angle between voltage and current, considering that the system is inductive, and therefore, the fault current lags the voltage. As mentioned above, this may not happen in heavily IBR-dependent systems and directional elements fail in detecting fault-current direction.
- (ii) **Non-universal fault current pattern:** non-universal control methods for IBRs make the fault patterns irregular and non-uniform in IBR-based grids, which make use of some conventional protection schemes impossible for protection of the grids [19, 23].
- (iii) **Short fault current transient:** the transient of fault currents in conventional grids is mainly associated with the sub-transient impedance of generators and X-to-R ratio of the driving point impedance. However, a limited and relatively low amount of energy stored in inverters' DC-bus capacitances leads to a rapid decay in the short-circuit current in converter-dominated grids

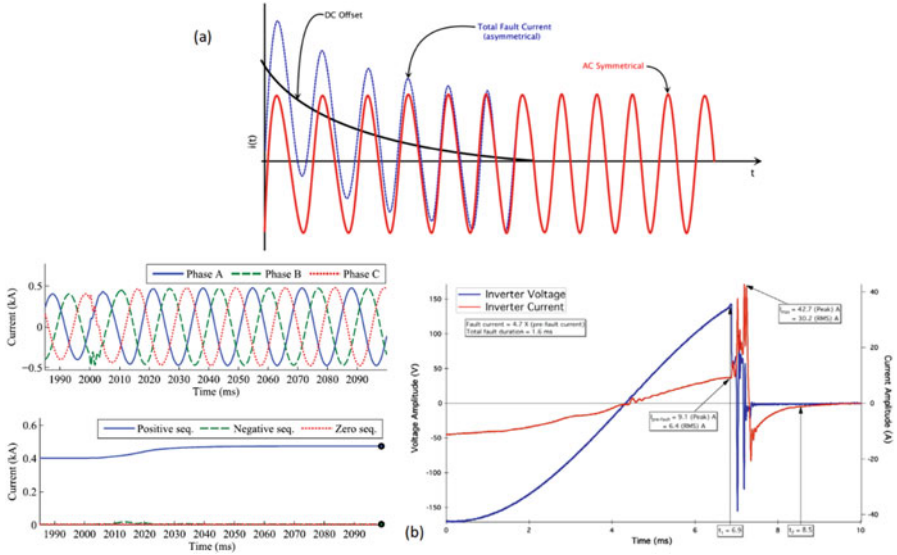


Fig. 5.9 Fault responses of conventional and inverter-based generators. (a) A typical fault current in conventional systems. (b) Examples of the fault responses of IBRs. (The figures are from Kobet and Pourbeik [25], Keller and Kroposki [26])

[27, 28]. Moreover, inverters are rarely controlled to mimic the behavior of generators during a fault.

Accordingly, in IBR-based grids, protection schemes have to mostly rely on voltage, sequential components, or extracting other features from during-fault current or voltage. This will be elaborated in the next sections.

Moreover, Fig. 5.10 shows the voltages and currents at Bus 1. The fault is bolted A-G. The voltage pattern is analogous to conventional systems. However, during-fault currents are significantly different. It is obvious in Fig. 5.10 that (i) the phase currents are nearly in-phase with one another because of the high zero-sequence current produced by the synchronous generator. (ii) The magnitude of B-phase current is the largest although the fault is A-G. (iii) Regardless of the inductive nature of the transmission line (TL), the current and voltage of phases are somehow in phase [23].

Accordingly, protection algorithms trusting the fault-current magnitude, the phase differences between the phase currents, and the phase differences between currents and voltages are no longer reliable in heavily IBR-contaminated grids. Therefore, overcurrent, directional, and distance relays have no use in such grids, yet differential relays are still useful [23].

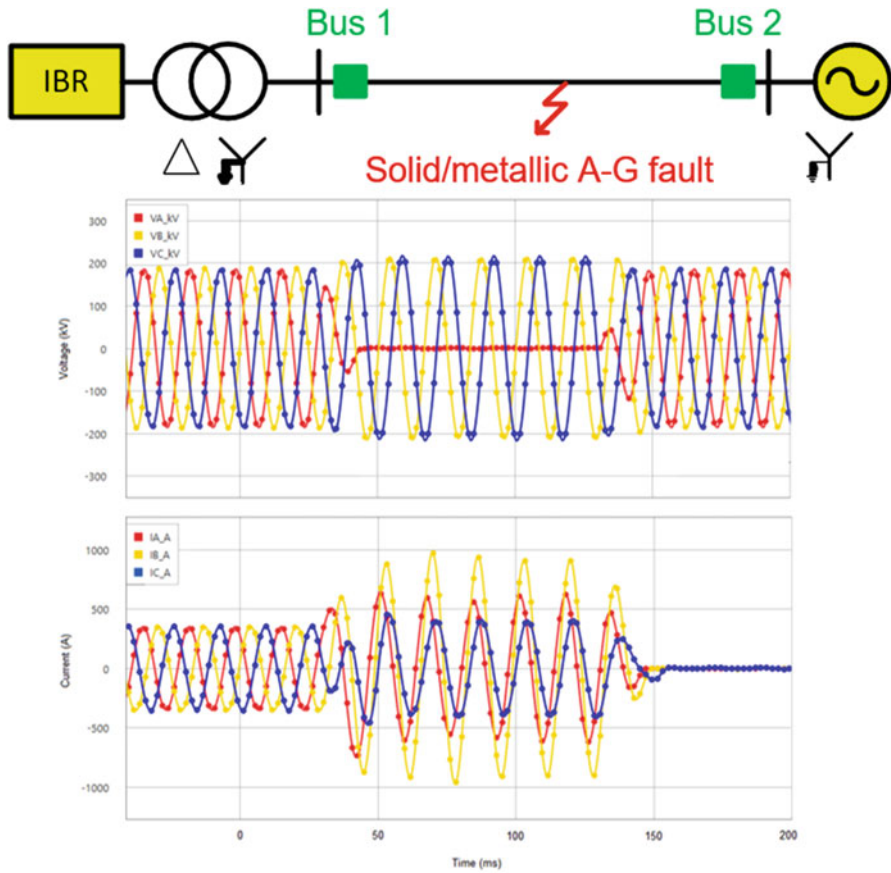


Fig. 5.10 A system including synchronous generators and IBRs. The AC parts of pre-, during-, and post-fault voltages and currents are shown as well [23]

Table 5.1 General control methods of IBRs

Control scheme	Control parameters	Inverter type
Grid forming	VF control	VSI ^a
Grid feeding	PQ control	CSI ^b
Grid supporting	Droop control	CSI or VSI

^aVoltage Source Inverter

^bCurrent Source Inverter

5.4 IBR Control Schemes and Grid Protection

In order to profoundly dig into the arising issues from IBRs, first, their control methods should be reviewed. There are three core control schemes for IBRs summarized in Table 5.1 [27].

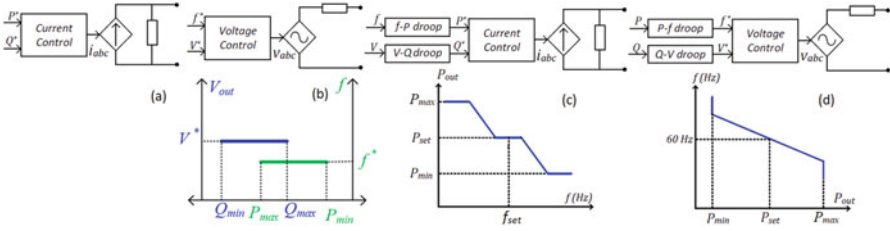


Fig. 5.11 Summarized general controllers and their characteristics. (a) Grid feeding. (b) Grid forming and its controller characteristics. (c) CSI grid supporting. (d) VSI grid supporting

- In the grid forming scheme (also referred to as voltage-frequency control, V/F control), the inverter actively regulates its output voltage and frequency. Therefore, the inverter has to consciously supply the grid. The V/F-controlled IBRs can be modelled with a controlled voltage source in series with impedance [27, 29]. The need to control the output power is answered by controlling their output frequency to adjust their bus angle [27]. Figure 5.11b shows the principal structure and control characteristics of grid-forming inverters. It is noteworthy that at least one grid-forming inverter should be in any autonomous grid.
- Pursuing the grid feeding scheme (or real-and-reactive power control, PQ-control), the inverter tracks the voltage angle and frequency of the system mainly using PLLs and supplies a current to the grid proportional to the reference values for real and reactive powers. These inverters work as a current source inverter (CSI), and they do not undertake frequency and voltage correction tasks. In today’s practical grids, all the inverters must be CSI [30]. If harmonic analysis and internal aspects of inverters are not under question, the equivalent circuit of a PQ-controlled IBR (CSI) can be a power-controlled current source with or even without a parallel impedance [31] as shown in Fig. 5.11a. This scheme efficiently controls the power injection to the grid since the inverters are relaxed from controlling the voltage and frequency.
- The grid supporting control scheme combines the droop controller with any of the other two schemes to lessen the immediate demand-supply mismatch. However, the power quality issue is a concern whenever the grid supporting scheme is followed [27, 32]. Figure 5.11c, d, respectively, shows grid-supporting CSI and voltage source inverter (VSI) basic structures and droop curves.
- The critical point in IBR controllers is that the controllers usually require a quarter of a power cycle to react to the fault which can be seen in Fig. 5.9b as some sort of disturbance. Therefore, the protective devices should be agile enough to detect the fault in that short period.

5.4.1 Solutions to IBR Protection Issues

Different methods have been proposed to overcome the protection issues arising from the IBRs where the short-circuit current of the system is quite low. In the next sections, those will be reviewed.

5.4.1.1 Emulation of Synchronous-Generator Fault Response

One of the methods for enabling protective devices to detect faults is to repeat the synchronous generators' fault responses. The relays largely rely on the high and unbalanced currents generated by synchronous generators for detection of faults [33]. There is a wide body of research working on the development of the negative-sequence current loop to generate currents suitable enough for relays in case of unbalanced faults (e.g., SLG, LL, LLG) as Fig. 5.12 shows [33, 34]. Moreover, it should be taken into account that the DC bus usually does not have enough storage capacity for supplying the inverter to make high fault currents.

5.4.1.2 Active Protection Methods

Active protection is defined as injection of sort of waves with a frequency considerably other than the nominal frequency into the grid and identification of faults by means of measuring the parameters of the injected waves [35]. In active protection methods, IBRs are mainly responsible to generate some harmonics. The point is that the intentionally generated harmonics should drastically differ from the ones generated by nonlinear loads, saturated transformers, etc. This is critical, and extra care

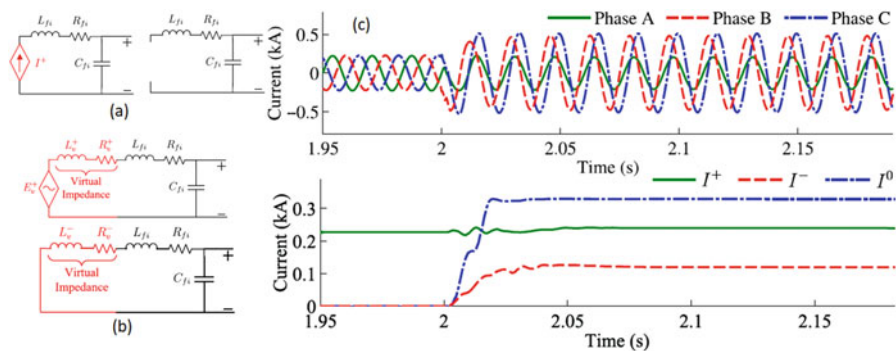


Fig. 5.12 Conventional positive- and zero-sequence inverter model (a). (b) Positive- and zero-sequence models of the inverters equipped with controllers to mimic generators' fault currents. (c) Unbalanced fault response of the inverters with such controllers. (This figure is mainly based on Banaieemoqadam et al. [34])

should be taken that in the future, such harmonic sources will never be added to the grid. There are two ways for harmonic generation:

- Fault-triggered harmonic injection in that IBRs start producing harmonics only after fault occurrence [34–36]. The problem with this strategy is that the harmonic generator module should rely on a fault detector as a third party, such as [35, 36], and correct detection of faults in weak grids with low fault levels is not always possible. In [34], the occurrence of a fault is detected at the location of the IBR when its terminal voltage drops below 0.9 p.u. Although [19] necessitates that DERs must keep generating during low-voltage situations to meet low voltage ride-through (LVRT) requirements, the issue arises from the fact that SLG faults in weak or non-effectively grounded grids do not drop the below range, and also the voltage drop can be caused by other contingencies such as a cut in generation.
- Continual harmonic injection in which IBRs produce harmonics continuously or repeatedly. This method does not have fault detection problems, however at the price of reducing power quality and power losses in harmonic generation [28].

5.4.1.3 Source-Independent Relays

Considering non-universal fault responses of inverters due to their software-defined and non-standard structure and control, protective methods independent of the source have been developed. One of the major types of source-independent relays is traveling wave (TW)-based relays, which are able to detect and locate a wide range of faults in highly complex systems [37, 38]. When a fault occurs, the fault-induced TWs start moving along TLs as Fig. 5.13a shows. The waves do not depend on the source specifications, but they are dependent on the fault parameters such as fault inception angle (FIA), fault impedance, location of the fault, and medium characteristics [39]. Then, TW-based protective devices detect and even locate the fault through the analysis of the wave parameters such as arrival time, peak, polarity, and frequency contents. The key to the efficient function of the TW-based relays is the method used for detection and evaluation of fault-induced waves. Different methods have been used to this end, including sliding-window digital Fourier, wavelet

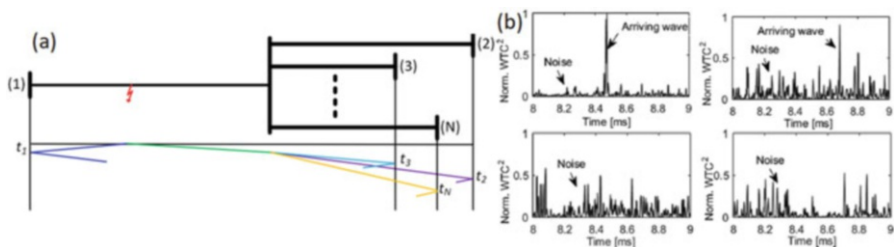


Fig. 5.13 A typical ladder diagram of TW propagation in an electrical grid (a). The TWs originate at the fault location and move along the TLs. When they reach discontinuities, they break into parts, and each continues traveling. (b) The TWs at the endpoints

Table 5.2 Comparison of different solutions to the arisen protective problems

Solution	Advantage	Disadvantage
Emulation of conventional generators	<ol style="list-style-type: none"> 1. The currently in-use relays can continue serving 2. The developed methods for prediction and monitoring of power system contingencies can continue working 3. Readily applicable for protection engineers 	<ol style="list-style-type: none"> 1. The main problem is that how the inverters become aware of the occurrence of the faults
Active protection	<ol style="list-style-type: none"> 1. Highly sensitive 	<ol style="list-style-type: none"> 1. Implementation is not always possible due to the unknown 2. Increasing the total harmonic distortion
Source-independent TW-based	<ol style="list-style-type: none"> 1. Highly sensitive 2. Able to detect the fault location 	<ol style="list-style-type: none"> 1. Hard to be practically implemented 2. Costly 3. In some cases (e.g., low fault angle, long lines, etc.), it cannot detect TWs

transformation with different mother wavelets, Hilbert, short-time matrix pencil method, and custom-defined methods such as [8]. Korean power transmission network installed several high-frequency measuring devices throughout a part of their system. Having collected their real-time measurements, TW-based relays efficiently detected different faults, and the system is working as a prototype for further development [40].

However, TW-based methods are largely prone to measurement noises. If FIA is low, then the TW is likely to vanish in the noises. For example, the two upper sub-figures in Fig. 5.13b show TWs discernible in the noises. However, in the two lower sub-figures, the TWs disappeared in the noises. Also, if there are several discontinuities in the grid, then the wave traveling pattern becomes quite complex, which makes the fault detection challenging. One of the practical examples of the TW-based relays is introduced in [41].

5.4.1.4 Comparison of the Solutions to Protection Methods

The solutions to the issues caused by a large number of IBRs can be summarized in Table 5.2.

5.5 Predictive Wide-Area Monitoring, Protection, and Control

For a profound insight into wide power outages originating from various unsettling events, it is useful to hypothetically divide power system operation into five situations as depicted in Fig. 5.14a [42].

5.5.1 Cascading Failures in Large Power Systems

The majority of power outages are resultant of cascading failures initiated by either a fault, line congestions, hardware dysfunction, extreme climate, or wildfires. Figure 5.14b illustrates the movement of cascading failures. Figure 5.15 shows the aggregate substantial power outages from 2011 to 2020 in each continent and also their grounds. It is obvious that severe weather condition is one of the major triggers to the total 250 blackouts.

5.5.2 Estimation Based on Synchronized Measurements

One of the remedies for reducing the number and intensity of blackouts is the use of phasor measurement units (PMUs) and intelligent electronic devices (IEDs). However, the power grids are already equipped with supervisory control and data acquisition (SCADA)-based measuring devices that do not provide accurate and

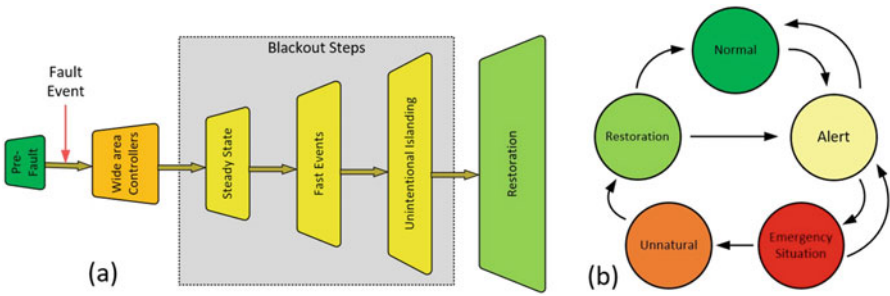


Fig. 5.14 Operation conditions of power systems (a) [42]. (b) Cascading failures inducing blackouts [43]

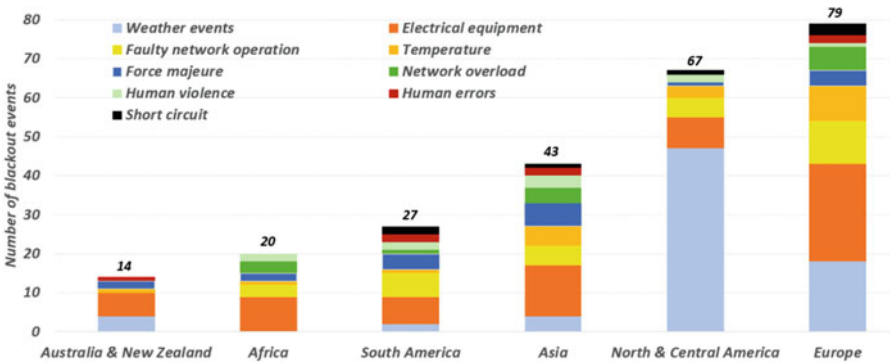


Fig. 5.15 The number and causes of the blackouts in different continents [43]

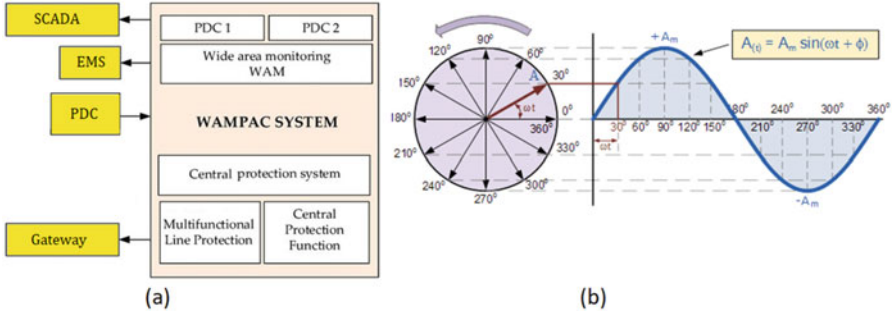


Fig. 5.16 The basic structure of the PWAM (a). (b) Sinusoidal to phasor conversion by PMUs

fast enough data from the purpose of semi-real-time monitoring, which is necessary to protection. The basic architecture of protective wide-area monitoring (PWAM) is shown in Fig. 5.16a.

With reference to Fig. 5.16a, the synchronized measurement technology (SMT) provides continuous time-stamped estimations. However, the PMU measurements are in the form of phasors, which are absolutely different than the data provided by conventional power system metering devices. Figure 5.16b clarifies transformation of a sine wave to a phasor using synchronization technology. The primary idea of PMUs is to measure the voltage and current phasors on distinguishable time arrays and communicate them to a PMU Data Collector (PDC) where the data can be evaluated and further processed. The essential functionalities of PMUs are as follows: (i) system observing/state estimation and (ii) fault recording.

Although PMUs are beneficial to the system observability, conventional state estimators are not capable of using unprocessed PMU data since there are two major differences between SCADA and PMU measurements: (i) the mathematical formulation of conventional state estimators is suitable to SCADA data, and (ii) the data rate of PMUs is much faster than that of SCADA [44]. Therefore, it is essential to convert PMU data to be compatible with conventional state estimators [45]. The most widely used method for state estimation is weighted least square (WLS), which is calculated as [46]:

$$\min_x J(\mathbf{x}) = [\mathbf{z} - \mathbf{h}(\mathbf{x})]^T \mathbf{R}^{-1} [\mathbf{z} - \mathbf{h}(\mathbf{x})], \quad (5.1)$$

where $J(\mathbf{x})$ is the objective function, \mathbf{R} is the measurement-error covariance matrix, $(.)^T$ symbolizes matrix transposition, \mathbf{z} is the measurement vector, $\mathbf{h}(\mathbf{x})$ is the system equation, and \mathbf{x} is the vector of states. Solving (5.1) through the Newton-Raphson method results in [46]:

$$\mathbf{G}(\mathbf{x}^k) \Delta \mathbf{x}^{k+1} = \mathbf{H}^T(\mathbf{x}^k) \mathbf{R}^{-1} [\mathbf{z} - \mathbf{h}(\mathbf{x}^k)], \quad (5.2)$$

where $\mathbf{G}(\mathbf{x}^k) = \mathbf{H}^T(\mathbf{x}^k)\mathbf{R}^{-1}\mathbf{H}(\mathbf{x}^k)$ is the gain matrix and $\mathbf{H}(\mathbf{x}^k)$ is the Jacobian matrix of $\mathbf{h}(\mathbf{x}^k)$, $\Delta\mathbf{x}^{k+1} = \mathbf{x}^{k+1} - \mathbf{x}^k$.

One of the powerful methods to remove the mismatch between the data rates of SCADA and PMU is compressive sensing, a way for compression and recovery of a sparse signals only utilizing a small number of linear projections. The sparsity is modeled as [44, 45]:

$$x_j = z + z_j, \quad j \in \{1, 2, \dots, J\}, \quad (5.3)$$

where z is the common component of compressed signals in that the common component and also the innovation terms are both sparse on Ψ , which is defined as [44, 45]:

$$z = \Psi\theta_z, \|\theta_z\|_0 = K \text{ and } z_j = \Psi\theta_j, \|\theta_j\|_0 = K_j. \quad (5.4)$$

Then, the vector of sparse coefficients is calculated through:

$$\hat{\theta} = \arg \min \|\theta\|_1 \text{ s.t. } y = \hat{\Phi}\hat{\Psi}\theta \quad (5.5)$$

and finally, the signal is recovered by:

$$x = \hat{\Psi}\hat{\theta}. \quad (5.6)$$

Using compressive sensing, the gaps between SCADA and PMU data can be filled by assuming SCADA data as sparsely compressed data [44, 45].

5.5.3 Protective Wide-Area Monitoring Structure

The PWAM framework essentially comprises several layers as shown in Fig. 5.17. It starts from the sensors connected to the electrical grid that measure electrical parameters, and then PMUs using synchronizing signals find the phasor values out of the sensory data and send them to the PDC. The PDC collects a large volume of data and prepares them for recording and visualization as well as other custom-defined applications. The protective algorithms can be implemented as a custom-defined function.

However, the protection at this stage has to be backed up, considering the delays and probable communication failures from the first level to the protection level, although the use of PWAM is such accurate and keen that it reduces 70% of significant power outages [47, 48]. There are several studies and real-world PWAM projects as follows: in [49], a multifunctional line protection system is designed using PWAM, which is able to prevent false trips due to complicated cases that distance relays falsely trip. Tokyo Electric Power Co. (TEPCO) utilized a

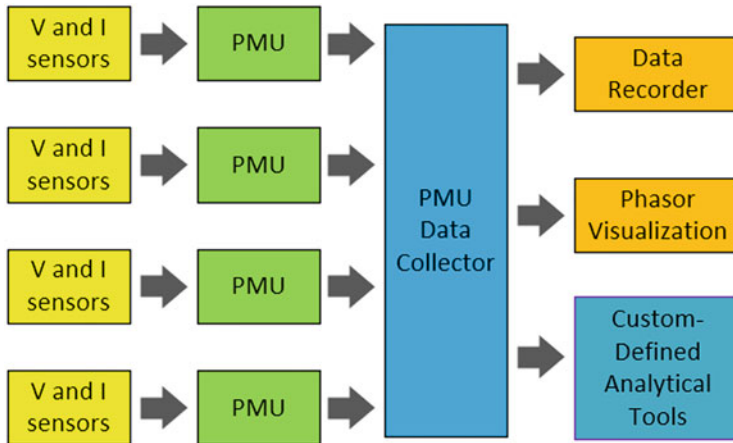


Fig. 5.17 Different layers for transferring and using PMU data

wide-area relay technology in light of power angle assessment technique. A major atomic generator was chosen as a locus generator, and its momentary power and voltages information were moved to each siphoned stockpiling plant by means of microwave communications. Then, relays used the received and local information to detect oscillations, out-of-phase, frequency deviations [50].

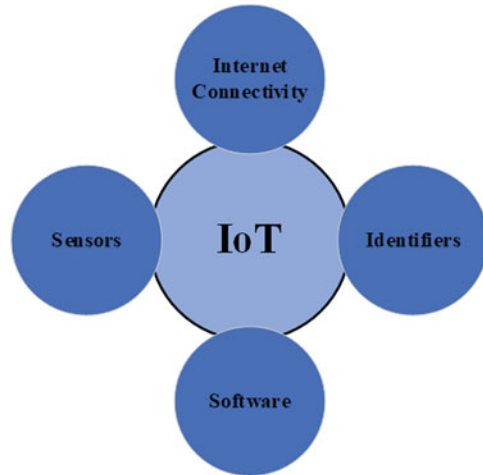
5.6 IoT, Auxiliary Protection, and Monitoring Methods

As smart grid's topology and renewable generations connected to it are both uncertain, a different yet efficient approach is IoT, which involves the Internet for data transmission. The flow of data through the Internet keeps relays and monitoring centers aware of the semi-real-time changes in the system topology, generation, and demand. However, protection has to be a subordinate auxiliary service of IoT due to IoT intermittency and reliability issues [30, 51, 52].

The ability of machine-to-machine coordination has made IoT a matter of greater interest. IoT was first defined in 1999 [53]. As Fig. 5.18 shows, IoT comprises the following portions: (i) sensors for collection of data, (ii) identifiers for identification of the data source, (iii) software for analysis of the data, and (iv) Internet connectivity for communication among all the associated machines.

One of the prominent uses of IoT is seen in power systems. The use of IoT in power systems emphasizes (i) IoT in protection [54] and (ii) IoT in monitoring [55].

Fig. 5.18 Components of IoT



5.6.1 IoT in Protection

IoT-based protection is defined as the protection of equipment and subsystems with the main focus on fault diagnosis and cyberattacks [56], however, as the backup protection scheme. The IoT-based protection is applicable to situations where the fault is not intense or imminent. For example, in [57], an IoT protection scheme is introduced to monitor the distribution transformers' parameters such as temperature, rise or fall of the oil level, vibration, and oil humidity. Upon encountering any abnormality, it alerts the operators, and if no operator is not present on-site, it disconnects the transformers. In [58], another IoT-based distribution transformer protection is introduced that monitors overheating, deformation, short circuit, and suffocation of windings. The system also stores data and sends alerts to operators upon detecting any abnormality.

5.7 Artificial Intelligence-Based Protection

Artificial intelligence (AI) is most popular as it is precise in terms of problem classification and decision-making. It optimizes the management strategy as well as involves the process of making an intelligent decision based on its prior training [59]. AI is defined as the ability of computer systems to solve poorly defined problems using methods inspired by the human brain [60]. Over the years, AI has been implemented in various sectors as well as power systems from the 1990s. Several AI-based monitoring techniques are established and have proved to be effective [61]. There are several AI methods available, including (i) rule-based systems, (ii) knowledge-based systems, (iii) object-oriented methodologies, and (iv) case-based reasoning.

- Rule-based systems are defined as a system containing information from human in the form of rules (e.g., If-Then loops). Although it is simple and easily implementable, it is improper in the case of large or scalable systems. Moreover, the lack of flexibility and inability to adapt to changing environments reduces its applications [62].
- Knowledge-based systems are defined as human-centered systems. They attempt to understand and replicate human reactions through the training process. Then, knowledge-based systems use their learning when they encounter new situations. Knowledge-based system applications include after-the-fault analysis and power transmission protection [63].
- Object-oriented method combines one data object with a specific procedure. Rather than passing data to procedure, the program communicates by sending a message for an object to perform a procedure that is already embedded. It is heavily used in power capacity planning and power system maintenance [64].
- In case-based reasoning, different human experiences are recorded as cases. The system searches the storage with similar problem characteristics and finds the closest fit and applies it to the new ones.

Some of the implemented techniques in this area are artificial neural network (ANN) [65, 66], support vector machine (SVM) [67], genetic algorithm (GA) [7], fuzzy logic [68], and matching approach [69]. Each one of them has a different algorithm to monitor and protect the power grids.

5.7.1 ANN-Based Relays

ANN is one of the most prominent intelligent techniques used for power system monitoring and protection purposes. ANN shows a number of such qualities as mapping capacities, adaption of the internal failure, speculation, and fast data preparation [70]. ANN is essentially based on pattern recognition and training. The output decision is determined by comparison with the previous results during training procedure [71].

- *Transformer Protection with ANN*

In [72], the author has applied the Finite Impulse Response ANN (FIRANN), where it is used in a differential relay for protection of three-phase power transformers. Two different FIRANN were applied, where one was involved in determining the existence of the fault and the other one indicates whether the fault is inside the transformer. In [73], the authors have used ANN for detection of magnetization level in transformer cores. As the magnetic core saturation is directly related to the current harmonics, the method detects saturation through analysis of the current harmonics. In [74], an ANN-based algorithm is developed, which determines the transformer health investigating dissolved gases in the oil (e.g., hydrogen (H_2), methane (CH_4), ethene (C_2H_6), carbon monoxide (CO)), which are created from stresses on transformers such as internal sparking and

overheating. In [75], an ANN-based differential protection is designed, which is able to distinguish different events such as inrush currents, sympathetic inrush, and overexcitation.

- *Generator Protection with ANN*

In [76], the authors have proposed an ANN-based detection and classification of winding faults in windmill generators. The authors have concluded that ANN-based algorithm provides higher accuracy at a small computation cost. In [77], an ANN-based method for detecting loss of excitation (LOE) in synchronous generators is proposed. The ability of generator protection in differentiating LOE and stable power swing is essential for enhancing the traditional LOE protection. The results clearly demonstrate that the ANN-based method has a promising performance compared to conventional generator protection relays.

- *Transmission Line Protection with ANN*

Another prominent application of ANN is the protection of TLs. In [72], an ANN-based method for the protection of TLs is developed. As power systems are integrated and complex, the ANN is trained with 100,000 patterns. Therefore, for more complex systems, training the ANN algorithm can be quite time-consuming if it is even technically possible. In [78], the researchers have established an ANN-based system with 99.91% fault classification accuracy. Although the established system provides greater success in fault classification, it lacks the capability of fault location in the system. In [79], the authors have presented a novel filter premised on ANN for fault detection, classification, and location. The results show that the accuracy is almost 96%. Another point of strength of ANN-based systems is its fast response time. In [80], the authors have proposed an ANN-based ultrafast fault detection system that has satisfactory classification accuracy with one-eighth of a cycle of post-event data. In [81], the authors have established an ANN-based protection system for STATCOM compensated TLs where detection, classification, and location of the fault are done in a quarter cycle (4 ms in case of 60 Hz system), which is suitable for IBR-based systems.

- *Detection of High Impedance Faults with ANN*

Another application of ANN is to detect high impedance faults (HIFs) in distribution systems with IBRs [82]. This is due to the fact that HIFs are difficult to be monitored using traditional digital relaying as their current is too low to detect and, in some cases, the fault current is only available during a short time duration. In [82], the input data are local current and voltage. The features of HIFs then will be detected by the proposed method, and it not only finds an HIF fault, but it also finds the location of the HIF in IBR-based grids.

- *ANN for Cybersecurity*

Another aspect of ANN is its application in the cybersecurity of power systems. As modern power systems involve an abundant number of cyber resources, it is evident that cyberattacks may be planned to cripple down the system most treacherously by “data spoofing” (i.e., gaining control of the system in disguise of trusted people). For cyberattack detection, an ANN-based algorithm is proposed in that the algorithm shows more flexibility in detection of attacks when the system does not work pursuing prior assumptions [83]. In [84],

the author had compared the state-of-the-art techniques and inferred that through ANN, cyberattacks can be prevented in cyber-physical systems such as smart grid. Moreover, along with the data spoofing, false data injection is also seen as a major threat in cyber protection, which ANN is able to detect them. The authors of [85] proposed an ANN-based algorithm that detects 92–99.5% of false injected data, and consequently, the protection system has a minimum number of false alarms. The ANN-based algorithm demonstrates stronger robustness than multiple nonlinear regression (MNR) for wind power forecasting against false data injection attacks [86]. Another application of ANN is to detect the reason for a reported event in the system whether it has a real source such as faults or it is initiated only based on communications failure or data attacks. This is critical especially when the event has a short duration and long-window filters and detectors are not able to detect that or wrongly classify that as a noise [87, 88].

- *Disadvantages of ANN*

Although ANN involves a vast area of power system application, it brings up some points of concern such as the need for a large training set, the issue of obtaining a stable solution, as well as the danger of overfitting [59]. Therefore, other AI algorithms have been established such as SVM and fuzzy logic. Their application in power system protection will be described in the next parts.

5.7.2 Relays Based on SVM

The disadvantages of ANN created serious concerns on power system protection and monitoring. Another approach is SVM. Similar to ANN, SVM also has been applied to different protection purposes. For those purposes, SVM-based techniques have played a key role and established themselves promising in power system protection. In SVM, a generalized model is created for a certain purpose via analysis of a certain dataset. Then, parts of the dataset are divided by planes defined as hyperplanes. Additional planes are created as the margins for the prime hyperplane. The marginal planes are established with respect to the nearest data or dataset available in the plane. These data or datasets are known as support vectors. By this, a generalized model is founded. Then SVM classifies new data which will be in one of the datasets [89]. SVM mainly has wide applications in classification and event detection.

- *SVM for Transformer Protection*

Similar to ANN-based systems, SVM-based techniques are also applied to transformer protection. In [90], an SVM-based fault classification is proposed for transformers. It is capable of classifying in-zone and out-of-the-zone faults more reliably compared to ANN-based algorithms. In [91], an SVM-based protection technique is proposed. It monitors magnetization hysteresis loop by voltage-differential current (V-DCurr) curves. It pinpoints faults by detection of changes in the hysteresis loop trajectory. The algorithm achieves a success rate greater than 98%. In [92], SVM is exploited to discriminate if the differential current (ΔI) is caused by CT saturation or internal faults.

- *Generator Protection Using SVM*

SVM-based techniques are also employed for generator protection. In [93], the authors have proposed SVM-based techniques for identification of generator LOE. In this technique, the SVM-based method is able to identify the LOE condition moderately fast before the power-flow direction changes. In [94], the LOE detection is advanced to a degree that the relay using SVM-based logic is able to differentiate total and partial LOE in synchronous generators. In [95], an SVM-based fault detection and classification technique is proposed that detects small spikes in the stator winding of synchronous generators, which the conventional generator relays are unable to find.

- *Transmission Line Protection with SVM*

Protection of TLs is also an important task for the SVM-based techniques. In [96], the authors used SVM for fault location, and their comparative study finds that SVM-based techniques are superior to ANN-based ones in this regard. In [97], the researchers have established an SVM-based protection algorithm for a multi-terminal high-voltage direct current (MT-HVDC) system. This protection algorithm has been able to identify, classify, and locate the fault within 0.15 ms, ensuring speedy DC grid protection. In [98], the authors proposed an effective method for fault location in TLs that use the fundamental components of voltages and currents of the faulty phases for fault detection and location. In [99], the researchers have used the radial basis function (RBF) neural network and SVM to identify the fault. This method utilizes three-phase voltage measurements, but it does not require current measurements. The authors of [100] used SVM as an intelligent tool to discriminate between different zonal faults in TLs in that apparent impedance values are collected from distance relay under different fault conditions. Then, after SVM gets trained, SVM is able to identify different faults along the TL. In [101], SVM is employed for fault classification in a series compensated TL with a fixed capacitor, which is placed at the center of the line. The method is able to successfully detect and locate the faults even during line energization.

- *SVM for Cybersecurity*

SVM-based methods are also beneficial to power system cybersecurity. In the twenty-first century, the reliability of the power systems largely depends on cyber protection. In [102], the authors have proposed an SVM-based malicious data detection and classification method. The results prove that the method is successfully able to classify intrusion data. Thus, cybersecurity of power grids can be improved using SVM. In [103], the authors have proposed a cyber intrusion protection system in that SVM is used for detecting suspicious behaviors of smart meters. In [104], SVM is utilized for dynamic security assessment of grids in which the changes of phase angles throughout the system are monitored and suspicious deviations are detected.

- *Disadvantages of SVM*

Although SVM demonstrated a great rate of success in event classification, there are some specific drawbacks in the application of SVM. For example, there are concerns about SVM real-time function since it is computationally expensive and needs large volumes of reliable memory in industrial and noisy environments. In addition, the training process is slower compared to ANN [105].

5.7.3 Fuzzy Logic

Fuzzy logic is an approach to evaluating the degree of situation/incident/problem, in contrast to the Boolean logic which defines the case as a whole true/false. For example, a fault in a TL can be defined for computers by 0 as no fault and 1 as fault. But in fuzzy logic, the fault might be a range within 0–1 by defining 0.2 as a mild fault, 0.4 general fault, 0.6 strong fault, and 0.9 as an extreme fault. By this, a new algorithm can be set to train the situation for a qualitative assessment of power system apparatus. Fuzzy logic can be used similar to ANN and SVM. However, it is capable of protecting power systems based on the severity of the fault. For example, an SLG fault in a non-grounded system sensitive to power disconnection can be postponed until a proper time, but an LL fault should be addressed almost without any delay. In [106], a fuzzy logic algorithm is introduced for recognizing inrush currents in transformers. A fuzzy logic-based method for turn-to-turn faults is devised in [107]. In [107], a novel method is proposed based on fuzzy logic for synchronous generator protection in which the fuzzy logic-based method is designed for fault identification and detection with high sensitivity. But the high sensitivity is not going to reduce the selectivity of the system in case of minor faults. In [108], a fuzzy logic-based fault detection algorithm is developed for series compensated TLs. The algorithm was extensively tested with a wide range of operating conditions. The results demonstrate its effectiveness and robustness against various FIAs, load angles, and source impedance. In [109], faults in double line TLs are successfully detected and located with the use of fuzzy logic. The results show strong evidence that the system is fast and reliable in detection of faults at different locations along the TL. Regardless of fuzzy logic advantages, it has the major problem of determining global extremums.

5.8 Conclusion

Digital transition of electric grids includes all the major sections of electricity delivery systems. Throughout this chapter, first, the fundamentals of protection were covered, and then the issues arising from the connection of inverter-based resources (IBRs) were explained. Some of the methods for overcoming the protection issues were discussed as well. In addition, the new measuring devices vary from

the conventional ones. Therefore, some new methods should be devised for making the outputs of the new measuring devices compatible with the well-developed and in-use monitoring systems.

The main conclusions of this chapter can be summarized as follows: as the fault response of IBRs differs from conventional electromechanical generators, currently in-use relays are often unable to detect the faults, or they cannot disconnect the faulty section selectively. Thus, the development of new protective devices (relays) and coordination techniques is indispensable for the integration of IBRs to the grids in large quantities. Additionally, artificial intelligence may assist the development of protection and monitoring; however, the results are not based on definite and closed mathematics, and more certain answers are expected for their application in power system protection.

References

1. Mahmood A, Javaid N, Razzaq S (2015) A review of wireless communications for smart grid. *Renew Sust Energ Rev* 41:248–260. <https://doi.org/10.1016/j.rser.2014.08.036>
2. Gao J et al (2018) Grid monitoring: secured sovereign blockchain based monitoring on smart grid. *IEEE Access* 6:9917–9925. <https://doi.org/10.1109/ACCESS.2018.2806303>
3. Alagoz BB, Kaygusuz A, Karabiber A (2012) A user-mode distributed energy management architecture for smart grid applications. *Energy* 44(1):167–177. <https://doi.org/10.1016/j.energy.2012.06.051>
4. Ci S, Lin N, Zhou Y, Li H, Yang Y. A new digital power supply system for Fog and Edge computing. In: 2018 14th International Wireless Communications & Mobile Computing Conference (IWCMC), 25–29 June 2018, pp 1513–1517. <https://doi.org/10.1109/IWCMC.2018.8450497>
5. Manohar M, Koley E, Ghosh S (2018) Microgrid protection under wind speed intermittency using extreme learning machine. *Comput Electr Eng* 72:369–382. <https://doi.org/10.1016/j.compeleceng.2018.10.005>
6. Rehmani MH, Reisslein M, Rachedi A, Erol-Kantarci M, Radenkovic M (2018) Integrating renewable energy resources into the smart grid: recent developments in information and communication technologies. *IEEE Trans Ind Inf* 14(7):2814–2825. <https://doi.org/10.1109/TII.2018.2819169>
7. Jalilzadeh Hamidi R, Ahmadian A, Patil R, Asadinejad A (2019) Optimal time-current graded coordination of multistage inverse-time overcurrent relays in distribution networks. *Int Trans Electr Energy Syst* 29(5):e2841. <https://doi.org/10.1002/2050-7038.2841>
8. Hamidi RJ, Livani H (2019) A recursive method for traveling-wave arrival-time detection in power systems. *IEEE Trans Power Delivery* 34(2):710–719. <https://doi.org/10.1109/TPWRD.2018.2877705>
9. Department of Energy's Advanced Grid Research and Development. https://www.smartgrid.gov/adms_research_and_development (accessed)
10. Li C, Rakhra P, Norman P, Niewczas P, Burt G, Clarkson P (2020) Modulated low fault-energy protection scheme for DC smart grids. *IEEE Trans Smart Grid* 11(1):84–94. <https://doi.org/10.1109/TSG.2019.2917540>
11. Rahman Fahim S, Sarker SK, Muyeen SM, Sheikh MRI, Das SK (2020) Microgrid fault detection and classification: machine learning based approach, comparison, and reviews. *Energies* 13(13):3460. [Online]. Available: <https://www.mdpi.com/1996-1073/13/13/3460>

12. Lotffard S, Faiz J, Kezunovic M (2012) Over-current relay implementation assuring fast and secure operation in transient conditions. *Electr Power Syst Res* 91:1–8. <https://doi.org/10.1016/j.epr.2012.02.001>
13. Yousaf M, Muttaqi KM, Sutanto D (2021) A control strategy to mitigate the sensitivity deterioration of overcurrent protection in distribution networks with the higher concentration of the synchronous and inverter-based DG units. *IEEE Trans Ind Appl* 57(3):2298–2306. <https://doi.org/10.1109/TIA.2021.3057304>
14. Pandya HS, Pandeji DM, Iyer RK, Purohit PM. Digital protection strategy of microgrid with relay time grading using particle swarm optimization. In: 2015 5th Nirma University International Conference on Engineering (NUICONE), 26–28 Nov 2015, pp 1–6. <https://doi.org/10.1109/NUICONE.2015.7449612>
15. Guo L, Ye C, Ding Y, Wang P (2021) Allocation of centrally switched fault current limiters enabled by 5G in transmission system. *IEEE Trans Power Delivery* 36(5):3231–3241. <https://doi.org/10.1109/TPWRD.2020.3037193>
16. Nikolaidis VC, Tsimtsios AM, Safigianni AS (2018) Investigating particularities of infeed and fault resistance effect on distance relays protecting radial distribution feeders with DG. *IEEE Access* 6:11301–11312. <https://doi.org/10.1109/ACCESS.2018.2804046>
17. Biswas S, Centeno V. A communication based infeed correction method for distance protection in distribution systems. In: 2017 North American Power Symposium (NAPS), 17–19 Sept 2017, pp 1–5. <https://doi.org/10.1109/NAPS.2017.8107226>
18. Usama M et al (2021) A comprehensive review on protection strategies to mitigate the impact of renewable energy sources on interconnected distribution networks. *IEEE Access* 9:35740–35765. <https://doi.org/10.1109/ACCESS.2021.3061919>
19. IEEE standard for interconnection and interoperability of distributed energy resources with associated electric power systems interfaces – Redline. In: *IEEE Std 1547-2018 (Revision of IEEE Std 1547-2003)* – Redline, 2018, pp 1–227
20. IEEE application guide for IEEE Std 1547(TM), IEEE standard for interconnecting distributed resources with electric power systems. In: *IEEE Std 1547.2-2008, 2009*, pp 1–217. <https://doi.org/10.1109/IEEESTD.2008.4816078>
21. Makwana YM, Bhalja BR (2019) Experimental performance of an islanding detection scheme based on modal components. *IEEE Trans Smart Grid* 10(1):1025–1035. <https://doi.org/10.1109/TSG.2017.2757599>
22. Reddy CR, Goud BS, Reddy BN, Pratyusha M, Kumar CVV, Rekha R. Review of islanding detection parameters in smart grids. In: 2020 8th International Conference on Smart Grid (icSmartGrid), 17–19 June 2020, pp 78–89. <https://doi.org/10.1109/icSmartGrid49881.2020.9144923>
23. Fischer N. Protection of inverter-based resources. Energy Systems Integration Group. <https://www.esig.energy/protection-of-inverter-based-resources/>. Accessed 31 Dec 2021
24. Nagpal M, Jensen M, Higginson M (2020) Protection challenges and practices for interconnecting inverter based resources to utility transmission systems. In: *Impact of inverter based resources on utility transmission system protection*. IEEE Power & Energy Society, USA
25. Kobet G, Pourbeik P (2019) Impact of inverter based generation on bulk power system dynamics and short-circuit performance. IEEE PES Resource Center
26. Keller J, Kroposki B (2010) Understanding fault characteristics of inverter-based distributed energy resources. National Renewable Energy Laboratory, USA
27. Khan MAU, Hong Q, Dyško A, Booth C, Wang B, Dong X. Evaluation of fault characteristic in microgrids dominated by inverter-based distributed generators with different control strategies. In: 2019 IEEE 8th International Conference on Advanced Power System Automation and Protection (APAP), 21–24 Oct 2019, pp 846–849. <https://doi.org/10.1109/APAP47170.2019.9224706>

28. Ravvys S, Broeck GVD, Hallemans L, Vecchia MD, Driesen J (2020) Fuse-based short-circuit protection of converter controlled low-voltage DC grids. *IEEE Trans Power Electron* 35(11): 11694–11706. <https://doi.org/10.1109/TPEL.2020.2988087>
29. Shuai Z, Shen C, Yin X, Liu X, Shen ZJ (2018) Fault analysis of inverter-interfaced distributed generators with different control schemes. *IEEE Trans Power Delivery* 33(3):1223–1235. <https://doi.org/10.1109/TPWRD.2017.2717388>
30. IEEE standard conformance test procedures for equipment interconnecting distributed energy resources with electric power systems and associated interfaces. In: *IEEE Std 1547.1-2020*, pp 1–282, 2020. <https://doi.org/10.1109/IEEESTD.2020.9097534>
31. Castilla M, Miret J, Camacho A, Matas J, Vicuna LG d (2013) Reduction of current harmonic distortion in three-phase grid-connected photovoltaic inverters via resonant current control. *IEEE Trans Ind Electron* 60(4):1464–1472. <https://doi.org/10.1109/TIE.2011.2167734>
32. Han H, Hou X, Yang J, Wu J, Su M, Guerrero JM (2016) Review of power sharing control strategies for islanding operation of AC microgrids. *IEEE Trans Smart Grid* 7(1):200–215. <https://doi.org/10.1109/TSG.2015.2434849>
33. Kelly D, Mysore P, Mohan N. A novel control scheme for utility-scale inverter-based resources to emulate synchronous generator fault response and retain existing protection infrastructure. In: *2021 74th Conference for Protective Relay Engineers (CPRE)*, 22–25 Mar 2021, pp 1–7. <https://doi.org/10.1109/CPRE48231.2021.9429836>
34. Banaieymoqadam A, Hooshyar A, Azzouz MA (2021) A comprehensive dual current control scheme for inverter-based resources to enable correct operation of protective relays. *IEEE Trans Power Delivery* 36(5):2715–2729. <https://doi.org/10.1109/TPWRD.2020.3025878>
35. Soleimanisardoo A, Karegar HK, Zeineldin HH (2019) Differential frequency protection scheme based on off-nominal frequency injections for inverter-based islanded microgrids. *IEEE Trans Smart Grid* 10(2):2107–2114. <https://doi.org/10.1109/TSG.2017.2788851>
36. Khan MAU, Hong Q, Dyško A, Booth C. An active protection scheme For islanded microgrids. In: *15th International conference on developments in power system protection (DPSP 2020)*, 9–12 Mar 2020, pp 1–6. <https://doi.org/10.1049/cp.2020.0020>
37. Hamidi RJ, Livani H, Rezaiesarlak R (2017) Traveling-wave detection technique using short-time matrix pencil method. *IEEE Trans Power Delivery* 32(6):2565–2574. <https://doi.org/10.1109/TPWRD.2017.2685360>
38. Wei S, Yanfeng G, Yan L. Traveling-wave-based fault location algorithm for star-connected hybrid multi-terminal HVDC system. In: *2017 IEEE conference on energy internet and energy system integration (EI2)*, 26–28 Nov 2017, pp 1–5. <https://doi.org/10.1109/EI2.2017.8245645>
39. Hamidi RJ, Livani H. A travelling wave-based fault location method for hybrid three-terminal circuits. In: *2015 IEEE Power & Energy Society general meeting*, 26–30 July 2015, pp 1–5. <https://doi.org/10.1109/PESGM.2015.7286247>
40. Lee JW, Kim WK, Han J, Jang WH, Kim CH (2016) Fault area estimation using traveling wave for wide area protection. *J Mod Power Syst Clean Energy* 4(3):478–486. <https://doi.org/10.1007/s40565-016-0222-7>
41. Selinc. “SEL-T400L”. <https://selinc.com/products/T400L/> (accessed)
42. He J, Liu L, Li W, Zhang M (2016) Development and research on integrated protection system based on redundant information analysis. *Prot Control Mod Power Syst* 1(1):13. <https://doi.org/10.1186/s41601-016-0024-y>
43. Jurišić G, Havelka J, Capuder T, Sučić S (2018) Laboratory test bed for analyzing fault-detection reaction times of protection relays in different substation topologies. *Energies* 11(9): 2482. [Online]. Available: <https://www.mdpi.com/1996-1073/11/9/2482>
44. Hamidi RJ, Khodabandehlou H, Livani H, Fadali MS. Application of distributed compressive sensing to power system state estimation. In: *2015 North American Power Symposium (NAPS)*, 4–6 Oct 2015, pp 1–6. <https://doi.org/10.1109/NAPS.2015.7335114>
45. Hamidi RJ, Khodabandehlou H, Livani H, Sami-Fadali M. Hybrid state estimation using distributed compressive sensing. In: *2016 IEEE Power and Energy Society General Meeting (PESGM)*, 17–21 July 2016, pp 1–5. <https://doi.org/10.1109/PESGM.2016.7742038>

46. Abur A, Gómez Expósito A (2004) Power system state estimation theory and implementation, 1st edn. Taylor & Francis Group, Boca Raton, FL, p 327
47. Wen J, Liu WHE, Arons PL, Pandey SK (2014) Evolution pathway towards wide area monitoring and protection—a real-world implementation of centralized RAS system. *IEEE Trans Smart Grid* 5(3):1506–1513. <https://doi.org/10.1109/TSG.2013.2278660>
48. Eissa MM (2019) A novel centralized wide area protection “CWAP” in phase portrait based on pilot wire including phase comparison. *IEEE Trans Smart Grid* 10(3):2671–2682. <https://doi.org/10.1109/TSG.2018.2808207>
49. Ivanković I, Kuzle I, Holjevac N (2017) Wide area information-based transmission system centralized out-of-step protection scheme. *Energies* 10(5):633. [Online]. Available: <https://www.mdpi.com/1996-1073/10/5/633>
50. W. G. C-6. Wide area protection and emergency control. IEEE Power Engineering Society, USA
51. Carrasco JM et al (2006) Power-electronic systems for the grid integration of renewable energy sources: a survey. *IEEE Trans Ind Electron* 53(4):1002–1016. <https://doi.org/10.1109/TIE.2006.878356>
52. Blaabjerg F, Teodorescu R, Liserre M, Timbus AV (2006) Overview of control and grid synchronization for distributed power generation systems. *IEEE Trans Ind Electron* 53(5):1398–1409. <https://doi.org/10.1109/TIE.2006.881997>
53. Atzori L, Iera A, Morabito G (2010) The internet of things: a survey. *Comput Netw* 54(15):2787–2805. <https://doi.org/10.1016/j.comnet.2010.05.010>
54. Liao W, Salinas S, Li M, Li P, Loparo KA (2017) Cascading failure attacks in the power system: a stochastic game perspective. *IEEE Internet Things J* 4(6):2247–2259. <https://doi.org/10.1109/JIOT.2017.2761353>
55. Santos D, Ferreira JC (2019) IoT power monitoring system for smart environments. *Sustainability* 11(19):5355. [Online]. Available: <https://www.mdpi.com/2071-1050/11/19/5355>
56. Lee I, Lee K (2015) The internet of things (IoT): applications, investments, and challenges for enterprises. *Bus Horiz* 58(4):431–440. <https://doi.org/10.1016/j.bushor.2015.03.008>
57. Srivastava D, Tripathi MM. Transformer health monitoring system using internet of things. In: 2018 2nd IEEE international conference on power electronics, intelligent control and energy systems (ICPEICES), 22–24 Oct 2018, pp 903–908. <https://doi.org/10.1109/ICPEICES.2018.8897325>
58. Jamal H, Khan MFN, Anjum A, Janjua MK. Thermal monitoring and protection for distribution transformer under residential loading using internet of things. In: 2018 IEEE global conference on internet of things (GCIoT), 5–7 Dec 2018, pp 1–6. <https://doi.org/10.1109/GCIoT.2018.8620135>
59. Bhattarai BP et al (2019) Big data analytics in smart grids: state-of-the-art, challenges, opportunities, and future directions. *IET Smart Grid* 2(2):141–154. <https://doi.org/10.1049/iet-stg.2018.0261>
60. Koranne S (2011) Artificial intelligence and optimization. In: *Handbook of open source tools*. Springer, Boston, MA, pp 391–392. ch. 18
61. Gururajapathy SS, Mokhlis H, Illias HA (2017) Fault location and detection techniques in power distribution systems with distributed generation: a review. *Renew Sust Energy Rev* 74:949–958. <https://doi.org/10.1016/j.rser.2017.03.021>
62. Grosan C, Abraham A (2011) Rule-based expert systems. Springer, Berlin
63. Orduna E, Garces F, Handschin E (2003) Algorithmic-knowledge-based adaptive coordination in transmission protection. *IEEE Trans Power Delivery* 18(1):61–65. <https://doi.org/10.1109/TPWRD.2002.806683>
64. Kawahara K, Sasaki H, Kubokawa J, Asahara H, Sugiyama K (1998) A proposal of a supporting expert system for outage planning of electric power facilities retaining high power supply reliability. *IEEE Trans Power Syst* 13(4):1453–1458. <https://doi.org/10.1109/59.736289>

65. Bahmanyar AR, Karami A (2014) Power system voltage stability monitoring using artificial neural networks with a reduced set of inputs. *Int J Electr Power Energy Syst* 58:246–256. <https://doi.org/10.1016/j.ijepes.2014.01.019>
66. Siddiqui SA, Verma K, Niazi KR, Fozdar M (2018) Real-time monitoring of post-fault scenario for determining generator coherency and transient stability through ANN. *IEEE Trans Ind Appl* 54(1):685–692. <https://doi.org/10.1109/TIA.2017.2753176>
67. Yang Z, Zhou Q, Wu X, Zhao Z (2019) A novel measuring method of interfacial tension of transformer oil combined PSO optimized SVM and multi frequency ultrasonic technology. *IEEE Access* 7:182624–182631. <https://doi.org/10.1109/ACCESS.2019.2954899>
68. Zhang S, Mishra Y, Shahidehpour M (2016) Fuzzy-logic based frequency controller for wind farms augmented with energy storage systems. *IEEE Trans Power Syst* 31(2):1595–1603. <https://doi.org/10.1109/TPWRS.2015.2432113>
69. Mokhlis H, Li H (2011) Non-linear representation of voltage sag profiles for fault location in distribution networks. *Int J Electr Power Energy Syst* 33(1):124–130. <https://doi.org/10.1016/j.ijepes.2010.06.020>
70. Prasad A, Belwin Edward J, Ravi K (2018) A review on fault classification methodologies in power transmission systems: part—I. *J Electr Syst Inf Technol* 5(1):48–60. <https://doi.org/10.1016/j.jesit.2017.01.004>
71. Silva INd, Spatti DH, Flauzino RA, Liboni LHB, Alves SFdR (2017) Artificial Neural network architectures and training processes. In: *Artificial neural networks*. Springer, Switzerland, pp 25–27. ch. 2
72. Orille-Fernandez AL, Ghonaim NKI, Valencia JA (2001) A FIRANN as a differential relay for three phase power transformer protection. *IEEE Trans Power Delivery* 16(2):215–218. <https://doi.org/10.1109/61.915485>
73. Dezelak K, Pihler J, Stumberger G, Klopčič B, Dolinar D (2010) Artificial neural network applied for detection of magnetization level in the magnetic core of a welding transformer. *IEEE Trans Magn* 46(2):634–637. <https://doi.org/10.1109/TMAG.2009.2031976>
74. Ghoneim SSM, Taha IBM, Elkalashy NI (2016) Integrated ANN-based proactive fault diagnostic scheme for power transformers using dissolved gas analysis. *IEEE Trans Dielectr Electr Insul* 23(3):1838–1845. <https://doi.org/10.1109/TDEI.2016.005301>
75. Silva AF, Silveira EG, Alipio R (2021) Artificial neural network applied to differential protection of power transformers. *J Control Autom Electr Syst*. <https://doi.org/10.1007/s40313-021-00845-3>
76. Gketsis ZE, Zervakis ME, Stavrakakis G (2009) Detection and classification of winding faults in windmill generators using wavelet transform and ANN. *Electr Power Syst Res* 79(11): 1483–1494. <https://doi.org/10.1016/j.epsr.2009.05.001>
77. Barakat ZA, Hajjar AA, Kherbek T, Alhelou HH (2019) Discriminating between loss of excitation and power swings in synchronous generator based on ANN. *J Control Autom Electr Syst* 4:545–556
78. Upendar J, Gupta CP, Singh GK, Ramakrishna G (2010) PSO and ANN-based fault classification for protective relaying. *IET Gener Transm Distrib* 4(10):1197–1212. <https://doi.org/10.1049/iet-gtd.2009.0488>
79. Fathabadi H (2016) Novel filter based ANN approach for short-circuit faults detection, classification and location in power transmission lines. *Int J Electr Power Energy Syst* 74: 374–383. <https://doi.org/10.1016/j.ijepes.2015.08.005>
80. Abdullah A (2018) Ultrafast transmission line fault detection using a DWT-based ANN. *IEEE Trans Ind Appl* 54(2):1182–1193. <https://doi.org/10.1109/TIA.2017.2774202>
81. Rathore B, Mahela OP, Khan B, Alhelou HH, Siano P (2021) Wavelet-alienation-neural-based protection scheme for STATCOM compensated transmission line. *IEEE Trans Industr Inform* 17(4):2557–2565. <https://doi.org/10.1109/TII.2020.3001063>
82. Bretas AS, Pires L, Moreto M, Salim RH (2010) A BP neural network based technique for HIF detection and location on distribution systems with distributed generation. In: *Computational intelligence*. Springer, Berlin

83. Kalech M (2019) Cyber-attack detection in SCADA systems using temporal pattern recognition techniques. *Comput Secur* 84:225–238. <https://doi.org/10.1016/j.cose.2019.03.007>
84. Ali SS, Choi BJ (2020) State-of-the-art artificial intelligence techniques for distributed smart grids: a review. *Electronics* 9(6):1030. [Online]. Available: <https://www.mdpi.com/2079-9292/9/6/1030>
85. Mousavian S, Valenzuela J, Wang J (2013) Real-time data reassurance in electrical power systems based on artificial neural networks. *Electr Power Syst Res* 96:285–295. <https://doi.org/10.1016/j.epsr.2012.11.015>
86. Zhang Y, Lin F, Wang K (2020) Robustness of short-term wind power forecasting against false data injection attacks. *Energies* 13(15):3780. [Online]. Available: <https://www.mdpi.com/1996-1073/13/15/3780>
87. Khoshdeli M, Niazazari I, Hamidi RJ, Livani H, Parvin B. Electromagnetic transient events (EMTE) classification in transmission grids. In: 2017 IEEE Power & Energy Society General Meeting, 16–20 July 2017, pp 1–5. <https://doi.org/10.1109/PESGM.2017.8273984>
88. Niazazari I, Jalilzadeh Hamidi R, Livani H, Arghandeh R (2020) Cause identification of electromagnetic transient events using spatiotemporal feature learning. *Int J Electr Power Energy Syst* 123:106255. <https://doi.org/10.1016/j.ijepes.2020.106255>
89. Pisner DA, Schnyer DM (2020) Support vector machine. In: *Machine learning methods and applications to brain disorders*. Elsevier, London, pp 101–121. ch. 6
90. Bigdeli M, Vakilian M, Rahimpour E (2012) Transformer winding faults classification based on transfer function analysis by support vector machine. *IET Electr Power Appl* 6(5):268–276. [Online]. Available: <https://digital-library.theiet.org/content/journals/10.1049/iet-epa.2011.0232>
91. Jiao Z, Li Z (2018) Novel magnetization hysteresis-based power-transformer protection algorithm. *IEEE Trans Power Delivery* 33(5):2562–2570. <https://doi.org/10.1109/TPWRD.2018.2837022>
92. Simões LD, Costa HJD, Aires MNO, Medeiros RP, Costa FB, Bretas AS (2021) A power transformer differential protection based on support vector machine and wavelet transform. *Electr Power Syst Res* 197:107297. <https://doi.org/10.1016/j.epsr.2021.107297>
93. Pajuelo E, Gokaraju R, Sachdev MS (2013) Identification of generator loss-of-excitation from power-swing conditions using a fast pattern classification method. *IET Gener Transm Distrib* 7(1):24–36. [Online]. Available: <https://digital-library.theiet.org/content/journals/10.1049/iet-gtd.2012.0340>
94. Rasoulpour M, Amraee T, Sedigh AK (2020) A relay logic for total and partial loss of excitation protection in synchronous generators. *IEEE Trans Power Delivery* 35(3):1432–1442. <https://doi.org/10.1109/TPWRD.2019.2945259>
95. El-Saadawi M, Hatata A (2017) A novel protection scheme for synchronous generator stator windings based on SVM. *Prot Control Mod Power Syst* 2(1):24. <https://doi.org/10.1186/s41601-017-0057-x>
96. Jaya Bharata Reddy M, Gopakumar P, Mohanta DK (2016) A novel transmission line protection using DOST and SVM. *Eng Sci Technol Int J* 19(2):1027–1039. <https://doi.org/10.1016/j.jestch.2015.12.011>
97. Muzzammel R, Raza A (2020) A support vector machine learning-based protection technique for MT-HVDC systems. *Energies* 13(24):6668. [Online]. Available: <https://www.mdpi.com/1996-1073/13/24/6668>
98. Salat R, Osowski S (2004) Accurate fault location in the power transmission line using support vector machine approach. *IEEE Trans Power Syst* 19(2):979–986. <https://doi.org/10.1109/TPWRS.2004.825883>
99. Janik P, Lobos T (2006) Automated classification of power-quality disturbances using SVM and RBF networks. *IEEE Trans Power Delivery* 21(3):1663–1669. <https://doi.org/10.1109/TPWRD.2006.874114>

100. Ravikumar B, Thukaram D, Khincha HP (2008) Knowledge-based approach using support vector machine for transmission line distance relay co-ordination. *J Electr Eng Technol* 3(3): 363–372. <https://doi.org/10.5370/JEET.2008.3.3.363>
101. Parikh UB, Das B, Maheshwari R (2010) Fault classification technique for series compensated transmission line using support vector machine. *Int J Electr Power Energy Syst* 32(6): 629–636. <https://doi.org/10.1016/j.ijepes.2009.11.020>
102. Zhang Y, Wang L, Sun W, Green IRC, Alam M (2011) Distributed intrusion detection system in a multi-layer network architecture of smart grids. *IEEE Trans Smart Grid* 2(4):796–808. <https://doi.org/10.1109/TSG.2011.2159818>
103. Sun CC, Cardenas DJS, Hahn A, Liu CC (2021) Intrusion detection for cybersecurity of smart meters. *IEEE Trans Smart Grid* 12(1):612–622. <https://doi.org/10.1109/TSG.2020.3010230>
104. Rizwan ul H, Li C, Liu Y (2021) Online dynamic security assessment of wind integrated power system using SDAE with SVM ensemble boosting learner. *Int J Electr Power Energy Syst* 125:106429. <https://doi.org/10.1016/j.ijepes.2020.106429>
105. Drucker H, Donghui W, Vapnik VN (1999) Support vector machines for spam categorization. *IEEE Trans Neural Netw* 10(5):1048–1054. <https://doi.org/10.1109/72.788645>
106. Bejmert D, Rebizant W, Schiel L (2014) Transformer differential protection with fuzzy logic based inrush stabilization. *Int J Electr Power Energy Syst* 63:51–63. <https://doi.org/10.1016/j.ijepes.2014.05.056>
107. Granados-Lieberman D, Razo-Hernandez JR, Venegas-Rebollar V, Olivares-Galvan JC, Valtierra-Rodriguez M (2021) Harmonic PMU and fuzzy logic for online detection of short-circuited turns in transformers. *Electr Power Syst Res* 190:106862. <https://doi.org/10.1016/j.epsr.2020.106862>
108. Eristi H (2013) Fault diagnosis system for series compensated transmission line based on wavelet transform and adaptive neuro-fuzzy inference system. *Measurement* 46(1):393–401. <https://doi.org/10.1016/j.measurement.2012.07.014>
109. Goli RK, Gafoor Shaik A, Tulasi Ram SS (2015) A transient current based double line transmission system protection using fuzzy-wavelet approach in the presence of UPFC. *Int J Electr Power Energy Syst* 70:91–98. <https://doi.org/10.1016/j.ijepes.2015.01.024>

Chapter 6

Optimizing Wind Power Participation in Day-Ahead Electricity Market Using Meta-heuristic Optimization Algorithms



Hamed Dehghani and Behrooz Vahidi

Abstract Recently, use of wind generation due to its clean and cheap power has been considerably increased. The presence of wind sources in power systems brings several challenges for the operators. They have difficulties to make suitable decisions for electricity market, due to uncertain nature of wind power. In this chapter, a new objective function considering wind power uncertainty is proposed to minimize total expected costs. To do so, a new procedure is presented to quantify probability density function (PDF) of each uncertainty interval based on wind power plant's information. Considering the derived PDF, the objective function is formed and optimized by using meta-heuristic optimization algorithms. The results reveal a reduction in total expected cost has up to 20%.

Keywords Electricity market · Day-ahead market · Social welfare · Spot market · Wind power · Uncertainty · Locational marginal price · Cost function · Optimal bidding · TLBO · PSO-GSA · ALO · Normal distribution function · Weibull distribution function · Prediction intervals

6.1 Introduction

Nowadays, renewable energy source (RES) penetration in power systems has been considerably increased. RESs are taken into account by many researchers as a unique solution for global warming and energy security [26, 33, 39, 40].

Because of technical advantages in conversion systems of wind energy, they are significantly used in power systems in comparison with other RESs, such as photovoltaics (PVs). Moreover, in large scales, wind energy resources occupy less area. These advantages can be very useful, especially in electricity market applications [31, 44]. One of the main challenges in power systems is the uncertainty of the wind power. Several stochastic approaches have been presented by Reddy et al. [37], to

H. Dehghani · B. Vahidi (✉)

Department of Electrical Engineering, Amirkabir University of Technology (Tehran Polytechnic), Tehran, Iran

e-mail: hamed.dehghani@aut.ac.ir; vahidi@aut.ac.ir

handle the uncertainties in renewable energy sources. In [1], a new probabilistic optimization approach has been proposed to analyze the effects of position and various control methods on prices of electricity market.

Most restructured power systems include two types of markets:

- Real-time market
- Day-ahead market

In a day-ahead market [13, 42], ISO takes the offer of all sellers and buyers and plans them so as to minimize the power generation costs (maximizing social welfare). The price of the day-ahead market is very low under high penetration level of wind power plant due to its almost zero marginal cost. However, its fluctuations can affect the day-ahead market and ancillary services. Imprecise wind power prediction leads to unwanted deviation between available and scheduled power. To guarantee secure operation of the system, ancillary reserve services should be provided in order to manage deviations, while very short-term unbalancing could occur in a real-time market.

Numerous researches have assessed the impacts of wind energy uncertainties in electricity markets. Flexible resources such as demand response programs and peaking units is one of the empirical solutions to cope with aforementioned challenges [2, 9].

The negative effects of uncertainty in wind power can be reduced by participating dispatchable distributed energy resources (DERs) in the electricity markets [18, 29, 30, 35, 43, 47, 49].

A new method based on information sharing is addressed by Exizidis et al. [14]. In this method, each participant anticipates its own power and shares the predicted power with each other in day-ahead market. In [6], the optimized amount of wind power in the electricity market is determined based on recorded data of wind speed considering uncertainties. The above approaches need a large amount of data and are time-consuming.

In [3, 20, 27, 45], evaluating the uncertainties' effects is carried out based on two probabilistic methods: ARIMA and Monte Carlo.

In [16, 28], demand response programs have been considered as the auxiliary resources. In [19], robust programming along with demand response programs has been used to minimize the cost of market in the presence of uncertainty in wind power. Optimal bidding strategy for wind power has been carried out in [5, 46], taking locational marginal price (LMP) mechanism and penalty factors into account.

Reddy et al. [36] present a market clearing mechanism considering the effects of uncertainties in loads and wind power. In [7, 17], wind power owners can cope with their uncertainties by participating in a bilateral energy and reserve markets. Wind power producers' (WPPs) participation in the electricity market as the price takers is studied in [8]. WPP participation in the day-ahead and real-time markets as the price makers is evaluated in [8, 44]. The results show that capacity of real-time market, demand elasticity, and RES special subsidies can facilitate the effective contribution of WPPs to the electricity market. On the other hand, to overcome the wind power producers' market power, a deviation penalty factor should be determined.

A bilevel game model (one-leader multi-follower) in a scenario-based market has been proposed to minimize operation cost and maximize social welfare [48].

According to this literature review, a great deal of attention has been drawn on minimizing the costs, considering wind power uncertainties by applying Monte Carlo-based methods or statistical models. These methods have two main disadvantages:

1. They do not consider uncertainty intervals in optimum point determining process.
2. They need a large amount of data and are time consuming.

In all of these methods, uncertainties create optimum intervals, causing system operator to face problem in making a definitive choice about the optimum point. In [11, 12], the effects of prediction intervals (PI) on the day-ahead electricity market price, profits, and losses have been investigated. The authors of the mentioned study have presented a new method to maximize social welfare via optimizing the wind power share in demand supply. However, the reserve market is not taken into account, and probability density function (PDF) of wind power is estimated with normal distribution function. In this chapter, a method is presented to calculate the optimum amount of wind power, considering uncertainty intervals with the goal of minimizing total expected cost. In other words, the method is a hybrid mathematical-heuristic one, which is offered in order to optimize the total expected costs [11, 12] of wind power and thermal plants during a day in a day-ahead electricity market.

The main contributions of this chapter can be concluded as follows:

1. Calculating wind power PDF based on a new approach for obtaining considering uncertainties intervals
2. Determining optimum amounts instead of optimum ranges throughout a day by presenting a new hybrid mathematical-heuristic method
3. Simultaneous participation in both real-time and reserve markets mechanisms
4. Using different model of meta-heuristic optimization algorithm and evaluating their performance in terms of minimizing the proposed objective function

The reminder of the chapter can be organized as follows.

The electricity market modelling and wind farm power uncertainty are presented in Sects. 6.2 and 6.3, respectively. In Sect. 6.4, the problem formulation is proposed. Simulations are carried out on a sample network in Sect. 6.5, and the results are evaluated. Finally, in Sects. 6.6 and 6.7, future works and conclusions are given.

6.2 Electricity Market Modeling

One of the most substantial ISO duties is the determining of market clearing price using the following objective function [4, 22]:

$$\min \left(\sum_{i=1}^n C_{Gi}(P) \right) \quad (6.1)$$

$$C_{Gi} = a.P^2 + b.P + c \quad (6.2)$$

where:

a, b, c : coefficients

$C_{Gi}(P)$: cost function of the generator

P : produced power

n : number of generators

The above equation is solved via DCOPF [15]. The optimization problem's constraints can be stated as:

1. *Net injected active power at bus i*

$$P_i - PD_i = I_i = \sum_{j=1}^n Y_{ij}(\theta_i - \theta_j) \quad j = 1, \dots, n \quad (6.3)$$

where:

P_i : generated power at i^{th} bus

PD_i : consumed power at i^{th} bus

I_i : net injected power at i^{th} bus

Y_{ij} : mutual admittance

θ_i : i^{th} bus angle

2. *Transmission lines thermal limit*

$$Y_{ij}(\theta_i - \theta_j) \leq P_{ij}^{\max} \quad j, i = 1, \dots, n \quad (6.4)$$

where:

P_{ij}^{\max} : maximum allowable active power.

3. *Generation units' capacity limit*

$$P_i^{\min} \leq P_i \leq P_i^{\max} \quad (6.5)$$

Lagrange function of the optimization problem is obtained based on the above constraints as follows:

$$\begin{aligned}
l = & \sum_{i=1}^n C(I_i) + \sum_{i=1}^n \pi_i \left[I_i - \sum_{j=1}^n Y_{ij}(\theta_i - \theta_j) \right] + \sum_{i=1}^n \\
& \times \sum_{j=1}^n \mu_{ij} \left[P_{ij}^{\max} - Y_{ij}(\theta_i - \theta_j) \right] \quad (6.6)
\end{aligned}$$

Optimal conditions are met by taking partial derivative from this function with respect to the variables. Therefore, the LMP of each bus can be calculated by taking the derivative from the Lagrangian function with respect to the net injected power of each bus as follows:

$$\frac{\partial l}{\partial I_i} = \frac{dC_i}{dI_i} - \pi_i = 0 \quad i = 1, \dots, n \quad (6.7)$$

where:

π_i : LMP for i^{th} bus

6.3 Calculation of Uncertainty in Wind Power

Wind power should be determined so that the LMPs can be calculated and the market be cleared by the ISO. Wind speed has to be predicted in order to calculate its power. The forecasting method suffers from uncertainties. However, they are of high accuracy. In this study, in order to simulate the aforementioned uncertainties, a method based on quantile regression is used [23]. Applying this method leads to a specific interval, $[V_l, V_u]$. It should be noted that, with a certain level of confidence, the exact wind speed will be in range of $[V_l, V_u]$. The wind power can be calculated by the following equations [34]:

$$\begin{aligned}
P_w &= 0 \text{ for } v < v_{\text{cut in}} \text{ or } v > v_{\text{cut out}} \\
P_w &= P_r \left(\frac{v - v_{\text{cut in}}}{v_r - v_{\text{cut in}}} \right) \text{ for } v_{\text{cut in}} \leq v \leq v_r \\
P_w &= P_r \text{ for } v_r \leq v \leq v_{\text{cut out}} \quad (6.8)
\end{aligned}$$

where:

P_r : rated power

v_r : nominal wind speed of related turbine

By using Eq. (6.8) and resulted range for wind speed, $[V_l, V_u]$, wind power will be in the range of $[P_l, P_u]$.

The wind power PDF is needed to implement the uncertainties. Weibull distribution function has been introduced by many researchers in order to assign wind speed variations. This function is stated as:

$$f_V(v) = \left(\frac{k}{c}\right) \left(\frac{v}{c}\right)^{(k-1)} (e)^{-\left(\frac{v}{c}\right)^k} \tag{6.9}$$

where:

c : scale

k : shape factors

Wind power's PDF can be provided considering Eqs. (6.8) and (6.9) as:

$$P = g(v) = \alpha v + \beta \quad \text{for } v_{\text{cut in}} \leq v \leq v_r \tag{6.10}$$

$$f_P(p) = f_V(g^{-1}(p)) \left[\frac{dg^{-1}(v)}{dp} \right] = \frac{1}{\alpha} f_V\left(\frac{p-\beta}{\alpha}\right) \tag{6.11}$$

So,

$$f_p(p) = \frac{k \cdot v_{\text{cut in}} \cdot \lambda}{c} \times \left(\frac{(\lambda \cdot p + p_r) v_{\text{cut in}}}{p_r \cdot c} \right)^{k-1} \times \exp\left(- \left(\frac{(\lambda \cdot p + p_r) v_{\text{cut in}}}{p_r \cdot c} \right)^k \right)$$

$$\lambda = \left(\frac{v_r - v_{\text{cut in}}}{v_{\text{cut in}}} \right) \tag{6.12}$$

As can be seen from Eq. (6.12), the density function $f_p(p)$ has two setting parameters: c and k . If the wind speed distribution function is determined properly, the wind speed would limit between upper and lower bounds for the assigned CL. To do so, c and k must be derived for each PI as follows. This can be done based on two assumptions:

- Expected value is equal to predicted wind speed.
- CL is equal to probability of wind speed occurrence at $[V_l, V_u]$.

The above assumptions can be stated as:

$$\begin{cases} \int_{v_l}^{v_u} v f_V(v) dv = v_{\text{pre}} \\ \int_{v_l}^{v_u} f_V(v) dv = \text{CL} \end{cases} \tag{6.13}$$

where:

v_{pre} : anticipated wind speed

6.4 Main Focus of the Chapter

Wind power plant participation in electricity markets, due to their uncertain nature, has become a serious challenge for system operators. In one hand, if the available wind power surpasses the scheduled amount, ISO must buy the additional amount. On the other hand, if the available wind power is less than the scheduled, ISO must provide the power shortage from real-time and reserve markets. These cases imply that the wind power uncertainty can increase costs of systems. So, a probabilistic approach should be implemented to manage the costs [11].

Equation (6.14) calculates the expected costs based on penalty factors in case available wind power surpasses the scheduled amount (underestimating).

$$C_{us} = K_u \int_{P_i}^{P_u} (p - P_i) f_p(p) dp \quad (6.14)$$

$$K_u = \pi_{rt}$$

where:

P_i : scheduled wind power

π_{rt} : price of real-time market

C_{us} : cost of underestimating

Equation (6.15) calculates the expected cost resulted by overestimating the wind power in case, when available power is less than scheduled one. If the price of energy is cheaper in real-time market than the reserve market, the power shortage will be provided from real-time market. Otherwise, if the power shortage does not meet the reserve market limitation, all the lack of power will be provided from the reserve market. In this case, the price of reserve market will be considered as the penalty factor. When the power shortage meets the reserve market limitation, the rest of power shortage will be provided from real-time market. In this situation, the price of real-time market will be considered as the penalty factor.

$$\left\{ \begin{array}{l} C_{os} = K_{o,1} \int_{P_l}^{P_i} (P_i - p) f_p(p) dp \quad \text{if } \Delta P \leq P_{lim.res} \\ C_{os} = K_{o,1} \int_{P_l}^{P_l + P_{lim.res}} (P_i - p) f_p(p) dp + K_{o,2} \int_{P_l + P_{lim.res}}^{P_i} (P_i - p) f_p(p) dp \quad \text{if } \pi_{res} \leq \pi_{rt} \\ C_{os} = K_{o,2} \int_{P_l}^{P_i} (P_i - p) f_p(p) dp \quad \text{if } \pi_{res} > \pi_{rt} \end{array} \right. \quad (6.15)$$

where:

$$\Delta P = P_i - P_l \quad , \quad K_{o,1} = \pi_{\text{res}} \quad , \quad K_{o,2} = \pi_{\text{rt}}$$

C_{os} : cost of over-estimation.

The wind power plant's generation cost can be given as follows:

$$C_{\text{Pw}} = \pi_j \cdot P_i \quad (6.16)$$

where:

π_j : LMP of j^{th} bus

Considering the above discussion, production costs of thermal and wind power plants should be minimized by ISO. Therefore, the objective function can be presented as below:

$$\min \left\{ \left(\sum_{i=1}^n C_{Gi} \right) + C_{\text{us}} + C_{\text{Pw}} + C_{\text{os}} \right\} \quad (6.17)$$

where:

n : number of thermal power plants

As can be seen, the goal of Eq. (6.17) is to minimize total expected cost. This study tries to minimize 24-h expected costs in a day-ahead market. Finally, the objective function is expressed as follows:

$$\min \left\{ \sum_{h=1}^{24} \left(\left(\sum_{i=1}^n C_{Gi} \right)_h + C_{\text{us},h} + C_{\text{Pw},h} + C_{\text{os},h} \right) \right\} \quad (6.18)$$

Equation (6.18) shows that the determining of wind plant's power in range of $[P_l, P_u]$ has a considerable effect on LMPs and thermal power plants' generations, as well. The system operator must choose the best amount of power production for wind and thermal plants in order to minimize the total costs and satisfy its constraints. Overall framework of probabilistic method is shown in Fig. 6.1 [11].

6.5 Results of Analysis

In this section, a sample transmission system, shown in Fig. 6.2, is used to carry out mentioned framework in a day-ahead electricity market and determine the optimal wind power with the aim of optimizing the objective function [21]. Tables 6.1 and 6.2 present the information of the network. The hourly scaling factor is used to form the hourly consumption pattern of loads using Eq. (6.19). The load scaling factor is shown in Fig. 6.3.

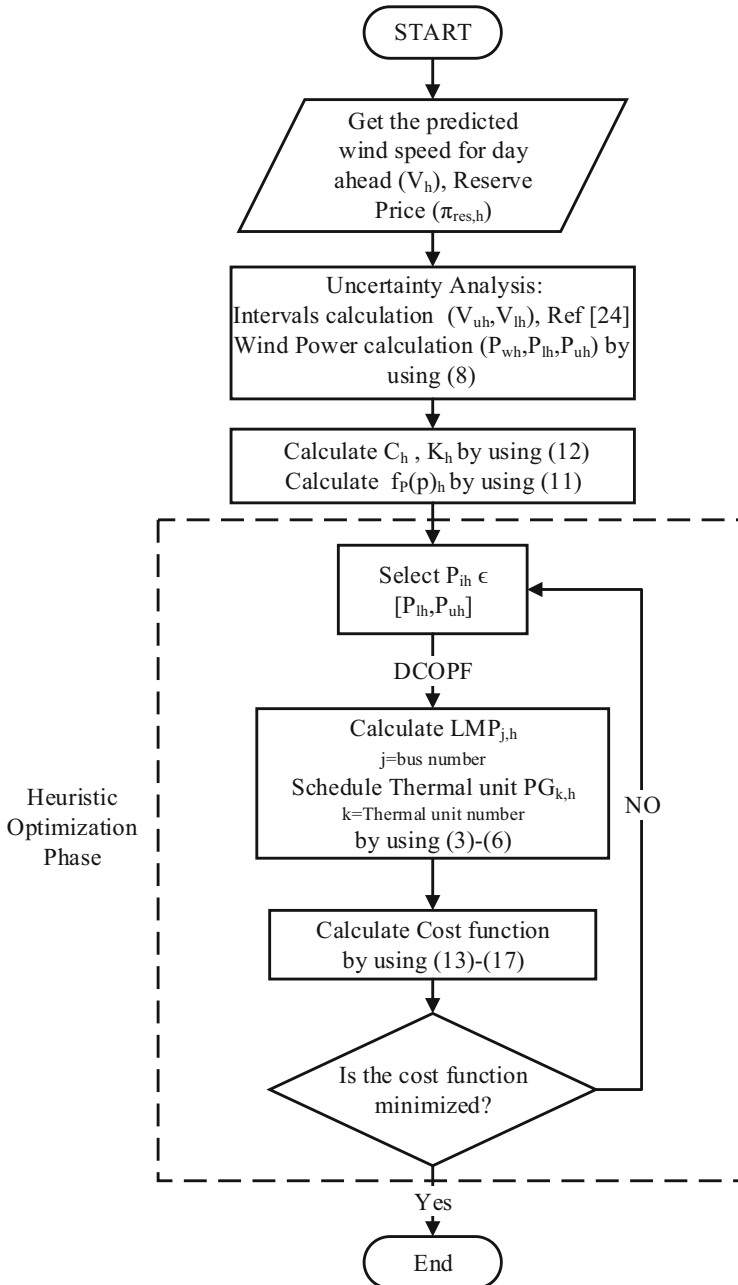


Fig. 6.1 Flowchart of probabilistic method

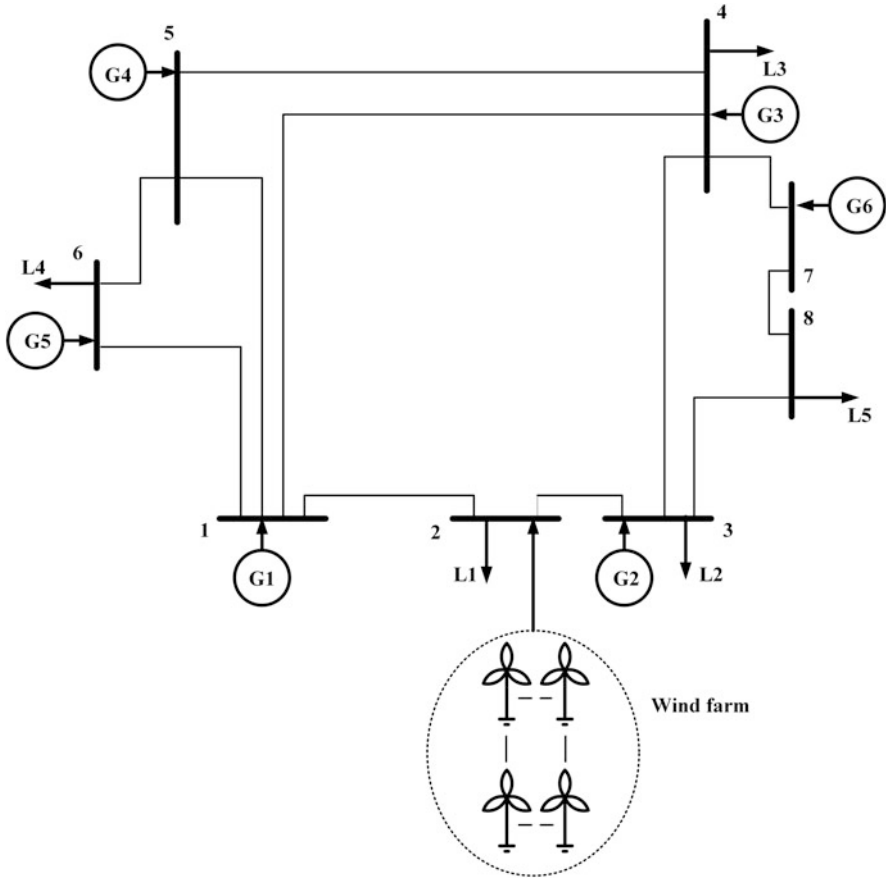


Fig. 6.2 Sample transmission system

Table 6.1 Bus data

Bus	a (\$/MWh ²)	b (\$/MWh)	C (\$/h)	P_{\min} (MW)	P_{\max} (MW)	Pd (MW)
1	0.0048193	14.37181	89.62	0	35	0
2	0	0	0	0	0	15
3	0.0245283	37.60189	17.64	0	20	11
4	0.0730337	26.34562	31.60	0	32	15
5	0.002	13.39	79.78	0	40	0
6	0.01	13.47	49.75	0	20	15
7	0.05	25.47	24.05	0	12	0
8	0	0	0	0	0	15

Table 6.2 Lines data

Line	From	To	Reactance (p.u.)	Limit (MW)
1	1	2	0.0300	9.0
2	1	4	0.0300	15.0
3	1	5	0.0065	20.0
5	2	3	0.0110	10.0
6	3	4	0.0300	10.0
7	4	5	0.0300	20.0
8	5	6	0.0200	10.0
9	6	1	0.0250	19.0
10	7	4	0.0150	19.0
11	7	8	0.0220	20.0
12	8	3	0.0180	15.0

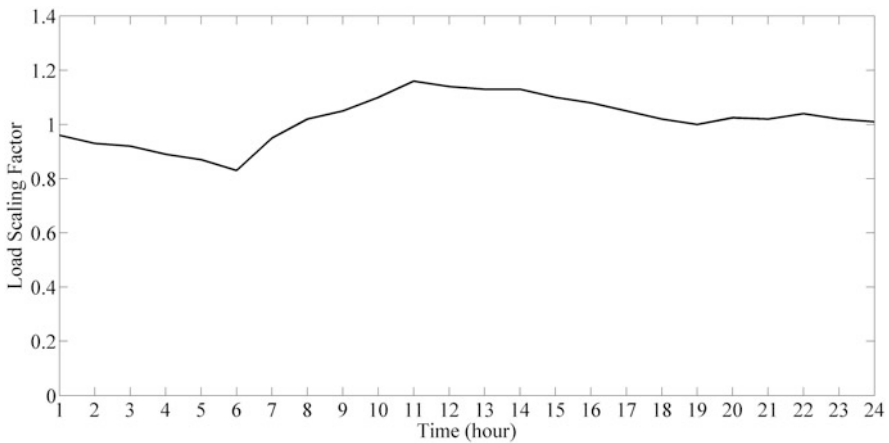


Fig. 6.3 Load scaling factor

$$P_{load\ j,h} = P_{d_j} \cdot \text{Scaling Factor}_h \tag{6.19}$$

The wind speed is forecasted for May 11, 2015, based on the historical data provided from Khaf City, Iran, between January 2015 and April 2015. The forecasted wind speed along with its upper and lower bounds (PIs) corresponding to 95% of confidence level is depicted in Fig. 6.4.

Wind power and its uncertainty intervals are calculated using Eq. (6.8) and shown in Fig. 6.5. To do this, $v_{cut\ in}$, v_r , $v_{cut\ out}$, and P_r are assumed to be 5 m/s, 25 m/s, 45 m/s, and 10 MW, respectively.

The available reserve capacity is assumed to be 5% of network’s hourly power consumption. Besides, the next day reserve market price is given in Fig. 6.6.

Using DCOPF for each hour, hourly LMPs are derived. Furthermore, the reserve and day-ahead market prices are usually lower than those of real-time market.

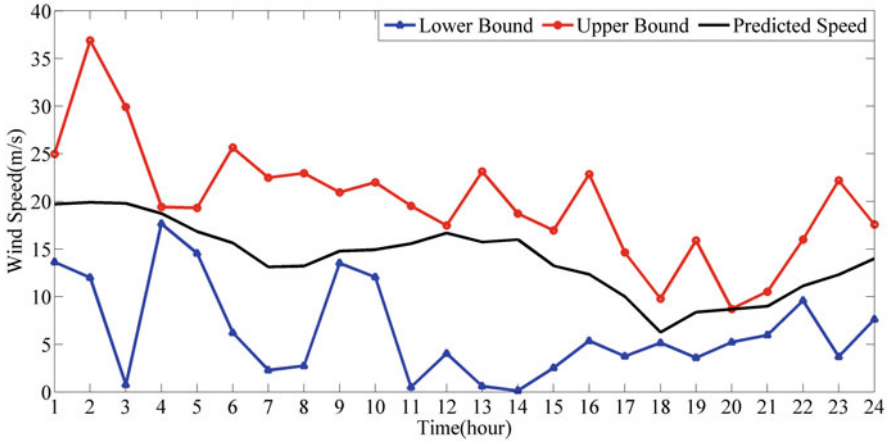


Fig. 6.4 Forecasted wind speed along with its uncertainty intervals [10]

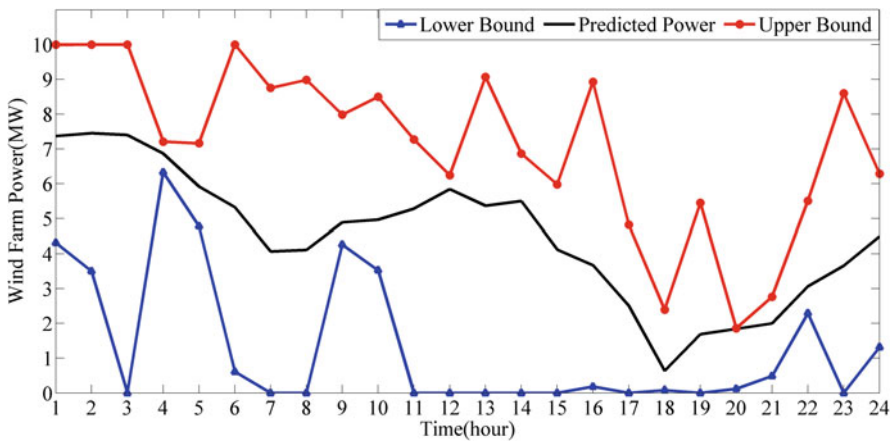


Fig. 6.5 Forecasted wind power along with its uncertainty intervals [10]

Therefore, to simplify the calculation and based on what is presented in ([11, 12]), real-time market price will be assumed to be a coefficient of the most expensive bus price in each hour.

$$\pi_{rt,h} = \mu \cdot \max(\pi_{j,h}), \quad \mu = 1.4, h = 1, \dots, 24, \quad j = 1, \dots, 8 \quad (6.20)$$

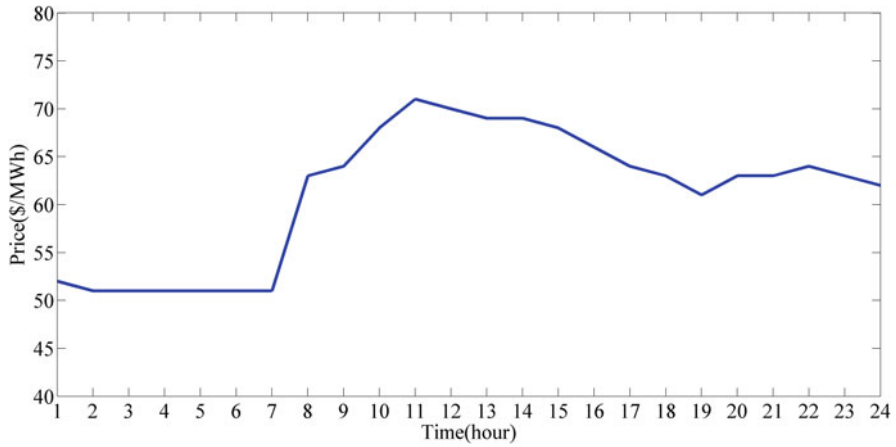


Fig. 6.6 Next day reserve market price

Table 6.3 Total expected cost values under various scenarios of wind power at bus 2

	Scenarios				
	1	2	3	4	5
	P_1	$0.5 * (P_1 + P_{pre})$	P_{pre}	$0.5 * (P_u + P_{pre})$	P_u
Total cost ($\times 10^4$ \$)	6.8	5.9	5.5	5.4	5.73

6.5.1 Meta-heuristic Optimization Algorithms Application in Minimizing Total Expected Costs

First, the PDF of wind power and its related c and k parameters are calculated by using Eqs. (6.8), (6.9), (6.10), (6.11), (6.12) and (6.13), considering Figs. 6.4 and 6.5. By adding the wind power plant to bus 2, shown in Fig. 6.2, the objective function is evaluated under five scenarios of wind power:

1. P_1
2. $0.5 * (P_1 + P_{pre})$
3. P_{pre}
4. $0.5 * (P_u + P_{pre})$
5. P_u as scheduled

The results of Table 6.3 show that applying the marginal points of bound leads to a greater value of the objective function.

These scenarios are not optimum, and the optimum one should be within these intervals. As the problem is complex and nonlinear, meta-heuristic methods are the best choice to solve it. So, three heuristic optimization algorithms, inspired by nature, have been used for minimizing the given objective function in Eq. (6.18). Three mentioned algorithms are:

Table 6.4 Optimum wind power for each hour and optimum total expected costs under three optimization algorithms

hour	Optimum (MW)			hour	Optimum (MW)		
	TLBO	PSO-GSA	ALO		TLBO	PSO-GSA	ALO
1	8.47	8.88	9.59	13	6.35	6.49	6.75
2	8.25	8.69	8.49	14	6.22	5.955	5.07
3	7.145	7.28	6.805	15	4.78	4.635	5.17
4	6.98	6.33	6.96	16	5.48	5.47	5.59
5	6.12	7.16	6.31	17	3.025	3.15	3.51
6	6.94	7.05	6.96	18	1.43	1.59	1.66
7	5.38	5.44	5.36	19	2.98	3.02	2.49
8	5.41	5.35	5.29	20	1.79	1.86	1.28
9	7.54	7.98	4.96	21	2.21	2.30	2.45
10	7.64	7.64	7.76	22	5.03	5.04	4.95
11	6.79	6.78	6.30	23	5.02	5.11	4.88
12	6.16	6.24	4.55	24	5.24	4.82	3.45
<i>Total cost ($\times 10^4$ \$)</i>					<i>TLBO</i>	<i>PSO-GSA</i>	<i>ALO</i>
					5.27	5.26	5.30

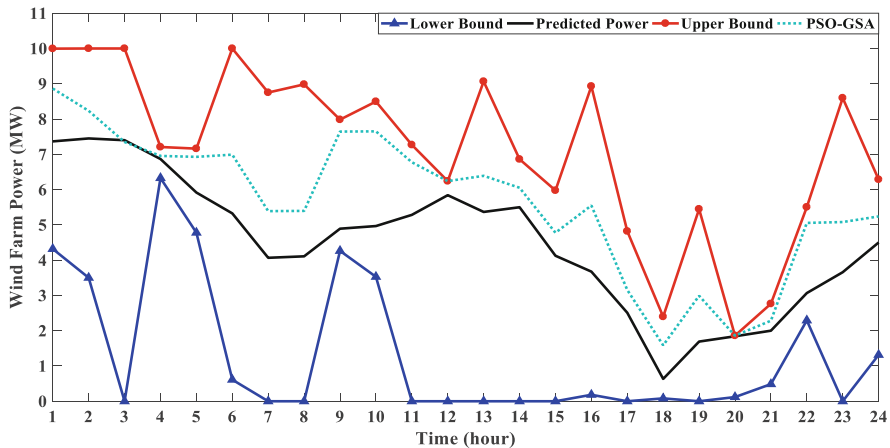


Fig. 6.7 The optimum wind power provided by PSO-GSA algorithm [10]

- Teaching learning-based optimization (TLBO) [32]
- Particle swarm optimization-gravity search algorithm (PSO-GSA) [25]
- Ant Lion Optimizer (ALO) [24]

The results of optimum wind power for each hour and optimum total expected costs under three optimization algorithms have been tabulated in Table 6.4. As revealed by the results, three aforementioned algorithms have a close performance in minimizing the total expected cost values. As the PSO-GSA algorithm has the least amount of total expected costs, it is chosen as the best solution. In this regard, the optimum wind power provided by PSO-GSA algorithm is shown in Fig. 6.7.

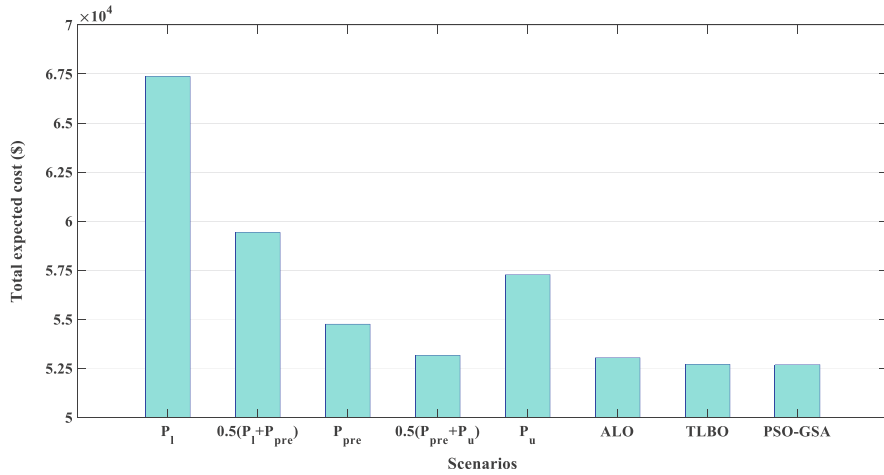


Fig. 6.8 The total expected cost under various scenarios [10]

Table 6.5 Total expected cost values under various scenarios of wind power at bus 8

	Scenarios				
	1	2	3	4	5
	P_1	$0.5 * (P_1 + P_{pre})$	P_{pre}	$0.5 * (P_u + P_{pre})$	P_u
Total cost (×10 ⁴ \$)	6.75	6.02	5.51	5.36	5.77

As stated before, Fig. 6.7 implies that optimized amount of wind power values is different from predicted value, upper and lower bounds. Furthermore, in most cases, the derived value is more than the predicted one. This is due to the fact that in lack of wind power conditions, the power or part of it can be provided with a lower price from the reserve market than the real-time market.

The total expected costs under various scenarios are shown in Fig. 6.8. As revealed by the results of this figure, applying meta-heuristic algorithms has reduced the total cost by 14,681\$, 6735.7\$, 477.5\$, and 4584.4\$ for scenarios 1, 2, 4, and 5, respectively. Also, as can be seen, when ISO applies the predicted power without any uncertainties (scenario 3), the total cost is raised by 2062.8\$.

To demonstrate the effectiveness of the proposed approach, the wind plant is added to bus 8, and all above analyses have been conducted. The results of these analyses are tabulated in Tables 6.5 and 6.6. The obtained results verify the efficiency of presented method in terms of minimizing the total expected cost.

As shown in Tables 6.5 and 6.6, applying meta-heuristic algorithms has reduced the total cost, considerably. Among them, TLBO algorithm has the best performance. The amount of cost reduction under TLBO algorithm implementation for scenarios 1 to 5 is 14310.1\$, 7031.5\$, 1933.2\$, 424.3\$, and 4591.2\$, respectively.

All calculated results have carried out from producers' point of view. Customers' behavior is important, and their viewpoint must be considered, too. Therefore, their

Table 6.6 Optimum wind power for each hour and optimum total expected costs under three optimization algorithms

Hour	Optimum(MW)			Hour	Optimum (MW)		
	TLBO	PSO-GSA	ALO		TLBO	PSO-GSA	ALO
1	8.86	4.32	9.00	13	6.61	6.63	6.76
2	8.21	8.28	7.95	14	6.20	6.19	4.62
3	7.10	7.30	6.615	15	4.78	4.87	5.34
4	6.89	7.21	6.34	16	6.27	6.27	6.27
5	6.18	7.15	6.39	17	3.31	3.455	3.225
6	6.92	7.035	6.65	18	1.42	1.43	1.76
7	5.40	5.53	5.06	19	3.06	2.87	2.10
8	5.37	5.55	5.36	20	0.44	0.17	0.77
9	7.17	7.54	7.20	21	2.29	2.61	2.62
10	7.69	7.73	7.79	22	4.97	4.96	5.06
11	5.996	6.23	6.6	23	5.11	5.03	5.08
12	5.95	5.79	5.35	24	5.10	5.25	5.66
<i>Total cost ($\times 10^4$ \$)</i>					<i>TLBO</i>	<i>PSO-GSA</i>	<i>ALO</i>
					5.32	5.33	5.34

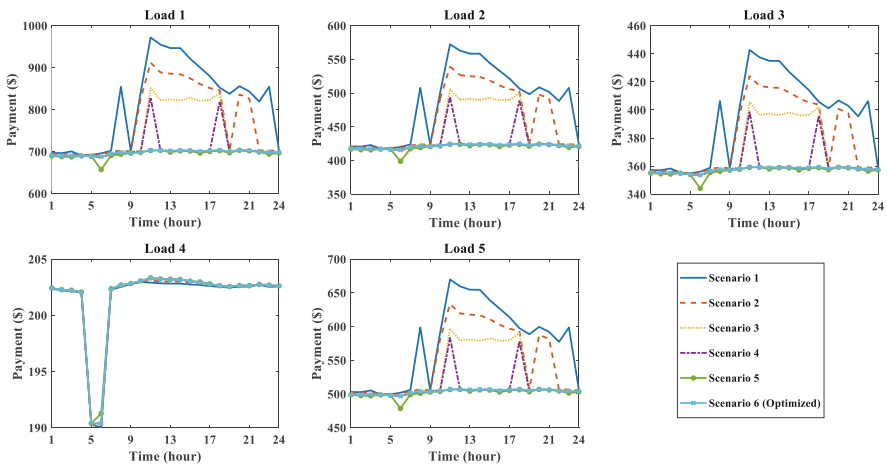


Fig. 6.9 Payments of customers under various scenarios of wind at bus 2 [10]

payments are calculated by Eq. (6.21). Figure 6.9 depicts these payments under various scenarios of wind at bus 2.

$$Payment_{l,h} = P_{loadl,h} \times \pi_{busload\ 1,h} \quad l = 1, \dots, 5, \quad h = 1, \dots, 24 \quad (6.21)$$

where:

$\pi_{busload\ l,h}$: LMP of l^{th} bus at h^{th} hour.

Table 6.7 Total expected cost and total payments under various scenarios of wind power at bus 2

No.	Scenarios	Expected cost	Payments	Total
1	P_1	67,370	59,302.3	126,672.3
2	$0.5 * (P_1 + P_{pre})$	59,430	56,844.6	116,274.6
3	$0.5 * (P_u + P_{pre})$	54,750	54,933	109,683
4	P_{pre}	53,170	52,956.6	106,126.6
5	P_u	57,280	52,194.4	109,474.4
6	Optimum ^a	52,691.8	52,374.4	105,066.2
7	Optimum ^b	52,695.4	52,367.6	105,063

^aNeglecting payments

^bConsidering payments

As mentioned earlier, the higher the amount of wind power, the lower the amount of LMPs. As can be seen from Fig. 6.9, in fifth scenario, the highest amount of wind power leads to the lowest amount of payments.

ISO can satisfy all the participants by simultaneously minimizing costs of sellers and buyers. For this purpose, a new objective function can be given as follows:

$$\min \left\{ \sum_{h=1}^{24} \left(\sum_{j=1}^m \text{Payment}_{j,h} + \left(\sum_{i=1}^n C_{G_i} \right)_h + C_{Pw,h} + C_{us,h} + C_{os,h} \right) \right\} \quad (6.22)$$

where:

m : the number of loads

By solving Eq. (6.22) using the mentioned meta-heuristic algorithms, the results have been calculated and tabulated in Table 6.7.

According to the results of Table 6.7, optimization results have the lowest values. So, these results are suitable from power plants’ point of view. However, from customers’ point of view, the result of upper bound is desirable. Taking both customers’ and producers’ viewpoints into account, scenarios 6 and 7 have the best performance. Moreover, implementing scenario 7 reduces the amount of total expected cost and payments by 4\$ compared to scenario 6. These reductions indicate that the presented objective function has an excellent ability to reduce costs of both producers and customers. So, the optimum equilibrium points can be found by ISO so as to satisfy all the participants.

6.6 Future Work

The future suggested works in the probabilistic cost minimization of day-ahead electricity market based on meta-heuristic optimization algorithms would be considering energy storage systems, photovoltaic power plants, and simultaneous

demand response program implantation [41]. Also, wake effect among wind turbines can affect the delivered power [38]. Therefore, considering probable wake effects in electricity markets planning can lead to interesting results.

6.7 Conclusion

This chapter proposes a probabilistic technique to minimize the daily total expected cost considering uncertainty in the output power of wind farm in the day-ahead market.

Using the wind farm data, an approach is presented to calculate PDF of uncertainty intervals. Then, the costs of underestimation and overestimation are calculated based on the market rules. These costs should be paid by ISO. The model exploits the reserve and real-time markets to obtain lack of power. Furthermore, additional costs due to uncertainties are modeled by proposing two new objective functions. These objective functions are used to minimize the generation costs of thermal and wind power plants along with the costs of uncertainties.

In order to evaluate the efficiency of the proposed method, meta-heuristic optimization algorithms have been applied to optimize the proposed objective functions. The results indicate that the highest amount of wind power (upper bound) is desirable for the customers. However, the predicted amount is suitable for power producers. By applying the presented procedure, the value of total costs reduced ranging from 1063.7\$ to 21609.3\$ under various scenarios. According to the results, it is found that the optimum amount of wind power in uncertainty intervals is usually different from predicted amount. Due to non-linearity of the optimization problem, meta-heuristic optimization algorithm can solve it with high accuracy, which shows their importance in electric markets problems.

References

1. Awad AS, Ahmed MH, El-Fouly TH, Salama MM (2017) The impact of wind farm location and control strategy on wind generation penetration and market prices. *Renew Energy* 106:354–364
2. Bahmani R, Karimi H, Jadid S (2020) Stochastic electricity market model in networked microgrids considering demand response programs and renewable energy sources. *Int J Electr Power Energy Syst* 117:105606
3. Banaei M, Raouf-Sheybani H, Oloomi-Buygi M, Boudjadar J (2021) Impacts of large-scale penetration of wind power on day-ahead electricity markets and forward contracts. *Int J Electr Power Energy Syst* 125:106450
4. Bhattacharya K, Bollen MH, Daalder JE (2012) *Operation of restructured power systems*. Springer Science & Business Media, New York
5. Bitar EY, Rajagopal R, Khargonekar PP, Poolla K, Varaiya P (2012) Bringing wind energy to market. *IEEE Trans Power Syst* 27(3):1225–1235
6. Bremnes JB (2004) Probabilistic wind power forecasts using local quantile regression. *Wind Energy* 7(1):47–54

7. Dai T, Qiao W (2013) Trading wind power in a competitive electricity market using stochastic programming and game theory. *IEEE Trans Sustain Energy* 4(3):805–815
8. Dai T, Qiao W (2015) Optimal bidding strategy of a strategic wind power producer in the short-term market. *IEEE Trans Sustain Energy* 6(3):707–719
9. De Jonghe C, Hobbs BF, Belmans R (2013) Value of price responsive load for wind integration in unit commitment. *IEEE Trans Power Syst* 29(2):675–685
10. Dehghani H (2015) Investigation of the wind power forecast uncertainty in power market for optimization of clearing price, MSc thesis, Amirkabir university of technology (Tehran polytechnic), Iran
11. Dehghani H, Faramarzi D, Vahidi B, Saeidi M (2017a) A probabilistic method for cost minimization in a day-ahead electricity market considering wind power uncertainties. *J Renew Sustain Energy* 9(6):063301
12. Dehghani H, Vahidi B, Hosseini SH (2017b) Wind farms participation in electricity markets considering uncertainties. *Renew Energy* 101:907–918
13. Du Y, Li F, Zandi H, Xue Y (2021) Approximating Nash equilibrium in day-ahead electricity market bidding with multi-agent deep reinforcement learning. *J Mod Power Syst Clean Energy* 99:1–11
14. Exizidis L, Kazempour SJ, Pinson P, de Greve Z, Vallée F (2016) Sharing wind power forecasts in electricity markets: a numerical analysis. *Appl Energy* 176:65–73
15. Fu, Y, Li Z (2006) Different models and properties on LMP calculations. In: 2006 IEEE Power Engineering Society General Meeting
16. Hakimi SM, Hasankhani A, Shafie-khah M, Catalão JP (2021) Stochastic planning of a multi-microgrid considering integration of renewable energy resources and real-time electricity market. *Appl Energy* 298:117215
17. Hassan Q (2021) Assessing of renewable energy for electrical household ancillary based on photovoltaics and wind turbines. *IOP Conf Ser: Mater Sci Eng* 1076(1):012006
18. Hirth L (2016) The benefits of flexibility: the value of wind energy with hydropower. *Appl Energy* 181:210–223
19. Ji L, Huang G-H, Huang L-C, Xie Y-L, Niu D-X (2016) Inexact stochastic risk-aversion optimal day-ahead dispatch model for electricity system management with wind power under uncertainty. *Energy* 109:920–932
20. Khaloie H, Abdollahi A, Shafie-khah M, Siano P, Nojavan S, Anvari-Moghaddam A, Catalão JP (2020) Co-optimized bidding strategy of an integrated wind-thermal-photovoltaic system in deregulated electricity market under uncertainties. *J Clean Prod* 242:118434
21. Li T, Shahidehpour M (2005) Price-based unit commitment: a case of Lagrangian relaxation versus mixed integer programming. *IEEE Trans Power Syst* 20(4):2015–2025
22. Litvinov E (2010) Design and operation of the locational marginal prices-based electricity markets. *IET Gener Transm Distrib* 4(2):315–323
23. Liu H, Chen Z (2012) Aggregated modelling for wind farms for power system transient stability studies. In: 2012 Asia-Pacific Power and Energy Engineering Conference
24. Mirjalili S (2015) The ant lion optimizer. *Adv Eng Softw* 83:80–98
25. Mirjalili S, Hashim SZM (2010) A new hybrid PSO-GSA algorithm for function optimization. In: 2010 international conference on computer and information application
26. Moradi-Dalvand M, Mohammadi-Ivatloo B, Amjadi N, Zareipour H, Mazhab-Jafari A (2015) Self-scheduling of a wind producer based on information gap decision theory. *Energy* 81:588–600
27. Morales JM, Conejo AJ, Pérez-Ruiz J (2010) Short-term trading for a wind power producer. *IEEE Trans Power Syst* 25(1):554–564
28. Motaleb M, Thornton M, Reihani E, Ghorbani R (2016) A nascent market for contingency reserve services using demand response. *Appl Energy* 179:985–995
29. Opathella C, Venkatesh B (2013) Managing uncertainty of wind energy with wind generators cooperative. *IEEE Trans Power Syst* 28(3):2918–2928

30. Patnam BSK, Pindoriya NM (2021) Demand response in consumer-centric electricity market: mathematical models and optimization problems. *Electr Power Syst Res* 193:106923
31. Prol JL, Steininger KW, Zilberman D (2020) The cannibalization effect of wind and solar in the California wholesale electricity market. *Energy Econ* 85:104552
32. Rao RV, Savsani VJ, Vakharia D (2012) Teaching–learning–based optimization: an optimization method for continuous non-linear large scale problems. *Inf Sci* 183(1):1–15
33. Razmjoo A, Kaigutha LG, Rad MV, Marzband M, Davarpanah A, Denai M (2021) A technical analysis investigating energy sustainability utilizing reliable renewable energy sources to reduce CO2 emissions in a high potential area. *Renew Energy* 164:46–57
34. Reddy SS (2017) Optimal scheduling of thermal-wind-solar power system with storage. *Renew Energy* 101:1357–1368
35. Reddy SS, Momoh JA (2015) Realistic and transparent optimum scheduling strategy for hybrid power system. *IEEE Trans Smart Grid* 6(6):3114–3125
36. Reddy SS, Abhyankar A, Bijwe P (2012) Market clearing for a wind-thermal power system incorporating wind generation and load forecast uncertainties. In: 2012 IEEE power and energy society general meeting
37. Reddy SS, Sandeep V, Jung C-M (2017) Review of stochastic optimization methods for smart grid. *Front Energy* 11(2):197–209
38. Sadeghian O, Oshnoei A, Tarafdar-Hagh M, Kheradmandi M (2020) A clustering-based approach for wind farm placement in radial distribution systems considering wake effect and a time-acceleration constraint. *IEEE Syst J* 15(1):985–995
39. Sadeghian O, Oshnoei A, Tarafdar-Hagh M, Khezri R (2021) A clustering-based technoeconomic analysis for wind farm and shunt capacitor allocation in radial distribution systems. *Int Trans Electr Energy Syst* 31(1):e12708
40. Sinsel SR, Riemke RL, Hoffmann VH (2020) Challenges and solution technologies for the integration of variable renewable energy sources—a review. *Renew Energy* 145:2271–2285
41. Vahidi B, Dehghani H (2020) Linear and nonlinear modeling of demand response programs. In book: demand response application in smart grids. Springer, Cham, pp 79–92
42. Vilim M, Botterud A (2014) Wind power bidding in electricity markets with high wind penetration. *Appl Energy* 118:141–155
43. Wang X, Zhang H, Zhang S, Wu L (2021) Impacts of joint operation of wind power with electric vehicles and demand response in electricity market. *Electr Power Syst Res* 201:107513
44. Xiao Y, Wang X, Wang X, Dang C, Lu M (2016) Behavior analysis of wind power producer in electricity market. *Appl Energy* 171:325–335
45. Xu Y, Hu Q, Li F (2013) Probabilistic model of payment cost minimization considering wind power and its uncertainty. *IEEE Trans Sustain Energy* 4(3):716–724
46. Zeynali S, Nasiri N, Marzband M, Ravadanegh SN (2021) A hybrid robust-stochastic framework for strategic scheduling of integrated wind farm and plug-in hybrid electric vehicle fleets. *Appl Energy* 300:117432
47. Zhang B, Johari R, Rajagopal R (2015) Competition and coalition formation of renewable power producers. *IEEE Trans Power Syst* 30(3):1624–1632
48. Zhang C, Wang Q, Wang J, Korpås M, Pinson P, Østergaard J, Khodayar ME (2016) Trading strategies for distribution company with stochastic distributed energy resources. *Appl Energy* 177:625–635
49. Zhao H, Wu Q, Hu S, Xu H, Rasmussen CN (2015) Review of energy storage system for wind power integration support. *Appl Energy* 137:545–553

Chapter 7

Robust Energy Management of Virtual Energy Hub Considering Intelligent Parking Lots for the Plug-In Hybrid Electric Vehicles



Mohammad Seyfi, Mehdi Mehdinejad, and Heidarali Shayanfar

Abstract Energy systems transitions have faced a big challenge with the advent of multi-energy systems. Smart grid and virtual energy hub (VEH) concepts provide the opportunity for the integration of multiple energy carriers with electrical energy. A VEH formed by smart grid framework can operate the plug-in hybrid electric vehicles (PHEV) and manage their behavior in a smart way. In this chapter, the energy management problem for the participation of VEH in the electrical and thermal energy markets considering intelligent parking lots is presented. For modeling PHEVs, the uncertainty of entrance and exit times of PHEVs is considered, which affects their charging and discharging process. In addition to PHEVs' behavior, the output power of renewable energy resources, energy price, and energy demand have uncertain nature. For dealing with these uncertainties, robust optimization is a promising option, which provides the opportunity for managing the system for the worst-case scenarios.

Keywords Virtual energy hub · Intelligent parking lot · Robust optimization · Plug-in hybrid electric vehicles · Demand response program

7.1 Introduction

7.1.1 Background and Motivations

Distributed energy resources (DER) are the one significant option for the reduction of environmental pollutants [1]. This category of energy generation consists of small-scale energy generation units with a particular focus on renewable energy resources (RES). DERs can produce energy at a location near the consumption centers, which cause to reduce the transmission loss by shortening the energy

M. Seyfi · M. Mehdinejad (✉) · H. Shayanfar
Center of Excellence for Power Systems Automation and Operation, School of Electrical Engineering, Iran University of Science and Technology, Tehran, Iran

pathway. The mentioned specifications of DERs allow them to be considered seriously in the novel power systems framework. DERs based on their structure can produce electrical energy, thermal energy, cooling energy, etc. This product differentiation of DERs forms the basics of integrated multi-energy systems, which means the integration of power systems with other energy carriers. The virtual energy hub (VEH) concept [2], a combination of energy hub (EH) [3] and virtual power plant (VPP) [4], can aggregate and control multiple types of DERs and their related energy carriers. The VEH framework allows the DERs to participate in multiple energy markets and benefit from the opportunities of these markets. The operator of VEH schedules DERs using the local operating system and manages their participation in the energy markets. High rate of spreading in the distribution network makes it extremely hard to operate the whole DERs altogether, and conventional central operation of power systems can't be reliable for scheduling them. It is better to aggregate the DERs by local operating, which causes the central system operator to consider them as a united power plant. Under this situation, DERs of any size can participate in energy and ancillary markets and gain profit by selling their energy and services in these markets. VEH can local operate these DERs and manage their related energy carriers. Therefore, DERs can participate in multiple energy and ancillary markets [5].

Given the features of VEH, various types of DERs can be part of the VEH structure. VEH can aggregate distributed generators, RESs, electric vehicles (EV), energy storage systems, demand-side services, etc. EVs are one of the efforts of the international community to address pollutant emissions concerns. These vehicles consume electrical energy to drive using produced power by the electric motor. As a result, they do not produce environmental pollutants. VEH can benefit the hardware and software of the smart grid in the energy management of DERs, which provides high-end technologies for communication to transmit information between DERs fast and safely. Participation of electric vehicles in smart grids planning and operation is a challenge that has drawn much attention from researchers. A smart VEH, VEH formed by the smart grid structure, can ease the integration and management of plug-in hybrid electric vehicles (PHEV). Intelligent parking lot (IPL) is the aggregator of PHEVs, which can schedule the PHEVs and determine their charging and discharging planning automatically. IPL has access to real-time energy price data using smart grid communication systems. Thus, it updates the charging and discharging planning of PHEVs in response to the price variations. The aggregation of a high number of electric vehicles helps the VEH operator use their battery capacity as an energy storage system.

7.1.2 Related Works

Multi-energy systems are studied in numerous works in the literature. In [6], stochastic programming is used to assess the effects of an ice storage system on the energy hub performance. The obtained results show the importance of a proper

cooling energy storage system for improving the energy hub performance. This energy hub consists of renewable energy resources and consumers capable of participating in the demand response program (DRP). The authors of [7] have used particle swarm optimization to optimally design an energy hub to reduce pollutant emissions and increase energy consumption. Electrical energy, thermal energy, natural gas, and wood chips are the included energy carriers in this energy hub. In [8], multi-objective operation of a multi-energy system using multi-objective particle swarm optimization is presented. A two-stage combined planning and operation for a multi-energy system is presented in [9]. Particle swarm optimization is a metaheuristic method and can be utilized in convex and convex optimization problems. Although metaheuristic algorithms can optimize complex optimization problems, they perform on a random basis and yield different solutions every time. It is better to develop and implement mathematical optimization models for the scheduling and planning problems related to energy hubs and integrated energy systems. The authors of [10] presented the self-scheduling of a smart energy hub for participating in the energy and regulation markets. Electric vehicles, CHP units, boilers, diesel generators, wind turbines, and energy storage systems are considered in the smart energy hub model. This smart energy hub can participate in electrical and natural gas markets. Participation of a VEH in the multiple energy and reserve markets is studied in [5].

With the advent of thermal networks, and consequently the thermal markets, participation of DERs in these markets becomes very important. DERs should be able to sell their produced thermal energy to earn money. However, the reviewed papers are neglected the participation of DERs in thermal markets. For addressing this, the authors of [4] have proposed the new model for multi-energy systems, called VEH, which can provide more options for DERs for gaining profit by participating in multiple energy markets. In this work, the IGDT approach is used for scheduling the developed VEH by risk-averse and risk-seeking strategies. A cooperative scheduling of a VEH considering the active and reactive power flows is studied in [11]. Because the VEH notion is a development on the VPP, it can participate in the ancillary markets, associated with multiple energy carriers. Participation of a VEH in the multiple energy and reserve markets is studied in [5]. In these references, hybrid CNG and plug-in electric vehicles are studied, which can use CNG as their alternative energy resource. The integration of power systems, thermal networks, natural gas grid, and transportation systems is addressed in this reference by considering hybrid CNG and plug-in electric.

Recently, attention to electric vehicles as the next generation of transportations has dramatically increased in the literature [12]. The spreading of electric vehicles can lead to huge reduction in pollutant emissions released by transportation systems. However, the integration of these vehicles with power systems and multi-energy systems is an important challenge. IPLs have been proposed in many works to provide a control mechanism for scheduling the charging and discharging of electric vehicles. IPLs can adjust the planning of charging and discharging of electric vehicles automatically. In [13], energy management for charging and discharging of electric vehicles in an IPL is presented. The uncertain behavior of drivers is taken

into account. The authors of [14] have investigated the performance of IPL for electric vehicles in the presence of the hydrogen storage system.

Uncertainties and power systems are inseparable duos. Generally, the uncertainties of energy price, energy demand, and RESs are the most common uncertainties that exist in power systems problems [15]. Since VEH consists of a high number of DERs that can produce electrical, thermal, cooling, and other energies, especially RESs, the VEH scheduling problem requires proper uncertainty modeling methods. Many efforts for modeling the uncertainties and their impact on multi-energy systems can be found in the literature. Stochastic programming is suitable for the problems, in which the information of probability distribution function of uncertain parameters is achievable. A risk-based stochastic optimization using scenario generation method for energy management of an energy hub considering electrical and thermal DRPs is presented in [16]. Stochastic modeling for uncertainties of RESs in an energy hub scheduling problem is presented in [17]. Beta and Weibull probability distribution functions have been used for modeling the uncertainties of solar radiation and wind speed, respectively. The developed energy hub is optimized using particle swarm optimization approach. A hybrid IGD/stochastic approach is developed in [18] to determine the bidding strategy of a wind-based energy hub. When the data related to the statistical behavior of uncertain parameters are limited, fuzzy methods can be the proper approach for handling the uncertainties.

Robust optimization (RO) is one of the most used approaches to deal with uncertainties. RO methods deal with uncertainties in a conservative way to ensure that the real solution of the problem will be better than the calculated one. In other words, in robust optimization approaches, the worst case of related problem is investigated. In RO, the variations of the uncertain parameter are determined by the uncertainty set, which can be a box, ellipsoidal, etc. In [19], robust optimization is used to optimize the load dispatch of a community energy hub. The objective function of mentioned work is to minimize the operation cost and pollutant emissions. RO has been used in [20] to coordinately operate multiple energy hubs. The objective function is to minimize the total cost of energy hubs. The uncertainties of energy price and RESs are modeled by the RO and uncertainty sets. The authors of [21] presented a RO for the operation of a multi-energy microgrid. The developed microgrid is a renewable-based system integrated with flexibility and storage systems. This microgrid is connected to the electrical network, thermal network, and natural gas grid and supplies the associated demands. Energy management of multiple energy distribution company considering multi-energy conversion and storage technologies is developed in [13]. RO optimization is used in this reference to model the uncertainties lying in hourly wind speed and solar radiation.

7.1.3 Novelties and Contributions

In this chapter, a novel VEH structure is developed to integrate the electrical and thermal energy carriers. The RO method is developed for day-ahead self-scheduling

of a VEH, including IPL, to manage the participation of DERs in the energy markets. The uncertainties associated with the arrival and departure times, state of charge of the battery, nominal battery capacity, and required surplus energy of electric vehicles when they are exiting from parking are taken into account. The developed VEH can participate in the thermal and electrical energy markets to buy/sell energy from/to these markets.

The rest of the paper is organized as follows: In the problem modeling section, the mathematical modeling of developed VEH and its component are presented. The data relating to the VEH components and the simulation results of developed multi-energy system is presented. At the end, the conclusion section concludes the presented work.

7.2 Problem Modeling

In this chapter, a novel VEH structure that contains IPL for managing electric vehicles is presented. The VEH is connected to the electrical grid and thermal networks and can have energy trading with these markets. Moreover, the VEH is connected to the natural gas grid and provides the natural gas needed by DERs by importing it from the natural gas grid. The operator of VEH analyzes the real-time price and consuming energy data and, based on that, operates the DERs of the VEH. Also, the operator should manage and moderate the energy transactions with the energy markets to ensure that the profit of VEH will be equal to its maximum possible value. In other words, the operator determines the behavior of distributed generators, energy storage systems, flexible loads, and the energy transactions with markets to maximize the profit of VEH.

The developed VEH in this chapter includes combined heat and power (CHP) units, boilers, wind farm, IPL, electric vehicles, and thermal buffer tank (BT). CHP units produce electrical and thermal energy together, which can be used to provide the required electrical and thermal energy demands. Boiler units can produce thermal energy by consuming natural gas imported from the natural gas grid. The wind farm in this structure is comprised of a large number of wind turbines and can convert the energy of wind to electrical energy. IPL is considered in this chapter to aggregate the electric vehicles and manage their charging and discharging plan in an efficient way. IPL can provide electrical storage capacity for the operator of VEH by aggregating the battery capacity of the existing electric vehicles. For providing the thermal energy storage capacity, the thermal buffer tank is considered and modeled linearly. VEH fulfills the demand of end consumers, which can participate in the demand response program to increase the possible maximum profit for the VEH. Figure 7.1 shows the proposed VEH structure.

Some parameters of developed VEH are uncertain. It is important to model these parameters by proper uncertainty modeling methods. In this chapter, the RO is used to deal with the existed uncertainties. The RO ensures that the actual profit of VEH will

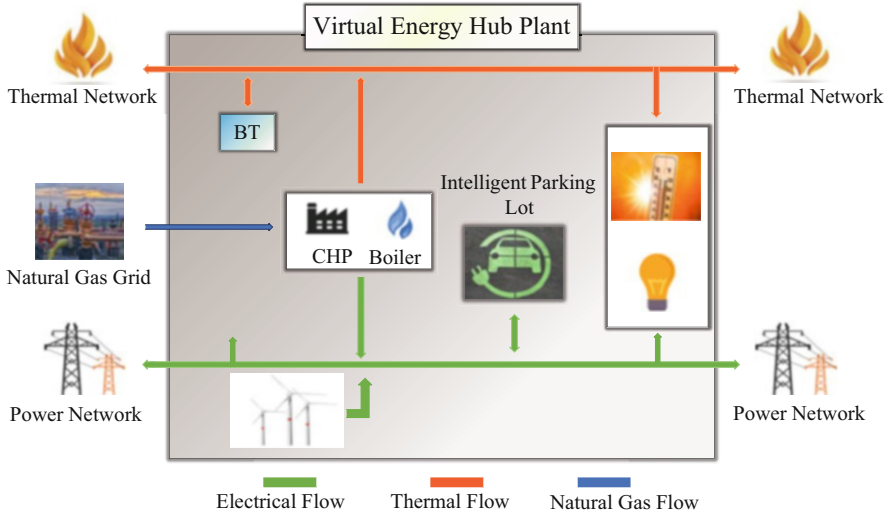


Fig. 7.1 The developed VEH structure

not be lower than the calculated one, which causes the omission of the economic risk of the problem. Figure 7.2 shows the optimization problem of the developed VEH.

In the following, the mathematical formulation of VEH and the optimization model are presented. In these equations, t stands for time index, i is CHP units index, k is boilers index, and v is the index of PHEVs.

7.2.1 Objective Function

The objective function of the developed system is to maximize the profit of VEH achieved by participating in electrical and thermal markets. Equation (7.1) states the objective function of the proposed VEH. The cost of CHP units, boiler units, electrical and thermal markets, and the profit of selling energy to end consumers and electric vehicles are the terms of this objective function. CHP, B , EMarket, THMarket, IPL, and Cons denote CHP units, boiler units, electrical market, thermal maker, intelligent parking lot, and consumers, respectively.

$$\max \text{Profit} = \sum_{t=1}^{n_t} (-\text{Cost}_t^{\text{CHP}} - \text{Cost}_t^B - \text{Cost}_t^{\text{EMarket}} - \text{Cost}_t^{\text{THMarket}} + \text{Profit}_t^{\text{IPL}} + \text{Profit}_t^{\text{Cons}}) \quad (7.1)$$

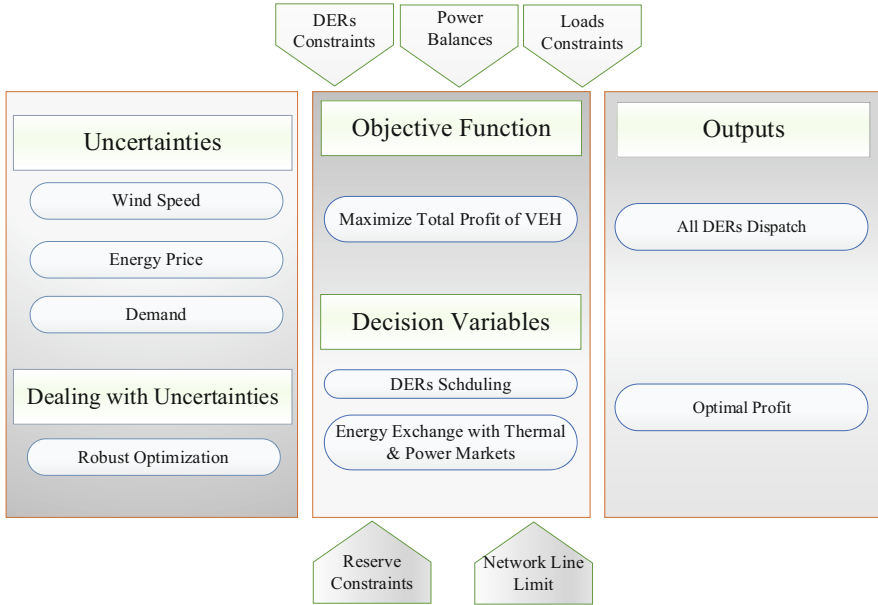


Fig. 7.2 The optimization problem of developed VEH

7.2.2 CHP

The CHP unit can consume natural gas and produce both electrical and thermal energies. The cost related to CHP units is given by (7.2). This cost is comprised of the cost of consuming natural gas cost, start-up cost, and shutdown cost. The output electrical and thermal energy of CHP units are correlated, and they should be in the feasible operational region (FOR) related to the CHP unit. Equation (7.3) states the correlation of output electrical and thermal energy of CHP units, which depends on heat to power ratio and heat exchanger efficiency. Furthermore, the output power of CHP has a minimum and maximum values. Equation (7.4) states the limitation related to the output power of CHP units. In these equations, $P_{i,t}^{CHP}$ and $T_{i,t}^{CHP}$ are output electrical and thermal powers, and $SU_{i,t}^{CHP}$ and $SD_{i,t}^{CHP}$ are start-up and shutdown binary variables. Also, λ^{NG} , $C_i^{CHP,U}$, and $C_i^{CHP,D}$ are natural gas cost, start-up cost, and shutdown cost, respectively.

$$\text{Cost}_t^{CHP} = \sum_{i=1}^{N_{CHP}} \left(\left(\lambda^{NG} \times \frac{P_{i,t}^{CHP}}{\eta_i^{CHP}} \right) + (C_i^{CHP,U} \times SU_{i,t}^{CHP}) + (C_i^{CHP,D} \times SD_{i,t}^{CHP}) \right) \quad (7.2)$$

$$T_{i,t}^{CHP} = P_{i,t}^{CHP} \times \text{HPR}_{CHP} \times \eta_{HE} \quad (7.3)$$

$$P_{\min}^{CHP} \leq P_{i,t}^{CHP} \leq P_{\max}^{CHP} \quad (7.4)$$

7.2.3 Boiler

The VEH can use the thermal output energy of boiler units to supply the thermal demand. The cost of the boiler unit can be written similarly to the CHP units. The cost of the boiler unit is given by (7.5). This cost is comprised of consuming the natural gas cost, start-up cost, and shutdown cost. The maximum and minimum power of boiler units is stated by (7.6).

$$\text{Cost}_B^t = \sum_{k=1}^{N_B} \left(\left(\lambda^{\text{NG}} \times \frac{T_{k,t}^B}{\eta_k^B} \right) + (C_k^{B,U} \times \text{SU}_{k,t}^B) + (C_k^{B,D} \times \text{SD}_{k,t}^B) \right) \quad (7.5)$$

$$P_{\min}^B \leq T_{k,t}^B \leq T_{\max}^B \quad (7.6)$$

7.2.4 Wind Farm

Wind turbines can produce electrical energy with a near-to-zero production cost. Therefore, in this chapter, it is assumed that the operation costs of wind turbines are zero. Wind turbines convert the energy of wind to electrical energy. Therefore, the output power of a wind turbine is dependent on the wind speed. In other words, during the 24 hours of a day, the output power of the wind turbine, denoted by P_t^{wind} , varies based on the wind speed. Wind turbines have three important specifications: rated wind speed, cut-in wind speed, and cut-off wind speed. When the wind speed is more than the rated speed of the wind turbine, the output power of the turbine reaches its nominal value. But it should be mentioned that wind turbines cannot produce electrical energy when the wind speed is excessive. The cut-off speed determines the maximum wind speed that wind turbine is capable of generating electrical energy. On the other hand, the cut-in speed determines the minimum wind speed required to a wind turbine to start energy production. In other words, the wind turbine cannot generate energy at speeds below the cut-in speed. When the wind speed is higher than the cut-in speed and lower than the nominal value, the output power of the wind turbine is calculated through a third-order function of wind speed. These explanations can be seen in (7.7) [22].

$$P_t^{\text{wind}} = \begin{cases} 0 & v_t^{\text{wind}} \leq v^{\text{cut-in}} \\ P^{\text{rated}} \times \left(\frac{v_t^{\text{wind}} - v^{\text{cut-in}}}{v^{\text{rated}} - v^{\text{cut-in}}} \right)^3 & v_t^{\text{wind}} \in [v^{\text{cut-in}}, v^{\text{rated}}] \\ 0 & v_t^{\text{wind}} \geq v^{\text{cut-off}} \end{cases} \quad (7.7)$$

7.2.5 Intelligent Parking Lot

In this chapter, electric vehicles are two-rolled distributed energy resources. They can offer their battery capacity to the operator of VEH for providing the required electrical energy storage capacity. Also, for distance traveling, they need to consume some portion of stored energy in their battery. It is a challenge for the VEH operator to manage these vehicles one by one. To address this, the intelligent parking lot is considered in the developed VEH model. The intelligent parking lot can aggregate the electric vehicles and their battery capacity and offer it to the operator of VEH. The arrival time of electric vehicles is uncertain. In other words, each vehicle can reach the intelligent parking lot at a different time. It is assumed that when vehicles arrive at the parking lot, they have the minimum of their battery SOC. Also, their departure time and their required surplus energy that should be stored in their battery when leaving the intelligent parking lot are uncertain. Therefore, the role of the intelligent parking lot for moderating and scheduling the behavior of electric vehicles is so significant. The electric aspects of electric vehicles are important when they reach the intelligent parking lot and when they are plugged in. During the time that vehicles are in the lot, their charging and discharging are under the control of the intelligent parking lot. The intelligent parking lot measures the real-time voltage and current of plugged-in electric vehicles to assess their state of charge (SOC), charging power, discharging power, and available capacity [23].

The profit achieved by selling electrical energy to electric vehicles in the intelligent parking lot is calculated by (7.8), where λ_t^E is the hourly electrical energy price and $Pch_{v,t}^{PHEV}$ and $Pdch_{v,t}^{PHEV}$ are hourly charging and discharging powers of vehicles, respectively. Equation (7.9) gives the SOC of electric vehicles at the arriving hour, which is assumed to be equal to the minimum SOC of vehicles. According to (7.10), the difference of SOC at an hour with the previous hour is equal to the electric current taken from the battery, which can be either positive or negative. In this equation, η_v^I denotes the current efficiency of batteries. The electrical current of battery can be calculated by having the open-circuit voltage (OCV) and closed-circuit voltage (CCV) through (7.11)–(7.13). In these equations, V_n is nominal voltage of PHEVs, α is Sensitivity parameter between SOC & OCV, F is the faraday constant, T is the temperature of battery, Rin_v^{Batt} is batteries internal resistance, and Cap_v^{PHEV} is the nominal capacity of PHEVs. Equations (7.15) and (7.16) express the amount of possible charge and discharge power of the battery, which depends on the current level of SOC, where η_v^{PHEV} represents the efficiency of PHEVs. Equations (7.17) and (7.18) state the maximum charge and discharge power that the battery is capable of, regardless of the current SOC. It should be mentioned that according to (7.20), the battery cannot be charged and discharged simultaneously, which can be controlled by $Uch_{v,t}^{PHEV}$ and $Udch_{v,t}^{PHEV}$. According to (7.21), electric vehicles cannot charge or discharge their battery, while they are disconnected from the grid. When vehicles are leaving the intelligent parking lot, they should have the required energy for their distance traveling denoted by δ_v^{PHEV} , which is given by (7.22).

$$\text{Prof}_t^{\text{HPEV}} = \sum_v^{N_v} (\lambda_t^E \times (\text{Pch}_{v,t}^{\text{PHEV}} - \text{Pdch}_{v,t}^{\text{PHEV}})) \quad (7.8)$$

$$\text{SOC}_{v,t=i_{v,t}^{\text{in}}}^{\text{PHEV}} = \text{SOC}_{v,t}^{\text{PHEV, min}} \quad t = t_{v,t}^{\text{in}} \quad (7.9)$$

$$\text{SOC}_{v,t}^{\text{PHEV}} = \text{SOC}_{v,t-1}^{\text{PHEV}} + \eta_v^I \times I_{v,t}^{\text{Batt}} \quad t_{v,t}^{\text{in}} \leq t \leq t_{v,t}^{\text{out}} \quad (7.10)$$

$$\text{OCV}_{v,t}^{\text{Batt}} = V_n + \alpha \times \frac{\mathfrak{R} \times T}{F} \log \left(\frac{\text{SOC}_{v,t}^{\text{PHEV}}}{\text{Cap}_v^{\text{PHEV}} - \text{SOC}_{v,t}^{\text{PHEV}}} \right) \quad t_{v,t}^{\text{in}} \leq t \leq t_{v,t}^{\text{out}} \quad (7.11)$$

$$\text{CCV}_{v,t}^{\text{Batt}} = \text{OCV}_{v,t}^{\text{Batt}} + \text{Rin}_v^{\text{Batt}} \times I_{v,t}^{\text{Batt}} \quad t_{v,t}^{\text{in}} \leq t \leq t_{v,t}^{\text{out}} \quad (7.12)$$

$$I_{v,t}^{\text{Batt}} = \frac{\sqrt{\text{OCV}_{v,t}^{\text{Batt}^2} + 4 \times \text{Rin}_v^{\text{Batt}} \times (\text{Pch}_{v,t}^{\text{PHEV}} - \text{Pdch}_{v,t}^{\text{PHEV}})} - \text{OCV}_{v,t}^{\text{Batt}}}{2 \times \text{Rin}_v^{\text{Batt}}} \quad t_{v,t}^{\text{in}} \leq t \leq t_{v,t}^{\text{out}} \quad (7.13)$$

$$\text{Pch}_{v,t}^{\text{PHEV}} - \text{Pdch}_{v,t}^{\text{PHEV}} = \text{CCV}_{v,t}^{\text{Batt}} \times I_{v,t}^{\text{Batt}} \quad (7.14)$$

$$\text{Pch}_{v,t}^{\text{PHEV}} \times \eta_v^{\text{PHEV}} \leq \text{Cap}_v^{\text{PHEV}} \times (1 - \text{SOC}_{v,t}^{\text{PHEV}}) \times \text{Uch}_{v,t}^{\text{PHEV}} \quad (7.15)$$

$$\frac{\text{Pch}_{v,t}^{\text{PHEV}}}{\eta_v^{\text{PHEV}}} \leq \text{Cap}_v^{\text{PHEV}} \times (\text{SOC}_{v,t}^{\text{PHEV}}) \times \text{Udch}_{v,t}^{\text{PHEV}} \quad (7.16)$$

$$\eta_v^I \times I_{v,t}^{\text{Batt}} \leq \text{Pch}_v^{\text{Max}} \times \text{Uch}_{v,t}^{\text{PHEV}} \quad (7.17)$$

$$\eta_v^I \times I_{v,t}^{\text{Batt}} \geq -\text{Pdch}_v^{\text{Max}} \times \text{Udch}_{v,t}^{\text{PHEV}} \quad (7.18)$$

$$\text{SOC}_{v,t}^{\text{PHEV, min}} \leq \text{SOC}_{v,t}^{\text{PHEV}} \leq \text{SOC}_{v,t}^{\text{PHEV, max}} \quad (7.19)$$

$$\text{Uch}_{v,t}^{\text{PHEV}} + \text{Udch}_{v,t}^{\text{PHEV}} \leq 1 \quad t_{v,t}^{\text{in}} \leq t \leq t_{v,t}^{\text{out}} \quad (7.20)$$

$$\text{Uch}_{v,t}^{\text{PHEV}} + \text{Udch}_{v,t}^{\text{PHEV}} = 0 \quad t_{v,t}^{\text{in}} \geq t \text{ or } t \geq t_{v,t}^{\text{out}} \quad (7.21)$$

$$\text{SOC}_{v,t=i_{v,t}^{\text{in}}}^{\text{PHEV}} = \text{SOC}_{v,t}^{\text{PHEV, min}} + \delta_v^{\text{PHEV}} \quad t = t_{v,t}^{\text{out}} \quad (7.22)$$

7.2.6 Thermal Buffer Tank

The thermal buffer tank is considered for the thermal energy storage system in the developed VEH model. The thermal energy stored in the thermal buffer tank at the end of each hour is calculated by (7.23), where Loss^{BT} is the loss rate, η^{BT} is the efficiency of storage, and $T_t^{\text{BT, in}}$ and $T_{\text{out}}^{\text{BT}}$ are the hourly charging and discharging power of storage, respectively. Equations (7.24)–(7.26) determine the maximum and minimum values of capacity, hourly charging energy, and hourly discharging energy of buffer tank.

$$E_t^{\text{BT,Th}} = (1 - \text{Loss}^{\text{BT}}) \times E_{t-1}^{\text{BT,Th}} + (\eta^{\text{BT}} \times T_t^{\text{BT,in}}) - \left(\frac{T_{\text{out}}^{\text{BT}}}{\eta^{\text{BT}}} \right) \quad (7.23)$$

$$\text{Cap}^{\text{BT,min}} \leq E_t^{\text{BT,TH}} \leq \text{Cap}^{\text{BT,max}} \quad (7.24)$$

$$0 \leq T_{\text{in},t}^{\text{BT}} \leq T_{\text{in}}^{\text{BT,max}} \quad (7.25)$$

$$0 \leq T_{\text{out},t}^{\text{BT}} \leq T_{\text{out}}^{\text{BT,max}} \quad (7.26)$$

7.2.7 Electrical and Thermal Markets

As mentioned, the developed virtual energy hub is connected to the power systems and the thermal network and participates in the electrical and thermal energy markets. The cost associated with buying energy from the upstream electrical market is given by (7.27). Similarly, the cost of buying energy from the thermal network can be calculated by (7.28). In these equations, P_t^{Market} and T_t^{Market} are the electrical and thermal powers, and λ_t^E and λ_t^{TH} are the hourly electrical and thermal energy prices. Equations (7.29) and (7.30) state the maximum limits for electrical and thermal networks, respectively.

$$\text{Cost}_t^{\text{EMarket}} = \lambda_t^E \times P_t^{\text{Market}} \quad (7.27)$$

$$\text{Cost}_t^{\text{THMarket}} = \lambda_t^{\text{TH}} \times T_t^{\text{Market}} \quad (7.28)$$

$$- P_{\text{max}}^{\text{line}} \leq P_t^{\text{Market}} \leq P_{\text{max}}^{\text{line}} \quad (7.29)$$

$$- T_{\text{max}}^{\text{line}} \leq T_t^{\text{Market}} \leq T_{\text{max}}^{\text{line}} \quad (7.30)$$

7.2.8 End Consumers

The VEH assures its internal end consumers to supply their electrical and thermal energy demands. The profit of selling electrical and thermal energy to the consumers is calculated by (7.31), where Load_t^E and $\text{Load}_t^{\text{TH}}$ are end consumers' electrical and thermal loads, respectively.

$$\text{Profit}_t^{\text{Cons}} = (\lambda_t^E \times \text{Load}_t^E) + (\lambda_t^{\text{TH}} \times \text{Load}_t^{\text{TH}}) \quad (7.31)$$

7.2.9 Demand Response

The consumers can participate in the demand response program and shift a percent of their hourly demand to other hours. They can shift their demand from hours with high energy prices to hours with lower prices to reduce their energy purchasing cost. Equations (7.32) and (7.33) give the demand of consumers after participating in the load shifting demand response program. Equation (7.34) states that the summation of shifted loads should be equal to zero. Equation (7.35) states the maximum amount of load that consumers can shift. In these equations, $\text{Load}_t^{E,\text{DRP}}$ is the proportion of hourly load being shifted, and δLoad_t^E is the amount of shifted power in each hour.

$$\text{Load}_t^{E,\text{Shifted}} = \text{Load}_t^E + \delta\text{Load}_t^E \quad (7.32)$$

$$\delta\text{Load}_t^E = \text{Load}_t^{E,\text{DRP}} \times \text{Load}_t^E \quad (7.33)$$

$$\sum_{t=1}^{24} \delta\text{Load}_t^E = 0 \quad (7.34)$$

$$-\text{Load}_{t,\text{max}}^{E,\text{DRP}} \leq \text{Load}_t^{E,\text{DRP}} \leq \text{Load}_{t,\text{max}}^{E,\text{DRP}} \quad (7.35)$$

7.2.10 Power Balance

One of the most important constraints in power systems and multi-energy systems problems is power balance constraints. Based on the power balance constraint, total energy production should be equal to total energy consumption. Energy production is referred to the energy generation of DERs, energy bought from the energy market, and discharge of energy storage systems. On the other hand, energy consumption is referred to the consumption of end consumers, energy sold to the energy market, and charge of energy storage systems. With these explanations, the electrical power balance is given by (7.36). Similarly, (7.37) states the thermal balance.

$$P_t^{\text{Wind}} + \sum_{i=1}^{N_{\text{CHP}}} P_{i,t}^{\text{CHP}} + \sum_{v=1}^{n_v} P_{\text{dch}_{v,t}}^{\text{PHEV}} + P_t^{\text{Market}} = \text{Load}_t^{E,\text{Shifted}} + \sum_{v=1}^{n_v} P_{\text{ch}_{v,t}}^{\text{PHEV}} \quad (7.36)$$

$$\sum_{i=1}^{N_{\text{CHP}}} T_{i,t}^{\text{CHP}} + \sum_{k=1}^{N_B} T_{k,t}^B + T_{\text{out}}^{\text{BT}} + T_t^{\text{Market}} = \text{Load}_t^{\text{TH}} + T_t^{\text{BT,in}} \quad (7.37)$$

7.2.11 Robust Optimization

In this chapter, it is considered that the parameters related to energy demand, energy price, and wind speed are uncertain. Therefore, it is not rational to study and investigate the developed VEH model by deterministic methods. Using deterministic study for a problem with uncertain parameters will lead to a large amount of economic risk imposed on VEH and its DERs. Robust optimization is one of the well-known methods for dealing with uncertainties. In robust optimization, the uncertain parameters are considered to be limited in space, called uncertainty set. Different types of uncertainty sets are developed and used in the literature.

In this chapter, we use the simple uncertainty set called the “box” uncertainty set. The box uncertainty set is the most conservative one, and it is usually used when the decision-maker wants to follow a risk-averse strategy [24]. In other words, when using the box uncertainty set for modeling the uncertain parameters, reaching the worst-case scenario that all of the uncertain parameters have their worst values is possible, while other uncertainty sets like polyhedral, ellipsoidal, etc. are less conservative and lead to solutions better than the real worst case.

Let the uncertain parameter \tilde{a} have an uncertainty set as $\tilde{a} \in [\underline{a}, \bar{a}]$. It can be rewritten using the nominal value of the uncertain parameter and its upper and lower bounds. Let \hat{a} be maximum fluctuations of the uncertain parameter \tilde{a} . Using an auxiliary variable ξ that is part of the infinity norm set U_∞ , we can write:

$$\tilde{a} = a + \xi \times \hat{a} \quad (7.38)$$

$$\xi \in U_\infty \rightarrow -\psi \leq \xi \leq \psi \quad (7.39)$$

Consider a standard form of maximization problem that has uncertain parameters in its constraints as follows:

$$\max \sum_{i=1}^{n_i} c_i \times x_i \quad (7.40)$$

S.t.

$$\sum_{i=1}^{n_i} \tilde{a}_{i,j} \times x_i \leq \tilde{b}_j \quad \forall j \quad (7.41)$$

By using (7.38), we can change the model as:

$$\max \sum_{i=1}^{n_i} c_i \times x_i \quad (7.42)$$

S.t.

$$\sum_{i=1}^{n_i} a_{i,j} \times x_i + \xi_{i,j} \times \sum_{i=1}^{n_i} \hat{a}_{i,j} \times x_i \leq b_j + \xi_j^b \times \hat{b}_j \quad \forall j \quad (7.43)$$

In robust optimization methods, the worst-case scenario is investigated. Therefore, this model can be written as:

$$\max \sum_{i=1}^{n_i} c_i \times x_i \tag{7.44}$$

S.t.

$$\sum_{i=1}^{n_i} a_{i,j} \times x_i + x_0 \times b_j + \max \left(\xi_{i,j} \times \sum_{i=1}^{n_i} \hat{a}_{i,j} \times x_i + \xi_{0,j} \times \hat{b}_j \times x_0 \right) \leq 0 \quad \forall j \tag{7.45}$$

where x_0 is an artificial variable, which is equal to -1 . By finding the maximum of enclosed term, the final optimization model using RO uncertainty modeling will be as follows:

$$\max \sum_{i=1}^{n_i} c_i \times x_i \tag{7.46}$$

S.t.

$$\sum_{i=1}^{n_i} a_{i,j} \times x_i + x_0 \times b_j + \psi \left(\sum_{i=1}^{n_i} \hat{a}_{i,j} \times |x_i| + \hat{b}_j \times x_0 \right) \leq 0 \quad \forall j \tag{7.47}$$

If $x_i \geq 0 \quad \forall i$, then we can use x_i itself instead of the absolute value. But if not, the developed model can be linearized as follows:

$$\max \sum_{i=1}^{n_i} c_i \times x_i \tag{7.48}$$

S.t.

$$\sum_{i=1}^{n_i} a_{i,j} \times x_i + \psi \left(\sum_{i=1}^{n_i} \hat{a}_{i,j} \times u_i - \hat{b}_j \right) \leq b_j \quad \forall j \tag{7.49}$$

$$-u_i \leq x_i \leq u_i \tag{7.50}$$

$$u_i \geq 0 \tag{7.51}$$

Now, consider a standard form of maximization problem that in addition to the constraints, it also has uncertain parameters in the objective function as follows:

$$\max \sum_{i=1}^{n_i} (\tilde{c}_i \times x_i + \tilde{d}_i) \tag{7.52}$$

$$\begin{aligned} & \text{S.t.} \\ & \sum_{i=1}^{n_i} \tilde{a}_{i,j} \times x_i \leq \tilde{b}_j \quad \forall j \end{aligned} \quad (7.53)$$

In order to implement the robust uncertainty set, this model should be converted as follows:

$$\max Z \quad (7.54)$$

$$\begin{aligned} & \text{S.t.} \\ & Z - \sum_{i=1}^{n_i} (c_i \times x_i) \leq \sum_{i=1}^{n_i} \tilde{d}_i \end{aligned} \quad (7.55)$$

$$\sum_{i=1}^{n_i} \tilde{a}_{i,j} \times x_i \leq \tilde{b}_j \quad \forall j \quad (7.56)$$

With the same procedure, we can implement the robust modeling of uncertainties using the box uncertainty set.

7.3 Simulation

In this section, the simulation results of the developed VEH structure and the intelligent parking lot are presented. The developed system is a mixed integer nonlinear programming (MINLP) problem because of the logarithmic function in the intelligent parking lot modeling. It should be simulated using proper software and be optimized using strong solvers. The proposed optimization problem is simulated using the GAMS software and SBB solver, which show acceptable performance when dealing with nonlinear problems. The computer system that is used for running the optimization problem has an Intel Core i7 CPU and 8 gigabytes of RAM.

Developed VEH has various aspects for investigating. We study and discuss the developed multi-energy system in two case studies. In case study 1, the VEH model and the intelligent parking lot are optimized without the load shift demand response program. By concluding case study 1, we will have a benchmark to discuss the impacts of the demand response program on the VEH profit and the intelligent parking lot scheduling. In case study 2, we discuss the effects of the demand response program on the VEH performance and its energy transactions.

7.3.1 Input Data

The developed VEH is connected to power systems and the thermal network and supplies electrical and thermal demand of end consumers. Figure 7.3 shows the hourly electrical and thermal data [25]. The VEH operator schedules the DERs and energy transactions with electrical and thermal energy markets based on the hourly electrical and thermal energy prices. The electrical and thermal energy prices are given by Fig. 7.4. The data related to the electrical energy demand and the electrical price are assumed to be uncertain, and the nominal values of them are depicted in these figures. The maximum power limit between the VEH and electrical and thermal network is considered equal to 1000 kWh and 500 kWh, respectively. Also, the data associated with the hourly wind speed is taken from [25].

The thermal buffer tank data can be found in Table 7.1. Two CHP units and two boiler units as conventional power plants are considered in the VEH structure. The data related to CHP units is given by Table 7.2. Also, the data related to boiler units

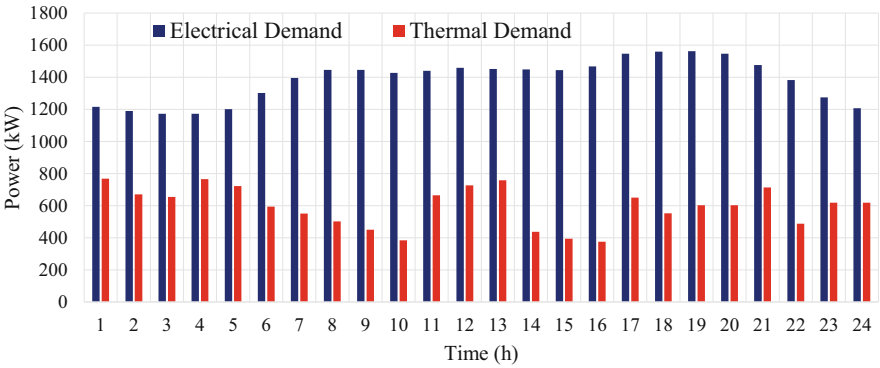


Fig. 7.3 Data related to the electrical and thermal demand

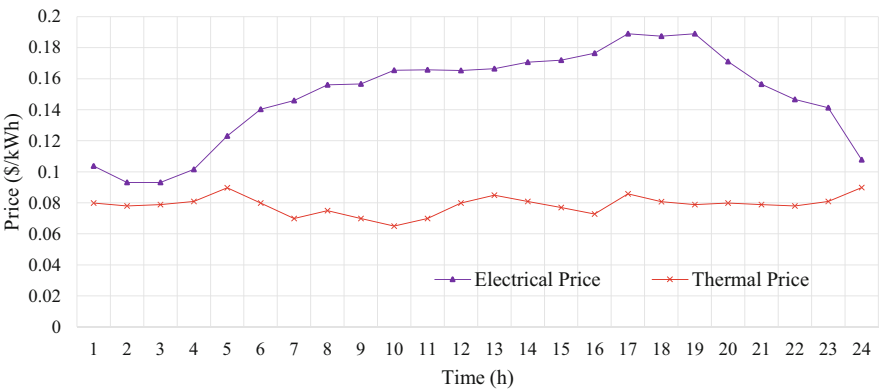


Fig. 7.4 Data related to the electrical and thermal energy price

Table 7.1 Data related to the BT

Parameter	Value
η_c	0.98
η_{dc}	0.98
Loss	0.02
Cap^{\max}	1800 kW
Cap^{\min}	400 kW
P_{ch}^{\max}	800 kW
$P_{dch}^{BSS, \max}$	800 kW

Table 7.2 Data related to the CHP units

Unit	Elec./ther. conversion efficiency	Capacity (kW)	Startup/shutdown cost (\$)
#1	0.36/0.38	350	2.1/2.1
#2	0.45/0.5	350	2.1/2.1

Table 7.3 Data related to the boiler units

Unit	Efficiency	Capacity (kW)	Startup/shutdown cost (\$)
#1	0.70	150	0.3
#2	0.80	150	0.3

are given in Table 7.3. These units use natural gas to produce electrical and thermal energies for selling in the energy markets or supplying the end consumers’ demand. The natural gas price is considered constant equal to 0.45 \$/kWh.

The studied VEH contains one intelligent parking lot for smart charging and discharging of electric vehicles. It is considered that twenty electric vehicles exist in the VEH territory. These vehicles have random and uncertain behaviors. Therefore, their arrival time, departure time, and required energy for the rest of the day after departing the intelligent parking lot are uncertain parameters. We assume that vehicles can enter the intelligent parking lot after hour 6. It is also assumed that they can stay in the intelligent parking lot for 8 hours, but they can leave the lot earlier. Also, because the vehicles are equipped with different types of batteries, the nominal capacity of the vehicle’s battery is random. Any of these uncertain parameters are handled by producing random numbers for modeling the random behavior of electric vehicles. The data related to the electric vehicles and intelligent parking lot are derived from [23], which is presented in Table 7.4.

Table 7.4 The specifications of the intelligent parking lot and electric vehicles

Parameter	Value	Parameter	Value
$SOC_{v,t}^{PHEV, max}$	1	t_v^{in}	[6,16]
$SOC_{v,t}^{PHEV, min}$	0.1	Staying time	[2,8]
Pch_v^{Max}	[0.9,1]	F	9,650,000
$Pdch_v^{Max}$	[0.9,1]	α	15
η_v^{PHEV}	0.95	\mathfrak{R}	8.31
δ_v^{PHEV}	[0.3,0.6]	T	35
η_v^t	0.85	V_n	120
Cap_v^{PHEV}	[90,110]	R_{in}	0.4

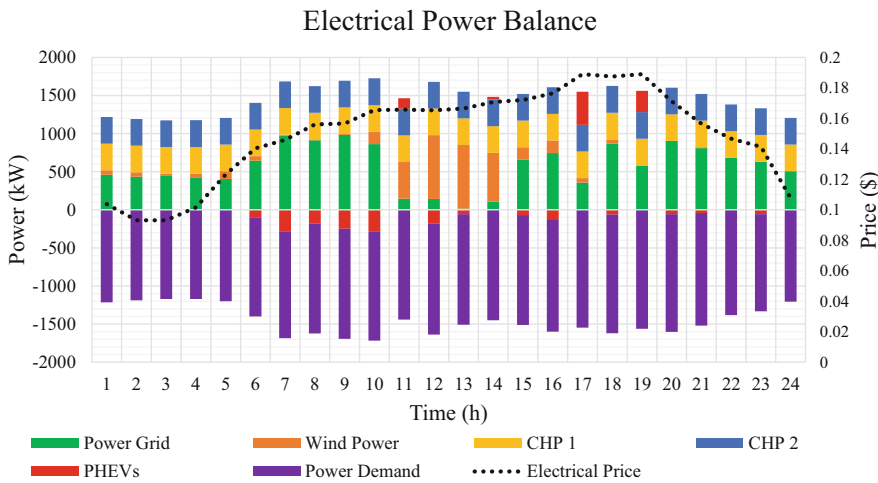


Fig. 7.5 The electrical power balance

7.3.2 Case Study 1

In this case study, the developed system is simulated without considering the emission tax and demand response program. It is assumed that all uncertain parameters have variations as 0.05% of their nominal values. The VEH model is optimized in this case by considering $\psi = 1$. In this situation, the optimal profit of VEH from participating in the electrical and thermal markets is \$2080.50. Since the worst-case robust optimization is used in this chapter, it is guaranteed that the real optimal profit of VEH will not be lower than this achieved value. Figure 7.5 shows the power balance related to electrical energy. At all hours, the equality of generation and consumption should be satisfied. This figure shows the scheduling of DERs and energy transactions between the electrical energy market and the VEH. All decision variables are taken value based on the hourly electrical and thermal energy prices. CHP units that can produce electrical and thermal energies are active during the

24 hours of the day to supply both electrical and thermal demands. They have high start-up and shutdown costs. Therefore, it will impose a big cost to the VEH if CHP units get shut down and start up again. When the energy price is high, the VEH operator tries to sell the generated power by its DERs in the upstream electrical market to gain the most possible money. On the other hand, when the energy price is low, the operator decides to buy more energy from the electrical energy market and sell lower amount of energy in this market. As a result, at low-energy price hours, the energy storage systems are charged with the energy generated by DERs and shift this charged power to the hours that have high energy prices. In this chapter, the intelligent parking lot is considered to play the role of an energy storage system. It can be seen that at hours 17 and 19, where the energy price has its maximum values, the discharge of PHEVs supplies a significant amount of electrical energy demand. As seen in Fig. 7.5, because the energy demand level is more than the total capacity of DERs, during the 24 hours of the day, the VEH decides to import energy from the energy market to fulfill some percent of electrical energy demand. At the middle hours of the day, when the wind speed is high enough, the wind farm starts to generate energy. At hours 10 to 14, wind turbines supply a large amount of energy demand that causes a big reduction in the energy bought from the electrical energy market.

The intelligent parking lot controls the charging and discharging of electric vehicles when they arrive and get connected to the electrical grid. The total amount of hourly charging and discharging power of electric vehicles in the intelligent parking lot is shown in Fig. 7.10. As mentioned earlier, the arrival time and departure time of electric vehicles are uncertain. The random numbers are produced to determine when vehicles enter the intelligent parking lot and when they leave it. The entrance time, leaving time, and the SOC of electric vehicles when they are in the intelligent parking lot are shown in Figs. 7.6, 7.7, 7.8, and 7.9. Because the SOC of electric vehicles when they are driving is not important, the SOC of these vehicles when they are out of the intelligent parking lot is neglected. When vehicles arrive at the intelligent parking lot, they have their minimum SOC. Therefore, most of their battery capacity is free to use for charging the electrical energy. The intelligent parking lot tries to charge these vehicles when the energy price is low and profitable. Because many of the vehicles have arrived before the expensive hours, the intelligent parking lot has charged their battery to near to full. When the energy price rises, like hours 11, 14, 15, and 17 o'clock, the intelligent parking lot discharge the stored energy in batteries of electric vehicles to earn more money. When vehicles are ready for leaving, they charge their battery a bit to get the required energy for their traveling for the rest of the day. Fig. 7.10 shows the total amount of charging and discharging of electric vehicles that are aggregated by intelligent parking lot. The two peaks of discharging have happened at hours 15 and 17, where the energy price reached its maximum numbers, according to Fig. 7.4.

In order to analyze the thermal part of the developed VEH, the thermal power balance is shown in Fig. 7.11. As same as the electrical energy, the equality between the generation and consumption of thermal energy should be satisfied at all hours of the day. It can be seen that the thermal power balance constraint is totally satisfied at all hours. As mentioned in the electrical power balance part, the CHP units are active

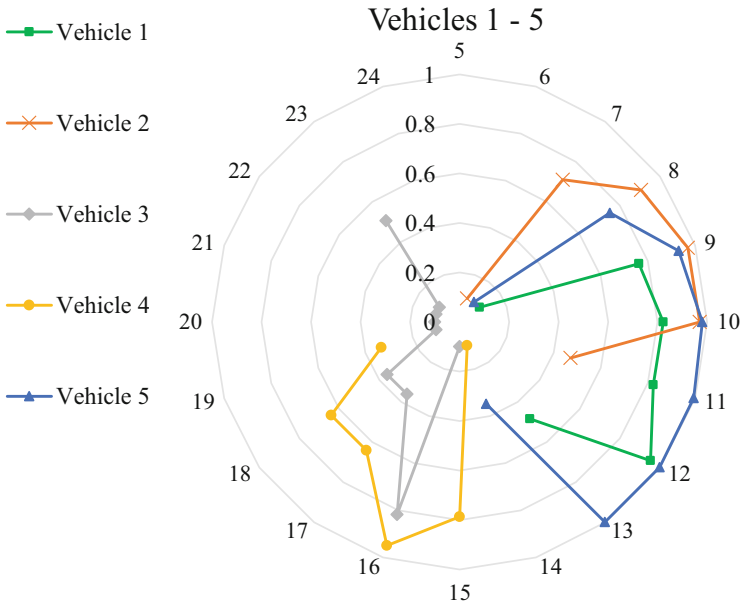


Fig. 7.6 SOC of vehicles (vehicles 1–5)

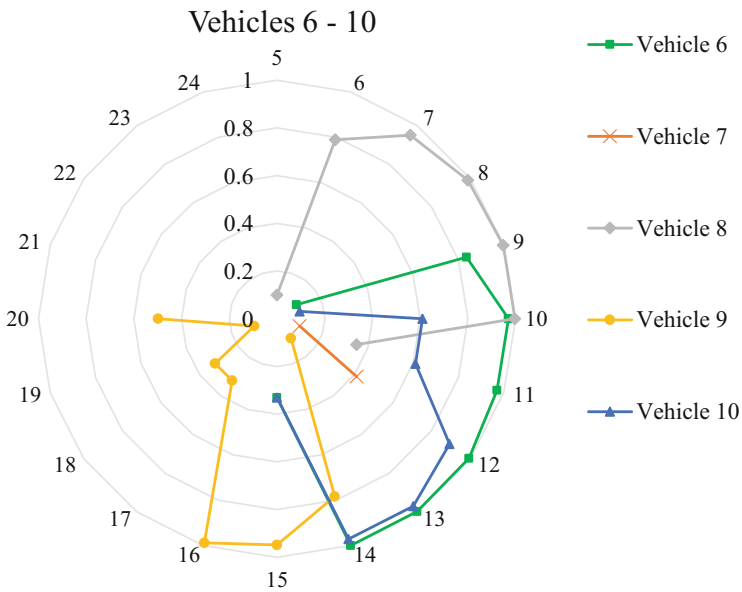


Fig. 7.7 SOC of vehicles (vehicles 6–10)

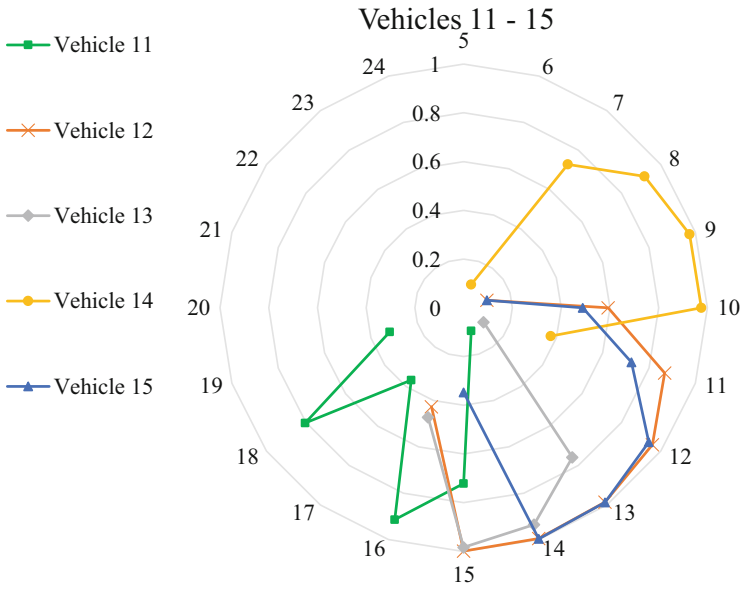


Fig. 7.8 SOC of Vehicles (Vehicles 11–15)

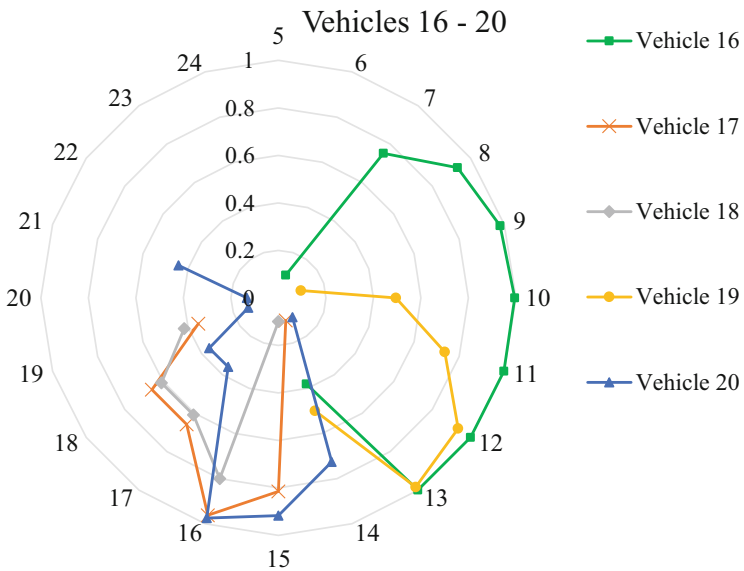


Fig. 7.9 SOC of vehicles (vehicles 16–20)

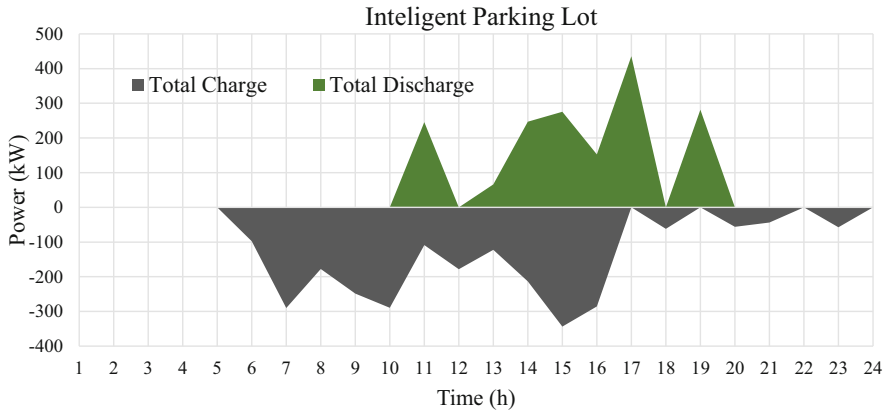


Fig. 7.10 Total charging and discharging of electric vehicles in the intelligent parking lot

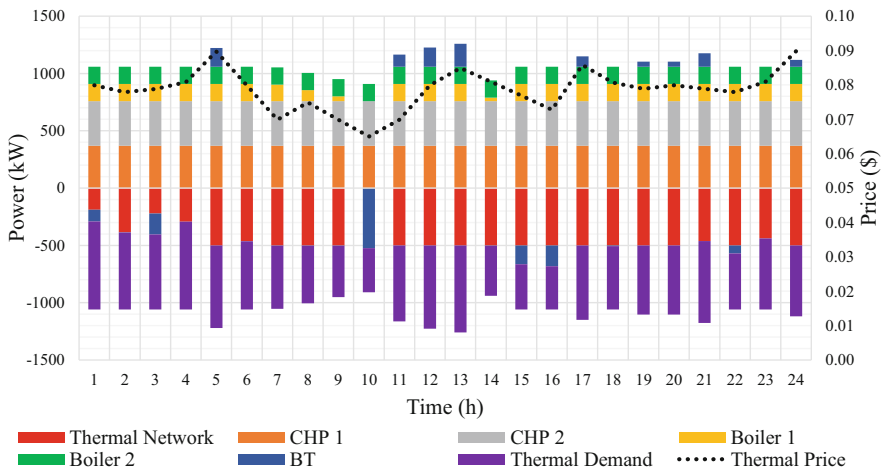


Fig. 7.11 Thermal power balance

during the 24 hours of the day. They provide the most of thermal energy demand required by end consumers. In addition to the CHP units, the boilers also can generate thermal energy. Boiler 2 is more cost-effective than boiler 1. As a result, it produces maximum capacity. On the other hand, boiler 1 just produces energy when the thermal energy price is high enough to make the production of boiler 1 profitable. For example, at 10 o'clock, when the thermal energy price is so low, boiler 1 stops the energy generation.

The energy transactions with the upstream thermal markets depend on the hourly thermal energy price. When the thermal energy price is high, it is more profitable to sell the thermal energy in these markets. In contrast, when the energy price reaches the lower number, the VEH can buy energy from the thermal energy market. It can

be seen that because the thermal energy price is high enough in almost all hours of the day, except hour 10, the VEH operator decides to sell energy produced by its DERs to earn money.

The thermal buffer tank performs in a way to maximize the total profit gained by VEH. For that, it should be charged in cheap hours and discharge the stored power at hours with higher thermal energy prices. For example, it can be observed that at 10 o'clock, the BT has been charged heavily. Then, it discharges the energy at 11, 12, and 13 o'clock. This process leads to energy shifting from hours with low-energy prices to the expensive hours in order to sell the thermal energy at higher prices.

7.3.3 Case Study 2

In this case study, the effects of the demand response program on the performance of developed VEH are investigated. The demand response can reduce the cost of energy production in peak-load hours. It is possible that at peak-load hours, the VEH is forced to turn on a unit with high operation cost, which can increase the final energy price in the energy markets. Demand response program can reduce these peaks and the energy price. On the other hand, the end consumers try to shift their load to hours that have lower prices to reduce their energy purchasing cost. Therefore, the electrical demand is reduced at the expensive hours and is increased at the hours with the low level of electrical energy price. By considering a maximum 20% of hourly shifting load, the profit of VEH is increased to \$2102.16. The electrical demand of end consumers before and after the participation in the demand response

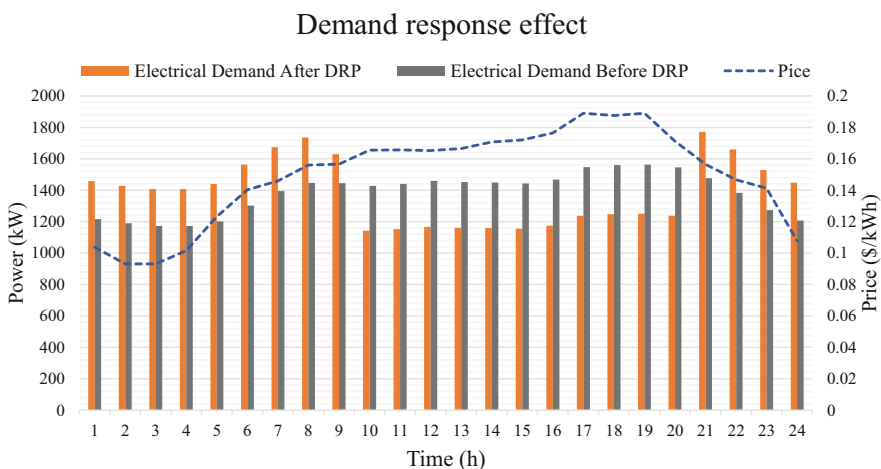


Fig. 7.12 Electrical demand before and after the demand response program

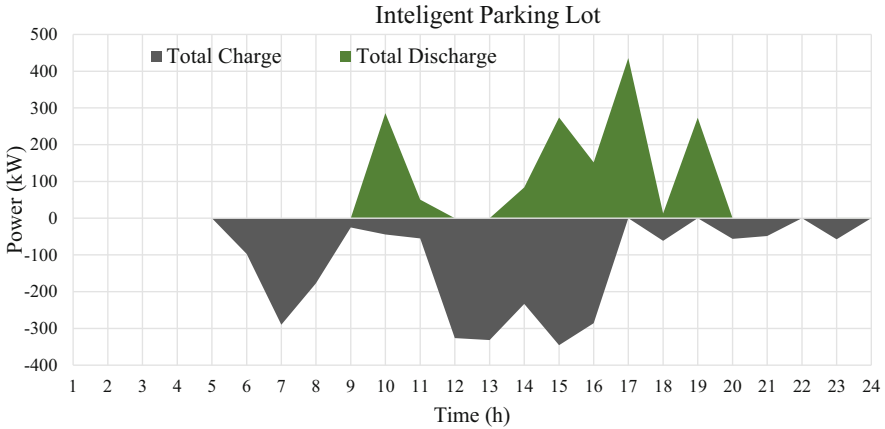


Fig. 7.13 Charging and discharging of the intelligent parking lot after demand response program

program is shown in Fig. 7.12. It can be seen that end consumers have reduced their consuming load at hours 10–20 o'clock and shifted the reduced load to the other hours. For example, their demand at early and late hours of the day is increased to get their energy demand at lower prices. It should be mentioned that the method of demand response that is used in this chapter is the load shifting demand response program. In this method, the total amount of consuming load of consumers remains the same. However, they can consume some of their non-priority demands at other hours than it supposed to be.

Demand response can affect the performance of intelligent parking lot and electric vehicles in it. It can be noticed from Fig. 7.10 that the electric vehicles are doing charge and discharge during the mid-hours. Because a large percentage of demand is shifted from mid-hours of the day, the effects of demand response program on the scheduling of the intelligent parking lot can be significant. We can say that demand response programs can reduce the need for large energy storage systems. In other words, the load shifting demand response is much similar to shifting generated energy by energy storage systems. As a result, the required investment for developing the multi-energy systems can be reduced by participation of end consumers in the demand response program. The total amount of charging and discharging of electric vehicles operated by the intelligent parking lot is shown in Fig. 7.13. Compared to case study 1, the total discharged energy from electric vehicles during the 24 hours is reduced from 1704.45 to 1567.39 kWh.

7.4 Conclusion

In this chapter, the short-term self-scheduling of a VEH for participating in the electrical and thermal markets was presented. The VEH consists of various DERs for supplying the electrical and thermal energy demands. The plug-in hybrid electric

vehicles were considered in the VH structure. For handling and aggregating the plug-in hybrid electric vehicles, the intelligent parking lot was modeled to be able to operate the electric vehicles in a smart way. The electric vehicles' random behavior was considered to simulate the VEH in near-to-reality situations. We used the RO method to deal with uncertainties and optimize the developed VEH model. This model can be a high potential solution to be able to integrate the power systems with thermal networks and transportation system. Also, we investigated the effects of the demand response program on the need for energy storage equipment. The result showed that by considering a 20% demand response program, the charging and discharging energy of energy storage systems is reduced.

References

1. Akorede MF, Hizam H, Pouresmaeil E (2010) Distributed energy resources and benefits to the environment. *Renew Sust Energ Rev* 14(2):724–734. <https://doi.org/10.1016/J.RSER.2009.10.025>
2. Jadidbonab M, Mohammadi-Ivatloo B, Marzband M, Siano P (2021) Short-term self-scheduling of virtual energy hub plant within thermal energy market. *IEEE Trans Ind Electron* 68(4): 3124–3136. <https://doi.org/10.1109/TIE.2020.2978707>
3. Mohammadi M, Noorollahi Y, Mohammadi-ivatloo B, Yousefi H (2017) Energy hub: from a model to a concept – a review. *Renew Sust Energ Rev* 80:1512–1527. <https://doi.org/10.1016/J.RSER.2017.07.030>
4. Saboori H, Mohammadi M, Taghe R (2011) Virtual power plant (VPP), definition, concept, components and types. In: *Asia Pacific Power & Energy Engineering Conference (APPEEC)*. <https://doi.org/10.1109/APPEEC.2011.5749026>
5. Seyfi M, Mehdinejad M, Mohammadi-Ivatloo B, Shayanfar H (2022) Scenario-based robust energy management of CCHP-based virtual energy hub for participating in multiple energy and reserve markets. *Sustain Cities Soc* 80:103711. <https://doi.org/10.1016/J.SCS.2022.103711>
6. Heidari A, Mortazavi SS, Bansal RC (2020) Stochastic effects of ice storage on improvement of an energy hub optimal operation including demand response and renewable energies. *Appl Energy* 261:114393. <https://doi.org/10.1016/J.APENERGY.2019.114393>
7. Zhang H, Cao Q, Gao H, Wang P, Zhang W, Yousefi N (2020) Optimum design of a multi-form energy hub by applying particle swarm optimization. *J Clean Prod* 260:121079. <https://doi.org/10.1016/J.JCLEPRO.2020.121079>
8. Tan Z, Yang S, Lin H, De G, Ju L, Zhou F (2020) Multi-scenario operation optimization model for park integrated energy system based on multi-energy demand response. *Sustain Cities Soc* 53:101973. <https://doi.org/10.1016/J.SCS.2019.101973>
9. Luo XJ, Oyedele LO, Akinade OO, Ajayi AO (2020) Two-stage capacity optimization approach of multi-energy system considering its optimal operation. *Energy AI* 1:100005. <https://doi.org/10.1016/J.EGYAI.2020.100005>
10. Najafi A, Tavakoli A, Pourakbari-Kasmaei M, Lehtonen M (2021) A risk-based optimal self-scheduling of smart energy hub in the day-ahead and regulation markets. *J Clean Prod* 279: 123631. <https://doi.org/10.1016/J.JCLEPRO.2020.123631>
11. Zahedmanesh A, Muttaqi KM, Sutanto D (2021) A cooperative energy management in a virtual energy hub of an electric transportation system powered by PV generation and energy storage. *IEEE Trans Transp Electr* 7(3):1123–1133. <https://doi.org/10.1109/TTE.2021.3055218>
12. Ahrabi M, Abedi M, Nafisi H, Mirzaei MA, Mohammadi-Ivatloo B, Marzband M (2021) Evaluating the effect of electric vehicle parking lots in transmission-constrained AC unit

- commitment under a hybrid IGDT-stochastic approach. *Int J Electr Power Energy Syst* 125. <https://doi.org/10.1016/j.ijepes.2020.106546>
13. Mirzaei MA, Zare K, Mohammadi-Ivatloo B, Marzband M, Anvari-Moghaddam A (2021) Robust network-constrained energy management of a multiple energy distribution company in the presence of multi-energy conversion and storage technologies. *Sustain Cities Soc* 74: 103147. <https://doi.org/10.1016/J.SCS.2021.103147>
 14. Razipour R, Moghaddas-Tafreshi SM, Farhadi P (2019) Optimal management of electric vehicles in an intelligent parking lot in the presence of hydrogen storage system. *J Energy Storage* 22:144–152. <https://doi.org/10.1016/J.EST.2019.02.001>
 15. Yu S, Fang F, Liu Y, Liu J (2019) Uncertainties of virtual power plant: problems and countermeasures. *Appl Energy* 239:454–470. <https://doi.org/10.1016/j.apenergy.2019.01.224>
 16. Tian MW et al (2019) Risk-based stochastic scheduling of energy hub system in the presence of heating network and thermal energy management. *Appl Therm Eng* 159:113825. <https://doi.org/10.1016/J.APPLTHERMALENG.2019.113825>
 17. Shahrabi E, Hakimi SM, Hasankhani A, Derakhshan G, Abdi B (2021) Developing optimal energy management of energy hub in the presence of stochastic renewable energy resources. *Sustain Energy Grids Netw* 26:100428. <https://doi.org/10.1016/J.SEGAN.2020.100428>
 18. Dolatabadi A, Jadidbonab M, Mohammadi-Ivatloo B (2019) Short-term scheduling strategy for wind-based energy hub: a hybrid stochastic/IGDT approach. *IEEE Trans Sustain Energy* 10(1): 438–448. <https://doi.org/10.1109/TSTE.2017.2788086>
 19. Lu X, Liu Z, Ma L, Wang L, Zhou K, Feng N (2020) A robust optimization approach for optimal load dispatch of community energy hub. *Appl Energy* 259:114195. <https://doi.org/10.1016/J.APENERGY.2019.114195>
 20. Lu X, Liu Z, Ma L, Wang L, Zhou K, Yang S (2020) A robust optimization approach for coordinated operation of multiple energy hubs. *Energy* 197:117171. <https://doi.org/10.1016/J.ENERGY.2020.117171>
 21. Lekvan AA, Habibifar R, Moradi M, Khoshjahan M, Nojavan S, Jermisittiparsert K (2021) Robust optimization of renewable-based multi-energy micro-grid integrated with flexible energy conversion and storage devices. *Sustain Cities Soc* 64:102532. <https://doi.org/10.1016/J.SCS.2020.102532>
 22. SoltaniNejad Farsangi A, Hadayeghparast S, Mehdinejad M, Shayanfar H (2018) A novel stochastic energy management of a microgrid with various types of distributed energy resources in presence of demand response programs. *Energy* 160:257–274. <https://doi.org/10.1016/j.energy.2018.06.136>
 23. Nosratabadi SM, Jahandide M, Guerrero JM (2021) Robust scenario-based concept for stochastic energy management of an energy hub contains intelligent parking lot considering convexity principle of CHP nonlinear model with triple operational zones. *Sustain Cities Soc* 68:102795. <https://doi.org/10.1016/J.SCS.2021.102795>
 24. Guan Y, Wang J (2014) Uncertainty sets for robust unit commitment. *IEEE Trans Power Syst* 29(3):1439–1440. <https://doi.org/10.1109/TPWRS.2013.2288017>
 25. Seyfi M, Mehdinejad M, Shayanfar H (2021) Deep Learning-based self-scheduling of virtual energy hub considering phase change material-based thermal energy storage. In: 2021 11th Smart Grid Conference (SGC 2021). <https://doi.org/10.1109/SGC54087.2021.9664174>

Chapter 8

Hybrid Interval-Stochastic Optimal Operation Framework of a Multi-carrier Microgrid in the Presence of Hybrid Electric and Hydrogen-Based Vehicles Intelligent Parking Lot



Masoud Agabalaye-Rahvar, Amir Mirzapour-Kamanaj, Kazem Zare, and Amjad Anvari-Moghaddam

Abstract As to deliver sustainable and reliable energy to demands with low emission, a multi-carrier microgrid (MCMG) structure has been proposed. Hybrid electric and hydrogen-based vehicles (HEHVs) have been introduced to facilitate decarbonized and decentralized coupled energy systems for decision-makers. So, HEHVs intelligent parking lot (IPL) integrated with MCMG is an appropriate solution. Accordingly, the considered MCMG in this chapter supplies multi-energy demands (MEDs), i.e., electrical, thermal, and cooling, via various technologies besides exchanging power and natural gas from the respective upstream grids. The uncertainty of HEHVs' driving patterns, generation of renewable energy sources (RESs), and consumption of MEDs are modeled via the scenario-based stochastic; however, an interval-based optimization approach is taken for the market price uncertainty. Consequently, numerical results indicated the effectiveness of the introduced hybrid interval-stochastic model in which the deviation of overall operation cost is reduced up to 67.47%, while the average cost approximately is increased up to 1.87%.

Keywords Multi-carrier microgrid · Interval optimization framework · Optimal integrated operation · Electric and hydrogen-based vehicles · Renewable energy sources · Multi-energy storages · Uncertainty management · SCENRED tool

M. Agabalaye-Rahvar (✉) · A. Mirzapour-Kamanaj · K. Zare
Faculty of Electrical and Computer Engineering, University of Tabriz, Tabriz, Iran
e-mail: m.agabalaye@tabrizu.ac.ir; a.mirzapour@tabrizu.ac.ir; kazem.zare@tabrizu.ac.ir

A. Anvari-Moghaddam
Department of Energy Technology, Aalborg University, Aalborg, Denmark
e-mail: aam@et.aau.dk

8.1 Introduction

Since the population growth trend has increased worldwide in recent decades, supplying multi-energy demands (MEDs) has been given remarkable attention by policymakers and researchers in terms of low greenhouse gas emissions, low operation cost, more energy efficiency, and more robustness. So achieving the mentioned goals and integrating various energy infrastructures along with increasing the penetration rates of renewable energy sources (RESs) have been indispensable [1]. Also, to provide an accessibility vision of coordinating these networks, integrated analysis has been accomplished in [2]. In this environment, the concept of multi-carrier microgrids (MCMGs) has appeared sufficiently with clean energy sources (CESs) as well as hydrogen-based emerging technologies [3, 4]. One of these CESs is producing hydrogen from RESs via deploying electrolyzers, which could be directly injected into hydrogen-based industries and/or utilized in fuel cells to produce power in terms of having a stable, flexible, and reliable system. The other great motivation for facilitating the path to obtaining considered goals, applications of hydrogen vehicles (HVs) and electric vehicles (EVs) in smart microgrids (SMGs) have been hastened as a promising mobility option [5]. These EVs and HVs could be executed in the vehicle-to-grid (V2G) mode to provide ancillary services and large-capacity provisions, while the grid-to-vehicle (G2V) mode acts as a load in off-peak times of the system [6].

Accordingly, various researches have been conducted around the optimal scheduling and optimal planning structures of MCMGs with different flexible emerging technologies. In this way, several methodologies were adopted to deal with the upcoming challenges. Authors in [7] have introduced optimal planning and sizing of components for MCMG by considering net zero-emission (NZE), which was modeled as a two-stage proposed method. In another work [8], cooperative optimal planning and design of MCMG have been performed with regard to the demand response program (DRP). In order to improve reliability, reduce greenhouse gas emissions, and also reduce network losses, co-optimizing formulation of the reliability-constrained MCMG has been represented in [9], acquiring the best type and size of each component as well as optimal dispatch. Reference [10] has specified two-stage cost-effective planning and scheduling model for MG coupled with compressed air energy storage (CAES). The first stage of that is determining the optimal location and size via considering two objectives as power loss and voltage deviation, while stochastic scheduling is performed in the second stage. For the integrated energy system of several sub-networks, i.e., electrical, natural gas, and district heating types in [11], optimal day-ahead operational planning has been proposed and investigated flexibility provisions of energy storage systems (ESSs) via novel pricing policy-based economic approach. Also, for the interdependent mentioned three sub-networks in [11], the day-ahead optimal scheduling of networked MCMG has been provided by [12] to increase energy efficiency, reliability, and security of the system. Despite the metaheuristic optimization algorithm, i.e., modified whale optimization algorithm was used as a solution method in [12], a

mixed-integer linear programming (MILP) approach has been utilized through [13] to achieve optimum energy management constrained with the AC power flow model in MCMG. Owing to occur severe uncertainties in renewable-based MCMG, authors in [14] have offered the probabilistic optimal power flow dispatch coordinated with novel time-based demand-side management (DSM) via mixed-integer nonlinear programming (MINLP). Another work to realize the optimal scheduling of MCMGs is about taking external shocks. So, Ref. [15] has made known resiliency-oriented day-ahead and optimal real-time scheduling of multi-carrier energy systems, which was modeled as an iterative three-stage optimization form. An optimum resilient three-stage optimization model for a multi-carrier distribution system [16] has been proposed in which non-utility plug-in EV (PEV) aggregators and ESSs aggregators could sell their electricity. A robust framework based on the model predictive control (MPC) approach has been utilized in [17] for optimal energy scheduling of MCMG under uncertainties related to RESs' generations and electrical/thermal consumption demands. A hybrid robust-stochastic technique has been presented in [5] to overcome all random parameters such as RESs, local demands, driven patterns of EVs, and also market price for the proposed MCMG. The strategically scheduled offering/bidding of PEVs and wind farm has been modeled with a bilevel multi-objective hybrid robust-stochastic algorithm in [18], such that minimizing two objectives as cost and emission in the upper level while maximizing the social welfare in the lower level has been performed. The other hybrid framework called stochastic-interval has been indicated in [19] to preserve heterogeneous uncertainties in the decision-making operation strategy of MCMG such that a scenario-based two-stage method has been utilized. Operational scheduling and management of MCMG integrated with EV IPL and price-based and incentive-based DRP flexible technologies have been demonstrated in [20]. Consideration of two objectives as economic and environmental in optimal scheduling of renewable-based MCMG equipped with EV IPL and incentive-based DRP has been taken via [21]. Therefore, the hybrid robust-stochastic deployed model for the problem [21] has been formulated through the MILP approach. As hydrogen deployment is increased in recent years due to having significant benefits of green and clean energy, hydrogen storage systems (HSSs) coordinated with MCMGs. Authors in [22] have presented a suitable scheduling environment for an optimum complemented hydrogen-based smart energy hub (EH) that addressed system fluctuations with the hybrid robust-stochastic procedure. Stochastic scheduling of smart multi-carrier EH coordinated with HSS and DRP in terms of economic and environmental aspects has been conducted in [23] to fulfill the obtained system's profits. In Ref. [24], HVs have been incorporated with real specifications of multi-carrier ESSs to obtain optimal deterministic scheduling. Optimal coordinative HVs, price-based DRP, and ESSs have been indicated in [25], along with utilizing modified risk-constrained stochastic scheduling to address the uncertainties appropriately within the MILP approach. For the hydrogen-based MCMG that participates in power, natural gas, thermal, and hydrogen market [26], a risk-averse hybrid robust-stochastic technique is integrated into the model not only to handle fluctuations of RESs and market price but also take techno-economic benefits. Also, authors in [27] have

investigated the application of power-to-hydrogen (P2H) technology in interconnected power, natural gas, and thermal networks via the conditional value at risk (CVaR)-based stochastic scheduling model. The power-to-gas (P2G) and P2H flexible technologies in modern coupled power and hydrogen networks [28] highlighted the synergy operation between these energy carriers to achieve maximum daily profit using the probabilistic-based Monte Carlo simulation (MCS) method. Another CVaR-based stochastic scheduling framework for considered EH consists of RESs, combined heat and power (CHP), fuel cell power plant (FCPP), PEVs, and electrical/thermal DRP [29] developed in order to reduce emission expenditure.

According to the scrutinization of the aforementioned studies and researches in the literature, some research gaps could be determined. So in most previous works, some uncertain parameters such as RESs, several considered demands, electricity market price, and driving patterns of EVs/HVs are handled through the hybrid robust-stochastic frameworks in MCMG infrastructure. Furthermore, despite providing several advantages by the applications of flexible emerging green energy called hydrogen production from RESs in integrated energy systems, it has only been taken in a few recent studies. Also, coordinated operations of EVs/HVs in the concept of IPL have not been widely modeled and investigated under the unpredictable behaviors of these fleets. Thus, to solve the abovementioned shortcomings, a renewable-based MCMG integrated with EVs/HVs IPL is proposed within the existence of inherent uncertainties in this chapter. The main contributions are categorized as follows:

1. Managing uncertainty of RESs outputs, i.e., PV and wind generations, considered electrical, thermal, and cooling demands, unpredictable behavior of HEHVs owners, and also electricity market price has been handled via an appropriate hybrid stochastic-interval method.
2. Smart charging and discharging provisions of each EVs/HVs in IPL have been illustrated to obtain cost-effective strategies in the MCMG decision-making process framework.
3. Another flexible technology called green hydrogen energy is developed either to be directly used in fueling HVs or converted back to power in required peak demands.

The rest of this chapter is organized as follows: Sect. 8.2 provides detailed descriptions of the renewable-based MCMG model integrated with HEHV IPL, and then in Sect. 8.3, the proposed problem formulation is defined. Various case studies along with simulation results are indicated in Sect. 8.4. Finally, the outstanding findings conclude in Sect. 8.5.

8.2 Problem Description

Various actions such as storing, or controlling multiple energies for diverse purposes can be accomplished via the MCMGs concept [30]. In other words, multiple energies could be entered as input for MCMG such that after converting, storing, and

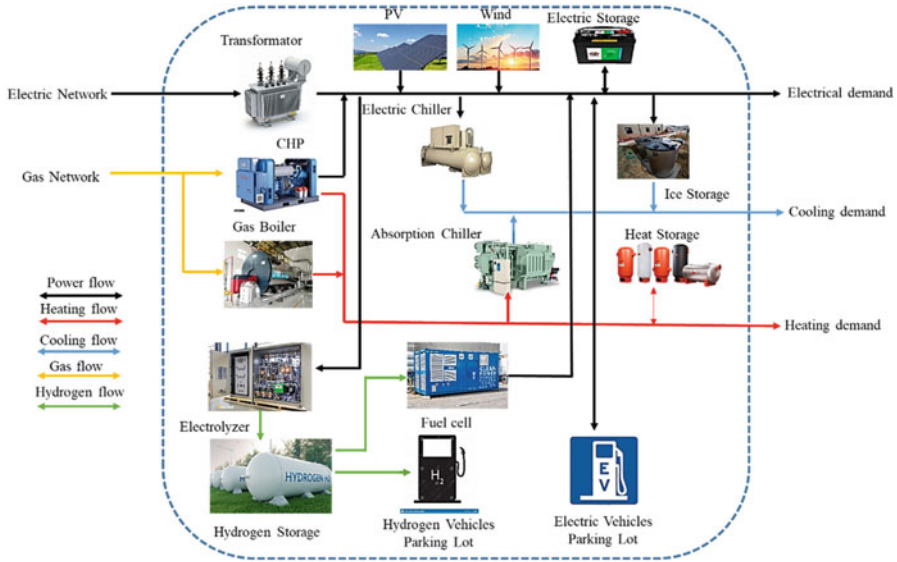


Fig. 8.1 Schematic structure of the proposed model for MCMG

controlling multi energies can result as output for supplying various types of demands. According to the definition, the schematic structure of the proposed model is represented in Fig. 8.1. RESs, i.e., wind and PV units, various types of facilities, and also hybrid vehicle parking lots are integrated into the proposed MCMG. Power and natural gas are used as input energies, while electrical, thermal, and cooling demands are used as output energies. Electrical demand can be supplied by RESs, the upstream network, and the CHP system. The gas boiler (GB), the CHP system, and the heat storage system (HTSS) are responsible for supplying thermal demand. Also, the electric chiller (EC), absorption chiller (AC), and ice storage system (ISS) can provide cooling demand. Different ESSs are used for the flexibility enhancement of the proposed MCMG. Also, the operator will be amenable to the optimal operation of the HEHVs IPL. It means that the operator of MCMG can control the charge and discharge power of EVs in the IPL, and also, the hydrogen demand of HVs must be supplied by MCMG. The produced hydrogen by electrolyzer (EZ) can be stored in the HSS for supplying the hydrogen demand of vehicles. In addition, the stored hydrogen can be converted to power by the fuel cell (FC) in a shortage of electric power or high electricity market price intervals. Stochastic programming is adopted for uncertainty assessment of PV and wind generation as well as various intended demands. Also, for modeling the unpredictable behavior of HEHV owners, the arrival time, departure time, and initial energy of EVs are modeled through stochastic programming. For simplicity, the hydrogen demand of the HV IPL is just taken into account. To be clear, the modeling of the hydrogen-based vehicles is not taken into account. Finally, the interval optimization approach is applied for the assessment of electricity market price uncertainty.

8.3 Problem Formulation

As it has been identified in the previous section about how to supply the several demands considered in Fig. 8.1, the main objective of the decision-making operator for renewable-based MCMG structure is minimizing overall operation cost under different intensive uncertainties. Therefore, the mathematical model related to that is represented below.

8.3.1 Stochastic-Based Proposed Model

8.3.1.1 Objective Function

The expected daily operational cost function is defined as the imported power and natural gas from the relevant upstream grids, which should be minimized (8.1).

$$\text{Cost} = \sum_{\omega} \omega_s \sum_t (\gamma_{t,\omega}^E P_{t,\omega}^{\text{Net}} + \lambda^G G_{t,\omega}^{\text{Net}}) \quad (8.1)$$

where t and ω are indices of time intervals and reduced scenarios; $\gamma_{t,\omega}^E$ and λ^G denote the electricity market price at hour t in scenario ω and natural gas price; $P_{t,\omega}^{\text{Net}}$ and $G_{t,\omega}^{\text{Net}}$ are the imported electrical and natural gas energies at hour t in scenario ω ; and ω_s is the probability of each considered scenario ω .

8.3.1.2 Gas-Based Non-renewable Energy Source Constraints

The two gas-fired energy sources are taken herein as CHP and GB to help the system operator in meeting electrical and thermal intended demands. The consumption of natural gas by CHP unit results in producing electric and heat powers according to energy efficiencies, i.e., $\eta^{E,\text{CHP}}$, $\eta^{H,\text{CHP}}$ which are declared in (8.2) and (8.3), respectively. Also, these productions of CHP units are restricted by (8.4) and (8.5). However, the consumed natural gas by GB unit generates heat only power regards to the energy efficiency of η^{GB} (8.6) such that its limitation is defined via (8.7).

$$P_{t,\omega}^{\text{CHP}} = \eta^{E,\text{CHP}} G_{t,\omega}^{\text{CHP}} \quad \forall t, \omega \quad (8.2)$$

$$H_{t,\omega}^{\text{CHP}} = \eta^{H,\text{CHP}} G_{t,\omega}^{\text{CHP}} \quad \forall t, \omega \quad (8.3)$$

$$0 \leq P_{t,\omega}^{\text{CHP}} \leq P^{\text{CHP,Max}} \quad \forall t, \omega \quad (8.4)$$

$$0 \leq H_{t,\omega}^{\text{CHP}} \leq H^{\text{CHP,Max}} \quad \forall t, \omega \quad (8.5)$$

$$H_{t,\omega}^{\text{GB}} = \eta^{\text{GB}} G_{t,\omega}^{\text{GB}} \quad \forall t, \omega \quad (8.6)$$

$$0 \leq H_{t,\omega}^{\text{GB}} \leq H^{\text{GB,Max}} \quad \forall t, \omega \quad (8.7)$$

where $P_{t,\omega}^{\text{CHP}}$ and $H_{t,\omega}^{\text{CHP}}$ represent the electric and heat power productions by CHP unit at hour t in scenario ω ; $P^{\text{CHP, Max}}$ and $H^{\text{CHP, Max}}$ are the maximum limits of electric and heat power production via CHP unit; $G_{t,\omega}^{\text{CHP}}$ and $G_{t,\omega}^{\text{GB}}$ are the consumed natural gas of CHP and GB units at hour t in scenario ω ; and $H^{\text{GB, Max}}$ is the maximum limit of produced heat power in GB unit.

8.3.1.3 Renewable Energy Source Constraints

Since the probabilistic nature of RESs, i.e., PV and wind energy sources, exist, the power productions relevant to the solar irradiance, ambient temperature, and wind speed variations should be modeled appropriately as in (8.8) and (8.9), respectively. Other details for specifying the behaviors of wind speed and solar irradiance could be determined through the Rayleigh and Beta probability density functions (PDFs), which are completely found in [31].

$$P_{t,\omega}^{\text{PV}} = \eta^{\text{PV}} S^{\text{PV}} I_{t,\omega} (1 - 0.005(T_{t,\omega} - 25)) \quad \forall t, \omega \quad (8.8)$$

$$P_{t,\omega}^{\text{WT}} = \begin{cases} 0 & ; V_{t,\omega}^{\text{WT}} < V^{\text{CI}} \text{ or } V_{t,\omega}^{\text{WT}} \geq V^{\text{CO}} \\ \frac{V_{t,\omega}^{\text{WT}} - V^{\text{CI}}}{V^{\text{R}} - V^{\text{CI}}} P^{\text{WT,R}} & ; V^{\text{CI}} \leq V_{t,\omega}^{\text{WT}} < V^{\text{R}} \\ P^{\text{WT,R}} & ; V^{\text{R}} \leq V_{t,\omega}^{\text{WT}} < V^{\text{CO}} \end{cases} \quad \forall t, \omega \quad (8.9)$$

where η^{PV} and S^{PV} are the energy efficiency and effective area of installed PV array; I_t and T_t are hourly predicted sunlight irradiance and ambient temperature; $P_{t,\omega}^{\text{PV}}$ is the forecasted power of PV array at hour t in scenario ω ; V^{CI} , V^{CO} , and V^{R} denote the cut-in, cut-out, and rated wind speeds; $P^{\text{WT,R}}$ and $P_{t,\omega}^{\text{WT}}$ are the rated and hourly forecasted scenario-based powers of a wind turbine; and $V_{t,\omega}^{\text{WT}}$ is the forecasted wind speed at hour t in scenario ω .

8.3.1.4 Hydrogen Energy-Based Source Constraints

A flexible green energy source named HSS is developed to help system operators much better in different situations by preventing energy from being wasted. So, the excess power of RESs and also power in off-peak intervals could be utilized in the EZ facility to produce hydrogen energy according to its energy efficiency η^{EZ} (8.10) in which the limitation of consumed power is expressed in (8.11) [32]. To contribute to supplying the rest of the electrical demand in peak intervals, the FC facility which consumes hydrogen is deployed with energy efficiency η^{FC} (8.12), whose production is limited by (8.13) [32]. In order to convert the output energy of EZ and also FC facilities to their corresponding real units, a coefficient γ^{P2Hy} is applied in Eqs. (8.10) and (8.12), respectively.

$$Hy_{t,\omega}^{EZ} = \frac{\eta^{EZ} P_{t,\omega}^{EZ}}{\gamma^{P2Hy}} \quad \forall t, \omega \quad (8.10)$$

$$0 \leq P_{t,\omega}^{EZ} \leq P^{EZ,Max} \quad \forall t, \omega \quad (8.11)$$

$$P_{t,\omega}^{FC} = \eta^{FC} Hy_{t,\omega}^{FC} \gamma^{P2Hy} \quad \forall t, \omega \quad (8.12)$$

$$0 \leq P_{t,\omega}^{FC} \leq P^{FC,Max} \quad \forall t, \omega \quad (8.13)$$

where $Hy_{t,\omega}^{EZ}$ and $Hy_{t,\omega}^{FC}$ are the produced and consumed hydrogen energy by EZ and FC facilities at hour t in scenario ω ; $P_{t,\omega}^{EZ}$ and $P_{t,\omega}^{FC}$ are the consumed and produced electric power by EZ and FC facilities at hour t in scenario ω ; and $P^{EZ, Max}$ and $P^{FC, Max}$ represent the maximum limit of consumed and produced electric power of EZ and FC facilities.

8.3.1.5 Cooling Energy Constraints

As a response to supply cooling intended demand in the proposed MCMG structure, integrating AC and EC technologies is indispensable [33]. Therefore, producing cooling energy by AC and EC sources is realized with their corresponding coefficient of the performance (COP) [33], i.e., COP^{AC} and COP^{EC} which are stated in (8.14) and (8.16), respectively. The produced cooling energy has been limited via the maximum allowable bound of heat and electric powers consumed in the AC and EC facilities, which are defined in (8.15) and (8.17), respectively.

$$C_{t,\omega}^{AC} = COP^{AC} H_{t,\omega}^{AC} \quad \forall t, \omega \quad (8.14)$$

$$0 \leq H_{t,\omega}^{AC} \leq H^{AC,Max} \quad \forall t, \omega \quad (8.15)$$

$$C_{t,\omega}^{EC} = COP^{EC} P_{t,\omega}^{EC} \quad \forall t, \omega \quad (8.16)$$

$$0 \leq P_{t,\omega}^{EC} \leq P^{EC,Max} \quad \forall t, \omega \quad (8.17)$$

where $C_{t,\omega}^{AC}$ and $C_{t,\omega}^{EC}$ are the produced cooling energy by AC and EC facilities at hour t in scenario ω ; $H_{t,\omega}^{AC}$ and $P_{t,\omega}^{EC}$ are the consumed heat and electric powers in AC and EC facilities at hour t in scenario ω ; and $H^{AC, Max}$ and $P^{EC, Max}$ are the maximum limit of consumed heat and electric powers in AC and EC facilities.

8.3.1.6 Energy Storage System Constraints

ESS is another flexible source that provides required electric power in peak intervals with minimum energy cost [22]. The hourly stored energy of ESS has been calculated with regard to the charging and discharging powers and their related energy efficiencies in (8.18). The stored energy at the first and final intervals must be equivalent, which are defined in (8.19) and (8.20) such that this energy is maintained

in the specified range for each hour and each scenario (8.21). Similar to that, the acceptable limitations for charging and discharging powers are denoted by (8.22) and (8.23). One of these two operation modes of ESS is selected at the same time (8.24).

$$E_{t,\omega}^{\text{ESS}} = E_{t-1,\omega}^{\text{ESS}} + \left(P_{t,\omega}^{\text{ESS,ch}} \eta^{\text{ESS,ch}} - \frac{P_{t,\omega}^{\text{ESS,dch}}}{\eta^{\text{ESS,dch}}} \right) \quad \forall t, \omega \quad (8.18)$$

$$E_{t,\omega}^{\text{ESS}} = E^{\text{ESS,Initial}} \quad \forall t = 1, \omega \quad (8.19)$$

$$E_{t,\omega}^{\text{ESS}} = E^{\text{ESS,Initial}} \quad \forall t = T, \omega \quad (8.20)$$

$$E^{\text{ESS,Min}} \leq E_{t,\omega}^{\text{ESS}} \leq E^{\text{ESS,Max}} \quad \forall t, \omega \quad (8.21)$$

$$0 \leq P_{t,\omega}^{\text{ESS,ch}} \leq P^{\text{ESS,ch,Max}} B_{t,\omega}^{\text{ESS,ch}} \quad \forall t, \omega \quad (8.22)$$

$$0 \leq P_{t,\omega}^{\text{ESS,dch}} \leq P^{\text{ESS,dch,Max}} B_{t,\omega}^{\text{ESS,dch}} \quad \forall t, \omega \quad (8.23)$$

$$B_{t,\omega}^{\text{ESS,ch}} + B_{t,\omega}^{\text{ESS,dch}} \leq 1 \quad \forall t, \omega \quad (8.24)$$

where $P_{t,\omega}^{\text{ESS,ch}}$ and $P_{t,\omega}^{\text{ESS,dch}}$ are the charging and discharging powers at hour t in scenario ω ; $\eta^{\text{ESS,ch}}$ and $\eta^{\text{ESS,dch}}$ are charging and discharging energy efficiencies; $P^{\text{ESS,ch,Max}}$ and $P^{\text{ESS,dch,Max}}$ are the maximum limit of charging and discharging powers; $B_{t,\omega}^{\text{ESS,ch}}$ and $B_{t,\omega}^{\text{ESS,dch}}$ are the binary decision variables in charging and discharging modes at hour t in scenario ω ; $E^{\text{ESS,Min}}$ and $E^{\text{ESS,Max}}$ are the minimum and maximum allowable amount of stored energy in ESS; $E^{\text{ESS,Initial}}$ is the initial amount of energy exists; and $E_{t,\omega}^{\text{ESS}}$ is the available stored energy of ESS at hour t in scenario ω .

8.3.1.7 Heat Storage System Constraints

Similar to the ESS modeling described in the previous section, HTSS is provided here as [22] to obtain the scheduling of interconnected energy carriers optimally. The thermal stored energy of THSS in (8.25) is updated at each hour and each scenario according to charging and discharging heat powers and energy efficiencies.

The first and final intervals of stored thermal energy should be identical according to Eqs. (8.26) and (8.27) which are located in the predetermined range for each hour and each scenario declared in (8.28). The charging and discharging heat powers are restricted via (8.29) and (8.30). Finally, to prevent occurring simultaneous operating modes of HTSS, constraint (8.31) is applied.

$$E_{t,\omega}^{\text{HTSS}} = E_{t-1,\omega}^{\text{HTSS}} + \left(H_{t,\omega}^{\text{HTSS,ch}} \eta^{\text{HTSS,ch}} - \frac{H_{t,\omega}^{\text{HTSS,dch}}}{\eta^{\text{HTSS,dch}}} \right) \quad \forall t, \omega \quad (8.25)$$

$$E_{t,\omega}^{\text{HTSS}} = E^{\text{HTSS,Initial}} \quad \forall t = 1, \omega \quad (8.26)$$

$$E_{t,\omega}^{\text{HTSS}} = E^{\text{HTSS,Initial}} \quad \forall t = T, \omega \quad (8.27)$$

$$E^{\text{HTSS,Min}} \leq E_{t,\omega}^{\text{HTSS}} \leq E^{\text{HTSS,Max}} \quad \forall t, \omega \quad (8.28)$$

$$0 \leq H_{t,\omega}^{\text{HTSS,ch}} \leq H^{\text{HTSS,ch,Max}} B_{t,\omega}^{\text{HTSS,ch}} \quad \forall t, \omega \quad (8.29)$$

$$0 \leq H_{t,\omega}^{\text{HTSS,dch}} \leq H^{\text{HTSS,dch,Max}} B_{t,\omega}^{\text{HTSS,dch}} \quad \forall t, \omega \quad (8.30)$$

$$B_{t,\omega}^{\text{HTSS,ch}} + B_{t,\omega}^{\text{HTSS,dch}} \leq 1 \quad \forall t, \omega \quad (8.31)$$

where $H_{t,\omega}^{\text{HTSS,ch}}$ and $H_{t,\omega}^{\text{HTSS,dch}}$ are the charging and discharging heat powers at hour t in scenario ω ; $\eta^{\text{HTSS,ch}}$ and $\eta^{\text{HTSS,dch}}$ are charging and discharging energy efficiencies; $H^{\text{HTSS,ch,Max}}$ and $H^{\text{HTSS,dch,Max}}$ are the maximum limit of charging and discharging heat powers; $B_{t,\omega}^{\text{HTSS,ch}}$ and $B_{t,\omega}^{\text{HTSS,dch}}$ are the binary decision variables in charging and discharging modes at hour t in scenario ω ; $E^{\text{HTSS,Min}}$ and $E^{\text{HTSS,Max}}$ are the minimum and maximum allowable amount of heat stored energy in HTSS; $E^{\text{HTSS,Initial}}$ is the initial amount of heat energy exists; and $E_{t,\omega}^{\text{HTSS}}$ is the available heat stored energy of HTSS at hour t in scenario ω .

8.3.1.8 Ice Storage System Constraints

In addition to supplying cooling demand by AC and EC technologies, utilizing the ISS facility is a good option in an optimum cooperation manner [26]. The requested cooling energy is produced via consuming electric power with consideration of related COP (8.32). The cooling stored energy of ISS in (8.33) is updated at each hour and each scenario regarding the charging and discharging cooling powers and energy efficiencies. At the first and final intervals, the stored energy should be the same through Eqs. (8.34) and (8.35) in which the acceptable variations for each hour and each scenario are limited by (8.36). The limitations of charging and discharging cooling powers are stated in (8.37) and (8.38). To obtain economic actions, only one of these modes is specified via (8.39).

$$C_{t,\omega}^{\text{ISS,ch}} = P_{t,\omega}^{\text{Ice}} \text{COP}^{\text{Ice}} \quad \forall t, \omega \quad (8.32)$$

$$E_{t,\omega}^{\text{ISS}} = E_{t-1,\omega}^{\text{ISS}} + \left(C_{t,\omega}^{\text{ISS,ch}} \eta^{\text{ISS,ch}} - \frac{C_{t,\omega}^{\text{ISS,dch}}}{\eta^{\text{ISS,dch}}} \right) \quad \forall t, \omega \quad (8.33)$$

$$E_{t,\omega}^{\text{ISS}} = E^{\text{ISS,Initial}} \quad \forall t = 1, \omega \quad (8.34)$$

$$E_{t,\omega}^{\text{ISS}} = E^{\text{ISS,Initial}} \quad \forall t = T, \omega \quad (8.35)$$

$$E^{\text{ISS,Min}} \leq E_{t,\omega}^{\text{ISS}} \leq E^{\text{ISS,Max}} \quad \forall t, \omega \quad (8.36)$$

$$0 \leq C_{t,\omega}^{\text{ISS,ch}} \leq C_{t,\omega}^{\text{ISS,ch,Max}} B_{t,\omega}^{\text{ISS,ch}} \quad \forall t, \omega \quad (8.37)$$

$$0 \leq C_{t,\omega}^{\text{ISS,dch}} \leq C_{t,\omega}^{\text{ISS,dch,Max}} B_{t,\omega}^{\text{CES,dch}} \quad \forall t, \omega \quad (8.38)$$

$$B_{t,\omega}^{\text{ISS,ch}} + B_{t,\omega}^{\text{ISS,dch}} \leq 1 \quad \forall t, \omega \quad (8.39)$$

where $C_{t,\omega}^{\text{ISS,ch}}$ and $C_{t,\omega}^{\text{ISS,dch}}$ are the charging and discharging cooling powers at hour t in scenario ω ; $P_{t,\omega}^{\text{Ice}}$ is the equivalent consumed electric power in the charging mode at hour t in scenario ω ; $\eta^{\text{ISS,ch}}$ and $\eta^{\text{ISS,dch}}$ are charging and discharging energy efficiencies; $C_{t,\omega}^{\text{ISS,ch,Max}}$ and $C_{t,\omega}^{\text{ISS,dch,Max}}$ are the maximum limit of charging and discharging cooling powers; $B_{t,\omega}^{\text{ISS,ch}}$ and $B_{t,\omega}^{\text{ISS,dch}}$ are the binary decision variables in charging and discharging modes at hour t in scenario ω ; $E^{\text{ISS,Min}}$ and $E^{\text{ISS,Max}}$ are the minimum and maximum allowable amount of stored energy in ISS; $E^{\text{ISS,Initial}}$ is the initial amount of cooling energy; and $E_{t,\omega}^{\text{ISS}}$ is the available stored cooling energy of ISS at hour t in scenario ω .

8.3.1.9 Hydrogen Storage System Constraints

The flexible green energy provider-based HSS technology is also coordinated in MCMG structures [22]. Since the HVs are getting noticed and implemented in some real recent case studies, supplying their required energy is getting much attention. Thus, the hourly stored hydrogen in HSS can be calculated through (8.40) such that the first and final stored energies must be equal as mentioned in (8.41) and (8.42). The allowable variations of stored hydrogen amount for each hour and each scenario are assigned by (8.43).

$$A_{t,\omega}^{\text{HSS}} = A_{t-1,\omega}^{\text{HSS}} + \text{Hy}_{t,\omega}^{\text{FC}} - \text{Hy}_{t,\omega}^{\text{EZ}} - \text{Hy}_{t,\omega}^{\text{L}} \quad \forall t, \omega \quad (8.40)$$

$$A_{t,\omega}^{\text{HSS}} = A^{\text{HSS,Initial}} \quad \forall t = 1, \omega \quad (8.41)$$

$$A_{t,\omega}^{\text{HSS}} = A^{\text{HSS,Initial}} \quad \forall t = T, \omega \quad (8.42)$$

$$A_{t,\omega}^{\text{HSS,Min}} \leq A_{t,\omega}^{\text{HSS}} \leq A_{t,\omega}^{\text{HSS,Max}} \quad \forall t, \omega \quad (8.43)$$

where $\text{Hy}_{t,\omega}^{\text{L}}$ is the hydrogen energy demand of HVs at hour t in scenario ω ; $A_{t,\omega}^{\text{HSS,Min}}$ and $A_{t,\omega}^{\text{HSS,Max}}$ are the minimum and maximum allowable amount of stored hydrogen in HSS; $A^{\text{HSS,Initial}}$ is the initial amount of hydrogen energy; and $A_{t,\omega}^{\text{HSS}}$ is the available stored hydrogen amount at hour t in scenario ω .

8.3.1.10 Electric Vehicle Intelligent Parking Lot Constraints

In order to overcome environmental challenges, the development of EVs along with deploying HVs have been increasingly motivated in recent years [34]. The charging

and discharging process of EVs in IPL should be economically accomplished in the MCMG structure. Therefore, the appropriate modeling of EVs is provided in the following constraints. The hourly available energy of each EV's battery is updated with charging and discharging powers at each hour between arrival-departure times and each scenario through Eq. (8.44). Since the arrival time of EVs has been considered as an uncertain parameter, the accessible energy in this time is equal to the predetermined scenario-based amount, i.e., $E_{v,\omega}^{\text{EV,arrival}}$ (8.45). For the departure time of EVs, the accessible energy is equal to a predetermined deterministic amount, i.e., $\psi_v^{\text{EV}} E_v^{\text{EV,Max}}$ (8.46). It is worth mentioning the coefficient of charging EVs in IPL is defined by ψ_v^{EV} . The allowable range of hourly available energy is stated in (8.47). Also, restrictions of charging and discharging powers are reported in (8.48) and (8.49). Similar to other mentioned storage devices, constraint (8.50) is utilized to prevent simultaneous operating modes. The total daily switching between these two modes must be less than the predetermined number, i.e., N_v^{Max} for each EV (8.51).

$$E_{t,v,\omega}^{\text{EV}} = E_{t-1,v,\omega}^{\text{EV}} + \left(P_{t,v,\omega}^{\text{EV,ch}} \eta_v^{\text{EV,ch}} - \frac{P_{t,v,\omega}^{\text{EV,dch}}}{\eta_v^{\text{EV,dch}}} \right) \quad \forall t_v^{\text{arrival}} < t < t_v^{\text{departure}}, v, \omega \quad (8.44)$$

$$E_{t,v,\omega}^{\text{EV}} = E_{v,\omega}^{\text{EV,arrival}} \quad \forall t = t_v^{\text{arrival}}, v, \omega \quad (8.45)$$

$$E_{t,v,\omega}^{\text{EV}} = \psi_v^{\text{EV}} E_v^{\text{EV,Max}} \quad \forall t = t_v^{\text{departure}}, v, \omega \quad (8.46)$$

$$E_v^{\text{EV,Min}} \leq E_{t,v,\omega}^{\text{EV}} \leq E_v^{\text{EV,Max}} \quad \forall t_v^{\text{arrival}} < t < t_v^{\text{departure}}, v, \omega \quad (8.47)$$

$$0 \leq P_{t,v,\omega}^{\text{EV,ch}} \leq P_v^{\text{EV,ch,Max}} B_{t,v,\omega}^{\text{EV,ch}} \quad \forall t_v^{\text{arrival}} < t < t_v^{\text{departure}}, v, \omega \quad (8.48)$$

$$0 \leq P_{t,v,\omega}^{\text{EV,dch}} \leq P_v^{\text{EV,dch,Max}} B_{t,v,\omega}^{\text{EV,dch}} \quad \forall t_v^{\text{arrival}} < t < t_v^{\text{departure}}, v, \omega \quad (8.49)$$

$$B_{t,v,\omega}^{\text{EV,ch}} + B_{t,v,\omega}^{\text{EV,dch}} \leq 1 \quad \forall t_v^{\text{arrival}} < t < t_v^{\text{departure}}, v, \omega \quad (8.50)$$

$$\sum_t (B_{t,v,\omega}^{\text{EV,ch}} + B_{t,v,\omega}^{\text{EV,dch}}) \leq N_v^{\text{Max}} \quad \forall t_v^{\text{arrival}} < t < t_v^{\text{departure}}, v, \omega \quad (8.51)$$

where $P_{t,v,\omega}^{\text{EV,ch}}$ and $P_{t,v,\omega}^{\text{EV,dch}}$ are the charging and discharging powers of EV v at hour t in scenario ω ; $\eta_v^{\text{EVES,ch}}$ and $\eta_v^{\text{EVES,dch}}$ are charging and discharging energy efficiencies of EV v ; $P_v^{\text{EV,ch,Max}}$ and $P_v^{\text{EV,dch,Max}}$ are the maximum limit of charging and discharging powers of EV v ; $B_{t,v,\omega}^{\text{EV,ch}}$ and $B_{t,v,\omega}^{\text{EV,dch}}$ are the binary decision variables in selecting charging and discharging modes of EV v at hour t in scenario ω ; $E_v^{\text{EV,Min}}$ and $E_v^{\text{EV,Max}}$ are the minimum and maximum allowable amount of stored energy in EV v ; and $E_{t,v,\omega}^{\text{EV}}$ is the available stored energy of EV v at hour t in scenario ω .

8.3.1.11 All Energy Balance Constraints

In Eqs. (8.52)–(8.55), determining the balancing constraints of electric power, heat power, cooling energy, and natural gas energy is done to show that injecting and consuming energies in meeting several demands should be equal at each hour and each scenario.

$$\begin{aligned}
 & P_{t,\omega}^{\text{Net}} \times \eta^T + P_{t,\omega}^{\text{PV}} + P_{t,\omega}^{\text{WT}} + P_{t,\omega}^{\text{CHP}} + P_{t,\omega}^{\text{ESS,dch}} + P_{t,\omega}^{\text{FC}} + \sum_v^V P_{t,v,\omega}^{\text{EV,dch}} \\
 & = P_{t,\omega}^L + P_{t,\omega}^{\text{ESS,ch}} + P_{t,\omega}^{\text{Ice}} + P_{t,\omega}^{\text{EC}} + P_{t,\omega}^{\text{EZ}} + \sum_v^V P_{t,v,\omega}^{\text{EV,ch}} \quad \forall t, \omega
 \end{aligned} \tag{8.52}$$

$$H_{t,\omega}^{\text{CHP}} + H_{t,\omega}^{\text{GB}} + H_{t,\omega}^{\text{HTSS,dch}} = H_{t,\omega}^L + H_{t,\omega}^{\text{AC}} + H_{t,\omega}^{\text{HTSS,ch}} \quad \forall t, \omega \tag{8.53}$$

$$C_{t,\omega}^{\text{EC}} + C_{t,\omega}^{\text{AC}} + C_{t,\omega}^{\text{ISS,dch}} = C_{t,\omega}^L \quad \forall t, \omega \tag{8.54}$$

$$G_{t,\omega}^{\text{Net}} = G_{t,\omega}^{\text{CHP}} + G_{t,\omega}^{\text{GB}} \quad \forall t, \omega \tag{8.55}$$

where η^T is the energy efficiency of the transformer between MCMG and upper grid and $P_{t,\omega}^L$, $H_{t,\omega}^L$, and $C_{t,\omega}^L$ represent the electrical, thermal, and cooling demands at hour t in scenario ω , respectively.

8.3.2 Interval-Based Stochastic Proposed Model

8.3.2.1 General Model Specifications

In this section, the uncertainty modeling of electricity market prices is modeled via the proposed interval optimization method. In this approach, a multi-objective problem for the objective function (8.1) is manufactured in which the average and deviation costs should be minimized [35]. Moreover, the weighted sum solution approach is deployed to achieve optimal Pareto solutions between the two aforementioned costs. Then, a min-max fuzzy approach is considered to identify the trade-off solutions from Pareto solutions.

At first, the full model for an optimization problem with input parameter Y , uncertainty parameter φ , and decision variable X is provided in (8.56)–(8.58).

$$\text{Min } F(X, Y, \varphi) \tag{8.56}$$

$$\text{s.t.} \tag{8.57}$$

$$H(X, Y, \varphi) = 0 \tag{8.57}$$

$$G(X, Y, \varphi) \leq 0 \tag{8.58}$$

In this method, the upper and lower bounds for the uncertainty parameter are considered as an interval $[\varphi^{\text{Min}}, \varphi^{\text{Max}}]$. According to this, the entire constraints and also objective function are declared within intervals. Hence, the upper and lower amounts of the objective function are determined as in Eqs. (8.59) and (8.60), respectively. Afterward, the minimization of average cost and deviation cost simultaneously could be obtained as a bi-objective problem (8.61). With regard to the obtained upper and lower amounts, the average cost and deviation cost, i.e., $F^M(X)$ and $F^W(X)$, are calculated from Eqs. (8.62) and (8.63), respectively.

$$F^{\text{Max}}(X) = \max_{\varphi \in Y} F(X) \quad (8.59)$$

$$F^{\text{Min}}(X) = \min_{\varphi \in Y} F(X) \quad (8.60)$$

$$\text{Min } F(X) = \text{Min}(F^M(X), F^W(X)) \quad (8.61)$$

$$F^M(X) = \frac{F^{\text{Max}}(X) + F^{\text{Min}}(X)}{2} \quad (8.62)$$

$$F^W(X) = \frac{F^{\text{Max}}(X) - F^{\text{Min}}(X)}{2} \quad (8.63)$$

8.3.2.2 Weighted Sum and Fuzzy Solution Approaches

Due to the nature of the weighted sum solution method, average cost and deviation cost are multiplied by weight factors, i.e., α and β , in which their summation is equal to one [36]. The formula for this method is shown in (8.64) and (8.65).

$$\text{Min } F(X) = \alpha F^M(X) + \beta F^W(X) \quad (8.64)$$

$$\alpha + \beta = 1 \quad (8.65)$$

Before achieving the best optimum solutions, the normalized forms of average cost and deviation cost must be accomplished, which are computed in (8.66) and (8.67), respectively. Afterward, the minimum value of N objective functions in each iteration is opted via (8.68), and as a result, the maximum value of these obtained N_p solutions from (8.68) is selected as the trade-off outcome indicated in (8.69).

$$F_{p.u}^M(X) = \frac{F^M(X) - F_{\text{Max}}^M(X)}{F_{\text{Min}}^M(X) - F_{\text{Max}}^M(X)} \quad (8.66)$$

$$F_{p.u}^W(X) = \frac{F^W(X) - F_{\text{Max}}^W(X)}{F_{\text{Min}}^W(X) - F_{\text{Max}}^W(X)} \quad (8.67)$$

$$F^n = \min(F_1^n, \dots, F_N^n) \quad \forall n = 1, \dots, N_P \quad (8.68)$$

$$F^{\max} = \max(F^1, \dots, F^{N_P}) \quad (8.69)$$

8.4 Simulation Results

8.4.1 All Input Data

The forecasted hourly electrical, thermal, and cooling demands of the MCMG structure are represented in Fig. 8.2. Electricity market price with upper and lower levels is illustrated in Fig. 8.3. Technical data of considered ESSs, AC, EC, CHP system, and GB are extracted from [37]. The required wind speed and solar irradiance are taken from [31] such that modifications of these parameters are accomplished to obtain similar output forecasted generations of [37]. So, the forecasted PV and wind generations are depicted in Fig. 8.4. The hydrogen demand of the HVs parking lot is shown in Fig. 8.5. Three types of EVs are taken into account, and the capacity of the EVs parking lot is assumed 50 numbers. The required data for EVs are provided in Table 8.1. Technical data of hydrogen storage, FC, and EZ are tabulated in Table 8.2. The Monte Carlo simulation (MCS) method is adopted to generate 1000 scenarios for different demands, arrival time, departure time, and initial energy of EVs. Due to the high computational burden of 1000 scenarios, the GAMS/SCENRED program is used to reduce scenarios into ten numbers. The proposed MILP problem is solved using a CPLEX solver in GAMS software on a PC with an Intel(R) Core(TM) i7-7500U CPU 2.7 GHZ and 12 GB RAM.

8.4.2 Case Studies and Analysis of Results

In this section, two different case studies are clarified in the subsequent sections. It could be stated that in case study 1, the stochastic programming of the proposed model has been considered. However, proceeding toward the real results, the uncertainty of electricity market price has been taken in case study 2 via an interval-based stochastic proposed model.

8.4.2.1 Stochastic-Based Simulation Results

As mentioned before, after applying the scenario reduction method, ten scenarios have been supposed to determine the performance and capability of the proposed method. The total operation cost of the MCMG structure under several scenarios is provided in Table 8.3. Regarding the probability of each scenario, the expected

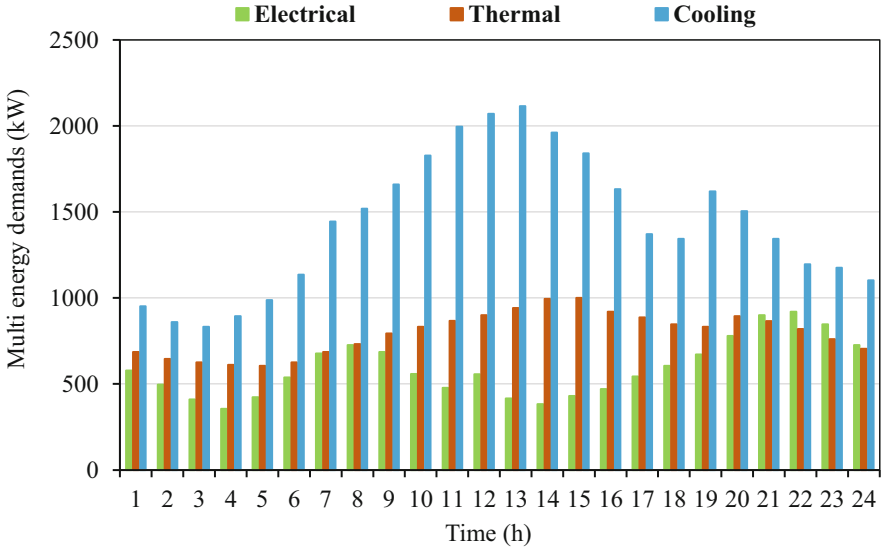


Fig. 8.2 Forecasted hourly electrical, thermal, and cooling demands of MCMG structure [37]

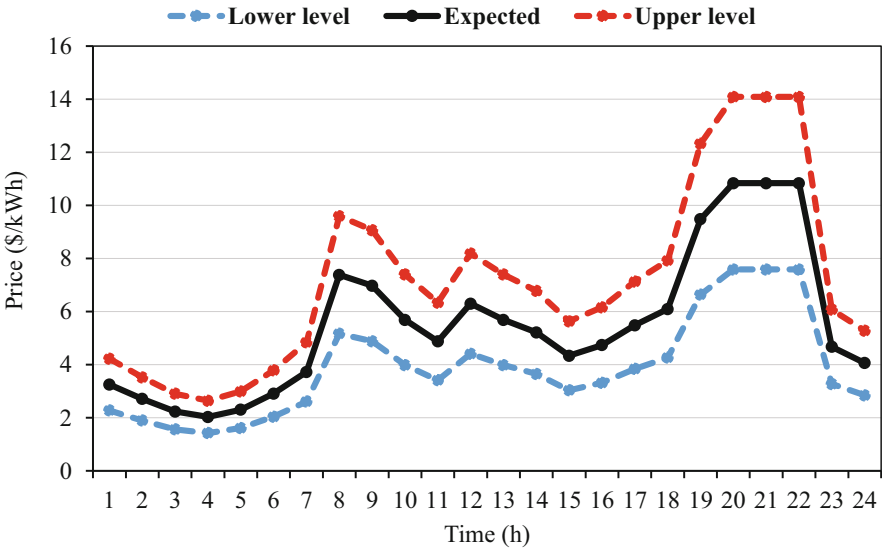


Fig. 8.3 Electricity market price [37]

operation cost could be obtained as \$137,825. It can be realized from Table 8.3 that due to the existence of various uncertainties, i.e., RESs outputs, multi-energy demands, and the behavior of EVs in IPL, scenario 3 is the worst scenario, which has the highest operation cost, i.e., \$143,196, while the best scenario is scenario 1,

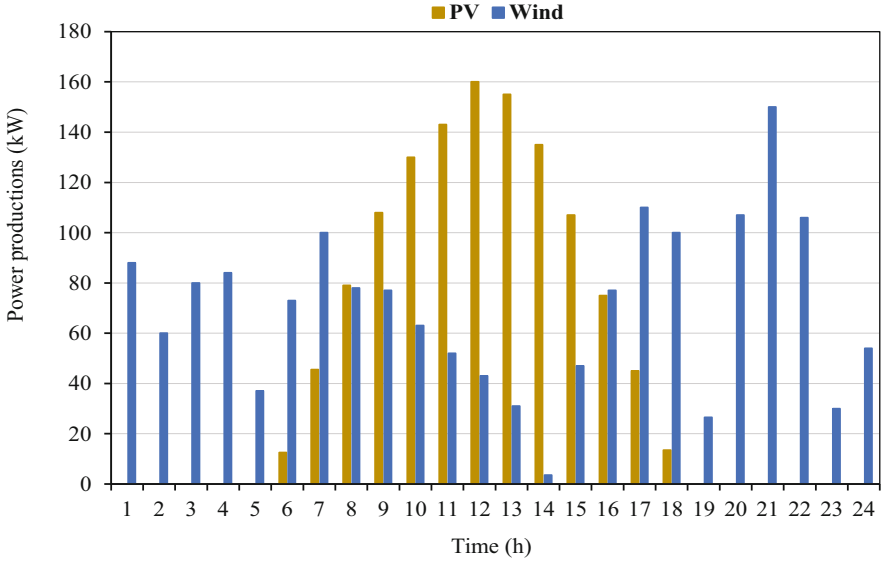


Fig. 8.4 Forecasted PV and wind generations [37]

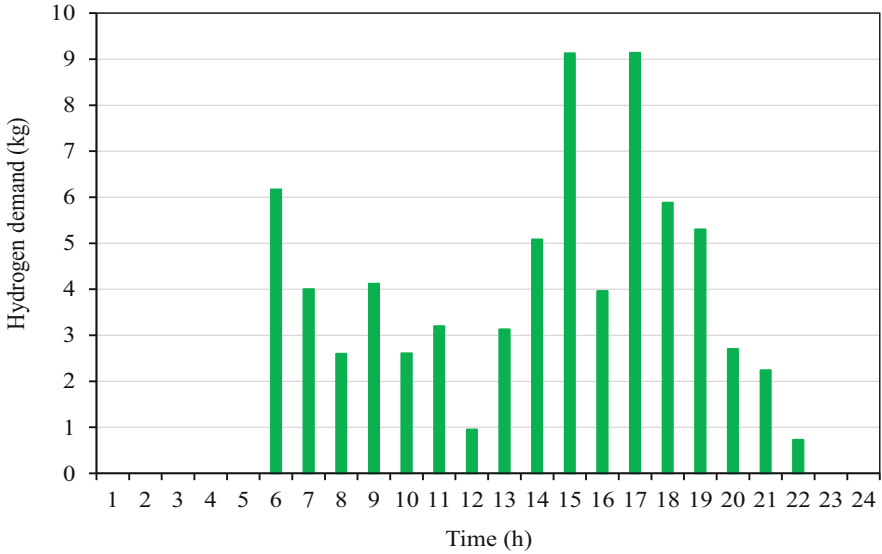


Fig. 8.5 Hydrogen demand of the HV parking lot [40]

which has the lowest operation cost, i.e., \$128,832. Thus, to indicate the effectiveness and performance of the proposed approach, the following obtained results are provided for scenario 3.

Table 8.1 Requirement data of EVs [38]

Model	$E_v^{EV,Cap}$ (kWh)	$P_v^{EV,ch,Max}$ (kW)	$P_v^{EV,dch,Max}$ (kW)	$E_v^{EV,Min}$ (kWh)	$E_v^{EV,Max}$ (kWh)	$\eta_v^{EV,ch}$ (%)	$\eta_v^{EV,dch}$ (%)
Tesla model S	100	17.2	17.2	10	90	90	95
Renault Zoe	41	20	20	4	37	88	90
Alliance other EV	25	12.5	12.5	2.5	22.5	90	93

Table 8.2 Technical data of hydrogen storage, fuel cell, and electrolyzer [39]

Parameter	Value	Parameter	Value
$P^{EZ, Max}$ (kW)	500	$P^{FC, Max}$ (kW)	500
η^{EZ} (%)	70	η^{FC} (%)	80
$A^{HSS, Min}$ (kg)	3	$A^{HSS, Max}$ (kg)	15
γ^{P2Hy} (kW/kg)	33.6		

Table 8.3 Total operation cost of MCMG for various scenarios of case 1

Scenario	Cost (\$)	Scenario	Cost (\$)
1	128,832	6	134,189
2	140,560	7	137,219
3	143,196	8	136,631
4	138,342	9	129,624
5	131,567	10	137,104

The whole produced electric power of all facilities in the MCMG structure should be equivalent to total electrical demand such that this total demand consists of baseload and consumed electric power by relevant facilities. According to this, Fig. 8.6 shows the electrical power balance along with the expected hourly forecasted market price. The purchased electric power from the upstream grid has occurred in off-peak intervals (i.e., hours 1–7 and 24), whereas in the remaining hours, which include mid-peak and peak intervals, CHP unit committed on with maximum generation due to its low cost and also supplying thermal demand. Also, as figured out in Fig. 8.6, the EC facility consumes electricity during the whole scheduling horizon, which is related to the required cooling demand. Similar to that, the EZ facility consumes electricity in some off-peak intervals and stores it in HSS, which could discharge to supply hydrogen demand such that this action reduces much more electricity consumption of the EZ in peak intervals (i.e., hours 19–22). It should be noted that with the high hydrogen demand of HVs in mid-peak (i.e., hours 12–18) and peak intervals, the FC facility does not have the opportunity to contribute to generating electrical power. The operated charging function of ESS technology has happened in off-peak intervals, while in peak intervals and also in relative peak interval (i.e., hour 8), it has discharged to meet the rest demand. The other outcoming from Fig. 8.6 is about charging and discharging of cumulative EVs in IPL, which is in the G2V mode in some off-peak and mid-peak intervals, while only two peak intervals (i.e., hours 18, 22) are in the V2G mode. The thermal power balance is shown in Fig. 8.7 with available thermal units. Due to the correlation of electrical

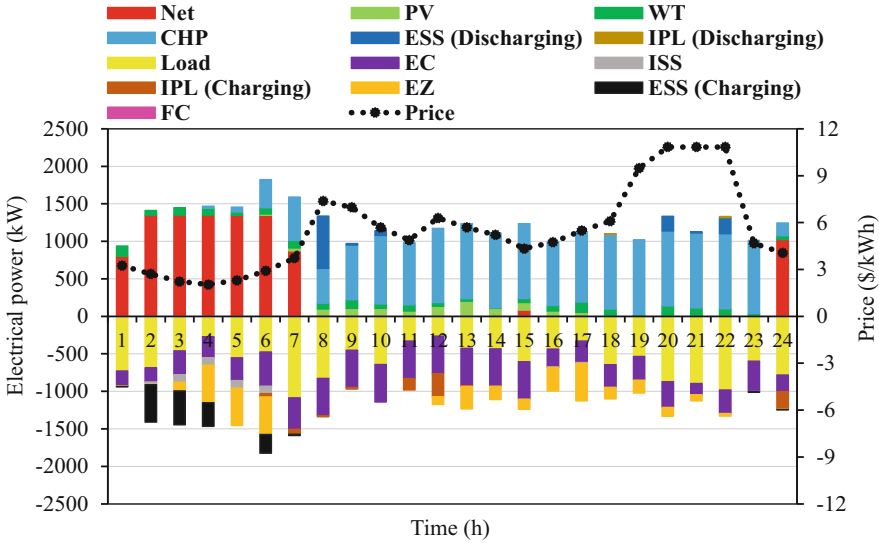


Fig. 8.6 Electrical power balance of MCMG for scenario 3

and thermal powers in CHP unit, the produced thermal power mostly exists in mid-peak and peak intervals. However, in some, off-peak intervals (i.e., hours 4–7 and 24) generated a small amount of power. To fully supply the thermal demand in off-peak intervals (i.e., hours 1–6), the GB unit committed on. In order to meet the rest of the thermal demand in two intervals (i.e., hours 15, 24), discharging power of HTSS is deployed, and in doing so, the charging power is accomplished in several hours of excess thermal power. The AC facility is developed to assist the EC facility in supplying cooling demand in peak and mid-peak intervals, with respect to high electricity market price and increased cooling demand, respectively. Thus, the cooling produced power of AC and EC facilities is demonstrated in Fig. 8.8. With the charging process of ISS in off-peak intervals (i.e., hours 2–6), it has the capability to respond to the increased cooling demand in some mid-peak intervals. According to the operation mode of GB and CHP units in the whole scheduling horizon, Fig. 8.9 represents the total gas consumption by these units, which is purchased from the upstream grid. It can be understood that this amount increases during mid-peak and peak intervals compared to off-peak intervals.

To focus more on the effects of cumulative EVs behaviors in IPL, Figs. 8.10 and 8.11 show the total charging and discharging power, respectively. It is worth mentioning that only three selected scenarios among ten scenarios are provided in these two figures in order to track better different charging power patterns. As it can be seen from Fig. 8.10, all of the requested power of EVs is drawn in off-peak and mid-peak intervals, wherein scenario 10 has the lowest amount of total charging power in comparison to the other two represented scenarios. The total injected power of EVs is accomplished in Fig. 8.11 such that the most discharging power has

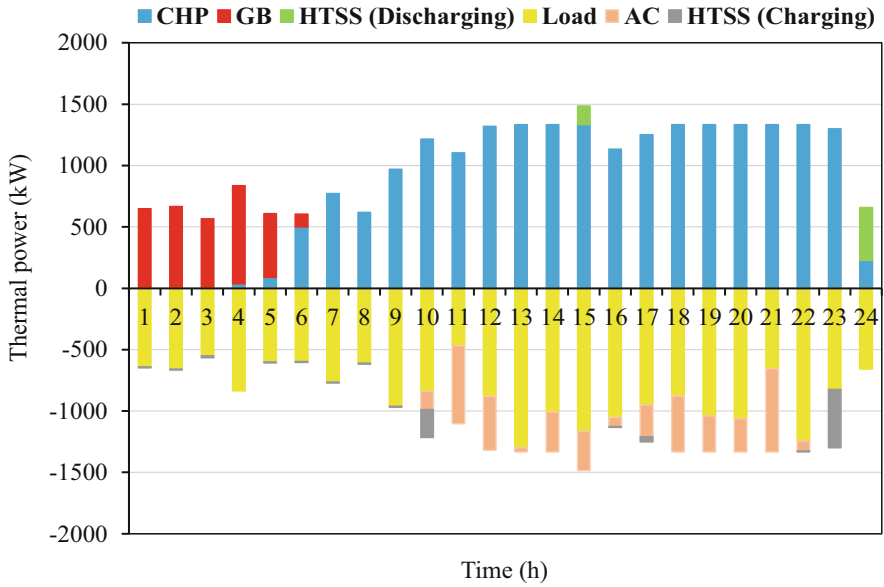


Fig. 8.7 Thermal power balance of MCMG for scenario 3

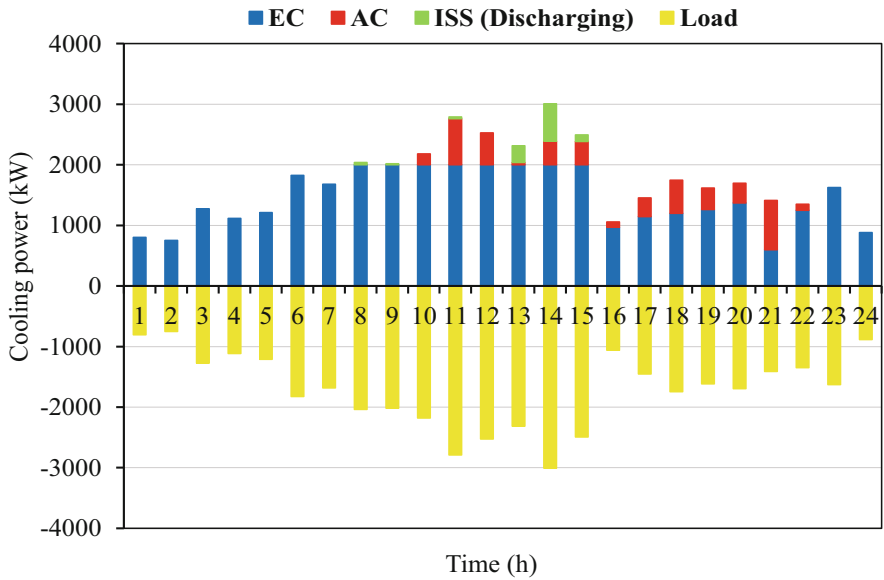


Fig. 8.8 Cooling power balance of MCMG for scenario 3

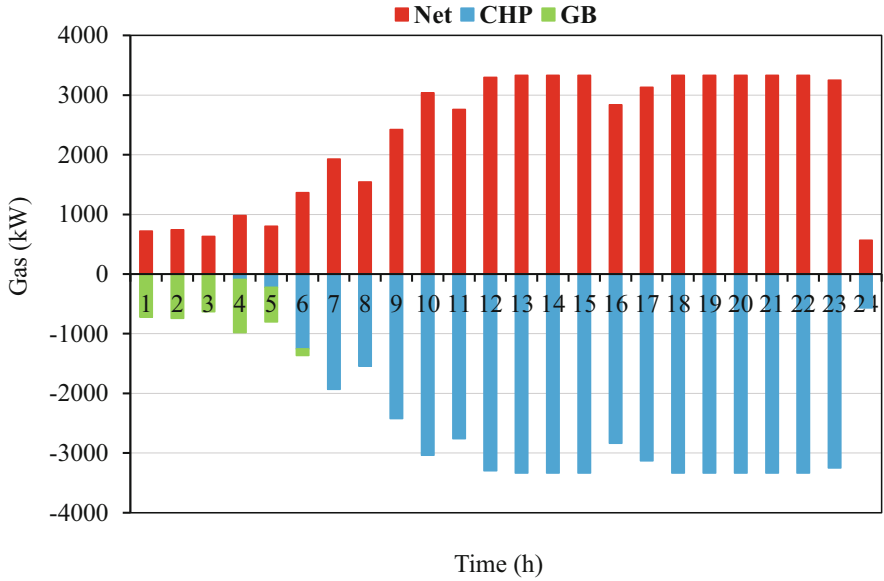


Fig. 8.9 Gas balance of MCMG for scenario 3

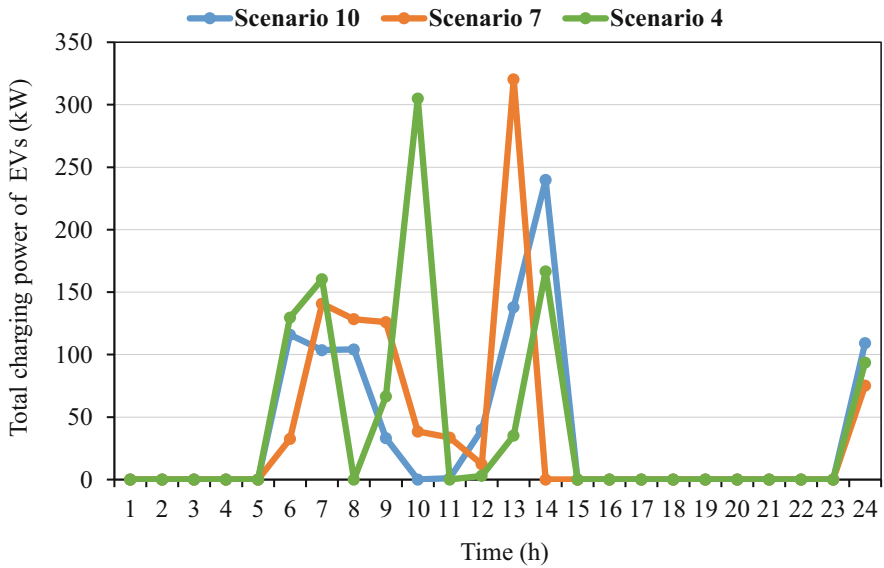


Fig. 8.10 Total charging EVs in IPL for three different scenarios

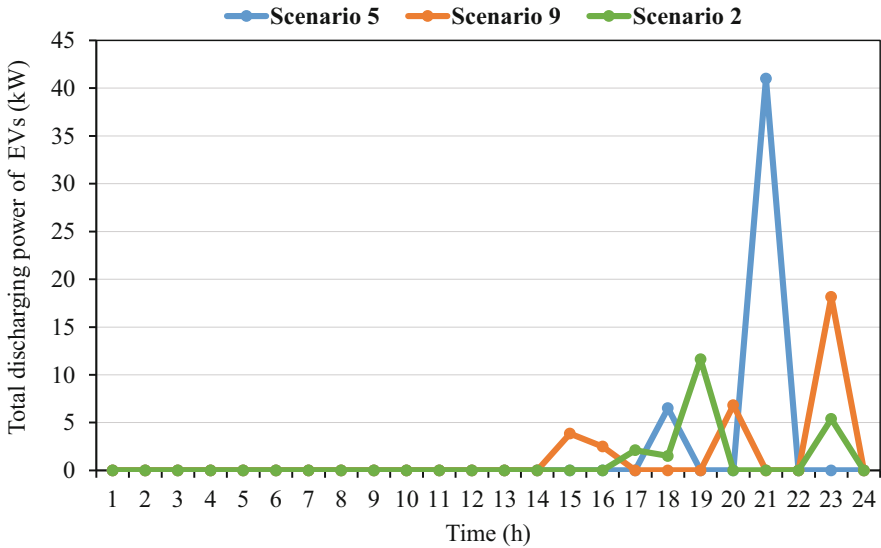


Fig. 8.11 Total discharging EVs in IPL for three different scenarios

happened in peak intervals. Also, it can be stated that scenario 5 has the highest amount of total discharging power rather than the other two depicted scenarios.

Also, the various scenarios for the EZ facility have been conducted in Fig. 8.12, which indicates the output hydrogen equivalent amount in terms of supplying HVs demand. By paying attention to this figure, it can be realized that despite the no-hydrogen demand in some off-peak intervals (i.e., hours 3–5), the EZ facility has been implemented to produce hydrogen and store it in HSS. Furthermore, regarding the increased HVs demand in most mid-peak intervals and also in all peak intervals, deploying the EZ to generate hydrogen energy has been essential. The same explanations have been established for hydrogen energy production and consumption under the worst scenario, i.e., scenario 3 through Fig. 8.13. In this way, the state of hydrogen amount in HSS technology, which is named as available hourly stored energy, is indicated with a pink line. To implement the sensitivity analysis of charging EVs in IPL, Fig. 8.14 has been presented. As shown in this figure, increasing an IPL coefficient not only leads to a higher operation cost of MCMG but also decreases the opportunity of achieving more profit for the decision-making operator. Thus, it could be denoted that a 30% increase in the charging power of EVs results in a 2.5% increment in total operation cost.

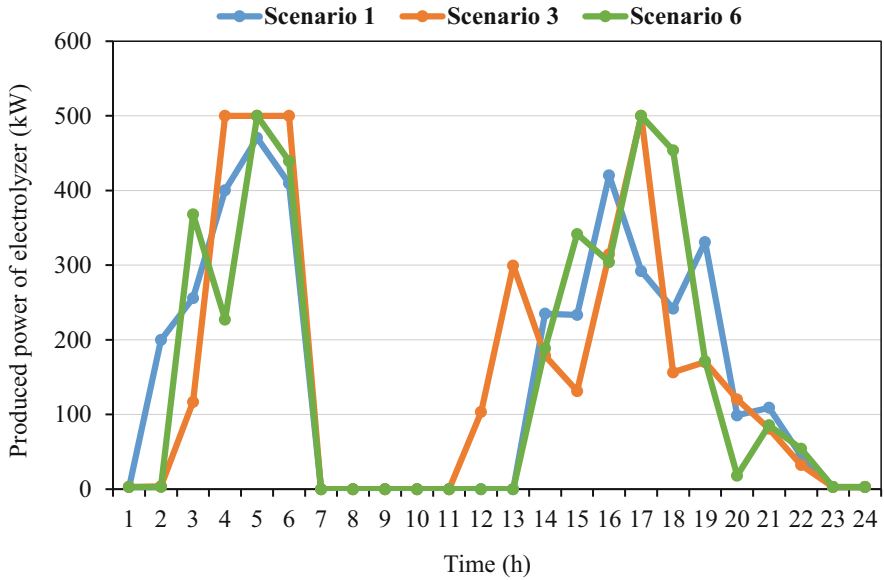


Fig. 8.12 Output power of EZ for three different scenarios

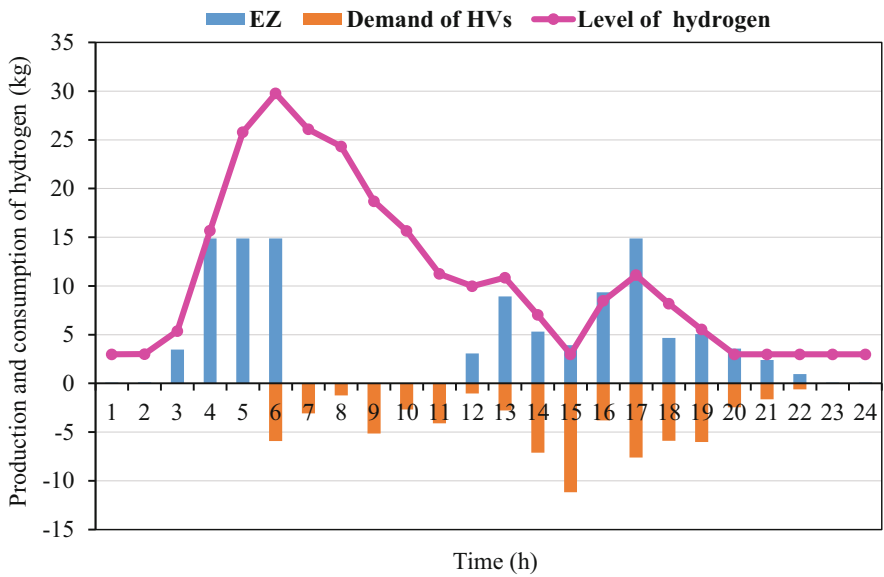


Fig. 8.13 Produced hydrogen of EZ and level of hydrogen of HSS for scenario 3

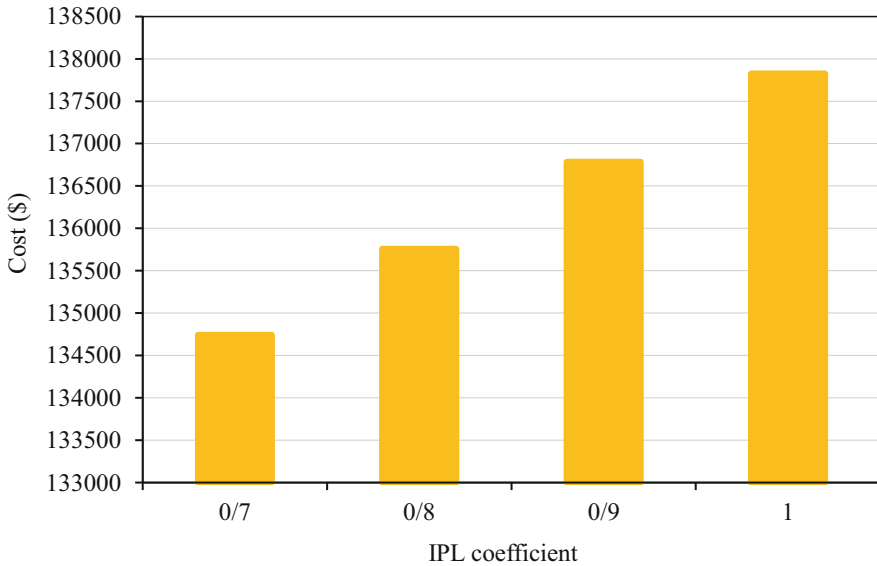


Fig. 8.14 Expected cost variation of MCMG for various IPL coefficient

Table 8.4 Numerical Pareto solutions for interval-based stochastic programming model of case 2

Solutions	α	β	F^M	F^W	$F_{p,u}^M$	$F_{p,u}^W$	$\text{Min}(F_{p,u}^M, F_{p,u}^W)$
1	1	0	135757.8	8426.2	1	0	0
2	0.9	0.1	135847.9	7131.9	0.99	0.15	0.15
3	0.8	0.2	136064.2	5992.6	0.97	0.28	0.28
4	0.7	0.3	136226.7	5576.1	0.96	0.33	0.33
5	0.6	0.4	136784.4	4540.5	0.91	0.46	0.46
6	0.5	0.5	137638.9	3494.1	0.84	0.58	0.58
7	0.4	0.6	138295.1	2993.6	0.78	0.64	0.64
8	0.3	0.7	140731	1780.2	0.58	0.78	0.58
9	0.2	0.8	146105.7	0	0.13	1	0.13
1	0.1	0.9	146105.7	0	0.13	1	0.13
11	0	1	147681.3	0	0	1	0

8.4.2.2 Interval-Based Simulation Results

As aforementioned in the formulation section, the optimal scheduling of renewable-based MCMG coordinated with HEHV IPL within the uncertainty of electricity market price should be modeled through the proposed hybrid interval-stochastic framework. So, the generated bi-objective model aims to minimize the average and deviation costs, simultaneously. In doing so, the weighted sum and fuzzy solution approaches are taken to achieve optimal results such that the numerical and explicative Pareto results are reported in Table 8.4 and Fig. 8.15. In Table 8.4, 10 Pareto

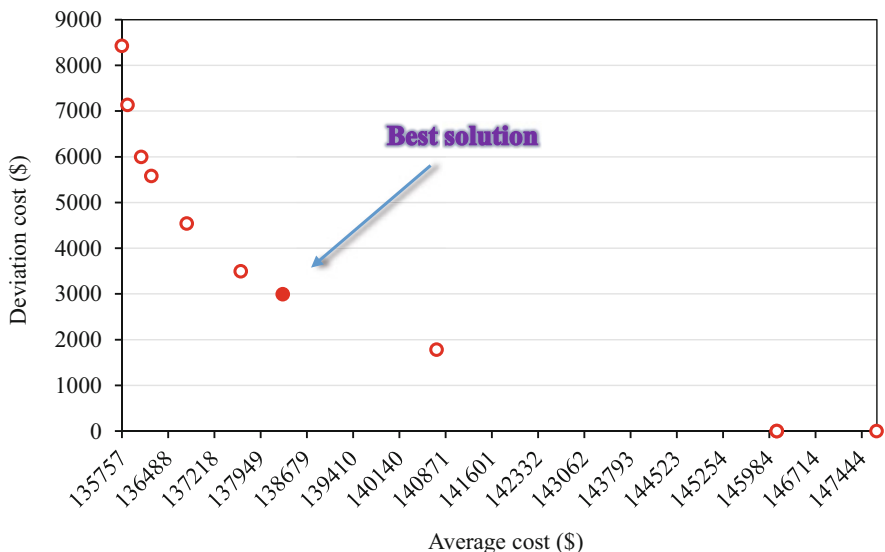


Fig. 8.15 Pareto solutions for interval-based stochastic programming model of case 2

front solutions are announced, with the highlighted row, i.e., solution #7, being the best trade-off solution with the corresponding values of 138295.1 \$ and 2993.6 \$ for average and deviation costs, respectively. Afterward, Fig. 8.15 is utilized to illustrate the best trade-off cost with a solid red circle. Compared to case 1 results, it could be outlined that to reduce the impact of electricity market price fluctuations, the average cost of introduced MCMG is increased by only 1.87%, and thus the deviation cost indicating uncertainty impact is decreased by 67.47%.

8.5 Conclusions

In the present chapter, an optimal scheduling framework for the renewable-based MCMG coordinated with HEHV IPL under several inherent uncertainties has been proposed. To address all variations relevant to HEHVs’ driving patterns, produced power of RESs, and consumption of MEDs, a scenario-based stochastic method has been considered. Furthermore, due to the impact of severe electricity market price uncertainty on the optimal results, the appropriate interval optimization technique has been applied. Thus, taking the weighted sum and fuzzy approaches to solving the bi-objective hybrid interval-stochastic model, Pareto solutions have been reached. Concerning these solutions, the best trade-off cost is conducted in which the uncertainty market price effect called deviation cost has been significantly diminished up to 67.47%. However, the average cost is almost increased by 1.87% compared to the expected obtained cost from a stochastic manner. In the end, to

specify the future works of this study, some recommendations include considering the interaction of different MCMGs, applying network constraints, and other uncertainty handling methods.

References

1. Wei W, Wang J (2020) Modeling and optimization of interdependent energy infrastructures. Springer
2. Xiang Y, Cai H, Gu C, Shen X (2020) Cost-benefit analysis of integrated energy system planning considering demand response. *Energy* 192:116632
3. Mansour-Saatloo A, Agabalaye-Rahvar M, Mirzaei MA, Mohammadi-Ivatloo B, Zare K (2021) Chapter 9 – Economic analysis of energy storage systems in multicarrier microgrids. In: Mohammadi-Ivatloo B, Mohammadpour Shotorbani A, Anvari-Moghaddam A (eds) *Energy storage in energy markets*. Academic Press, pp 173–190
4. Agabalaye-Rahvar M, Mansour-Saatloo A, Mirzaei MA, Mohammadi-Ivatloo B, Zare K, Anvari-Moghaddam AJE (2020) Robust optimal operation strategy for a hybrid energy system based on gas-fired unit, power-to-gas facility and wind power in energy markets. *Energies* 13(22):6131
5. Lekvan AA, Habibifar R, Moradi M, Khoshjahan M, Nojavan S, Jermisittiparsert K (2021) Robust optimization of renewable-based multi-energy micro-grid integrated with flexible energy conversion and storage devices. *Sustain Cities Soc* 64:102532
6. Das S, Acharjee P, Bhattacharya A (2020) Charging scheduling of electric vehicle incorporating grid-to-vehicle (G2V) and vehicle-to-grid (V2G) technology in smart-grid. In: 2020 IEEE international conference on Power Electronics, Smart Grid and Renewable Energy (PESGRE 2020). IEEE, pp 1–6
7. Amir V, Jadid S, Ehsan M (2017) Optimal design of a multi-carrier microgrid (MCMG) considering net zero emission. *Energies* 10(12):2109
8. Vahid A, Jadid S, Ehsan M (2018) Optimal planning of a multi-carrier microgrid (MCMG) considering demand-side management. *Int J Renew Energy Res* 8(1):238–249
9. Amir V, Azimian M, Razavizadeh AS (2019) Reliability-constrained optimal design of multicarrier microgrid. *Int Trans Electr Energy Syst* 29(12):e12131
10. Gao J, Chen J, Qi B, Zhao Y, Peng K, Zhang X (2021) A cost-effective two-stage optimization model for microgrid planning and scheduling with compressed air energy storage and preventive maintenance. *Int J Electr Power Energy Syst* 125:106547
11. Keihan Asl D, Hamed A, Reza Seifi A (2020) Planning, operation and flexibility contribution of multi-carrier energy storage systems in integrated energy systems. *IET Renew Power Gener* 14(3):408–416
12. Massrur HR, Niknam T, Fotuhi-Firuzabad M (2019) Day-ahead energy management framework for a networked gas–heat–electricity microgrid. *IET Gener Transm Distrib* 13(20):4617–4629
13. Shekari T, Gholami A, Aminifar F (2019) Optimal energy management in multi-carrier microgrids: an MILP approach. *J Mod Power Syst Clean Energy* 7(4):876–886
14. Amir V, Jadid S, Ehsan M (2017) Probabilistic optimal power dispatch in multi-carrier networked microgrids under uncertainties. *Energies* 10(11):1770
15. Zakernezhad H, Nazar MS, Shafie-khah M, Catalão JP (2021) Optimal resilient operation of multi-carrier energy systems in electricity markets considering distributed energy resource aggregators. *Appl Energy* 299:117271
16. Nazar MS, Heidari A (2021) Chapter 10 – Optimal resilient scheduling of multicarrier energy distribution system considering energy storages and plug-in electric hybrid vehicles

- contribution scenarios. In: Mohammadi-Ivatloo B, Mohammadpour Shotorbani A, Anvari-Moghaddam A (eds) *Energy storage in energy markets*. Academic Press, pp 191–215
17. Carli R, Cavone G, Pippia T, De Schutter B, Dotoli M (2020) A robust MPC energy scheduling strategy for multi-carrier microgrids. In: in 2020 IEEE 16th international conference on automation science and engineering (CASE). IEEE, pp 152–158
 18. Zeynali S, Nasiri N, Marzband M, Ravadanegh SN (2021) A hybrid robust-stochastic framework for strategic scheduling of integrated wind farm and plug-in hybrid electric vehicle fleets. *Appl Energy* 300:117432
 19. Jiang Y, Wan C, Chen C, Shahidehpour M, Song Y (2019) A hybrid stochastic-interval operation strategy for multi-energy microgrids. *IEEE Trans Smart Grid* 11(1):440–456
 20. Shafie-khah M, Vahid-Ghavidel M, Di Somma M, Graditi G, Siano P, Catalão JP (2020) Management of renewable-based multi-energy microgrids in the presence of electric vehicles. *IET Renew Power Gener* 14(3):417–426
 21. Ding X, Guo Q, Qiannan T, Jermittiparsert K (2021) Economic and environmental assessment of multi-energy microgrids under a hybrid optimization technique. *Sustain Cities Soc* 65: 102630
 22. Mansour-Satloo A, Agabalaye-Rahvar M, Mirzaei MA, Mohammadi-ivatloo B, Zare K, Anvari-Moghaddam A (2021) A hybrid robust-stochastic approach for optimal scheduling of interconnected hydrogen-based energy hubs. *IET Smart Grid* 4(2):241–254
 23. Agabalaye-Rahvar M, Mansour-Saatloo A, Mirzaei MA, Mohammadi-Ivatloo B, Zare K (2021) Economic-environmental stochastic scheduling for hydrogen storage-based smart energy hub coordinated with integrated demand response program. *Int J Energy Res* 45:20232
 24. Mei J, Wang X, Kirtley JL (2020) Optimal scheduling of real multi-carrier energy storage system with hydrogen-based vehicle applications. *IET Renew Power Gener* 14(3):381–388
 25. MansourLakouraj M, Niaz H, Liu JJ, Siano P, Anvari-Moghaddam A (2021) Optimal risk-constrained stochastic scheduling of microgrids with hydrogen vehicles in real-time and day-ahead markets. *J Clean Prod* 318:128452
 26. Mansour-Saatloo A, Mirzaei MA, Mohammadi-Ivatloo B, Zare K (2020) A risk-averse hybrid approach for optimal participation of power-to-hydrogen technology-based multi-energy microgrid in multi-energy markets. *Sustain Cities Soc* 63:102421
 27. Heris M-N et al (2020) Evaluation of hydrogen storage technology in risk-constrained stochastic scheduling of multi-carrier energy systems considering power, gas and heating network constraints. *Int J Hydrogen Energy* 45(55):30129–30141
 28. Chen H, Song J, Zhao J (2021) Synergies between power and hydrogen carriers using fuel-cell hybrid electrical vehicle and power-to-gas storage as new coupling points. *Energy Convers Manage* 246:114670
 29. Karkhaneh J, Allahvirdizadeh Y, Shayanfar H, Galvani S (2020) Risk-constrained probabilistic optimal scheduling of FCPP-CHP based energy hub considering demand-side resources. *Int J Hydrogen Energy* 45(33):16751–16772
 30. Mohammadi M, Noorollahi Y, Mohammadi-ivatloo B, Hosseinzadeh M, Yousefi H, Khorasani ST (2018) Optimal management of energy hubs and smart energy hubs—a review. *Renew Sustain Energy Rev* 89:33–50
 31. Mazidi M, Zakariazadeh A, Jadid S, Siano P (2014) Integrated scheduling of renewable generation and demand response programs in a microgrid. *Energy Convers Manage* 86:1118–1127
 32. Cau G, Cocco D, Petrollese M, Knudsen Kær S, Milan C (2014) Energy management strategy based on short-term generation scheduling for a renewable microgrid using a hydrogen storage system. *Energy Convers and Manage* 87:820–831
 33. Jin X et al (2016) Optimal scheduling approach for a combined cooling, heating and power building microgrid considering virtual storage system. In: 2016 IEEE Power and Energy Society General Meeting (PESGM). IEEE, pp 1–5

34. Liu J, Chen C, Liu Z, Jermstipparsert K, Ghadimi N (2020) An IGDT-based risk-involved optimal bidding strategy for hydrogen storage-based intelligent parking lot of electric vehicles. *J Energy Storage* 27
35. Marzoghi AF, Bahramara S, Adabi F, Nojavan S (2019) Optimal scheduling of intelligent parking lot using interval optimization method in the presence of the electrolyser and fuel cell as hydrogen storage system. *Int J Hydrog Energy* 44(45):24997–25009
36. Chamandoust H, Derakhshan G, Bahramara S (2020) Multi-objective performance of smart hybrid energy system with multi-optimal participation of customers in day-ahead energy market. *Energy Build* 216:109964
37. Ma T, Wu J, Hao L (2017) Energy flow modeling and optimal operation analysis of the micro energy grid based on energy hub. *Energy Convers Manage* 133:292–306
38. Aliasghari P, Mohammadi-Ivatloo B, Abapour M (2020) Risk-based scheduling strategy for electric vehicle aggregator using hybrid Stochastic/IGDT approach. *J Clean Prod* 248:119270
39. Mansour-Saatloo A, Agabalaye-Rahvar M, Mirzaei MA, Mohammadi-Ivatloo B, Abapour M, Zare K (2020) Robust scheduling of hydrogen based smart micro energy hub with integrated demand response. *J Clean Prod* 267:122041
40. Wu X, Qi S, Wang Z, Duan C, Wang X, Li F (2019) Optimal scheduling for microgrids with hydrogen fueling stations considering uncertainty using data-driven approach. *Appl Energy* 253:113568

Index

A

Ant Lion Optimizer (ALO), 176, 178
Autonomous grid, 142

C

Carbon dioxide capture, 90, 91, 93
Cost function, 45, 166, 214

D

Data analytics, 27, 28, 31, 32, 36, 38, 49
Data analytics application in power systems, 25, 28
Data mining, 26, 27, 33, 37, 39, 45, 46
Day-ahead market, 164, 170, 173, 180
Decarbonization, 2–21
Demand response program (DRP), 180, 185, 187, 194, 197, 200, 205–207, 210–212
Desalination, 54–57, 73, 74, 82
Digital energy system operation, 25–49
Direct methanol fuel cell (DMFC), 90, 91, 100, 103–108, 110, 113, 116, 123–127

E

Electric and hydrogen-based vehicles, 209–234
Electricity markets, 163–165, 169, 170, 179, 180, 212–214, 221, 223, 224, 227, 232, 233
Energy optimization, 2
Energy systems, 2–21, 27–29, 54, 67, 131, 185, 210–212

Exergies, 58–60, 66, 67, 70, 71, 73, 74, 76, 80–82, 90, 91, 108–111, 113, 116, 117, 126

F

Fault currents, 134, 137, 139, 140, 143, 152
Fault levels, 144
Fault responses, 140, 143, 144, 156

G

Goswami cycle, 56, 58, 67, 70

H

Heat storage, 65, 82, 213

I

Intelligent parking lot (IPL), 184–188, 191, 197, 199–201, 204, 206, 207, 211–213, 220, 224, 226, 227, 229, 230, 232, 233
Interval optimization framework, 221, 233
Inverter-based resource (IBR), 138–145, 152, 155, 156
Inverters, 139–145

L

Locational marginal price (LMP), 164, 167, 170, 178
Loss of power supply probability (LPSP), 2, 3, 7, 11, 12, 15, 16

M

Machine learning (ML), 28–30, 32–37, 39, 40, 45–47, 49
 Methanol, 88–91, 95, 96, 99–105, 107, 108, 110–112, 116, 120, 122, 123, 125–127
 Microgrid (MG) systems, 1–21
 Multi-carrier microgrid (MCMG), 210–214, 216, 219–221, 223, 224, 226–230, 232–234
 Multigeneration systems, 54, 56, 88, 110

N

Normal distribution function, 165

O

Optimal bidding, 164
 Optimization, 2–21, 32, 34, 40, 49, 56, 60, 67, 78–82, 164–166, 175, 176, 178–180, 185, 186, 188, 189, 196, 197, 210, 211, 213, 221, 233

P

Particle Swarm Optimization-Gravity Search Algorithm (PSO-GSA), 176, 178
 Plug-in hybrid electric vehicles (PHEV), 2, 184, 206, 207
 Prediction intervals (PI), 165, 168

R

Renewable energy resources, 183, 185
 Renewable energy source (RES), 2–7, 10, 11, 13–16, 18–21, 54, 88, 89, 112, 163, 164,

167, 183, 184, 186, 210–213, 215, 224, 233

Robust optimization (RO), 186, 187, 195, 196, 200, 207

S

SCENRED tool, 223
 Social welfare, 164, 165, 211
 Solar energy, 54–56, 63–65, 68, 74, 88, 90, 111, 112, 126
 Source-Independent Protection, 144

T

Teaching-learning-based optimization (TLBO), 176–178

U

Uncertainties, 35, 48, 131, 163–165, 167, 169, 173, 174, 177, 180, 186, 187, 195–197, 207, 211–214, 221–224, 232–234
 Uncertainty management, 212

V

Virtual energy hub (VEH), 184–193, 195, 197–201, 204–207

W

Waste utilization, 109
 Weibull distribution function, 167
 Wind power, 45, 48, 153, 163–165, 167–170, 173–180